Institut für LEICHTBAU
Universität der Bundeswehr München

der Bundeswehr Universität München

Effects of Surface Morphology on the Adhesive Bond Performance of PBF-LB/M Manufactured Ti6Al4V Parts

M.Sc. Emre Ertürk

Vollständiger Abdruck der von der Fakultät für Luft- und Raumfahrttechnik der Universität der Bundeswehr München zur Erlangung des akademischen Grades eines

Doktor-Ingenieurs (Dr.-Ing.)

angenommenen Dissertation.

Gutachter:

1. Prof. Dr.-Ing. Philipp Höfer
2. Prof. Dr. Lucas da Silva

Die Dissertation wurde am 14.01.2026 bei der Universität der Bundeswehr München eingereicht und durch die Fakultät für Luft- und Raumfahrttechnik am 26.03.2026 angenommen. Die mündliche Prüfung fand am 23.04.2026 statt.

Acknowledgments

I would like to express my sincere appreciation to my supervisor, Prof. Dr. Philipp Höfer, for giving me the opportunity to pursue this PhD and for his continuous support, guidance, and trust throughout the entire process. I am also grateful to Prof. Dr. Lucas F. M. da Silva for kindly agreeing to be part of my thesis examination committee, and to Prof. Dr. Eric Jägle for acting as the examination chair.

My sincere thanks go to the entire team of the Institute of Lightweight Engineering. It was a truly wonderful time at the University of the Bundeswehr Munich, and I am grateful that I was able to share this period with such great people. In particular, I would like to thank Dr. Pablo Vitale, Gregor Diez and Dr. Bruno Musil for the valuable exchanges and discussions, as well as the laboratory team for their support during the experimental work.

I also express my deepest gratitude to the Institute of Materials Science (University of the Bundeswehr Munich) and the Bundeswehr research institute WIWeB for providing me access to their laboratory facilities and equipment, which were essential for the progress of my research. I am especially grateful to Dr. Jens Holtmannspötter and Dr. Elisa Arikan for their highly valuable feedback on my research.

Thanks to the research project BLANCA, I was able to pursue this PhD. I sincerely thank the Bavarian Ministry of Economic Affairs, Regional Development and Energy (StMWi) for funding the project, and I appreciate the entire project team for the inspiring collaboration and the insightful exchanges.

Finally, I extend my heartfelt thanks to my family and friends for their unwavering support and encouragement, particularly during challenging and stressful periods. Their belief in me eased the path through this journey.

Abstract

Laser Powder Bed Fusion (PBF-LB/M) processed Ti6Al4V parts are widely used in high-performance applications, such as in aerospace. To fully utilize the lightweight potential of additively manufactured parts, structural adhesive bonding can be applied as a viable alternative to conventional joining methods. However, reliable adhesive bonding requires an in-depth understanding of the adherends surface morphology influences on bond performance. In the case of PBF-LB-Ti6Al4V surfaces, the bonding capabilities and limitations have to be investigated by considering the effects of their inherent surface roughness. Moreover, it is crucial to determine a suitable surface pretreatment process, potentially leveraging the inherent roughness, ensuring adhesive bonds with high strength, fatigue resistance and environmental durability.

This work presents advancements in structural adhesive bonding of PBF-LB-Ti6Al4V parts, with a primary focus on the influences of surface morphology on bond performance. The PBF-LB-surfaces were characterized in as-built and pretreated conditions, considering different build orientations. Subsequently, the surface-related effects on the bond performance were assessed for quasi-static, fatigue and environmental loading cases. Comprehensive fracture surface analysis assisted in analyzing the surface morphology influences and interactions between the surface features. The main adhesion-promoting surface features on the as-built surfaces were found to be the partially melted particles from the powder bed, which proved to be highly effective in causing mechanical interlocking in the adhesive. The number of particles correlated with the strengths and fatigue lifetimes of the adhesive bonds. However, in areas with no or few attached particles, the as-built surfaces exhibited substantial adhesive failure and poor bond durability.

To enhance bond performance, the pretreatment processes grit blasting and laser treatment were investigated. A particular focus was placed on laser treatment, which is a key novel contribution of this work for bond preparation of PBF-LB-Ti6Al4V parts. Different laser fluences were assessed and optimized to generate a distinct nanoporous oxide layer with uniform thickness on the surface. This resulted in a hierarchical surface morphology, consisting of the inherent surface roughness of the as-built surfaces superimposed with the laser-induced uniform nanoporous oxide layer. With this surface morphology, a significant improvement in bond performance was achieved compared to the as-built condition. An almost complete cohesive failure in the adhesive was reached across all applied loading cases. Digital image correlation measurements further revealed that laser treatment substantially slowed down crack growth in the adhesive bond during cyclic fatigue loading.

As an application, co-cured hybrid joints with pin-reinforcements between PBF-LB-Ti6Al4V and CFRP were examined, using as-built, release-agent-coated, and laser-treated titanium surfaces to evaluate the role of surface morphologies in hybrid joints. A highly similar mechanical performance was found for the hybrid joints with as-built and release-agent-coated surfaces. In contrast, laser treatment significantly enhanced the joint stiffness, limit load, and energy absorption, while the ultimate tensile shear strength increased moderately.

Kurzfassung

Mittels Laserstrahlschmelzen (PBF-LB/M) hergestellte Bauteile aus Ti6Al4V finden breite Anwendung in der Luft- und Raumfahrt. Um das Leichtbaupotenzial additiv gefertigter Bauteile voll auszuschöpfen, kann das strukturelle Kleben als eine Alternative zu konventionellen Fügeverfahren eingesetzt werden. Für eine zuverlässige Anwendung ist jedoch ein tiefgehendes Verständnis über die Einflüsse der Oberflächenmorphologie auf die Verbundeigenschaften erforderlich. Im Fall von PBF-LB-Ti6Al4V muss die Oberflächenadhäsion unter Berücksichtigung der inhärenten Rauheit bewertet werden. Zudem ist es notwendig, ein geeignetes Vorbehandlungsverfahren zu bestimmen, um hochfeste, ermüdungs- und alterungsbeständige Klebeverbindungen herzustellen.

In dieser Arbeit werden Fortschritte im strukturellen Kleben von PBF-LB-Ti6Al4V-Bauteilen vorgestellt, wobei der Schwerpunkt auf den Einflüssen der Oberflächenmorphologie auf die Verbundeigenschaften liegt. Die PBF-LB-Oberflächen wurden im gedruckten (as-built) und vorbehandelten Zustand charakterisiert. Dabei wurden verschiedene Bauteilorientierungen berücksichtigt. Anschließend erfolgte die Analyse der Oberflächeneinflüsse auf die Verbundeigenschaften für quasi-statische, ermüdungs- sowie umweltbedingte Belastungsfälle. Umfassende Bruchflächenanalysen unterstützten die Untersuchung der Oberflächeneffekte und deren Wechselwirkungen. Es hat sich gezeigt, dass bei den as-built Oberflächen insbesondere die teilverschmolzenen Pulverpartikel zur Adhäsion beitragen, indem eine mechanische Verankerung im Klebstoff induziert wird. Die Partikelanzahl korrelierte mit den Festigkeiten und Lebensdauern der Klebeverbindungen. In Bereichen mit wenigen oder fehlenden Partikeln zeigten die as-built Oberflächen hingegen ein deutliches Adhäsionsversagen und eine geringe Alterungsbeständigkeit in der Klebeverbindung.

Zur Verbesserung der Verbundeigenschaften wurden die Oberflächenvorbehandlungen mittels Sandstrahlen und eines Laserverfahrens untersucht. Ein besonderer Schwerpunkt lag auf der Laserbehandlung, die einen zentralen neuen Beitrag dieser Arbeit zur Vorbehandlung von PBF-LB-Ti6Al4V-Bauteilen darstellt. Verschiedene Laserfluenz-Einstellungen wurden betrachtet und optimiert, um eine nanoporöse Oxidschicht mit homogener Dicke zu erzeugen. Dadurch konnte eine hierarchische Oberflächenmorphologie hergestellt werden, bestehend aus der inhärenten Rauheit der PBF-LB-Oberfläche, die durch eine laserinduzierte Nanostruktur überlagert wird. Mit dieser Oberfläche konnte in allen untersuchten Lastfällen ein nahezu vollständiges kohäsives Versagen im Klebstoff erreicht werden.

Abschließend wurden Pin-verstärkte Hybridverbindungen zwischen PBF-LB-Ti6Al4V und CFK untersucht, die mittels co-curing hergestellt wurden. Dabei kamen unbehandelte, trennmittelbeschichtete sowie laserbehandelte Titanoberflächen zum Einsatz, um den Oberflächeneinfluss in hybriden Fügeverbindungen zu bewerten. Für die Verbindungen mit unbehandelter und trennmittelbeschichteter Titanoberfläche ergab sich ein ähnliches mechanisches Verhalten, während die Laserbehandlung zu signifikanten Erhöhungen der Verbundsteifigkeit, Grenzlast (Schadensinitiierung) und Energieaufnahme der Hybridverbindung führte.

Contents

List of Figures xi
List of Tables xiii
Nomenclature xv
1 Introduction 1
1.1 Motivation 1
1.2 Research scope and objectives of the thesis 2
1.3 Structure of the thesis 3
2 State of the Art 5
2.1 Additive manufacturing 5
2.1.1 PBF-LB/M processed Ti6Al4V 7
2.2 Structural adhesive bonding 9
2.2.1 Adhesion mechanisms 11
2.2.2 Surface pretreatment methods 14
2.2.3 Adhesive bond testing 18
2.2.4 Hybrid metal-composite joining 21
3 Materials and Methods 23
3.1 Materials 23
3.1.1 Substrates 23
3.1.2 Adhesives 24
3.2 Methods 24
4 Results 27
4.1 Analysis of surface morphologies and their effects on tensile bond strength (publication 1) 27
4.1.1 Influences of PBF-LB/M machine and adhesive on bond strength 28
4.2 Effects of surface morphologies under quasi-static, fatigue and environmental loading conditions (publication 2) 30
4.3 Optimizing the bond performance by laser-induced hierarchical surface morphologies (publication 3) 32
4.3.1 Comparison with anodization processes 34
4.4 Role of surface morphologies in hybrid structural joints (publication 4) 36
5 Conclusions and Outlook 37
References 41
Appendix 55

List of Figures

Figure 1: Schematic representation of powder-type metal AM-techniques: (a) PBF-LB/M, (b) PBF-EB/M and (c) DED-LB/p [41-43]. 6
Figure 2: Illustration of operating parameters in PBF-LB/M. Reprinted from Shipley et al. [49] with permission from Elsevier (© 2018). 7
Figure 3: SEM images of as-built PBF-LB-Ti6Al4V surfaces with 45° build orientation, showing both the upskin and downskin sides. Adapted from Nusom et al. [24] with permission from Elsevier (© 2018). 8
Figure 4: Influence of the build angle on the roughness of downskin surfaces for a PBF-LB-processed metal. Reprinted from Utley [58]. 9
Figure 5: Failure modes of adhesive joints: (a) cohesive failure in the adhesive, (b) cohesive failure in the adherend, (c) adhesive failure, (d) mixed-mode failure [15]. 10
Figure 6: Overview of adhesion theories [13]. 11
Figure 7: Summary of different surface pretreatment methods [25,74-76]. 14
Figure 8: Structural components of a laser system. Adapted from Islam et al. [83] with permission from Springer Nature (© 2023). 16
Figure 9: Laser processed Ti6Al4V surfaces: (a) laser micro-texturing of grid structures (adapted from Maressa et al. [93] with permission from Taylor & Francis (© 2014)), (b) laser induced nanoporous oxide layer (adapted from Kurtovic et al. [98] with permission from Elsevier (© 2013)). 18
Figure 10: Co-cured hybrid joint between stainless steel with pin structures and a glass fiber reinforced polyester composite material (Comeld^{Tm} joint) [137]. 21
Figure 11: Fracture cross-section evaluated by SEM of a pinned PBF-LB-Ti6Al4V-CFRP joint after mode II ENF fatigue testing, showing the damage state in the vicinity of a pin (adapted from Bagnato et al. [145] under the CC BY-NC license). 22
Figure 12: Overview of the applied methods. 25
Figure 13: Tensile bond strengths of PBF-LB-Ti6Al4V/epoxy CATT joints, shown for different surface conditions and build orientations. The results for a milled surface are depicted as a reference. 28
Figure 14: Comparison of tensile bond strengths between Ti6Al4V-adherends manufactured on a Concept Laser M2 and Trumpf TruPrint 5000 machine: (a) as-built surfaces, (b) laser-treated surfaces with A0 build orientation. All CATT joints were bonded with EA9395. 29
Figure 15: Comparison of tensile bond strengths between CATT joints bonded with EA9395 and EA9396: (a) as-built surfaces, (b) laser-treated surfaces with A0 build orientation. All Ti6Al4V-adherends were manufactured on a Trumpf TruPrint 5000 machine. 29

Figure 16: SEM images and height profile of a A90-oriented PBF-LB-Ti6Al4V surface after laser treatment. The IBM-prepared cross section views were evaluated at a laser pulse edge (A-A) and laser pulse depression (B-B). 31

Figure 17: SEM images of IBM-prepared cross-sections of laser-treated PBF-LB-Ti6Al4V surfaces for the power levels (a) P60, (b) P70 and (c) P90, evaluated at a laser pulse edge (A–A) and a laser pulse depression (B–B). 33

Figure 18: Comparison of tensile shear strengths between SLJs with laser-treated (P70) and NaTESi anodized PBF-LB-Ti6Al4V-adherends. 35

List of Tables

Table 1: Chemical and physical interaction forces at interfaces [13,59]. 12
Table 2: Tensile properties of PBF-LB-Ti6Al4V fabricated on a Concept Laser M2 machine for a build orientation in gas flow direction [149]. 23
Table 3: Orthotropic material properties of the used unidirectional (UD) and woven prepreg materials. 24
Table 4: Tensile shear properties of Loctite EA9395 and Loctite EA9396 for a standard cure of five days at 25°C according to the adhesive manufacturer [131,154,155]. 24
Table 5: NaTESi process parameters [78,79] 133

Nomenclature

Latin symbols

Symbol	Description	Unit
a	Crack length	mm
A_s	Laser spot area	mm^2
b	Substrate width	mm
d	Focused laser spot diameter	mm
e	Laser track spacing	mm
E	Young's modulus	MPa
E_d	Average laser fluence	J/mm^2
E_s	Tensile modulus	MPa
f	Frequency	Hz
G	Shear modulus	MPa
G_{IC}	Mode I fracture toughness	J/mm^2
h	Substrate thickness	mm
P	Force	N
P_0	Laser pump power	W
P_a	Average output power	W
$P_{max,a}$	Maximum average output power	W
R	Load ratio	-
R_a	Arithmetic mean height (line)	mm
S_a	Arithmetic mean height (area)	mm
v	velocity	mm/s
W	Total energy absorption	J
W_a	Work of adhesion	J/mm^2

Greek symbols

Symbol	Description	Unit
γ_1, γ_2	Surface free energy	J/mm^2
γ_{12}	Interfacial free energy	J/mm^2
γ_{LV}	Surface free energy at liquid/vapor interface	J/mm^2
δ	Crack mouth opening displacement	mm

ε	Strain	%
θ	Contact angle	°
λ	Wavelength	mm
σ	Normal stress	MPa
σ_{max}	Maximum stress during cyclic loading	MPa
τ	Shear stress	MPa
ν	Poisson's ratio	-
ψ	Tilt angle	°

Abbreviations

AB	As-built
AM	Additive manufacturing
BTF	Buy-to-fly
CAA	Chromic acid anodization
CAM	Contact angle measurement
CATT	Centrifugal adhesion testing technology
CC	Co-curing
CFRP	Carbon fiber reinforced polymer
CLSM	Confocal laser scanning microscopy
CMT	Cold metal transfer
CO_2	Carbon dioxide
CP	Control point
CTE	Coefficient of thermal expansion
DCB	Double cantilever beam
DED-LB/p	Directed energy deposition - laser beam/powder
DIC	Digital image correlation
EDM	Electrical discharge machining
ENF	End notched flexure
GB	Grit blasted
HCF	High cycle fatigue
HIP	Hot isostatic pressing
IBM	Ion beam milling
LCF	Low cycle fatigue
LPP	Low pressure plasma

LT	Laser-treated
NDT	Non-destructive testing
Nd:YAG	Neodymium-doped yttrium aluminum garnet
Nd:YVO_4	Neodymium-doped yttrium orthovanadate
PAA	Phosphoric acid anodization
PBF-EB/M	Powder bed fusion - electron beam/metal
PBF-LB/M	Powder bed fusion - laser beam/metal
PEEK	Polyetheretherketone
PT	Platinum
PTFE	Polytetrafluoroethylene
RA	Release-agent
RH	Relative humidity
RO	Research objective
SB	Secondary bonding
SBT	Simple beam theory
SE	Secondary electrons
SEM	Scanning electron microscopy
SLJ	Single step-lap joint
SLS	Single lap shear
TAST	Thick adherend shear test
TiO_2	Titanium dioxide
UD	Unidirectional
UV	Ultraviolet
vdW	van der Waals
XRD	X-Ray Diffraction

1 Introduction

1.1 Motivation

The growing need to reduce greenhouse gas emissions caused by transportation sectors such as aviation, along with the increasing scarcity of resources, underscores the importance of lightweight engineering. Additive manufacturing (AM) offers significant lightweight potential, as it enables the material-efficient production of complex, load path-optimized lightweight structures [1-3]. This is particularly advantageous for expensive materials such as titanium, where conventional manufacturing methods often result in significant material loss during machining. The ratio of the initial raw material weight to the final part weight, known as the buy-to-fly (BTF) ratio, is estimated to be 12-25:1 for titanium aircraft components produced by traditional manufacturing processes [1] and 3-12:1 when using AM [4].

In the aerospace industry, laser powder bed fusion (PBF-LB/M) processed Ti6Al4V parts are used for highly loaded structural components, such as load introduction elements (e.g., brackets and mounting structures) [5], engine components [6] and various other aerospace structures [2]. The main reason for the use of Ti6Al4V is its exceptional property profile, including outstanding weight-specific stiffness and strength, excellent corrosion resistance and good thermal stability [7,8]. In modern aerospace structures, hybrid joints combining titanium and composites have become more prevalent, as composite materials are commonly used for weight reduction. To fully utilize the lightweight potential of AM-parts in metal-composite and metal-metal components, structural adhesive bonding can be applied as a viable alternative to conventional joining methods. Mechanical joining via bolts, screws, or rivets is still often conducted, leaving a high potential for mass reduction [9-12].

Structural adhesive bonding offers several major advantages over mechanical joining methods. These include, a more uniform load distribution, enhanced resistance to fatigue and corrosion, a lower weight penalty and the structural integrity of the adherends is preserved, which is particularly important for composites [13,14]. Moreover, the combination of AM and structural adhesive bonding is particularly interesting, since the AM parts can be designed with tailored stiffness to reduce local stress concentrations within the adhesive bond that often arise from large stiffness gradients, and are a common problem limiting the load-bearing capability of adhesive bonds [15].

A decisive factor for the adhesive bond performance is the surface condition of the substrates. The most relevant surface properties for bonding are roughness, chemistry and wettability. The surface roughness is a crucial aspect, since it can enhance adhesion by increasing the contact area to the adhesive, facilitating the formation of chemical and dispersive interfacial bonds, and causing mechanical interlocking of the adhesive. Nevertheless, it can also negatively affect adhesion by reducing wettability and causing stress concentrations in the adhesive bond [15-17]. Therefore, it is of major importance to understand how surface morphologies influence adhesion and bond performance under various loading conditions.

The effects of surface textures on the structural behavior of bonded joints have been extensively investigated in the literature [18]. Most studies focused on evaluating general roughness values and attempted to correlate them with bond strengths, without systematically analyzing specific surface features and distinguishing between different roughness scales. Further research is therefore required to improve the understanding of surface-structure-related effects on adhesion and bond performance, particularly for fatigue loading [18]. In the case of PBF-LB-Ti6Al4V parts, the as-built (i.e., only degreased) surfaces exhibit distinct, process-induced inherent roughness, which is usually removed by surface finishing (e.g., machining) due to its detrimental effect on the fatigue performance of the parts [19-21]. However, this roughness may be beneficial for adhesive bonding applications. Therefore, the bonding capabilities and limitations of PBF-LB-Ti6Al4V surfaces should be investigated, considering the inherent roughness and application-relevant loading conditions. There have been only a few studies [22-24] addressing this topic, thereby solely focusing on quasi-static loading conditions.

Furthermore, bonding without surface pretreatments typically results in low adhesion because of contamination and suboptimal surface properties [25,26]. Consequently, numerous surface treatment methods have been developed based on different working principles, which result in various surface morphologies. However, due to increasingly stringent environmental and safety regulations, such as REACH [27], the number of approved and effective pretreatment methods is decreasing. This highlights the necessity to determine a sustainable surface pretreatment approach for PBF-LB/M-processed parts, which enables the fabrication of adhesive bonds with high strength, fatigue resistance and environmental durability.

1.2 Research scope and objectives of the thesis

This thesis presents experimental investigations on structural adhesive bonding of PBF-LB/M-processed Ti6Al4V parts. The primary focus lies in understanding the surface morphology influences on adhesive bond performance in metal–metal joints bonded with an epoxy adhesive. Surface characterization is conducted for as-built PBF-LB-Ti6Al4V surfaces (i.e., degreased only), considering different build orientations. Moreover, surface modifications induced by grit blasting and laser treatment are analyzed to assess their potential as surface pretreatment methods. In addition, milled and NaTESi-pretreated surfaces serve as references in this work.
The surface morphologies are characterized using Scanning Electron Microscopy (SEM) and Confocal Laser Scanning Microscopy (CLSM), while the macroscopic wettability is examined by contact angle measurements. For the laser-treated substrates, Ion Beam Milling (IBM) is applied to enable cross-sectional SEM analysis of both the surface and the underlying material. Furthermore, laser-induced residual stresses in the near-surface region are assessed using X-Ray Diffraction (XRD).

The effects of the surface morphologies on bond performance are investigated for quasi-static, fatigue and environmental loading conditions. In the quasi-static tests, the tensile bond strength is examined by centrifugal adhesion testing (CATT), while the mode I fracture toughness is determined by double cantilever beam (DCB) testing. Moreover, single step-lap joint (SLJ) testing is performed to comprehensively assess the bond strength, environmental bond durability and fatigue behavior under mixed-mode loading. In the SLJ-fatigue tests, cyclic loads

are applied at various levels to evaluate both low-cycle fatigue (LCF) and high-cycle fatigue (HCF) behavior, while digital image correlation (DIC) is used to monitor crack growth and assess surface-related effects. In this thesis, environmental bond durability is examined for a hydrothermal aging condition. In addition, extensive fracture surface analysis is carried out to assist in identifying the key contributions of the surfaces features to bond performance and determining interactions between different morphological structures.

Finally, as an application of PBF-LB-parts, co-cured hybrid SLJs between PBF-LB-Ti6Al4V and CFRP are investigated, as this material combination is prevalent in aerospace structures. The titanium adherend surface conditions as-built, release-agent-coated, and laser-treated are considered to evaluate the role of surface morphologies in hybrid joints.

The following five research objectives are addressed in this thesis:

RO$_1$ *Determine the surface morphology influences of PBF-LB-processed Ti6Al4V parts on adhesive bond performance for quasi-static, fatigue and environmental loading conditions.*

RO$_2$ *Assess the bonding capabilities and limitations of as-built PBF-LB-Ti6Al4V parts in adhesively bonded joints.*

RO$_3$ *Analyze surface treatment induced structural modifications and their effect on bond performance, with emphasis on the contributions and interactions of specific surface features.*

RO$_4$ *Develop a sustainable surface pretreatment process for PBF-LB-Ti6Al4V that enables the fabrication of adhesive bonds with high strength, fatigue resistance and environmental durability.*

RO$_5$ *Enhance the understanding of the role of surface morphologies in co-cured hybrid joints between PBF-LB-Ti6Al4V and CFRP.*

1.3 Structure of the thesis

This work is a cumulative thesis based on four peer-reviewed publications and is structured as follows. Chapter 2 provides the state of the art, covering general concepts and scientific work relevant to this thesis on additive manufacturing (Section 2.1) and structural adhesive bonding (Section 2.2). Subsequently, an overview of the utilized materials and methods is given in Chapter 3. The main findings of the publications are synthesized and discussed in Chapter 4. Each publication is addressed in a dedicated subchapter, with transition sections between them to maintain a coherent narrative flow and incorporate additional relevant information that supports the overall context of the thesis. Finally, Chapter 5 outlines the key conclusions of this dissertation and offers an outlook on future research opportunities. The full publications are included in the appendix. The order of the studies, their individual focus areas, and how they build upon each other is described in the following.

The first publication analyzes the surface morphology and wettability of PBF-LB-Ti6Al4V surfaces in as-built and pretreated conditions. Grit blasting and laser treatment are considered as surface treatment methods. With this initial study, the surface morphology influences on bond performance and the bonding potential of the as-built surfaces are investigated for uniform tensile loading. The second publication builds upon this study by examining the surface morphology effects in more detail for both as-built and pretreated surfaces. Tensile shear tests are conducted, considering quasi-static, fatigue and environmental loading conditions to obtain a broader understanding of the effects on bond performance. In the third study, the focus is specifically on laser treatment, as this pretreatment method proved effective in the preceding investigations. Three laser settings with low, medium and high laser power are evaluated to determine laser fluence-related effects. The laser-induced structural modifications of the substrate and their impact on tensile strength, mode I fracture toughness, environmental durability, and fatigue resistance of the adhesive bonds are analyzed in this study. The fourth publication explores the application of PBF-LB Ti6Al4V parts in co-cured hybrid joints with composite components, particularly focusing on the role of surface morphologies in hybrid joints. It should be noted that the research presented in these publications was conducted as part of the research project BLANCA. This project was a collaboration between the University of the Bundeswehr Munich and industrial partners to optimize load introductions in sandwich structures through the combined use of structural adhesive bonding and additive manufacturing.

A list of the publications, along with the research objectives addressed in each study, is provided below:

Publication 1: "*Surface morphology influences of PBF-LB manufactured Ti6Al4V parts on adhesive bond strength—investigation of as-built and surface-treated conditions*"
Research objectives: RO_1, RO_2, RO_3

Publication 2: "*Surface morphology influences on the adhesive bond performance of PBF-LB manufactured Ti6Al4V parts – investigation of quasi-static and fatigue loading conditions*"
Research objectives: RO_1, RO_2, RO_3

Publication 3: "*Laser treatment of PBF-LB manufactured Ti6Al4V parts for structural adhesive bonding*"
Research objectives: RO_1, RO_3, RO_4

Publication 4: "*Hybrid structural joints between PBF-LB manufactured Ti6Al4V and CFRP – role of surface morphologies*"
Research objectives: RO_5

2 State of the Art

This chapter summarizes the theoretical background and scientific work relevant to this thesis on additive manufacturing (Section 2.1) and structural adhesive bonding (Section 2.2). More detailed information on scientific studies is provided in the attached publications. Section 2.1 begins with a brief overview of the most widely used AM-techniques for metals, followed by a more detailed explanation of the PBF-LB/M process. Particular attention is given to process-induced surface characteristics of PBF-LB-produced Ti6Al4V parts. Section 2.2 introduces fundamental adhesion theories and emphasizes the critical role of surface properties in adhesive bonding. In addition, an overview of common surface preparation techniques and adhesive bond testing methods is presented. This section concludes with a review of the state of the art on hybrid metal-composite joints.

2.1 Additive manufacturing

Originating in the 1980s as a tool for rapid prototyping, Additive Manufacturing (AM) has since evolved into a widely used production technology across various industries [28,29]. A standardized definition of AM is provided in ISO/ASTM 52900:2021 [30], which describes it as a "process of joining materials to make parts from 3D model data, usually layer upon layer, as opposed to subtractive manufacturing and formative manufacturing methodologies." The general procedure begins with the design of a digital 3D model of the part. This model is then sliced into discrete layers with defined thickness, while the orientation of the part in the build chamber and the process parameters are also specified. Based on this data, the part is typically layer-wise fabricated by repetitive deposition and melting of material using an energy source. Once all layers are built, the final component may undergo post-processing, such as heat treatment, support removal, or surface finishing, depending on the application-specific requirements [31,32]. Unlike conventional manufacturing processes, AM allows for the efficient production of complex, customized structures with high lightweight potential. Moreover, the extensive design freedom in combination with the low material waste renders AM highly suitable for the production of high-performance structures made from expensive and difficult-to-machine materials such as titanium [33-35].

AM-techniques for metals can be classified according to the type of material feedstock and energy source [36,37]. Frazier [36] proposed three main categories: powder bed, powder feed, and wire feed processes. For the fabrication of dense metallic structures, powder-based AM-techniques are mostly used and industrially established, particularly PBF-LB/M, Electron Beam Powder Bed Fusion (PBF-EB/M) and Directed Energy Deposition with powder feedstock (DED-LB/p) [38-40]. An illustration of these processes is provided in Figure 1. PBF-LB/M [41] is a powder bed-based process conducted in an inert gas atmosphere. In this production method, metal powder is moved from a reservoir to the build platform using a recoater, ensuring even deposition of a thin powder layer. Subsequently, the powder is selectively melted by a laser beam according to the scan paths defined in the 3D model of the part. Once a layer is completed,

the build platform is lowered by one layer thickness, and the process is repeated until the full part is fabricated. The same principle applies to PBF-EB/M [42], with the main differences being that an electron beam is used as an energy source and that the process operates under vacuum conditions. In contrast, DED-LB/p [43] is a powder feed process in which the metal powder is directly fed through a nozzle into a laser beam generated melt pool on a substrate surface. The powder is transported by an inert carrier gas to the melt zone, where it fuses with the substrate, forming a bead. Overlapping the beads, either layer by layer or along freeform geometries, results in the final part.

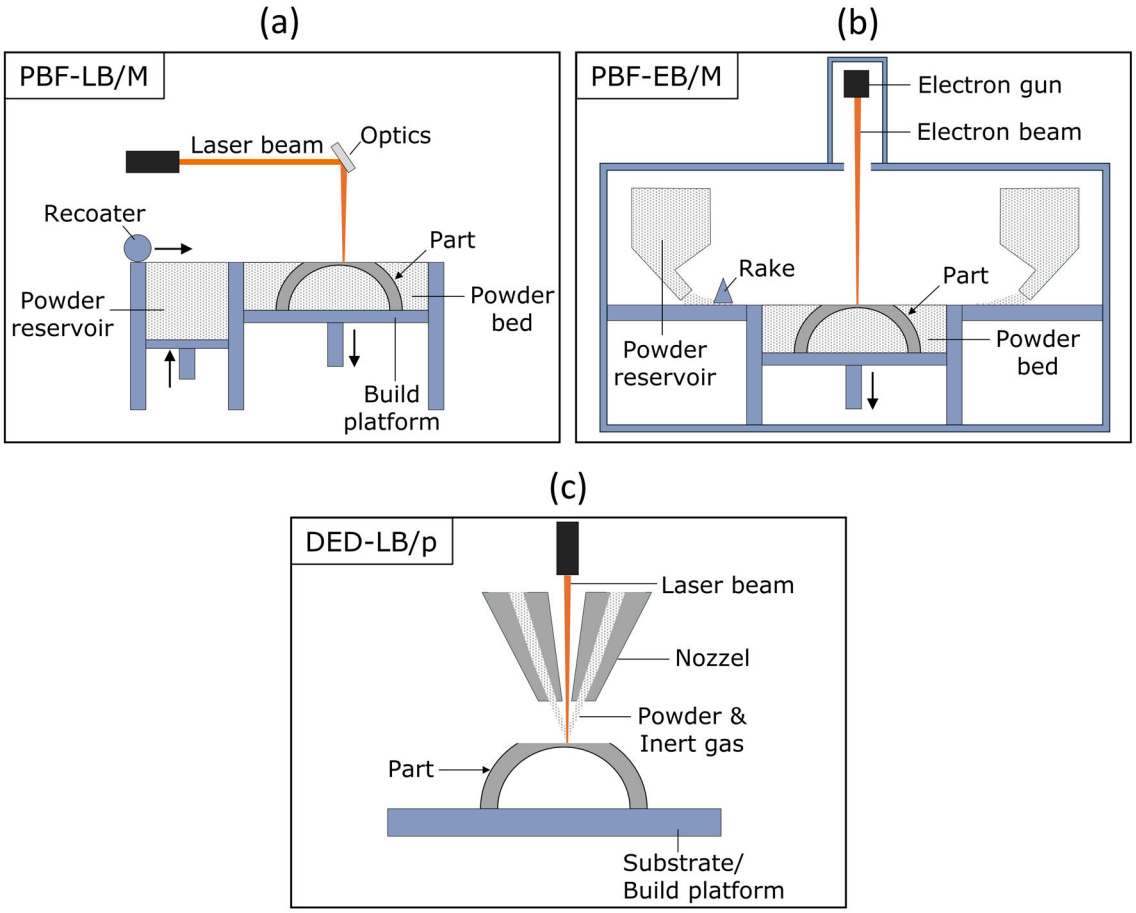


Figure 1: Schematic representation of powder-type metal AM-techniques: (a) PBF-LB/M, (b) PBF-EB/M and (c) DED-LB/p [41-43].

DED-techniques are capable of accurately adding material onto existing components, making them particularly suitable for repair applications and feature addition. However, a key limitation of DED is its inability to fabricate geometries as complex as those achievable with PBF-methods [2,31]. Among the AM-techniques presented, PBF-LB/M offers the highest resolution and dimensional accuracy. Furthermore, its broader material compatibility compared to PBF-EB/M and the absence of a vacuum requirement contribute to its widespread industrial adoption [44,45].

2.1.1 PBF-LB/M processed Ti6Al4V

Ti6Al4V is one of the most commonly used materials in additive manufacturing due to its exceptional mechanical and thermal properties. It offers excellent corrosion resistance, a high strength-to-weight ratio and thermal stability. Thus, the aerospace industry represents a major area of application, especially for manufacturing components subjected to high mechanical and thermal loads [46,47]. The industrial relevance of Ti6Al4V has also led to extensive scientific research on PBF-LB-processed Ti6Al4V, with numerous studies focusing on its microstructure, residual stress formation, defect characteristics, mechanical performance, and surface quality [36,46].

In general, the properties of PBF-LB-Ti6Al4V are strongly influenced by various process parameters, including laser power, layer thickness, scanning speed, hatch spacing and scanning strategy [48]. These operating parameters are illustrated in Figure 2. The process parameters collectively affect the thermal history within the material during processing, which is a decisive factor determining the resulting material properties.

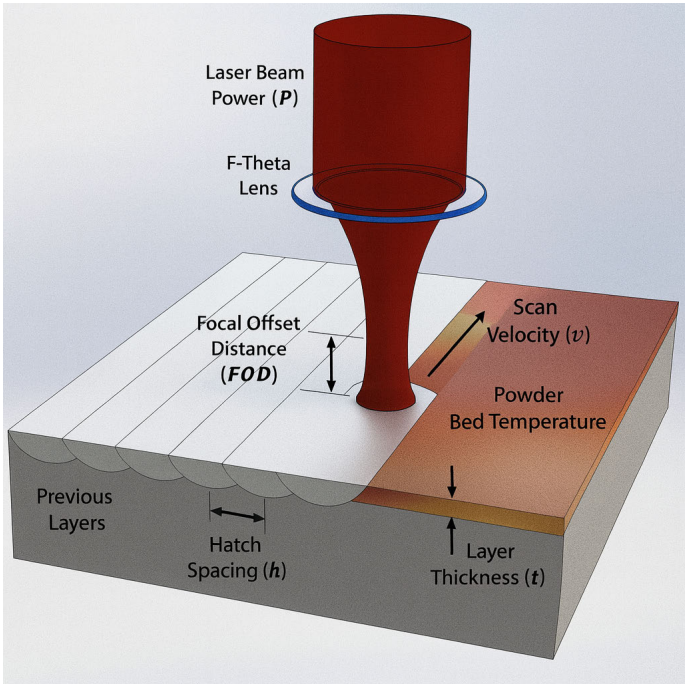


Figure 2: Illustration of operating parameters in PBF-LB/M. Reprinted from Shipley et al. [49] with permission from Elsevier (© 2018).

The as-built microstructure of PBF-LB-Ti6Al4V typically consists of a fine acicular martensitic α' phase within columnar prior-β grains, which are predominantly oriented along the build direction [50,51]. The α' phase is a common result of rapid cooling, typical for PBF-LB/M. It produces parts with higher strength, but reduced ductility compared to conventionally manufactured Ti6Al4V [38,51]. Through post-process heat treatments, such as stress relief annealing and hot isostatic pressing (HIP), it is possible to enhance the ductility by transforming the α' martensite to equilibrium α + β phases. This allows to achieve a more favorable balance between strength and ductility [52]. Further benefits of a post heat treatment are that it reduces the process-induced porosity and residual stresses in Ti6Al4V. Porosity is usually caused by non-optimal process parameters or gas entrapment, while the high thermal

gradients inherent to the PBF-LB-process generate substantial residual stresses. Both porosity and residual stress can significantly deteriorate the mechanical properties of the fabricated part and should therefore be minimized [46,51].

PBF-LB-Ti6Al4V parts exhibit under quasi-static tensile loading comparable or even superior mechanical properties than cast or wrought Ti6Al4V parts. However, their fatigue performance is often significantly inferior due to early crack initiation induced by process-related porosity, tensile residual stresses, and inherent surface roughness [38]. While porosity and residual stress can be effectively mitigated through post-process heat treatments, the surface roughness is typically reduced by surface finishing, particularly in critical applications that demand high fatigue resistance [19-21]. PBF-LB-processed Ti6Al4V components subjected to HIP and subsequent surface machining can exhibit fatigue properties similar to wrought Ti6Al4V [53,54].

The as-built surfaces of PBF-LB-Ti6Al4V are characterized by different process-generated surface structures, which form complex and irregular topographies. The main inherent surface features include partially melted particles from the powder bed, spattered particles caused by melt pool instabilities (balling effect) and stair-step structures on inclined surfaces due to the layer-wise manufacturing [51,55]. Moreover, melt-pool flow patterns and melt overflow bumps are further typical surface structures, while fissures or cracks and oxidized regions may also be present. These surface features are differently pronounced depending on several factors, including build orientation, process parameters and powder quality [55]. The surface morphologies of a PBF-LB-processed Ti6Al4V part, oriented at 45° relative to the build platform, are shown in Figure 3 for both the upskin and downskin sides.

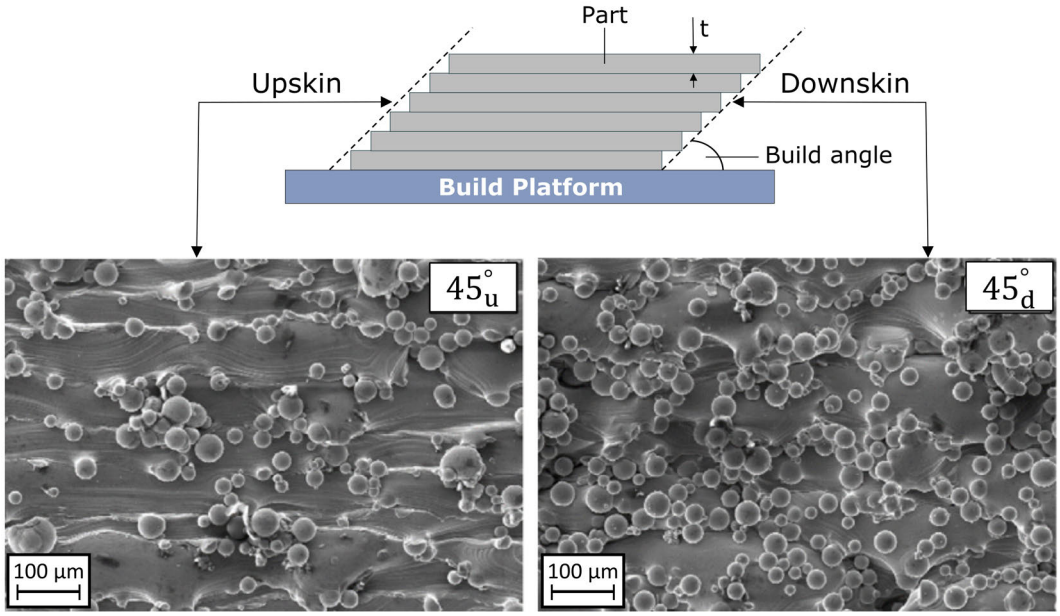


Figure 3: SEM images of as-built PBF-LB-Ti6Al4V surfaces with 45° build orientation, showing both the upskin and downskin sides. Adapted from Nusom et al. [24] with permission from Elsevier (© 2018).

The downward-facing surfaces exhibit significantly higher microscopic roughness due to slower heat dissipation and the presence of more adjacent powder particles on this side of the

part [56]. This leads to excessive sintering or adhering of particles on the surface, commonly referred to as dross formation [57]. The profile surface roughness R_a (i.e., arithmetical mean height) of PBF-LB-fabricated metals typically ranges from 5-30 µm for upskin and vertically oriented surfaces. In contrast, downskin surfaces can reach R_a values above 100 µm, depending on the build orientation angle [55]. The effect of the build angle on the roughness of downskin surfaces is illustrated in Figure 4 for PBF-LB-processed metal parts. With decreasing elevation angle, the downskin gets substantially rougher until the structural integrity can no longer be maintained once a certain angle is reached.

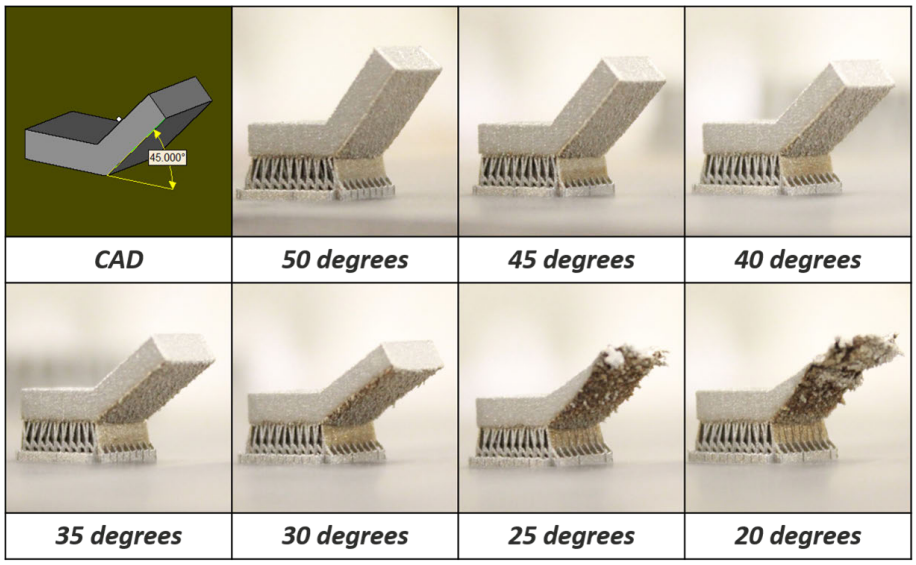


Figure 4: Influence of the build angle on the roughness of downskin surfaces for a PBF-LB-processed metal. Reprinted from Utley [58].

The inherent surface roughness of PBF-LB parts is generally considered undesirable. Nonetheless, it may offer advantages in designated joining areas for structural adhesive bonding. An overview of the fundamental principles and relevant scientific work on structural adhesive bonding is provided in the following subchapter.

2.2 Structural adhesive bonding

Adhesive bonding refers to the joining of two or more surfaces using a non-metallic material (i.e., adhesive) that transfers forces between the joining partners by adhering to their surfaces (adhesion) and developing adequate internal strength (cohesion) [13]. The joining partners are commonly referred to as substrates prior to bonding, while the term adherend is used once bonding is completed. In the present context, adhesion describes the attraction between the adhesive and the adherend through intermolecular forces, whereas cohesion pertains to the intermolecular forces within a single material, such as the adhesive [59].

In structural adhesive bonding, the joints must meet particularly high structural requirements, which necessitate the use of structural adhesives. These adhesives are specifically formulated to withstand significant loads and contribute substantially to the stiffness and strength of the joined structure [60]. Failure of an adhesive joint can generally be caused by cohesive failure,

adhesive failure, or a combination of both, as illustrated in Figure 5. Cohesive failure can occur within the adhesive or within one of the adherends, while adhesive failure (i.e., interfacial failure) takes place between the adherend and adhesive. When both cohesive and adhesive failure mechanisms are present, the failure is classified as mixed-mode. For structural bonding applications, adhesive failure is generally considered unacceptable, as it typically indicates insufficient surface preparation. According to Campbell [61], the acceptable failure modes for adhesively bonded structural joints include cohesive failure within the adhesive or adherend, as well as surface ply delamination in the case of composite adherends. A comprehensive classification of failure modes in adhesive joints, including more complex and uncommon cases, is provided in ISO 10365:2022 [62].

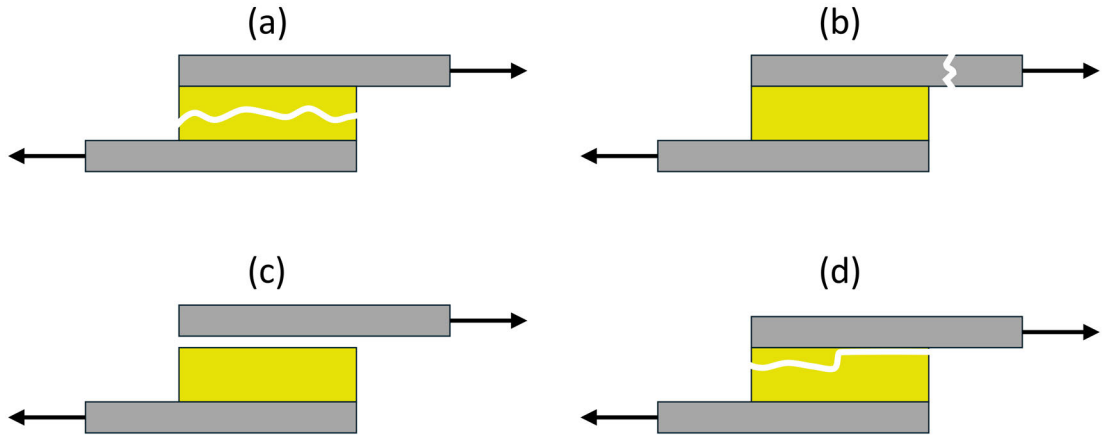


Figure 5: Failure modes of adhesive joints: (a) cohesive failure in the adhesive, (b) cohesive failure in the adherend, (c) adhesive failure, (d) mixed-mode failure [15].

Structural adhesives are predominantly thermosetting polymers, since their crosslinked molecular networks enable them to fulfill the material requirements for structural applications. However, in certain cases, some thermoplastic polymers [15] and high strength thermosetting elastomers [59] are also used for structural adhesive bonding. Among the various types of structural adhesives, epoxy systems are the most versatile, as they adhere well to many materials and offer a high degree of flexibility in tailoring their properties for specific applications. In addition, they exhibit high mechanical strength, good creep-resistance and a broad operating temperature range, which has led to their widespread use, particularly in the aerospace industry [59,60]. Due to their high industrial relevance, epoxy adhesives are investigated in the present thesis.

Epoxy adhesives are typically composed of an epoxy resin and a curing agent. The polymer network is generally formed through a polyaddition reaction, in which the oxirane rings of the epoxy resin are opened by functional groups of the curing agent (e.g., amines), resulting in a crosslinked structure. Common limitations that remain present for epoxy adhesives are their low peel and cleavage resistance, as well as their durability under environmental influences [13,59,63]. With the ongoing advancements in chemical formulations, increasingly high-performing structural adhesives are becoming available. To benefit from these improvements, it is essential to ensure sufficient adhesion within bonded joints. This necessitates a comprehensive understanding of the fundamental mechanisms governing adhesion.

2.2.1 Adhesion mechanisms

Adhesion is a complex phenomenon that cannot be fully explained by a single comprehensive model due to its multifaceted nature. Instead, several theoretical models have been developed to describe specific mechanisms contributing to adhesion. The most important adhesion theories are depicted in Figure 6.

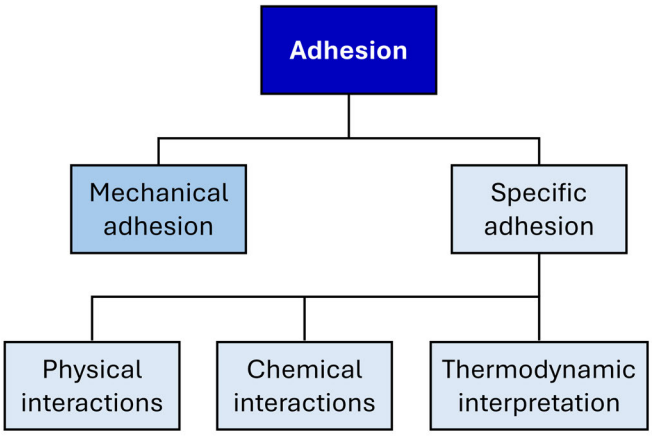


Figure 6: Overview of adhesion theories [13].

Adhesion is commonly categorized into mechanical adhesion and specific adhesion. The term specific adhesion includes the theories that explain adhesion through physical interactions (physisorption), chemical interactions (chemisorption) and from a thermodynamic perspective [13]. The principal theories are presented in the following:

Thermodynamic interpretation of adhesion

The thermodynamic approach interprets adhesion as the work needed to reversibly separate the interface between two materials into free surfaces. The work of adhesion W_a is defined by the Dupré-equation [64]:

$$W_a = \gamma_1 + \gamma_2 - \gamma_{12} \quad (1)$$

The variables γ_1 and γ_2 are the surface free energies of the two materials, while γ_{12} corresponds to the interfacial free energy between them. Higher adhesion is reflected in a lower interfacial free energy, leading to an increase in the work of adhesion. Since γ_{12} is difficult to measure directly, a practical approach to estimate W_a is by contact angle measurements. In these measurements, the wettability of a solid surface by a liquid is assessed by placing a liquid droplet on the surface and measuring the contact angle θ at the triple-phase boundary, where solid, liquid and vapor phases meet. Using this angle and the surface free energy of the liquid γ_{LV} under ambient atmosphere, W_a can be estimated by the Young-Dupré-equation [65]:

$$W_a = \gamma_{LV}(1 + \cos\theta) \quad (2)$$

The thermodynamic approach of explaining adhesion by analyzing interfacial energies has notable limitations. It relies on several assumptions that are generally not valid, such as neglecting the chemical interactions at the interface [13]. Thus, the thermodynamic model alone does not allow a reliable prediction of adhesion. However, it remains highly relevant, as it

established the fundamental understanding of how solid surfaces are wet by liquids and emphasized its importance for adhesion [13]. Wettability can be regarded as a requirement for adhesion and as an indicator for identifying surface-related issues that hinder bonding. Moreover, adequate wetting is not only a key element in the thermodynamic theory but also an essential requirement for the other adhesion theories [15,63].

Adhesion by chemical and physical interactions

The contribution of chemical and physical interaction forces to adhesion is addressed in the adsorption theory. This theory states that whenever two materials come into contact at a molecular level, forces of attraction will occur between them. The type of interatomic and intermolecular forces present between materials depends on the chemical characteristics of the respective surfaces [15]. In general, primary and secondary bonds can form at the interface. An overview of the different types of interfacial bonds, along with their associated bond energies and ranges, is provided in Table 1.

Table 1: Chemical and physical interaction forces at interfaces [13,59].

	Interaction type	Bond energy [kJ/mol]	Range [nm]
Chemical interactions (Primary bonds)	Covalent force	60-700	0.1 - 0.2
	Ionic force	600-1000	
Physical interactions (Secondary bonds)	Hydrogen bond	< 50	0.3 – 0.5
	Permanent dipoles*	< 20	
	Induced dipoles*	< 2	
	Dispersion force*	0.1 - 40	

*van der Waals forces

Primary bonds refer to the chemical interaction forces, which include the covalent and ionic forces. Compared to secondary bonds, these interactions exhibit significantly higher bond energies, as they involve the sharing or transfer of electrons. In contrast, secondary bonds are induced by weaker intermolecular forces. Covalent bonds are primarily responsible for the cohesive strength of adhesives. However, such bonds can also form at the adhesive-adherend interface, thereby contributing to adhesion through chemisorption. In the case of adhesively bonded titanium joints, Li et al. [66] experimentally proved the formation of Ti-O-C chemical bonds between amorphous titanium oxide and an epoxy adhesive. Moreover, physical interaction forces (secondary bonds), such as van der Waals (vdW) forces and hydrogen bonds, further contribute to adhesion. Among the vdW forces, London dispersion forces are of particular relevance, as they are universal in nature. This implies that, regardless of material pairing, dispersion forces are always present at the interface and contribute to adhesion [17,67]. For all types of bond interactions, the effective force range is typically below 1 nm, highlighting that the material surfaces must be in immediate proximity. In the context of adhesive bonding, this underscores the importance of sufficient wetting of the adhesive on the substrate surface.

Further adhesion theories that are based on physical interactions are the diffusion theory and the electrostatic theory. Both theories are generally considered less significant than the adsorption and mechanical adhesion theories [59]. The diffusion theory describes adhesion as

a result of interdiffusion of polymer chains between the adhesive and substrate. This mechanism is only accepted to occur in joints involving identical or very similar polymers [15]. In contrast, the electrostatic theory attributes adhesion to electrostatic forces, which are generated by the displacement of electronic or ionic charge carriers at the adhesive-adherend interface [68].

Mechanical adhesion

The mechanical theory of adhesion is based on the premise that real surfaces inherently exhibit a certain degree of roughness [59]. According to this theory, mechanical adhesion is induced by mechanical interlocking of an adhesive within surface irregularities, such as pores and undercut geometries. This mechanism requires the adhesive to fill the surface structures in order to anchor itself upon curing, which again emphasizes the importance of adequate wetting. Mechanical interlocking can be particularly effective on surfaces exhibiting nanoporous roughness. However, the effect of surface morphologies on adhesion is not limited only to the interlocking. Surface roughness increases the effective bonding area, thereby supporting other adhesion mechanisms, such as adsorption. Furthermore, specific surface structures, such as micro-fibrous morphologies, can promote cohesive failure within the adhesive and increase the fracture toughness of the joint. This is achieved by relocating stress concentrations from the adhesive–adherend interface into the bulk adhesive, where energy dissipation occurs through plastic deformation [69]. It is important to note that higher surface roughness does not necessarily result in improved adhesion, since excessive roughness may reduce wettability by causing air entrapment and complicating the removal of surface contaminants, which can ultimately hinder adhesion [70,71].

In addition to the adhesion theories presented, the weak boundary layer theory should also be addressed within this context. It is in essence a fracture theory for adhesive joints, which emphasizes important aspects relevant for understanding adhesion. According to this theory, bond failure occurring near the adhesive-adherend interface is due to cohesive failure within a thin, weak boundary layer, rather than the usually assumed adhesive failure. Reasons for the formation of a weak layer include surface contaminations, weak native oxide films on metals and environmental influences such as moisture [59,72]. The occurrence of weak boundary layers, as well as bond failure within them, has been reported in several scientific studies. This theory has therefore raised awareness for proper surface pretreatments and underscored the importance of thoroughly analyzing the locus of failure. It should be noted that this fracture theory is not universally valid, as failure near a bond interface can also occur in the complete absence of a weak boundary layer [15].

The contribution of the respective mechanisms to the overall adhesion in adhesively bonded joints is dependent on numerous factors. The surface properties, which include wettability, topography and chemistry, are central aspects. Moreover, the adhesive properties and the loading conditions are further important factors that need to be considered [15]. Additionally, for describing the interactions between the adhesive and adherend, it may not be appropriate to assume a single interface between both components. In practice, metallic adherends typically possess an oxide layer, while the adhesive properties may also differ in the vicinity of the adherends compared to the bulk adhesive. An interphase is therefore usually considered in the zone between adhesive and adherend [73]. This further complicates the analysis of adhesion.

Due to all these factors, the contribution of the individual mechanisms to the overall adhesion is still subject of ongoing scientific discussion [17]. Nonetheless, it is widely accepted that chemical bonding and dispersive forces can substantially contribute to adhesion, while for rough and porous surfaces, mechanical interlocking is also regarded as an important mechanism [15,69].

Since the surface condition of the substrates is a decisive factor influencing adhesion in structural adhesive joints, various surface pretreatment methods have been developed. Effective surface preparation can significantly enhance the performance and reliability of adhesive bonds. The following section provides an overview of surface pretreatment processes, with a particular focus on metallic adherends.

2.2.2 Surface pretreatment methods

Surface preparation is a crucial process step in structural adhesive bonding, which aims to enhance adhesion by modifying the physical and chemical properties of the substrate surfaces. A multistage process is usually applied, which involves surface cleaning as a fundamental step to remove surface contaminations and weak boundary layers, combined with further pretreatment steps used to modify surface chemistry or introduce surface roughness [25]. The pretreatment methods can be categorized according to their working principle, as shown in Figure 7. The depicted methods can be applied to both metallic and polymer adherends, except for anodizing, which is restricted to metals.

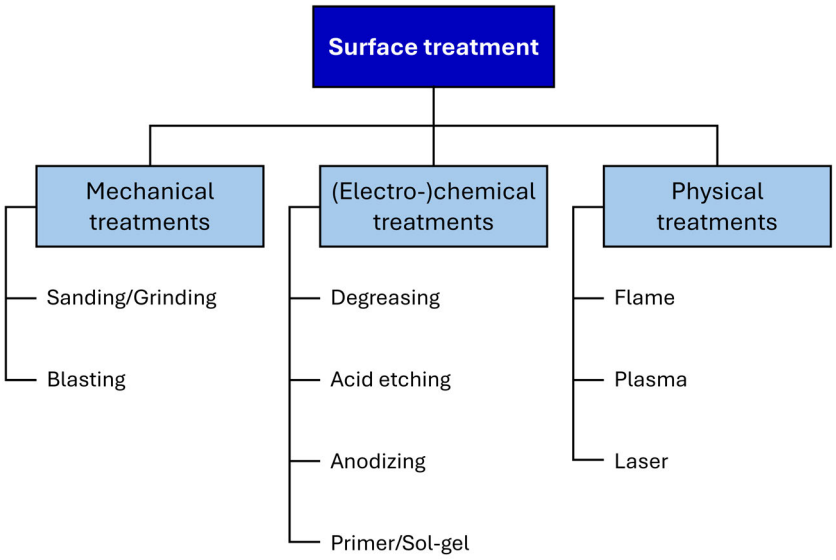


Figure 7: Summary of different surface pretreatment methods [25,74-76].

Mechanical treatments

Sanding and blasting methods are commonly used to increase the effective surface area by introducing roughness on macro- and micro-scale. In addition, surface contaminations and weak oxide layers are locally removed to a certain extent during these processes. Sanding represents the simplest form of mechanical treatment, as it only requires abrasive pads or papers to hand-abrade the surface. In contrast, blasting methods such as grit blasting utilize compressed air to propel abrasive particles (blasting agent) against the surface. By adjusting the process

parameters, a more controlled surface modification is possible compared to sanding [15]. A further advantage of grit blasting is that various blasting agents are available, which can be selected according to the substrate material and desired surface morphology. Following mechanical treatment, proper post-cleaning is necessary to remove residual material from the surface. Nevertheless, incised blasting particles can remain on the surface even after cleaning, including in the case of titanium [21]. This may negatively affect adhesion. Mechanical roughening of untreated metallic surfaces often improves adhesive bond strength. However, excessive microroughness can also have adverse effects, as it can promote air entrapment within the surface structures and increase the likelihood of embedded impurities. Moreover, sanding and blasting pretreatments alone usually cannot produce durable adhesive joints with metallic adherends due to the relatively thin remaining oxide layer after the treatment [75,76]. An exception is the SACO© process, in which silane-coated corundum is used as the blasting agent for grit blasting. Upon impact, the corundum particles deposit a silane layer on the substrate surface, thereby enhancing bond durability [76].

(Electro-)chemical treatments

Surface cleaning by degreasing encompasses relatively simple methods, such as solvent cleaning, which are usually sufficient to remove organic impurities on surfaces and thereby improve the wettability of the substrates [25]. In contrast, the presence of inorganic compounds may necessitate more intensive processes. Following degreasing, acid etching can be conducted to further clean the surface and additionally alter its topography. Depending on the solution composition and process parameters, roughness ranging from macro to nanoscale can be generated on the surface. Acid etching of metallic substrates can provide adequate initial adhesive bond strengths, similar to those achievable with mechanical pretreatments, but the bond durability is usually poor, because of a relatively thin oxide layer formed on the surface [15,75]. To enhance long-term durability, an organic primer layer containing coupling agents can be applied as the final pretreatment step. Coupling agents, such as silanes, promote adhesion by forming covalent bonds with both the substrate and the adhesive. In addition, the primer layer serves to protect the adhesive interface from environmental degradation and to conserve the surface during the interval between completed pretreatment and adhesive application [25,76]. Significant improvements in bond strength and environmental bond durability of adhesive joints with metallic adherends can also be achieved without priming, by applying electrochemical pretreatment processes such as phosphoric acid anodization (PAA) [77] or NaTESi [78]. It is known that anodizing processes can generate an open-porous, nanostructured oxide layer on titanium surfaces, which substantially enhances adhesion. This pretreatment method is therefore commonly used in high-performance applications, such as in aerospace [15,79]. However, a major disadvantage of anodizing processes is that hazardous chemicals are typically used, which pose safety and environmental risks and are therefore increasingly restricted by safety and health regulations such as REACH [27]. Consequently, the continuous development of environmentally friendly and safer pretreatment alternatives is necessary to meet progressively stringent requirements.

Physical treatments

Flame and plasma treatments are considered environmentally friendly compared to wet chemical processes, since they do not produce hazardous chemical waste [80,81]. Both methods are used to modify the surface chemistry and to remove fine, residual contaminations. During flame treatment, a controlled flame is passed over the surface for a short duration, whereas plasma treatment typically employs an oxygen plasma, in which ions, radicals, and UV radiation interact with the substrate. The surface is activated through oxidation, leading to the formation of polar functional groups [75,76]. For polymers, both methods are widely used, while only plasma treatment is commonly applied for metals. Akram et al. [82] demonstrated that atmospheric pressure plasma treatment of Ti6Al4V substrates improved their wettability, which reflected in a significant increase in the tensile shear strength of metal-metal joints bonded with a polyimide adhesive. A drawback of these physical treatment methods is that the surface activation can be preserved only for a limited time, necessitating bonding shortly after surface preparation or the application of cost-intensive primers [15]. Another environmentally friendly alternative to anodizing is laser treatment, which allows to create a broad range of surface morphologies on metallic substrates. In the following, lasers and their effects on metallic surfaces are discussed in detail, as this represents the primary pretreatment method investigated in this thesis.

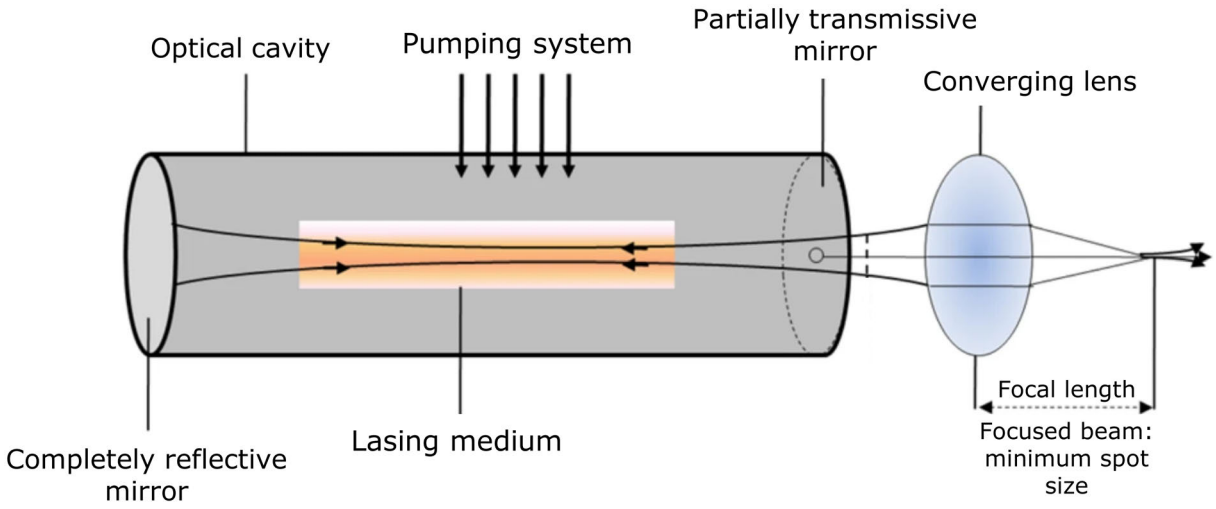


Figure 8: Structural components of a laser system. Adapted from Islam et al. [83] with permission from Springer Nature (© 2023).

A laser system (**L**ight **A**mplification by **S**timulated **E**mission of **R**adiation) consists of three main components: the lasing medium, the excitation system (“pump source”) and the optical resonator, as illustrated in Figure 8. In the first step, the lasing medium, for example a ruby crystal, is supplied with energy from the pump source, which may provide optical, electrical, or chemical excitation. The “pumping” of the lasing medium causes an excitation of its electrons to higher energy levels, thereby leading to a condition where more electrons at excited states are present in the medium than electrons at the ground state. This condition, known as population inversion, is a fundamental requirement for laser generation. Some of the electrons at higher energy levels return to lower states by emitting photons with random phase and direction (spontaneous emission). In the presence of population inversion, these photons can

stimulate other excited electrons to emit additional photons of identical phase, direction, and wavelength. This phenomenon, denoted as stimulated emission, enables the generation of monochromatic, coherent and directional light. The emitted photons are reflected back and forth by the mirrors of the optical resonator located at either end of the lasing medium, thereby amplifying the photon emission process. One of the mirrors is partially transmissive, allowing a fraction of the light to exit as the laser beam. This beam is typically focused through a lens to a defined spot size to enhance the energy density (fluence), improve the processing precision and limit the heat impact and damage of the processed material [84-86].

A laser can be operated in continuous or pulsed mode by regulating the energy input of the pumping system. The laser pulse durations can range from tenths of a second down to a few femtoseconds, while the average output power typically spans from the milliwatt to the kilowatt scale. Moreover, the emitted wavelength is determined by the lasing medium, which is either a solid, liquid, or gas, and can fall within the infrared, visible, or ultraviolet regions of the electromagnetic spectrum [85,87].

In the literature, pulsed lasers have been predominantly used to pretreat metallic substrates for enhanced adhesive bonding. Only a few scientific studies are available on laser processing of PBF-LB-Ti6Al4V for adhesive bonding, but several investigations have been conducted for conventionally manufactured titanium alloys. These investigations can be categorized into two main groups according to the laser-induced surface morphologies. One part of the studies performed laser treatment to generate microstructures, such as surface grooves, while the other part aimed to produce a nanoporous oxide layer.

Laser surface micro-texturing of pure titanium and Ti6Al4V substrates has been investigated in several studies [88-93] using different nanosecond laser systems. An example of micro-texturing is shown in Figure 9(a), which depicts a SEM image of a laser-ablated Ti6Al4V surface with grid structures [93]. In general, these studies reported that laser micro-texturing can significantly improve adhesive bond performance by inducing mechanical interlocking of the adhesive in the generated microstructures and by increasing the formation of interfacial bonds due to the enlarged surface area. However, laser micro-texturing can also cause structural damage and induce thermal stresses in the bulk material, as well as promote the formation of pores that can hinder adhesion [92,93]. To mitigate these negative effects, femtosecond lasers can be applied for surface texturing of Ti6Al4V [94,95]. Due to their shorter pulse duration compared to nanosecond lasers, femtosecond systems offer a lower heat input into the substrate and enable the generation of surface textures with higher precision. Regarding PBF-LB-Ti6Al4V, more recent studies have demonstrated the potential of performing laser micro-texturing directly during the PBF-LB/M process, thereby eliminating an additional surface preparation step [96,97]. Notably, these investigations did not report the formation of a distinct nanoroughness on the surface.

The laser intensity can be optimized to generate an open-porous, nanostructured oxide layer, as it was shown for conventionally manufactured titanium surfaces. The laser induces a plasma in the near-surface region that contains ablated material in the form of nanoparticles, which subsequently react with atmospheric oxygen and redeposit on the surface [79]. This generated nanoroughness was found to be highly effective in producing high-strength and durable

adhesive joints [98-100]. Kurtovic [79] demonstrated that laser treatment of Ti6Al4V parts with a Nd:YVO4 laser enables superior bond durability of metal/epoxy joints compared to wet chemical treatment methods like etching and anodizing. The high effectiveness of the laser-induced oxide layer was primarily attributed to the substantially enlarged surface area, which promotes the development of chemical and dispersive bonds at the adherend-adhesive interface as well as mechanical interlocking of the adhesive within the nanostructures. Wetting of epoxy adhesives in the nanoporous oxide layer was reported to be unproblematic [100]. However, this approach of laser processing also has the risk of damaging the sub-surface region of the titanium substrate and can induce tensile residual stresses that may deteriorate the fatigue behavior of the laser-treated parts [79,101,102]. No previous work had investigated laser-induced nanostructuring of PBF-LB/M-fabricated surfaces.

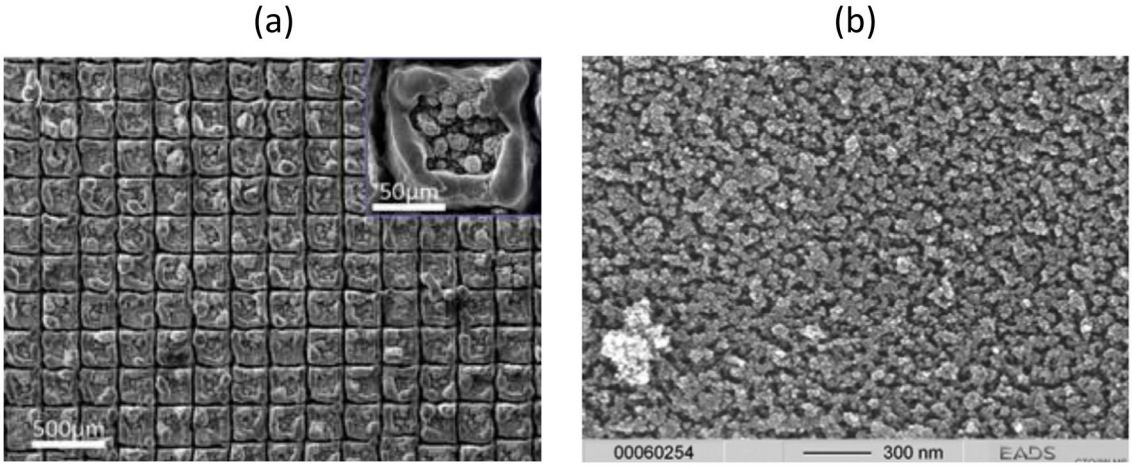


Figure 9: Laser processed Ti6Al4V surfaces: (a) laser micro-texturing of grid structures (adapted from Maressa et al. [93] with permission from Taylor & Francis (© 2014)), (b) laser induced nanoporous oxide layer (adapted from Kurtovic et al. [98] with permission from Elsevier (© 2013)).

In addition, laser treatment may also be used solely for the removal of surface contaminations and weak boundary layers, such as native oxide films, without generating distinct surface roughness [103-105]. This approach may be particularly relevant for high-precision applications. A similar cleaning effectiveness compared to chemical treatment methods was reported for Ti6Al4V surfaces pretreated with a Nd:YAG laser [105].

2.2.3 Adhesive bond testing

A wide range of adhesive bond testing methods have been developed to assess adhesive bond performance, determine the effectiveness of surface pretreatments, and generate data for material modeling. Non-destructive testing (NDT) techniques, such as ultrasonics [106] and thermography [107], can support quality assurance by detecting defects within the joint. However, NDT methods alone are not capable of quantitatively predicting bond strength, particularly the interfacial strength between substrate and adhesive [15,108]. For this reason, destructive test methods remain indispensable for evaluating adhesive bond performance under quasi-static, fatigue, and environmental loading conditions. In certain applications, impact testing [109] may also be relevant, but this is not within the scope of the present thesis.

Quasi-static testing

For the assessment of adhesive joints under quasi-static loading, several standardized test methods are available for the basic loading modes: tensile, compression and shear. Among these, compression testing is relatively uncommon, as it represents a less critical loading condition. Consequently, compressive tests are typically used only for the characterization of bulk adhesive properties rather than for the evaluation of bonded joints [15].

The standard procedure for tensile testing involves axially loading a butt-joint in a universal testing machine. In these butt-joint tests, a relatively homogeneous loading of the adhesive bond can be achieved when the adherends are properly aligned [110]. At the rim of the adhesive layer, a stress concentration remains present, which can be minimized by using stiff adherends with a circular geometry [17,110]. An alternative approach is the centrifugal adhesion test (CATT) [111]. In this test method, a centrifugal force is used to induce a tensile loading of a butt joint, consisting of a test stamp bonded to the substrate under investigation. Compared to conventional butt-joint testing, the main advantage of CATT lies in its cost-effectiveness, as it enables shorter testing times and requires less adherend material [17,112].

For pure shear loading of an adhesive joint, the most accurate test method is the torsional loading of a butt joint, such as in the napkin ring test [13,113]. A simpler, yet often sufficient alternative is the thick adherend shear test (TAST), which utilizes a single lap shear joint geometry [114]. In general, single lap joints are subjected to mixed-mode loading, comprising both non-uniform shear and peel stresses along the overlap. Therefore, thick adherends with a stepped geometry are used in TAST to minimize the stress concentrations at the overlap ends that arise from differential straining of the adherends and bending induced by eccentric loading. Despite the mixed-mode loading condition, single-lap joints are the most widely used specimen type for adhesive joint testing, as they are inexpensive to manufacture and reproduce joints encountered in various applications [15].

In addition to strength-based tests, several methods have been developed to determine the fracture toughness of adhesive joints. These methods are categorized according to the mode of crack opening into mode I (opening mode), mode II (in-plane shear) and mode III (out-of-plane shear) tests. It should be noted that mode III testing is rarely performed due to its limited practical relevance. The mode I fracture toughness can be investigated by double cantilever beam (DCB) testing [115], while for mode II loading, the end-notched flexure (ENF) test [116] is typically conducted. These test methods have in common that the adherends must deform in a linear-elastic manner to ensure the applicability of linear-elastic fracture mechanics. In cases where the bond performance under extensive deformation of the adherends is of interest, peel tests such as the floating roller peel test [117] or the T-peel test [118] can be performed. These tests are highly effective for evaluating the influence of surface treatments on adhesion, but they require at least one flexible adherend [110].

Fatigue testing

To evaluate the fatigue resistance of adhesive joints, cyclic loading experiments are usually conducted. The standard loading profile is sinusoidal, while the load ratio R (i.e., the ratio of minimum to maximum applied load) is selected according to the respective application. The

most frequently applied load ratio in the literature is $R = 0.1$ (tensile-tensile-loading), as it avoids complications due to buckling and is easier to realize in the testing procedure. For more severe fatigue conditions, a fully reversed loading with $R = -1$ can be used [119]. Furthermore, the testing frequency must be carefully chosen to prevent excessive heat generation within the adhesive, as this may alter its mechanical behavior [13]. In general, fatigue tests should be performed at several load levels to assess both low-cycle fatigue (LCF) and high-cycle fatigue (HCF) behavior [120]. The standard procedure is to conduct multiple tests at different constant amplitudes. Alternatively, variable amplitude fatigue testing can also be applied to better simulate the service load spectrum of a specific application [121]. Most specimen geometries used for quasi-static testing are also suitable for fatigue studies, with lap joints being among the most investigated configurations [122].

Besides fatigue strength and lifetime characterization, it is of particular interest to monitor crack growth. Various techniques have been employed for this purpose, including back-face strain measurement, ultrasonic inspection, and in-situ video microscopy [122]. These methods provide only localized or line-based information and often lack sufficient spatial resolution [123,124]. In contrast, digital image correlation (DIC) offers a significant advantage, as it enables full-field, quantitative monitoring of surface strain and displacement, thereby allowing precise monitoring of crack initiation and propagation under cyclic loading [125,126].

Environmental durability testing

The durability of adhesive bonds can be compromised by several environmental factors, including moisture, temperature, salt exposure and high-energy radiation. These influences can degrade the chemical and physical properties of the bulk adhesive, weaken adhesion at the adhesive–adherend interface, or damage the adherends [127,128]. Testing the bond performance under actual service conditions would generally require very long exposure times, rendering it impractical for most investigations. Therefore, accelerated aging tests are commonly used to simulate long service lifetimes within reasonable durations. Typical examples include aging in a climate chamber at elevated temperature and relative humidity (e.g., 95% RH) or immersion aging in water or other liquids to accelerate moisture diffusion into the adhesive bond [13].

Environmental aging can be combined with mechanical loading to simulate more severe service conditions. In such cases, adhesive joints are either pre-aged prior to mechanical testing or tested directly under environmental influences, allowing the simultaneous application of aging and quasi-static or fatigue loading. These combined approaches provide a more realistic assessment of the long-term performance of adhesive joints [129]. A widely used method for characterizing service disbond behavior under frequently encountered hydrothermal aging is the wedge test [130]. In this test method, a wedge is inserted into the bondline, and the subsequent crack growth is monitored over time under environmental exposure. In hydrothermal aging tests, it is generally essential that the specimen geometry and exposure duration allow sufficient moisture diffusion into the adhesive bond to ensure effective aging [131].

The mechanical performance of adhesive joints with PBF-LB-Ti6Al4V adherends has been investigated for metal-metal joints in only two studies. Ardila-Rodríguez et al. [22] demonstrated through standard butt-joint testing that similar tensile bond strengths can be achieved with as-built PBF-LB-Ti6Al4V surfaces and grit blasted surfaces. For mode I loading, Gulino et al. [23] reported that the steady-state fracture toughness obtained in DCB testing was approximately 41% lower for as-built surfaces compared with grit-blasted surfaces. The lower fracture toughness of the as-built surface was attributed to the formation of a brittle oxide layer during the standard heat treatment following PBF-LB manufacturing. Further studies on the bonding behavior of PBF-LB-Ti6Al4V are available within the context of hybrid metal-composite joints, which are addressed in the following chapter.

2.2.4 Hybrid metal-composite joining

Hybrid joining between metal and composite parts is typically done by combining adhesive bonding with mechanical fastening using screws, bolts, or rivets [11,12]. For thermoplastic composites, which are often employed in automotive applications, thermomechanical joining processes represent an alternative approach [132]. These processes are based on the ability of thermoplastics to melt under localized heating induced by a laser, friction, or ultrasonic vibration, enabling direct bonding of the thermoplastic matrix resin to the metallic part while simultaneously forming a mechanical interlock. In contrast, aerospace structures use predominantly composites with a thermoset matrix, which cannot be remelted [133]. Consequently, hybrid metal–composite joining in aerospace applications is generally done by combining adhesive bonding and mechanical fastening, which is discussed in the following.

The combination of multiple joining methods can provide enhanced damage tolerance, increased joint strength and improved structural redundancy [134]. However, the conventional approach of installing mechanical fasteners through drilling has significant disadvantages, such as damaging the composite, causing delamination and introducing stress concentrations. To overcome these drawbacks, extensive research has been devoted to the development of alternative through-thickness reinforcement concepts. The fundamental approach involves manufacturing macroscopic pins on the metallic substrate, embedding these structures into a prepreg or dry fabric, and subsequently joining both substrates by co-curing (i.e., simultaneous curing of the composite and bonding to the metallic substrate) [135,136]. Upon completion of co-curing, the pins act as mechanical interlocking features. An example of a pinned hybrid joint is shown in Figure 10, illustrating stainless steel joined with a glass fiber–reinforced polyester composite.



Figure 10: Co-cured hybrid joint between stainless steel with pin structures and a glass fiber reinforced polyester composite material (Comeld^{Tm} joint) [137].

In this example, the pins were manufactured by laser surface texturing with an electron beam. Besides laser surface restructuring [137,138], other methods for fabricating pin arrays onto metallic substrates are AM [139,140] and welding techniques like cold metal transfer (CMT) [141,142]. Among these methods, AM processes such as PBF-LB/M are particularly favorable, as they allow the simultaneous fabrication of the base metal part and the pin reinforcement in a single process step. Furthermore, the high design flexibility of AM enables the optimization of pin alignment and geometry to meet the specific loading conditions of the metal–composite joint [143].

The load transfer in co-cured metal-composite joints with pin-reinforcements occurs through mechanical interlocking of the pins and the adhesive bond between the adherends. Several studies [139,140,144-147] have investigated the mechanical performance of pinned hybrid joints between PBF-LB-Ti6Al4V and composite materials. The primary focus has been on assessing the influence of pin geometry and analyzing pin-related damage mechanisms under quasi-static and fatigue loading. In general, substantial improvements in joint performance were achieved for mode I, mode II and tensile shear loading, which were mainly attributed to pin-induced mechanical interlocking and crack bridging. Analyses of damage mechanisms were mostly concentrated on the pins, as they are decisive for the ultimate strength and fracture toughness. Typically, the adhesive bond between the metallic base surface and composite fails first, followed by crack initiation in the pins near their base, ultimately leading to rapid fracture. An example of the damage state in the vicinity of a pin after mode II fatigue testing is shown in Figure 11 for a PBF-LB-Ti6Al4V–CFRP joint.

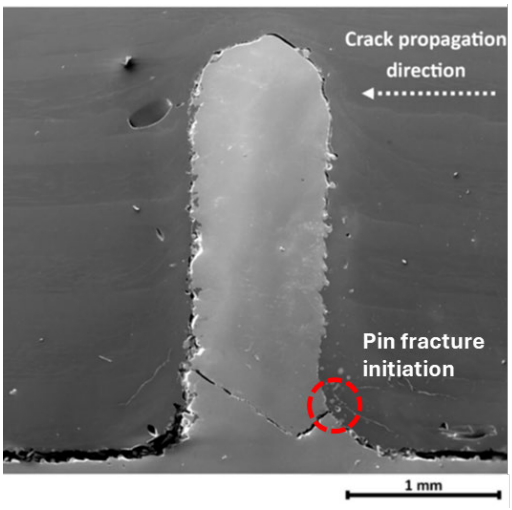


Figure 11: Fracture cross-section evaluated by SEM of a pinned PBF-LB-Ti6Al4V-CFRP joint after mode II ENF fatigue testing, showing the damage state in the vicinity of a pin (adapted from Bagnato et al. [145] under the CC BY-NC license).

The surface condition influence on the mechanical performance of co-cured, pinned Ti6Al4V–CFRP joints was addressed by Parkes et al. [148]. In their study, however, only the pins were produced by additive manufacturing, while the titanium substrate itself was conventionally fabricated. Consequently, the effect of the inherent roughness of PBF-LB-Ti6Al4V was not fully considered. Prior to the present work, no studies had systematically investigated the effects of surface morphology in hybrid metal-composite joints with a PBF-LB/M manufactured adherend.

3 Materials and Methods

The materials and methods used in this work are summarized in this chapter. Detailed descriptions are omitted here, as they are provided in the publications of this cumulative dissertation.

3.1 Materials

Metal-metal adhesive joints with PBF-LB/M-fabricated Ti6Al4V adherends were investigated in the publications 1-3, whereas publication 4 focused on hybrid metal–CFRP joints. It is important to note that between publication 1 and the subsequent studies, both the PBF-LB/M machine and the adhesive system had to be changed due to project-related decisions within the BLANCA project, which set the framework for this thesis. To ensure the comparability and transferability of the results, the adhesive joint tests from publication 1 were subsequently repeated using the PBF-LB/M machine and adhesive system applied in publications 2–4. The corresponding results are presented in Chapter 4.

3.1.1 Substrates

Ti6Al4V substrates were manufactured on a Concept Laser M2 machine for publication 1 and on a Trumpf TruPrint 5000 machine for publications 2-4. In both cases, Ti6Al4V powder supplied by GE Additive was used. The substrates were produced using standard process parameters for Ti6Al4V Grade 23 and underwent a standard stress-relief heat treatment to reduce residual stresses. A weak orthotropic material behavior was found for Ti6Al4V fabricated on the Concept Laser M2 machine during a previous material characterization [149]. The tensile properties of PBF-LB-Ti6Al4V, determined based on ASTM A370-19 [150] for specimens built in the gas flow direction, are given in Table 2.

Table 2: Tensile properties of PBF-LB-Ti6Al4V fabricated on a Concept Laser M2 machine for a build orientation in gas flow direction [149].

Young's modulus [MPa]	Tensile strength [MPa]	Fracture strain [%]
129000	1040	10

The CFRP substrates were manufactured by combining the unidirectional prepreg Q110-UD-268-34-10/ITS55-24K (Teijin, Japan) and woven prepreg Q110-2/2TW-285-38-10/HTS40-6k (Teijin, Japan), following the quasi-isotropic layup $\left[\pm 45^{\mathrm{W}}, 0^{\mathrm{UD}}, \pm 45^{\mathrm{W}}, 90_2^{\mathrm{UD}}, \pm 45^{\mathrm{W}}, 0^{\mathrm{UD}}\right]_{\mathrm{S}}$. This layup was selected to achieve a similar bending stiffness between the CFRP and Ti6Al4V adherends in the metal-composite joints. Both prepreg systems are based on epoxy resin matrices. Table 3 summarizes their orthotropic material properties, obtained within the BLANCA project. The tensile material data in longitudinal (E_1, ν_{12}, σ_1) and transversal (E_2, σ_2) directions were determined following ASTM D3039 [151], while the shear properties (G_{12}, τ_{12}) were examined using ASTM D5379 [152].

Table 3: Orthotropic material properties of the used unidirectional (UD) and woven prepreg materials.

	E_1 [MPa]	E_2 [MPa]	G_{12} [MPa]	ν_{12} [MPa]	σ_1 [MPa]	σ_2 [MPa]	τ_{12} [MPa]
UD	145252	7365	4922	0.34	2386	30.8	59.7
Woven	63152	57303	4910	0.05	986.4	876.8	88.4

3.1.2 Adhesives

Two-component epoxy adhesives from the Loctite EA939X series were used in this thesis. Loctite EA9395 was utilized in publication 1, while Loctite EA9396 was used in publications 2–4. Both are aerospace-grade structural adhesives capable of curing at ambient temperature or at elevated temperatures for an accelerated cure. The primary difference is that EA9395 contains silicon dioxide fillers, whereas EA9396 has no significant filler content, leading to its low viscosity. The mechanical properties of both adhesive systems were evaluated by the adhesive manufacturer Henkel through tensile shear testing according to ASTM D1002 [153]. The resulting material data is given in Table 4 for a standard cure of five days at 25°C [131,154,155].

Table 4: Tensile shear properties of Loctite EA9395 and Loctite EA9396 for a standard cure of five days at 25°C according to the adhesive manufacturer [131,154,155].

	Young's modulus [MPa]	Tensile shear strength [MPa]	Fracture strain [%]
Loctite EA9395	4940	27.6	2.6
Loctite EA9396	2750	24.1	3.5

3.2 Methods

An overview of the applied methods is shown in Figure 12. The effects of surface morphology on adhesive bond performance were investigated for PBF-LB-Ti6Al4V surfaces in as-built and surface-treated conditions. To account for the build orientation influence on PBF-LB/M-processed surfaces, the bonding surfaces of the specimens were manufactured at different angles relative to the build platform. For the as-built surface condition, the build orientations 0°, 45° and 90° were considered, while investigations of other surface conditions were limited to the 0° and 90° orientations.

The surface preparation methods degreasing, grit blasting, and laser processing were considered for pretreating the titanium alloy substrates of the metal-metal joints. Degreasing alone was applied to assess the adhesive bond performance of as-built PBF-LB-Ti6Al4V surfaces. In contrast, grit blasting was used as a standard postprocessing method for AM parts, whereas pulsed laser treatment was investigated as an environmentally friendly alternative to electrochemical processes for generating distinct nanoroughness on metallic surfaces. In addition, milled and NaTESi-pretreated Ti6Al4V surfaces were included as references.

Surface morphologies and fracture surfaces were analyzed using CLSM and SEM, while the macroscopic wettability of the surfaces was evaluated by contact angle measurements (CAM) using the sessile drop method. Detailed fracture surface analysis was performed to identify the

key contributions of surface features to bond performance and to determine interactions between different morphological structures. Furthermore, IBM was applied to enable cross-sectional SEM analysis of laser-induced oxide layers before and after adhesive joint testing, as well as to examine structural modifications in the underlying bulk material. In addition, residual stresses induced by laser treatment in the near-surface region were measured using X-ray diffraction (XRD) to assess their potential detrimental influence on fatigue resistance.

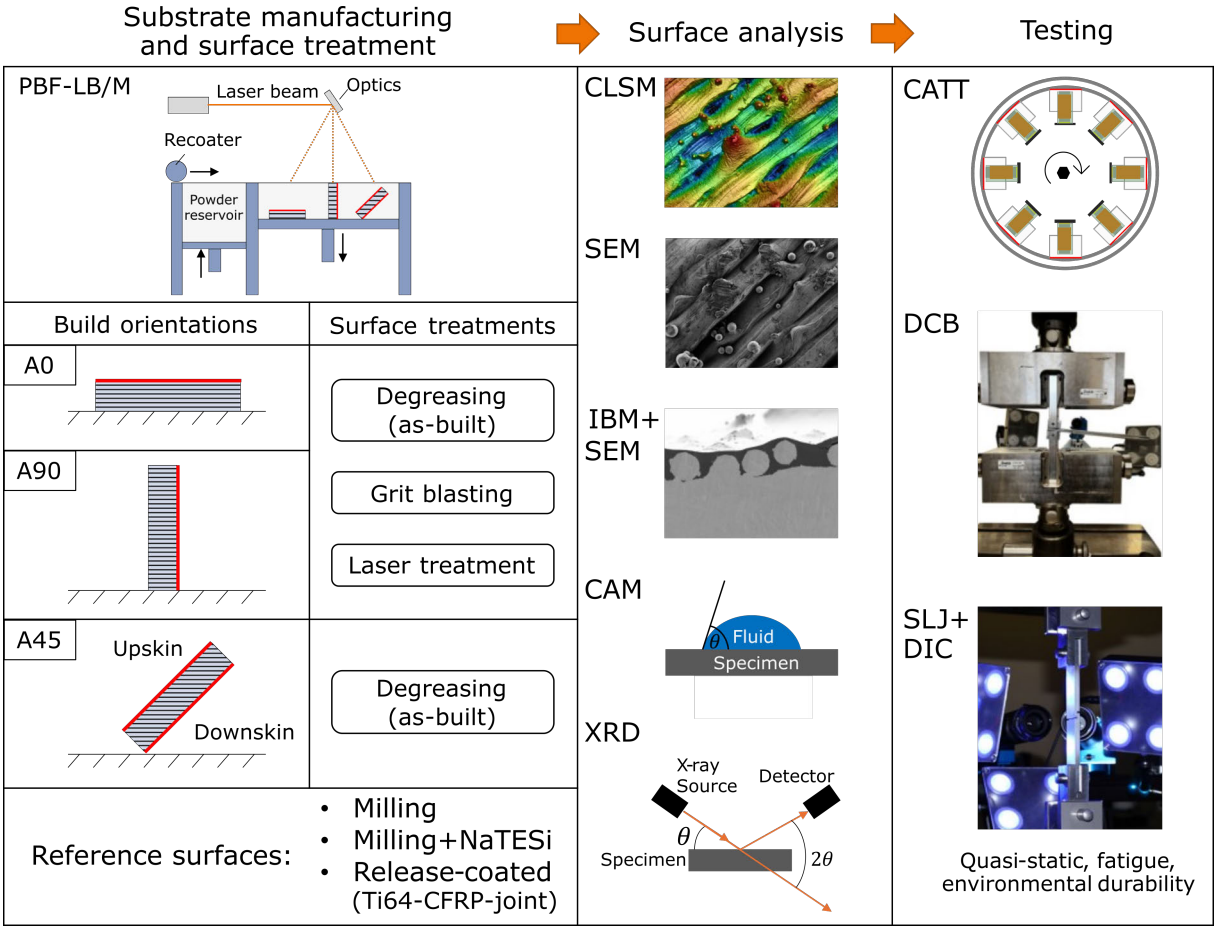


Figure 12: Overview of the applied methods.

The adhesive bond performance was evaluated for quasi-static, fatigue and environmental loading conditions. In the quasi-static tests, the surface morphology influence on adhesion was investigated under tensile loading by CATT, and the effect on mode I fracture toughness by DCB testing. Moreover, SLJ testing was performed to comprehensively assess the bond strength, environmental bond durability and fatigue behavior under mixed-mode loading. During SLJ testing, DIC was applied to measure strain distributions along the bondline and monitor crack growth, thereby assisting in analyzing surface-related effects. The SLJ-fatigue tests were conducted at several load levels to examine both LCF and HCF. Evaluation of the environmental bond durability was done for a hydrothermal aging condition.

For the hybrid metal–composite joints, the surface treatment methods degreasing, release-agent-coating, and laser processing were used for the PBF-LB-Ti6Al4V substrates, and low-pressure plasma treatment for the CFRP substrates. Surface characterization and fracture

surface analysis were conducted using CLSM and SEM, while the mechanical joint performance was evaluated by SLJ testing along with DIC strain measurements.

4 Results

This chapter provides a concise summary of the four peer-reviewed publications of this cumulative thesis and presents their main results. Additional information is included in the subchapters to complement this work. The full publications are provided in the Appendix.

4.1 Analysis of surface morphologies and their effects on tensile bond strength (publication 1)

An initial investigation into the adhesive bonding potential of PBF-LB-manufactured Ti6Al4V parts is presented in the first publication. The primary focus of this study was on the effects of surface morphologies on adhesion strength under tensile loading. PBF-LB-Ti6Al4V surfaces were evaluated in the as-built condition for the build orientations 0° (A0), 45° (A45-U/D) and 90° (A90). In addition, grit blasting and laser processing were applied to modify the surface morphology and examine their effect on bond strength. Laser treatment of PBF-LB-Ti6Al4V for adhesive bonding was conducted for the first time in this work, for which a tailored process was developed using a pulsed laser system. The surface morphologies were characterized by CLSM and SEM, while their macroscopic wettability was assessed through contact angle measurements. The adhesion strength between the Ti6Al4V surfaces and Loctite EA9395 was evaluated by CATT for tensile loading. This study provided an initial assessment of how PBF-LB-processed titanium surfaces influence bond performance and established a foundation for subsequent investigations.

The inherent roughness of as-built PBF-LB-Ti6Al4V surfaces was shown to be mainly determined by partially melted particles from the powder bed. The quantity and distribution of these particles depended strongly on build orientation, while additional process-related features such as stair-step structuring further influenced the surface topography. Contact angle measurements revealed complete wetting of all as-built surfaces with deionized water, except for the horizontally oriented specimens, which exhibited the lowest amount of partially melted particles. The particle density on the as-built surface was found to correlate with the macroscopic wettability and tensile bond strength. Most particles did not fracture from the surface during testing and thereby contributed to adhesion through mechanical interlocking in the adhesive. In contrast, the commonly applied arithmetic mean roughness parameter S_a and macroscopic contact angles did not correlate with the bond strength and are therefore unreliable parameters for predicting adhesive bond performance, as underscored in this study. Instead, analyzing the surface features with regard to their interlocking potential and distinguishing between different roughness scales was shown to be a more suitable approach.

In general, all specimens with as-built surfaces exhibited high tensile bond strengths, which were comparable to those of the grit blasted samples, as shown in Figure 13. This demonstrates the high bonding potential of PBF-LB-processed surfaces. Grit blasting primarily introduced microroughness while removing the attached particles from the surfaces, which resulted in

reduced macroscopic wettability. In contrast, laser treatment produced surfaces with excellent wettability and enabled a significant enhancement of bond strength due to the formation of an open-porous nanostructured oxide layer on top of the PBF-LB surface morphology. Since the partially melted particles were not removed during laser processing, the combination of laser-induced nanoroughness and particle-driven mechanical interlocking enabled a transition in the failure mode from mixed adhesive–cohesive to complete cohesive failure within the adhesive.

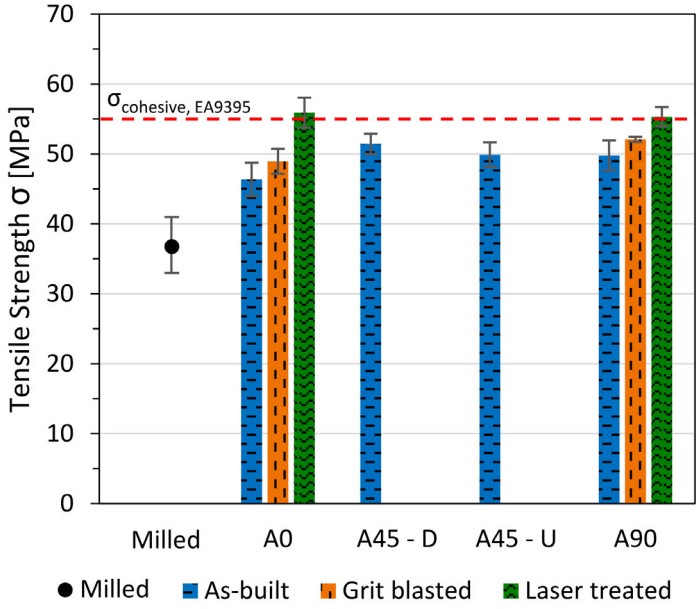


Figure 13: Tensile bond strengths of PBF-LB-Ti6Al4V/epoxy CATT joints, shown for different surface conditions and build orientations. The results for a milled surface are depicted as a reference.

4.1.1 Influences of PBF-LB/M machine and adhesive on bond strength

The investigations in publications 2-4 had to be conducted using a different PBF-LB/M machine and adhesive system, as explained in Chapter 3. For publication 1, a Concept Laser M2 machine and the adhesive EA9395 were used, while the subsequent studies were carried out with a Trumpf TruPrint 5000 system and the adhesive EA9396. To ensure comparability across all studies, the machine and adhesive influences on tensile bond strength were evaluated by conducting further CATT tests.

First, the effect of the PBF-LB/M machine was assessed, as shown in Figure 14. All specimens in this investigation were bonded with EA9395 to allow a direct comparison with the results from publication 1. The as-built surfaces fabricated on the Concept Laser M2 exhibited higher tensile bond strengths than those produced on the Trumpf TruPrint 5000 (Figure 14(a)). However, the qualitative influence of the build orientation on bond strength was consistent for both systems. This demonstrates that machine-related factors influence the absolute values of bond strength without affecting the build-orientation dependence. Surface characterization of the Ti6Al4V substrates revealed similar morphologies for both systems, though the Concept Laser M2 samples displayed moderately higher microroughness, which may explain their higher adhesion strength under tensile loading. Importantly, in the laser-treated surface condition (Figure 14(b)), a similar bond strength was found between both PBF-LB/M machines.

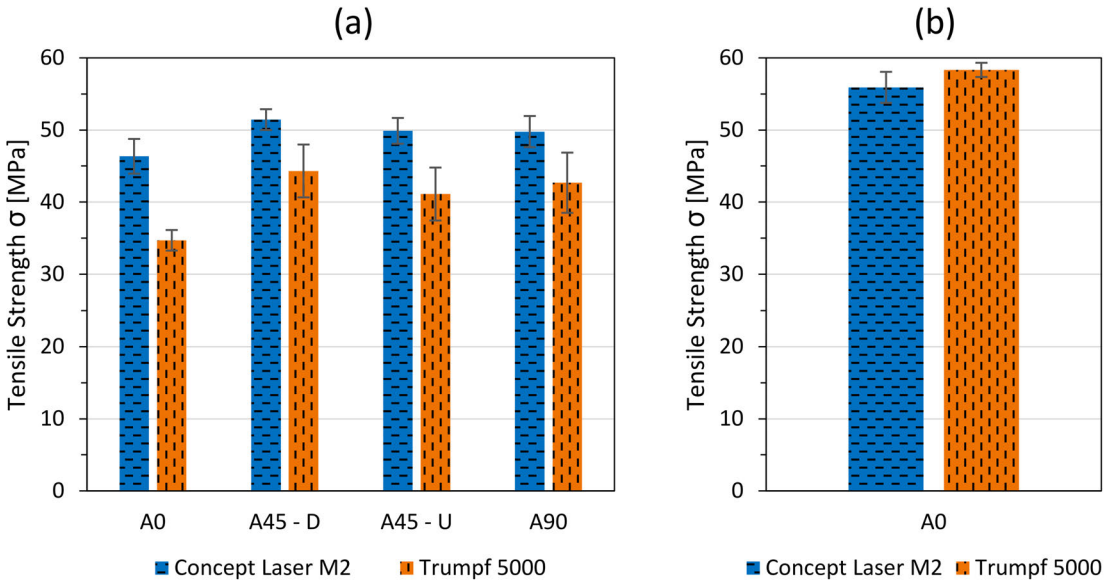


Figure 14: Comparison of tensile bond strengths between Ti6Al4V-adherends manufactured on a Concept Laser M2 and Trumpf TruPrint 5000 machine: (a) as-built surfaces, (b) laser-treated surfaces with A0 build orientation. All CATT joints were bonded with EA9395.

Second, the effect of the adhesive system was investigated by comparing CATT results of TruPrint 5000 specimens bonded with either EA9395 or EA9396 (Figure 15). This comparison revealed no significant differences in bond strength for both the as-built and laser-treated conditions, indicating that the change in adhesive system has a negligible influence on the bonding performance under tensile loading. It can be concluded that the surface morphology influence on tensile bond strength is qualitatively similar across the different PBF-LB/M systems and adhesive types, thereby ensuring the comparability of results between the studies.

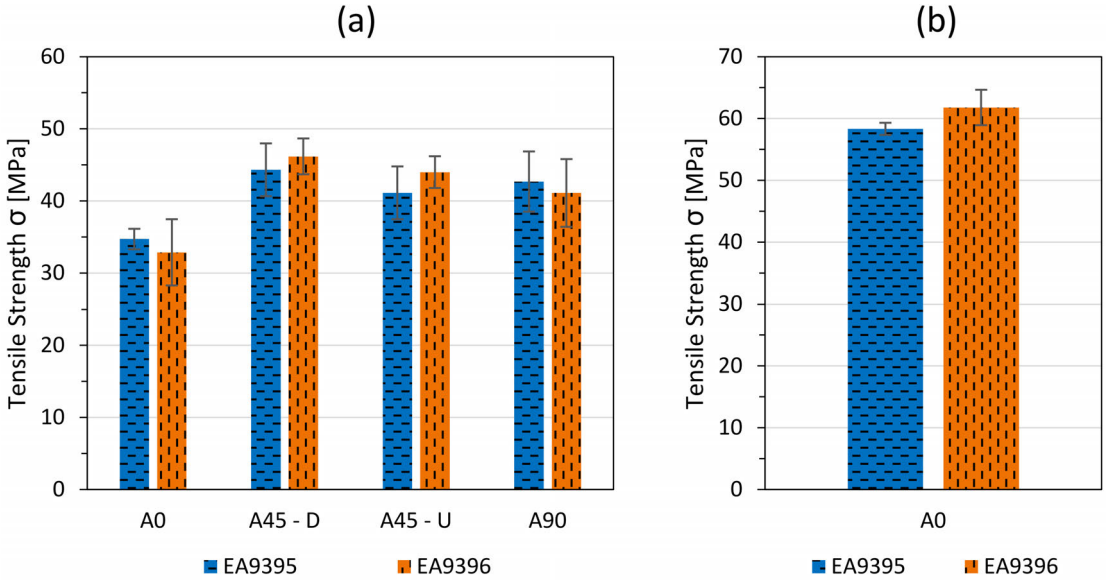


Figure 15: Comparison of tensile bond strengths between CATT joints bonded with EA9395 and EA9396: (a) as-built surfaces, (b) laser-treated surfaces with A0 build orientation. All Ti6Al4V-adherends were manufactured on a Trumpf TruPrint 5000 machine.

4.2 Effects of surface morphologies under quasi-static, fatigue and environmental loading conditions (publication 2)

The investigation on the effects of PBF-LB-Ti6Al4V surface morphologies on adhesive bond performance was deepened in the second publication, considering quasi-static, fatigue and environmental loading conditions. Similar to the preceding study, this investigation includes as-built surfaces with different build orientations, as well as surfaces modified by grit blasting and laser treatment. Following surface characterization by CLSM, SEM and SEM+IBM, single step-lap joint (SLJ) tests were conducted to evaluate tensile shear bond strength and bond lifetimes under cyclic fatigue loading. Moreover, the environmental durability of the adhesive bonds was assessed through quasi-static testing of hydrothermally aged SLJ specimens. During SLJ testing, DIC was used to assist in analyzing surface morphology effects by measuring strain distributions along the bondline and monitoring crack growth during fatigue loading. Extensive fracture surface analysis enabled the deduction of interactions between specific surface features and provided insights into surface-related failure mechanisms.

In the as-built condition, the partially melted particles were identified as the main surface feature influencing adhesive bond performance, which is consistent with the finding reported in publication 1 for tensile loading. The number and spatial distribution of the attached particles was found to correlate with both the tensile shear strength and fatigue resistance of the adhesive bond. Surfaces built in horizontal orientation (A0), characterized by a low particle density, allowed to reach only relatively low tensile shear strength values of around 12.8 MPa, which were similar to those obtained with conventionally milled surfaces. The as-built surfaces with intermediate particle densities (A45-U, A90) exhibited bond strengths comparable to grit blasted surfaces (about 25 MPa), while the highly structured 45° downskin surface (A45-D) surpassed these strengths by approximately 10%, owing to its dense particle coverage and stair-step topography. Furthermore, the fatigue tests revealed that increased particle density on PBF-LB surfaces also enhances bond lifetimes, primarily through particle-induced mechanical interlocking and the enlarged effective bonding area. Notably, longer lifetimes were reached with A45-D than with the grit blasted surfaces, demonstrating that even excessive amounts of attached particles do not adversely affect the bond behavior under fatigue loading. For all as-built and grit-blasted surfaces, bond fracture occurred as a combination of adhesive failure and cohesive failure within the adhesive for both quasi-static and fatigue loading. In the as-built condition, the cohesive failure predominantly occurred in the vicinity of partially melted particles, leading to a higher proportion of cohesive failure in the adhesive with more particles on the surface. Consequently, regions with few or no attached particles exhibited poor adhesion and thereby limited the overall bond performance, as these areas lacked pronounced microroughness and, in general, no distinct nanoroughness was found on the as-built surfaces.

Laser treatment of PBF-LB-Ti6Al4V enabled substantial improvements in tensile shear strength of up to 44 MPa, while shifting the failure mode to complete cohesive failure within the adhesive. Moreover, laser-treated adherends also significantly enhanced the fatigue resistance of adhesive bonds. Pulsed Nd:YVO4 laser irradiation produced a hierarchical surface morphology, consisting of the inherent surface features from the as-built condition superimposed with a laser-induced open-porous, nanostructured oxide layer, as illustrated in

Figure 16. In addition, the laser pulse imprints slightly increased surface roughness on micrometer scale.

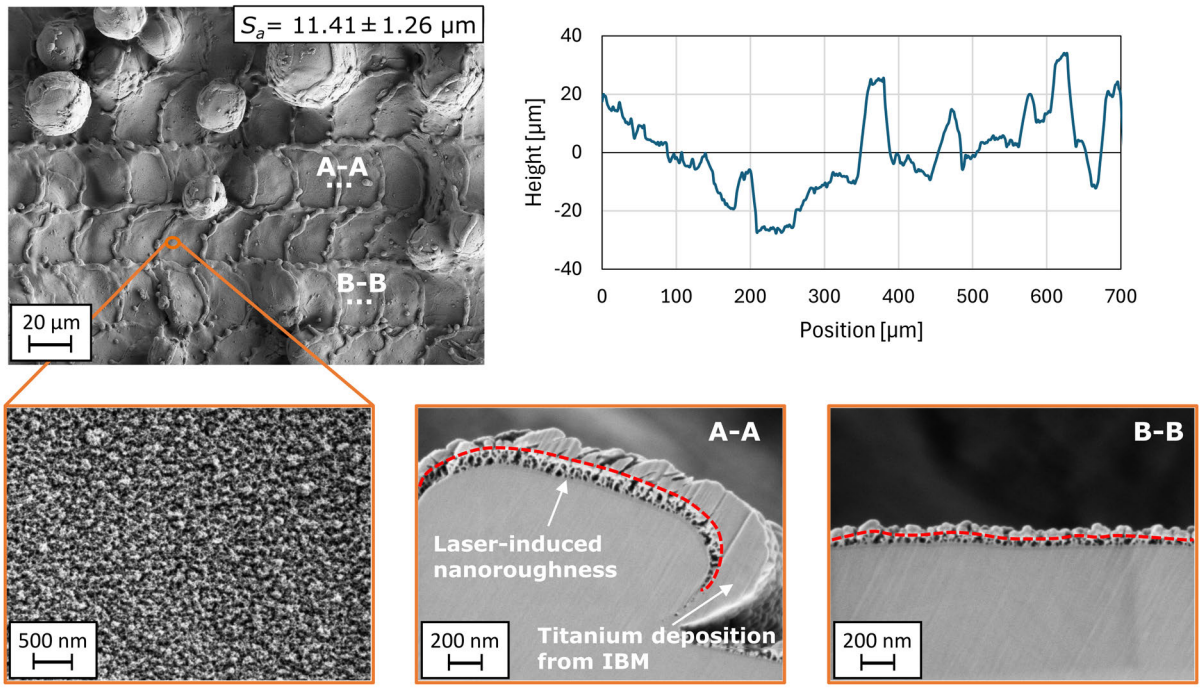


Figure 16: SEM images and height profile of a A90-oriented PBF-LB-Ti6Al4V surface after laser treatment. The IBM-prepared cross section views were evaluated at a laser pulse edge (A-A) and laser pulse depression (B-B).

In this surface morphology, the role of the partially melted particles can be summarized as inducing mechanical interlocking in the adhesive, enlarging the surface on which the nanoroughness can be formed and slowing down crack propagation during cyclic loading, primarily in the LCF-regime, by causing energy dissipation in the adhesive. The laser-induced nanoporous oxide layer, in turn, promotes the formation of chemical and dispersive interfacial bonds, enhances nanoscale interlocking of the adhesive and improves the fatigue resistance of adhesive bonds in both LCF and HCF. Analyzing the fracture behavior of the attached particles and oxide layer for different surface conditions revealed interactions between these surface features. An increased number of particles reduced the risk of oxide fracture, indicating that the particles effectively decrease the mechanical loading of the oxide layer. Conversely, a cohesively strong nanostructured oxide layer was found to reduce the number of fractured particles, thereby preserving more interlocking-sites. A differentiated assessment of the surface morphology effects on fatigue bond behavior was conducted, comparing the highly structured as-built surface A45-D with a particle-free, milled surface featuring laser-induced open-porous nanoroughness. The results demonstrated that the inherent roughness of PBF-LB-Ti6Al4V surfaces can be similarly effective to laser-induced nanoroughness in the LCF regime. However, under HCF loading conditions, the contribution of the nanoroughness to fatigue resistance of the adhesive bond becomes dominant, as the particle-induced interlocking effect diminished at lower stress levels due to the absence of significant plastic deformations in the adhesive. Crack growth analysis further confirmed that the particles do not act as defects under fatigue loading, but provide, in comparison to the laser-induced nanoroughness, less fatigue resistance.

Hydrothermal aging reduced the tensile shear bond strength in all cases, with laser-treated surfaces exhibiting losses of up to 30% due to extensive fracture of the nanoporous oxide layer. Oxide failure was found to occur primarily within the laser pulse depressions because of an inhomogeneous oxide layer thickness (see Figure 16). The insufficient environmental durability of the laser-induced oxide layer highlighted a critical limitation, emphasizing the need for further process optimizations to ensure long-term bond stability. Fracture of the nanoporous oxide layer was also observed in the fatigue-tested specimens, which suggested potential for further improvement of bond lifetime.

4.3 Optimizing the bond performance by laser-induced hierarchical surface morphologies (publication 3)

In the previous investigations, the inherent roughness of PBF-LB/M-fabricated Ti6Al4V surfaces proved to be generally beneficial for adhesive bonding. However, it was shown that an effective surface treatment beyond degreasing is still necessary to prevent interfacial bond failure. Since significant improvements in bond performance were achieved with laser pretreated surfaces, the third publication focused on laser treatment of PBF-LB-Ti6Al4V parts to comprehensively investigate the laser-induced structural modifications of the substrate and their impact on bond performance. This was done for three laser settings with low, medium and high laser fluence, aiming to optimize the surface morphology for structural adhesive bonding. The surfaces were characterized, addressing the laser-fluence-dependent pulse structuring and the formation of the nanoporous oxide layer. Moreover, potential structural damages in the bulk Ti6Al4V material were evaluated, and laser-induced residual stresses were examined by XRD. The laser fluence effects on tensile strength, mode I fracture toughness, environmental durability, and fatigue resistance of the adhesive bonds were analyzed. The weaknesses of laser-treated surfaces identified in the previous publication, namely insufficient hydrothermal bond durability and oxide fracture during cyclic fatigue loading, were evaluated in this study.

The different laser power settings produced hierarchical surface morphologies, in which the inherent roughness of the PBF-LB-Ti6Al4V surfaces was superimposed with differently pronounced nanoporous oxide layers. In general, increasing the laser fluence resulted in thicker oxide layers but with varying effects on thickness homogeneity. Applying a low laser fluence of 212 J/cm^2 (P60) generated a very thin oxide layer of roughly 15-25 nm with similar thicknesses in both the laser pulse depressions and laser pulse edges, as shown in Figure 17. In contrast, increasing the laser fluence to 248 J/cm^2 (P70) led to a highly inhomogeneous thickness distribution of the oxide layer, with thicknesses up to approximately 100 nm in the laser pulse edge regions and around 50 nm in the laser pulse depressions. Further increasing the laser fluence to 318 J/cm^2 (P90) produced again a remarkably uniform oxide layer with thicknesses slightly above 150 nm. The formation of this uniform, thick oxide layer at the highest applied laser fluence was attributed to extensive laser spattering at P90 and to a larger laser-induced plasma during processing. A similar laser-fluence-dependent oxide layer formation was observed on the partially melted particles of the PBF-LB-surfaces. Furthermore, SEM analysis of the IBM-prepared cross-sections revealed no laser-generated structural damage in the bulk Ti6Al4V material, while the XRD measurements showed that the applied

laser fluences induced relatively low tensile residual stresses in the near-surface region of up to around 50 MPa for the P90 laser setting.

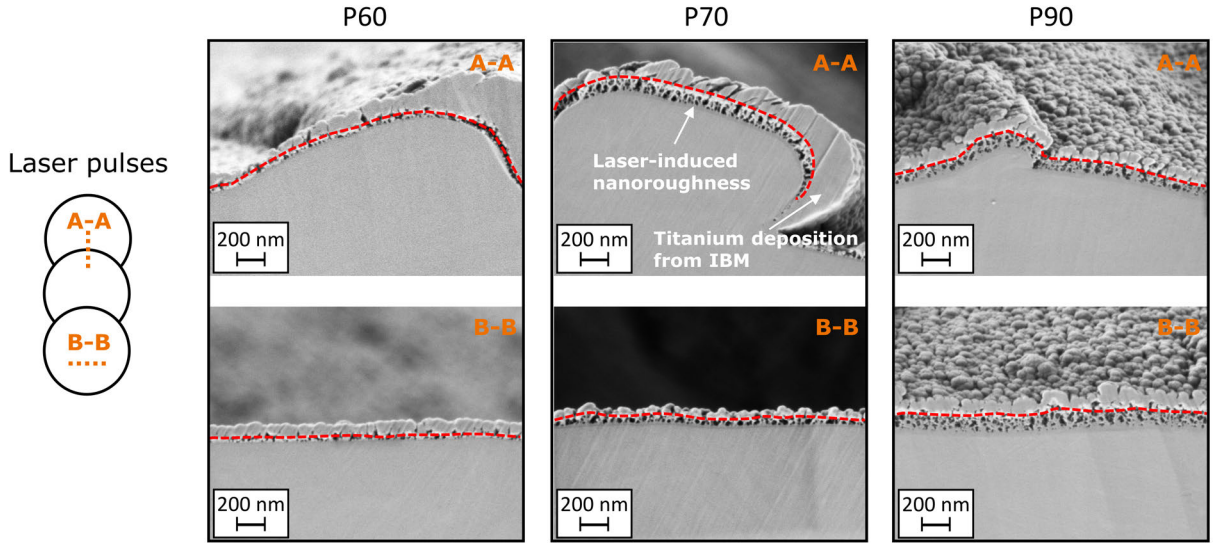


Figure 17: SEM images of IBM-prepared cross-sections of laser-treated PBF-LB-Ti6Al4V surfaces for the power levels (a) P60, (b) P70 and (c) P90, evaluated at a laser pulse edge (A–A) and a laser pulse depression (B–B).

The laser fluence was found to have a significant effect on bond performance, except for tensile loading, where the very thin, homogeneous oxide layer of P60 was already sufficient to achieve nearly complete cohesive failure in the adhesive, enabling a 43% increase in bond strength compared to the respective as-built PBF-LB-Ti6Al4V surface. In contrast to the predominantly uniform stress state during CATT testing, the high local stress concentrations present in the DCB- and SLJ-tests revealed pronounced differences between the applied laser fluences due to locally severe loading of the laser-induced oxide layer. The DCB-tests showed that the average mode I fracture toughness increased by approximately 220% with the P60 surface and by around 600% using the P70 and P90 surfaces compared to the as-built condition. The lower effectiveness of P60 was caused by extensive oxide fracture, whereas the thicker and more densely nanostructured oxides of P70 and P90 were able to withstand the mode I loading, despite P70 exhibiting an inhomogeneous oxide thickness. The most pronounced difference between the applied laser fluences was observed in the quasi-static SLJ tests after hydrothermal aging, demonstrating that this loading condition is highly sensitive for assessing different, distinct nanostructured oxide layers, even surpassing the mode I loading sensitivity. The uniform, thick oxide layer produced at high laser fluence enabled to achieve a 40% higher tensile shear bond strength after hydrothermal aging than with the other laser-treated surfaces and a 79% higher strength relative to the as-built surface. This cohesively strong oxide layer minimized oxide fracture, thereby allowing more particles to remain attached to the surface, which in turn contributed to the environmental bond durability.

The cyclic fatigue tests with SLJ specimens revealed that the most critical laser treatment influences on the fatigue bond performance are the thickness and uniformity of the nanoporous oxide layer. Neither the laser-induced tensile residual stresses in the near-surface region nor the microroughness generated by extensive laser spattering at high fluences were found to cause

earlier fatigue failure of the adhesive bond. The bond lifetimes obtained with the P60 surface were considerably lower than with P70 or P90. This difference became more pronounced towards the HCF regime, confirming the increasing contribution of the laser-induced nanoroughness to fatigue resistance at lower load levels. The more distinct and uniform oxide layer of P90 enabled complete cohesive failure within the adhesive in both the LCF and HCF regimes, while for P70 mainly oxide layer fracture occurred. However, the resulting fatigue lifetimes were similar for P70 and P90, with even slightly longer bond lifetimes in LCF for the P70 surface. This finding demonstrated that a locally weak oxide layer (P70) under fatigue loading can be partially compensated by the mechanical interlocking of the attached PBF-LB-particles, if the cracks propagate sufficiently close to the adherend surface, as observed for the P70 specimens. DIC analysis of the crack growth in LCF confirmed that cracks propagating through the oxide layer of P70 were more effectively slowed down due to the direct influence of the attached particles, compared to the cracks advancing through the adhesive layer in P90, outside the particle-affected region. Apart from this particle-related effect in LCF, strengthening the oxide layer with increasing laser fluence generally resulted in delayed crack initiation, slower crack propagation and a postponed onset of unstable crack growth during fatigue loading.

4.3.1 Comparison with anodization processes

Chromic acid anodizing (CAA) is a highly effective surface pretreatment for titanium alloys, which has been extensively used in demanding applications such as aerospace, due to its ability to generate nanoporous oxide layers that promote excellent adhesive bond strength and long-term durability [15]. The bond performance of CAA-treated PBF-LB-Ti6Al4V surfaces can therefore be expected to be comparable to that of the laser-treated surfaces in the present work. However, as hexavalent chromium compounds have been largely restricted or banned due to environmental and health regulations, CAA is no longer a viable option [156]. To replace CAA, several more environmentally friendly anodization processes have been developed. One of these is NaTESi anodizing, developed by Matz [78] for structural bonding of titanium alloys. This process was applied in multiple studies [98,157,158], showing that moderate to high adhesive joint strengths and good bond durability can be achieved. NaTESi anodizing of Ti6Al4V produces a relatively thick oxide layer of 540-650 nm, featuring open nanoporous structures, but also surface areas where the oxide appears closed due to its high density [157].

Kurtovic et al. [98] compared NaTESi anodizing with laser surface treatment of conventionally manufactured Ti6Al4V adherends in metal–metal adhesive joints. Their results showed that the peel resistance of NaTESi-pretreated surfaces was comparable to that of laser-treated surfaces exhibiting a distinct open-porous nanostructured oxide layer. However, the environmental durability of the adhesive bonds was found to be lower for NaTESi-anodized surfaces, as demonstrated by wedge testing.

In the present work, NaTESi anodizing was applied to milled PBF-LB-Ti6Al4V substrates used for SLJs, following the process parameters developed by Matz [78,79] (see Appendix A.2). Prior to anodizing, the substrates were degreased using an alkaline cleaner and pickled to remove the native oxide layer. Milled surfaces were chosen for NaTESi treatment, as the

partially melted particles on the as-built PBF-LB surfaces would otherwise be weakened or detached during the pickling process step and could promote non-uniform oxide formation during anodizing. The resulting tensile shear strengths, determined before and after hydrothermal aging, are compared with those of laser-treated PBF-LB-Ti6Al4V surfaces (P70) in Figure 18.

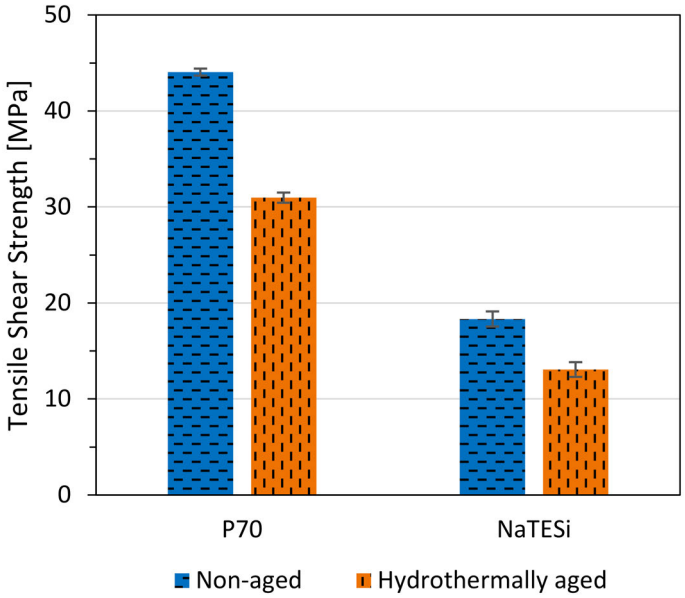


Figure 18: Comparison of tensile shear strengths between SLJs with laser-treated (P70) and NaTESi anodized PBF-LB-Ti6Al4V-adherends.

In both the non-aged and hydrothermally aged conditions, the bond strengths of NaTESi-pretreated specimens were found to be substantially lower in relation to the laser-treated samples, even compared to the P60 surfaces. These differences can be attributed to the partially closed oxide layer resulting from the NaTESi anodizing process and the absence of the inherent PBF-LB surface roughness on the milled, NaTESi-pretreated specimens. In contrast, the laser-induced oxides generated in the present study exhibited fully open-porous nanostructures, thereby promoting nanoscale interlocking of the adhesive and formation of interfacial bonds. These morphological differences did reflect in the failure modes of the SLJs. SEM analysis of NaTESi-pretreated joints revealed predominantly adhesive failure at the oxide–adhesive interface. Contrary, with the P70 surface, complete cohesive failure within the adhesive was reached in the non-aged condition, while partial oxide fracture occurred in the hydrothermally aged SLJs, which, however, could be minimized by increasing the applied laser fluence (P90).

It should be noted that improvements in bond strength may be achievable for NaTESi-pretreated specimens if the anodizing process is optimized to produce a predominantly open-porous nanostructure. However, the development of highly effective anodizing processes, comparable to CAA, is significantly constrained by progressively stringent environmental and safety regulations. This underscores the importance of alternative processes such as laser treatment.

4.4 Role of surface morphologies in hybrid structural joints (publication 4)

The application of PBF-LB-Ti6Al4V parts in adhesively bonded metal-composite joints was investigated in the fourth publication, with the primary focus on the influence of surface morphologies on mechanical performance. The mechanical behavior was evaluated by SLJ-testing, considering different joining methods and surface conditions. Initially, secondary bonding between PBF-LB-Ti6Al4V and CFRP was compared to a hybrid joining approach, in which additively manufactured pin-reinforcements on the metallic substrate are joined to the CFRP part by co-curing. To critically assess the enhancements achievable through co-cured hybrid joining, the secondary bonded joints were fabricated using properly pretreated adherend surfaces, representing an optimized bonding scenario, whereas the co-cured pinned joints were produced with as-built titanium surfaces. Subsequently, the effects of the titanium adherend surface conditions: as-built, release-agent-coated, and laser-treated on the quasi-static mechanical behavior of co-cured hybrid joints were investigated.

The ultimate joint strength of the secondary bonded SLJs with properly pretreated adherends was, as expected, limited by the delamination strength of the CFRP adherend. An enhancement of 44.4% in ultimate tensile shear strength was achieved by co-cured hybrid joining due to the pin-reinforcements, which also significantly increased the fracture shear strain and total energy absorption of the joint. However, despite the pin-reinforcements, the limit load (i.e., load at damage initiation) of the co-cured joints was found to be substantially lower compared to the secondary bonded joints. This was related to the insufficient adhesion of the as-built titanium surfaces used in the co-cured joints, which caused premature adhesive bond failure at the overlap ends. An effective surface treatment of PBF-LB-Ti6Al4V is therefore necessary to improve the limit load of co-cured hybrid joints. A direct comparison of the quasi-statically tested hybrid SLJs with as-built and release-agent-coated titanium adherends revealed a highly similar mechanical joint performance, except for the elastic joint stiffness. This demonstrated that the adhesive bond contribution to load transfer in pinned hybrid joints is highly limited when using as-built PBF-LB-Ti6Al4V surfaces. The effectiveness of the adhesive bond was significantly enhanced by using the laser-treated titanium surfaces, which led to a shift in failure mode from primarily adhesive failure on as-built surfaces to almost complete delamination of the CFRP adherend. The developed laser treatment process enabled a significant increase in the joint's elastic stiffness (+188.8%), total energy absorption (+48.4%) and limit load, while the ultimate tensile shear strength improved moderately by at least 9% compared to the as-built surface condition.

5 Conclusions and Outlook

The results presented in this thesis provide a comprehensive understanding of the interrelations between as-built PBF-LB-Ti6Al4V surface morphologies, surface modifications, and adhesive bond performance, as well as demonstrate how laser-induced hierarchical surface structures can enable adhesive joints with high strength, fatigue resistance, and environmental durability. The investigations were linked to the research objectives (RO1–RO5) defined in Section 1.2, which are addressed in the following.

Analyzing the influences of PBF-LB-Ti6Al4V surface morphologies on adhesive bond performance for quasi-static, fatigue and environmental loading conditions (RO1) revealed that the inherent roughness of as-built surfaces is generally beneficial for structural adhesive bonding. The primary surface features contributing to adhesion were identified as the partially melted particles originating from the powder bed. On inclined as-built surfaces, such as the 45° downskin orientation, the combination of attached particles and stair-stepping-induced surface waviness proved highly effective for bonding, particularly for enhancing fatigue resistance of adhesive joints under cyclic loading by delaying crack propagation. Other process-induced surface characteristics, such as smaller attached particles formed through the balling effect or melt-pool flow patterns and melt overflow bumps, were not observed to have significant effects on bond performance.
Most of the partially melted powder particles were found to adhere firmly to the bulk titanium material, which allowed them to remain attached to the surface in quasi-statically and fatigue-loaded adhesive joints. Thereby, the particles were able to effectively enhance adhesion by increasing the surface area for bonding and causing mechanical interlocking in the adhesive. The quantity and spatial distribution of attached particles was found to correlate with the macroscopic wettability and the bond strengths under tensile and tensile-shear (SLJ) loading. A negative effect of the inherent surface roughness on macroscopic wettability was not observed. Even on highly structured as-built surfaces with a large number of adhering particles, complete macroscopic wetting was achieved after ultrasonic cleaning in acetone. Fatigue SLJ-testing further demonstrated that increasing the particle density on PBF-LB surfaces also enhances bond lifetimes by decelerating crack growth, as confirmed by DIC measurements. The contribution of the particles to fatigue resistance is mainly pronounced in the LCF-regime, since particle-induced interlocking diminishes towards HCF due to the absence of considerable plastic deformations in the adhesive. Furthermore, hydrothermal aging of SLJs was not observed to weaken the connection between particles and bulk material. These surface features can therefore also contribute significantly to environmental bond durability.

The assessment of the bonding capabilities and limitations of as-built PBF-LB-Ti6Al4V parts (RO2) revealed a strong dependence on the build orientation of the bond surfaces for tensile shear loading. When horizontally oriented as-built surfaces, exhibiting few attached particles, were used, the resulting tensile shear bond strengths and fatigue lifetimes were relatively low and comparable to those of conventionally milled surfaces. In contrast, the rougher vertically oriented and upskin as-built surfaces allowed to reach a similar bond performance to grit blasted

PBF-LB-Ti6Al4V surfaces. Bonding with the highly structured 45° downskin surface even surpassed this bond performance, underscoring the bonding potential of as-built surfaces. Under tensile loading, however, the build orientation showed a less pronounced effect on bond strength, primarily due to the lower influence of particle-induced interlocking under tensile loading than under tensile shear loading. All examined as-built surfaces achieved similarly high tensile bond strengths, comparable to those obtained with grit-blasted surfaces.
The adhesion capability of as-built PBF-LB-Ti6Al4V surfaces was found to be limited by local areas with few or no attached powder bed particles. These regions exhibit weaker adhesion due to the absence of distinct surface roughness, thus acting as weak spots on the surface where damage initiation preferably occurs in adhesive joints. Fracture surface analysis revealed extensive adhesive failure in these areas, whereas particle-rich regions exhibited predominantly cohesive failure within the adhesive, as a result of particle-induced interlocking in the adhesive. Furthermore, the lack of distinct nanoroughness on the as-built surfaces generally limited the achievable bond strength, fatigue resistance and environmental bond durability.

To address the limitations of the as-built surfaces, grit blasting and laser treatment were investigated as potential pretreatment methods. The third research objective (RO3) focused on understanding the structural modifications induced by surface treatments and their effect on bond performance. Grit blasting removed the attached particles from the surface while simultaneously roughening the previously particle-free regions. This resulted in a surface with a more uniformly distributed roughness, but with no pronounced interlocking structures. Moreover, incised blasting media residues were detected on the surfaces that present damage in the bulk material and can influence wettability and bond performance. The macroscopic wettability of the grit blasted surfaces was found to be worse compared to the as-built surfaces, and no distinct nanoroughness was generated by grit blasting. The improvement in adhesion by roughening the former smooth surface areas was offset by the loss of particle-induced interlocking. These effects were identified as the main reasons for the generally similar bond performance and mixed-mode failure behavior of grit blasted surfaces compared to as-built surfaces with an intermediate number of attached particles.
Laser treatment significantly enhanced the bond performance by producing a hierarchical surface morphology that combines the inherent roughness of the as-built surfaces with a laser-induced open-porous, nanostructured oxide layer. With optimized laser parameters, either complete cohesive failure within the adhesive or in the case of hydrothermally aged SLJs nearly complete cohesive failure was achieved. In this surface morphology, the partially melted particles primarily contribute to mechanical interlocking at the micrometer scale, enlarging the surface on which the nanoroughness can be formed and decelerating crack propagation during cyclic loading by causing energy dissipation in the adhesive. The laser-induced nanoporous oxide layer, in turn, facilitates the formation of chemical and dispersive interfacial bonds, promotes nanoscale interlocking of the adhesive in the pores and enhances the fatigue resistance of adhesive bonds in both the LCF- and HCF-regimes. It was further shown that in LCF, the inherent roughness of highly structured PBF-LB-Ti6Al4V surfaces can be similarly effective as laser-generated nanoroughness, whereas under HCF loading conditions, the contribution of nanoroughness to the fatigue resistance of adhesive bonds becomes dominant due to the diminishing effect of particle-induced interlocking at lower load levels. Moreover, interactions between surface features were identified. An increased number of adhering powder bed

particles reduced the risk of oxide fracture, indicating that the particles effectively decrease the mechanical loading of the oxide layer. In contrast, a cohesively strong nanoporous oxide layer was found to reduce the number of fractured particles, thereby preserving interlocking-sites.
The most critical laser treatment influences on the adhesive bond performance of such hierarchical surface morphologies were found to be the thickness and uniformity of the laser-induced open-porous oxide layer. An insufficient laser fluence can result either in the formation of a uniform but excessively thin oxide layer or an inhomogeneous thick oxide layer with lower thicknesses within the laser pulse depressions. For oxide thicknesses below approximately 50 nm, extensive oxide fracture near the bulk material interface occurred under quasi-static tensile, mode I and fatigue SLJ loading conditions, typically within the laser pulse depression. Therefore, a substrate-dependent minimum laser fluence must be applied to ensure the formation of a thick, uniform oxide layer with sufficient structural strength to fully leverage the beneficial effects of the inherent PBF-LB surface roughness for structural adhesive bonding. The applied laser fluences caused no structural damage in the near-surface region, and laser-generated tensile residual stresses in the bulk material were not observed to adversely affect bond performance. In addition, microroughness generated at higher laser fluences in the form of extensive laser spattering was not found to deteriorate fatigue bond performance, underscoring that higher laser fluences should be preferred to ensure sufficient structural integrity of the induced oxide layer. With the developed laser treatment process for PBF-LB-Ti6Al4V, an environmentally friendly and highly efficient pretreatment method is provided, enabling the fabrication of adhesive bonds with high strength, fatigue resistance and environmental durability (RO4).

Finally, the application of PBF-LB-Ti6Al4V parts with pin-reinforcements in co-cured metal-composite joints was investigated to evaluate the role of surface morphologies in hybrid joints (RO5). Quasi-static SLJ-testing demonstrated that the adhesive bond contribution to load transfer in co-cured hybrid joints is decisive for the joint stiffness and limit load, while the macroscopic pin-reinforcements primarily determine the ultimate joint strength, ductility and energy absorption. Utilizing the as-built PBF-LB-Ti6Al4V surfaces resulted, except for the elastic joint stiffness, in no significant improvement compared to release-agent coated surfaces. This was attributed to the horizontal build orientation of the as-built surface, which was selected to facilitate precise manufacturing of the pin-reinforcements but provides only relatively low adhesion. In contrast, laser treatment of this as-built surface substantially enhanced the adhesive bond contribution to load transfer in the hybrid joint, leading to significant increases in elastic joint stiffness, limit load and energy absorption, along with moderate improvements in ultimate joint strength and a shift in failure mode from adhesive failure at the metal-composite interface to almost complete CFRP delamination. This demonstrates that surface morphologies can have significant positive influences on the mechanical behavior of co-cured hybrid joints with pin-reinforcements, provided that appropriate surface treatment is conducted.

Future research should focus on optimizing the PBF-LB/M process parameters to intentionally increase particle adhesion in areas dedicated for structural adhesive bonding, particularly on horizontally oriented surfaces where only limited particle attachment occurs. In addition, by adjusting the laser scanning strategy, micro-textures such as grooves can be generated on the horizontally oriented surfaces, which could further enhance the adhesion capability. The

findings of this work may be transferable to other PBF-LB-processed metallic materials, since the main process-related surface structuring mechanisms should be comparable. Moreover, the concept of exploiting the intrinsic surface morphology of AM-produced parts for adhesive bonding offers promising potential beyond PBF-LB/M. For instance, DED-LB/p surfaces typically exhibit significantly higher roughness levels than those investigated in this work, which could be advantageous for adhesive joints [43]. However, the high roughness of DED-LB/p-surfaces often necessitates subsequent machining due to insufficient geometrical accuracy, thus requiring a balanced surface design strategy.

Given the critical importance of environmental robustness for industrial implementation, further investigations into bond durability are required. This includes assessing service-like disbond behavior, for example through wedge testing, as well as evaluating bond performance under other application-relevant aging conditions.

Regarding the pinned hybrid metal-composite SLJs, further enhancements in mechanical joint performance are expected through reduction of the non-uniformity of the stress distribution along the overlap by optimization of pin alignment and geometry. Additionally, assessing hybrid joints under further loading conditions for different surface conditions will enable to extend the understanding of the role of surface morphologies in co-cured hybrid joints.

References

[1] Huang R, Riddle M, Graziano D, Warren J, Das S, Nimbalkar S, Cresko J, Masanet E (2016) Energy and emissions saving potential of additive manufacturing: the case of lightweight aircraft components. Journal of Cleaner Production 135:1559–1570. https://doi.org/10.1016/j.jclepro.2015.04.109

[2] Blakey-Milner B, Gradl P, Snedden G, Brooks M, Pitot J, Lopez E, Leary M, Berto F, du Plessis A (2021) Metal additive manufacturing in aerospace: A review. Materials & Design 209:110008. https://doi.org/10.1016/j.matdes.2021.110008

[3] Williams JC, Boyer RR (2020) Opportunities and Issues in the Application of Titanium Alloys for Aerospace Components. Metals 10:705. https://doi.org/10.3390/met10060705

[4] Allen J (2006) An Investigation into the Comparative Costs of Additive Manufacture vs. Machine from Solid for Aero Engine Parts. In: Cost Effective Manufacture via Net-Shape Processing, pp. 17-1 – 17-10. Meeting Proceedings RTO-MP-AVT-139, Neuilly-sur-Seine, France.

[5] Childerhouse T, Jackson M (2019) Near Net Shape Manufacture of Titanium Alloy Components from Powder and Wire: A Review of State-of-the-Art Process Routes. Metals 9:689. https://doi.org/10.3390/met9060689

[6] Zhang X, Liang E (2019) Metal additive manufacturing in aircraft: current application, opportunities and challenges. IOP Conference Series: Materials Science and Engineering 493:012032. https://doi.org/10.1088/1757-899X/493/1/012032

[7] Bartolomeu F, Gasik M, Silva FS, Miranda G (2022) Mechanical Properties of Ti6Al4V Fabricated by Laser Powder Bed Fusion: A Review Focused on the Processing and Microstructural Parameters Influence on the Final Properties. Metals 12:986. https://doi.org/10.3390/met12060986

[8] Kolesnikov B, Herbeck L, Fink A (2008) CFRP/titanium hybrid material for improving composite bolted joints. Composite Structures 83:368-380. https://doi.org/10.1016/j.compstruct.2007.05.010

[9] Xu J, Mkaddem A, Mansori M (2016) Recent advances in drilling hybrid FRP/Ti composite: A state-of-the-art review. Composite Structures 135:316-338. http://dx.doi.org/10.1016/j.compstruct.2015.09.028

[10] Fink A, Camanho PP, Andrés JM, Pfeiffer E, Obst A (2010) Hybrid CFRP/titanium bolted joints: Performance assessment and application to a spacecraft payload adaptor. Composites Science and Technology 70:305–317. https://doi.org/10.1016/j.compscitech.2009.11.002

[11] Galinska A (2020) Mechanical Joining of Fibre Reinforced Polymer Composites to Metals—A Review. Part I: Bolted Joining. Polymers 12:2252. https://doi.org/10.3390/polym12102252

[12] Galinska A, Galinski C (2020) Mechanical Joining of Fibre Reinforced Polymer Composites to Metals—A Review. Part II: Riveting, Clinching, Non-Adhesive Form-Locked Joints, Pin and Loop Joining. Polymers 12:1681. https://doi.org/10.3390/polym12081681

[13] Brockmann W, Geiß PL, Klingen J, Schröder B (2008) Adhesive Bonding: Materials, Applications and Technology. Wiley-VCH Verlag GmbH & Co. KGaA, Weinheim. http://dx.doi.org/10.1002/9783527623921

[14] European Cooperation for Space Standardization (2011) Space engineering Adhesive bonding handbook ECSS-E-HB-32-21A. ESA Requirements and Standards Division, Noordwijk.

[15] da Silva LFM, Öchsner A, Adams RD, editors (2018) Handbook of Adhesion Technology. Springer, Berlin, Heidelberg. https://doi.org/10.1007/978-3-319-55411-2

[16] Kubiak KJ, Wilson MCT, Mathia TG, Carval Ph (2011) Wettability versus roughness of engineering surfaces. Wear 271:523–528. https://doi.org/10.1016/j.wear.2010.03.029

[17] Arikan ES (2020) Oberflächenmodifikation von Polyetheretherketon (PEEK) für das strukturelle Kleben in der Luftfahrt. Dissertation, Universität der Bundeswehr München.

[18] Naat N, Boutar Y, Naimi S, Mezlini S, da Silva LFM (2023) Effect of surface texture on the mechanical performance of bonded joints: a review. The Journal of Adhesion 99:2, 166-258. https://doi.org/10.1080/00218464.2021.2008370

[19] Kahlin M, Ansell H, Basu D, Kerwin A, Newton L, Smith B, Moverare JJ (2020) Improved fatigue strength of additively manufactured Ti6Al4V by surface post processing. International Journal of Fatigue 134:105497. https://doi.org/10.1016/j.ijfatigue.2020.105497

[20] Witkin DB, Patel DN, Helvajian H, Steffeney L, Diaz A (2019) Surface Treatment of Powder-Bed Fusion Additive Manufactured Metals for Improved Fatigue Life. Journal of Materials Engineering and Performance 28:681–692. https://doi.org/10.1007/s11665-018-3732-9

[21] Bagehorn S, Mertens T, Greitemeier D, Carton L, Schoberth A (2015) Surface finishing of additive manufactured Ti-6Al-4V - a comparison of electrochemical and mechanical treatments. 6th European Conference for Aerospace Sciences.

[22] Ardila-Rodriguez LA, Rans C, Poulis JA (2021) Effect of surface morphology on the Ti–Ti adhesive bond performance of Ti6Al4V parts fabricated by selective laser melting. International Journal of Adhesion and Adhesives 110:102918. https://doi.org/10.1016/j.ijadhadh.2021.102918

[23] Gulino M, Lima RAA, Moroni F, Pirondi A, de Freitas ST (2025) Effect of the surface morphology of 3D printed titanium substrates on the mode I fracture toughness of metal-metal and metal-composite bonded joints. Theoretical and

Applied Fracture Mechanics 135:104778. https://doi.org/10.1016/j.tafmec.2024.104778

[24] Nusom Y, Srimanosaowapak S, Uthaisangsuk V (2023) Effects of 3D-printing surface morphologies on interfacial bonding strength between Ti–6Al–4V and CFRTP with PMCs interlayer. International Journal of Adhesion and Adhesives 121:103313. https://doi.org/10.1016/j.ijadhadh.2022.103313

[25] Ebnesajjad S, Ebnesajjad C (2013) Surface Treatment of Materials for Adhesive Bonding. Elsevier, Amsterdam. https://doi.org/10.1016/C2013-0-12914-5

[26] Encinas N, Oakley BR, Belcher MA, Blohowiak KY, Dillingham RG, Abenojar J, Martinez MA (2014) Surface modification of aircraft used composites for adhesive bonding. International Journal of Adhesion and Adhesives 50:157–163. https://doi.org/10.1016/j.ijadhadh.2014.01.004

[27] European Union (2006) Regulation (EC) No 1907/2006 of the European Parliament and of the Council of 18 December 2006 concerning the Registration, Evaluation, Authorisation and Restriction of Chemicals (REACH). Official Journal of the European Union, Brussels.

[28] Toyserkani E, Sarker D, Ibhadode OO, Liravi F, Russo P, Taherkhani K (2021) Metal Additive Manufacturing. John Wiley & Sons Ltd, Hoboken, New Jersey. ISBN: 978-1-119-21078-8

[29] Wong KV, Hernandez A (2012) A Review of Additive Manufacturing. ISRN Mechanical Engineering 2012:208760. https://doi.org/10.5402/2012/208760

[30] The International Organization for Standardization (2021) Additive manufacturing - General principles - Fundamentals and vocabulary ISO/ASTM 52900:2021.Vernier, Geneva.

[31] Gibson I, Rosen D, Stucker B, Khorasani M (2021) Additive Manufacturing Technologies. Springer, Cham. https://doi.org/10.1007/978-3-030-56127-7

[32] Reddy KS, Dufera S (2016) Additive Manufacturing Technologies. International Journal of Management, Information Technology and Engineering 4(7):89-112.

[33] Zhang T, Liu CT (2022) Design of titanium alloys by additive manufacturing: A critical review. Advanced Powder Materials 1:100014. https://doi.org/10.1016/j.apmate.2021.11.001

[34] Ford S, Despeisse M (2016) Additive manufacturing and sustainability: an exploratory study of the advantages and challenges. Journal of Cleaner Production 137:1573–1587. https://doi.org/10.1016/j.jclepro.2016.04.150

[35] Attaran M (2017) The rise of 3-D printing: The advantages of additive manufacturing over traditional manufacturing. Business Horizons 60:677–688. https://doi.org/10.1016/j.bushor.2017.05.011

[36] Frazier WE (2014) Metal Additive Manufacturing: A Review. Journal of Materials Engineering and Performance 23:1917–1928. https://doi.org/10.1007/s11665-014-0958-z

[37] Patel S, Liu Y, Siddique Z, Ghamarian I (2024) Metal additive manufacturing: Principles and applications. Journal of Manufacturing Processes 131:1179–1201. https://doi.org/10.1016/j.jmapro.2024.09.101

[38] Herzog D, Seyda V, Wycisk E, Emmelmann C (2016) Additive manufacturing of metals. Acta Materialia 117:371–392. https://doi.org/10.1016/j.actamat.2016.07.019

[39] Vafadar A, Guzzomi F, Rassau A, Hayward K (2021) Advances in Metal Additive Manufacturing: A Review of Common Processes, Industrial Applications, and Current Challenges. Applied Sciences 11:1213. https://doi.org/10.3390/app11031213

[40] AMPower (2025) AMPower Report 2025 Management Summary. https://additive-manufacturing-report.com/. Accessed 22 November 2025.

[41] Chowdhury S, Yadaiah N, Prakash C, Ramakrishna S, Dixit S, Gupta LR, Buddhi D (2022) Laser powder bed fusion: a state-of-the-art review of the technology, materials, properties & defects, and numerical modelling. Journal of Materials Research and Technology 20:2109–2172. https://doi.org/10.1016/j.jmrt.2022.07.121

[42] Zhang LC, Liu Y, Li S, Hao Y (2018) Additive Manufacturing of Titanium Alloys by Electron Beam Melting: A Review. Advanced Engineering Materials 20:1700842. https://doi.org/10.1002/adem.201700842

[43] Ahn DG (2021) Directed Energy Deposition (DED) Process: State of the Art. International Journal of Precision Engineering and Manufacturing-Green Technology 8:703–742. https://doi.org/10.1007/s40684-020-00302-7

[44] Calignano F, Manfredi D, Ambrosio EP, Biamino S, Lombardi M, Atzeni E, Salmi A, Minetola P, Iuliano L, Fino P (2017) Overview on Additive Manufacturing Technologies. Proceedings of the IEEE 105:593–612. https://doi.org/10.1109/JPROC.2016.2625098

[45] ZainElabdeen IH, Ismail L, Mohamed OF, Khan KA, Schiffer A (2024) Recent advancements in hybrid additive manufacturing of similar and dissimilar metals via laser powder bed fusion. Materials Science and Engineering: A 909:146833. https://doi.org/10.1016/j.msea.2024.146833

[46] Liu S, Shin YC (2019) Additive manufacturing of Ti6Al4V alloy: A review. Materials and Design 164:107552. https://doi.org/10.1016/j.matdes.2018.107552

[47] Mahale RS, Shamanth V, Hemanth K, Nithin SK, Sharath PC, Shashanka R, Patil A, Shetty D (2022) Processes and applications of metal additive manufacturing. Materials Today: Proceedings 54:228–233. https://doi.org/10.1016/j.matpr.2021.08.298

[48] Ni C, Zhu J, Zhang B, An K, Wang Y, Liu D, Lu W, Zhu L, Liu C (2025) Recent advance in laser powder bed fusion of Ti–6Al–4V alloys: microstructure,

mechanical properties and machinability. Virtual and Physical Prototyping 20:e2446952. https://doi.org/10.1080/17452759.2024.2446952

[49] Shipley H, McDonnell D, Culleton M, Coull R, Lupoi R, O'Donnell G, Trimble D (2018) Optimisation of process parameters to address fundamental challenges during selective laser melting of Ti-6Al-4V: A review. International Journal of Machine Tools and Manufacture 128:1–20. https://doi.org/10.1016/j.ijmachtools.2018.01.003

[50] Yang J, Yu H, Yin J, Gao M, Wang Z, Zeng X (2016) Formation and control of martensite in Ti-6Al-4V alloy produced by selective laser melting. Materials and Design 108:308–318. https://doi.org/10.1016/j.matdes.2016.06.117

[51] Villa R, Liu Y, Siddique Z (2024) Review of defects and their sources in as-built Ti6Al4V manufactured via powder bed fusion. The International Journal of Advanced Manufacturing Technology 132:4105–4134. https://doi.org/10.1007/s00170-024-13611-x

[52] Gaiani S, Ferrari E, Gozzi M, Di Giovanni MT, Gualtieri ML, Colombini E, Veronesi P (2023) Impact of Post-Process Heat Treatments Performed on Ti6Al4V Titanium Alloy Specimens Obtained Using LPBF Technology. Technologies 11:100. https://doi.org/10.3390/technologies11040100

[53] Kahlin M, Ansell H, Moverare JJ (2017) Fatigue behaviour of notched additive manufactured Ti6Al4V with as-built surfaces. International Journal of Fatigue 101:51–60. https://doi.org/10.1016/j.ijfatigue.2017.04.009

[54] Günther J, Krewerth D, Lippmann T, Leuders S, Tröster T, Weidner A, Biermann H, Niendorf T (2017) Fatigue life of additively manufactured Ti–6Al–4V in the very high cycle fatigue regime. International Journal of Fatigue 94:236–245. https://doi.org/10.1016/j.ijfatigue.2016.05.018

[55] Elambasseril J, Rogers J, Wallbrink C, Munk D, Leary M, Qian M (2023) Laser powder bed fusion additive manufacturing (LPBF-AM): the influence of design features and LPBF variables on surface topography and effect on fatigue properties. Critical Reviews in Solid State and Materials Sciences 48:132–168. https://doi.org/10.1080/10408436.2022.2041396

[56] Ilin A, Logvinov R, Kulikov A, Prihodovsky A, Xu H, Ploshikhin V, Günther B, Bechmann F (2014) Computer Aided Optimisation of the Thermal Management During Laser Beam Melting Process. Physics Procedia 56:390–399. https://doi.org/10.1016/j.phpro.2014.08.142

[57] Charles A, Elkaseer A, Paggi U, Thijs L, Hagenmeyer V, Scholz S (2021) Down-facing surfaces in laser powder bed fusion of Ti6Al4V: Effect of dross formation on dimensional accuracy and surface texture. Additive Manufacturing 46:102148. https://doi.org/10.1016/j.addma.2021.102148

[58] The SOLIDWORKS Blog (2017) An Introduction to Designing for Metal 3D Printing. https://blogs.solidworks.com/solidworksblog/2017/06/introduction-designing-metal-3d-printing.html. Accessed 22 November 2025.

[59] Petrie EM (1999) Handbook of Adhesives and Sealants. McGraw-Hill Professional, New York.

[60] Adams RD, editor (2021) Adhesive Bonding: Science, Technology, and Applications. Woodhead Publishing, Cambridge. https://doi.org/10.1016/C2019-0-00395-0

[61] Campbell FC (2004) Adhesive bonding and integrally cocured structure: a way to reduce assembly costs through parts integration. In: Campbell FC (editor) Manufacturing Processes for Advanced Composites. Elsevier Science, Amsterdam, pp. 241–301. https://doi.org/10.1016/B978-1-85617-415-2.X5000-X

[62] The International Organization for Standardization (2022) Adhesives - Designation of main failure patterns ISO 10365.Vernier, Geneva.

[63] Hartshorn SR, editor (1986) Structural Adhesives: Chemistry and Technology. Springer, New York. https://doi.org/10.1007/978-1-4684-7781-8

[64] Dupré A (1869) Théorie Mécanique de la Chaleur. Gauthier-Villars, Paris.

[65] Schrader ME (1995) Young-Dupre Revisited. Langmuir 11:3585–3589. https://doi.org/10.1021/la00009a049

[66] Li S, Lin J, Min J (2023) Experimental investigation and molecular simulation on the chemical bonding between laser-treated titanium alloy amorphous surface and epoxy adhesive. The Journal of Adhesion 101:144–163. https://doi.org/10.1080/00218464.2023.2277298

[67] Habenicht G (2009) Kleben: Grundlagen, Technologien, Anwendungen. Springer, Berlin, Heidelberg. https://doi.org/10.1007/978-3-540-85266-7

[68] Possart W (1988) Experimental and theoretical description of the electrostatic component of adhesion at polymer/ metal contacts. International Journal of Adhesion and Adhesives 8(2):77-83. https://doi.org/10.1016/0143-7496(88)90027-9

[69] Packham DE (2003) The Mechanical Theory of Adhesion. In: Pizzi A, Mittal KL, (editors) Handbook of Adhesive Technology. Marcel Dekker Inc., New York, pp. 69–93. ISBN: 9780203912225

[70] Azari S, Papini M, Spelt JK (2010) Effect of Surface Roughness on the Performance of Adhesive Joints Under Static and Cyclic Loading. The Journal of Adhesion 86:742–764. https://doi.org/10.1080/00218464.2010.482430

[71] Budhe S, Ghumatkar A, Birajdar N, Banea MD (2015) Effect of surface roughness using different adherend materials on the adhesive bond strength. Applied Adhesion Science 3:20. https://doi.org/10.1186/s40563-015-0050-4

[72] Bikerman JJ (1961) The Science of Adhesive Joints. Academic Press, New York.

[73] Sharpe LH (1972) The Interphase in Adhesion. The Journal of Adhesion 4:51–64. https://doi.org/10.1080/00218467208072210

[74] Dachev D, Kazilas M, Alfano G, Omairey S (2025) Towards Reliable Adhesive Bonding: A Comprehensive Review of Mechanisms, Defects, and Design Considerations. Materials 18:2724. https://doi.org/10.3390/ma18122724

[75] Molitor P, Barron V, Young T (2001) Surface treatment of titanium for adhesive bonding to polymer composites: a review. International Journal of Adhesion and Adhesives 21:129–136. https://doi.org/10.1016/S0143-7496(00)00044-0

[76] Marques AC, Mocanu A, Tomic NZ, Balos S, Stammen E, Lundevall A, Abrahami ST, Günther R, de Kok JM, de Freitas ST (2020) Review on adhesives and surface treatments for structural applications: recent developments on sustainability and implementation for metal and composite substrates. Materials 13:5590. https://doi.org/10.3390/ma13245590

[77] Wegman RF, van Twisk J (2013) Surface preparation techniques for adhesive bonding. William Andrew, Norwich. https://doi.org/10.1016/C2012-0-02158-8

[78] Matz C (1988) Optimization of the durability of structural titanium adhesive joints. International Journal of Adhesion and Adhesives 8(1):17-24. https://doi.org/10.1016/0143-7496(88)90053-X

[79] Kurtovic A (2014) Laserinduzierte Nanostrukturierung von Titanoberflächen für das strukturelle Kleben - Einfluss auf die Oberflächenmorphologie, Ermüdungs- und Adhäsionseigenschaften. Dissertation, Universität Paderborn.

[80] Takeda T, Yasuoka T, Sugimoto S, Iwahori Y (2022) Strength enhancement of adhesively bonded Ti-6Al-4V alloy joints by flame-based surface treatment. The Journal of Adhesion 98:1016–1035. https://doi.org/10.1080/00218464.2020.1870106

[81] Sun C, Min J, Lin J, Wan H (2019) Effect of Atmospheric Pressure Plasma Treatment on Adhesive Bonding of Carbon Fiber Reinforced Polymer. Polymers 11:139. https://doi.org/10.3390/polym11010139

[82] Akram M, Jansen KM, Ernst LJ, Bhowmik S (2011) Atmospheric pressure plasma surface modification of titanium for high temperature adhesive bonding. International Journal of Adhesion and Adhesives 31:598–604. https://doi.org/10.1016/j.ijadhadh.2011.05.009

[83] Islam MN, Das AK, Billah MM, Rahman KS, Hiziroglu S, Hattori N, Agar DA, Rudolfsson M (2023) Multifaceted Laser Applications for Wood – A Review from Properties Analysis to Advanced Products Manufacturing. Lasers in Manufacturing and Materials Processing 10:225–250. https://doi.org/10.1007/s40516-023-00204-x

[84] Svelto O (2010) Principles of Lasers. Springer, New York. https://doi.org/10.1007/978-1-4419-1302-9

[85] Thomas G, Isaacs R (2011) Basic principles of lasers. Anaesthesia & Intensive Care Medicine 12:574–577. https://doi.org/10.1016/j.mpaic.2011.09.013

[86] Siegman AE (1986) Lasers. University Science Books, Sausalito. ISBN: 0-935702-11-3

[87] Ion JC (2005) Laser Processing of Engineering Materials: Principles, Procedure and Industrial Application. Elsevier Butterworth-Heinemann, London. ISBN: 978-0-7506-6079-2

[88] Baburaj EG, Starikov D, Evans J, Shafeev GA, Bensaoula A (2007) Enhancement of adhesive joint strength by laser surface modification. International Journal of Adhesion and Adhesives 27:268-276.https://doi.org/10.1016/j.ijadhadh.2006.05.004

[89] Loumena C, Cherif M, Ali MT, Jumel J, Kling R (2017) Laser surface preparation for adhesive improvement of Ti6Al4V. Proceedings SPIE 10092, Laser-based Micro- and Nanoprocessing XI, 100921F. https://doi.org/10.1117/12.2252444

[90] Cakir FH (2022) Enhancing the adhesive bonding strength of Ti6Al4V sheets with fiber laser texturing. International Journal of Adhesion and Adhesives 114:103117. https://doi.org/10.1016/j.ijadhadh.2022.103117

[91] Rotella G, Alfano M, Candamano S (2015) Surface modification of Ti6Al4V alloy by pulsed Yb-laser irradiation for enhanced adhesive bonding. CIRP Annals - Manufacturing Technology 64:527-530. https://doi.org/10.1016/j.cirp.2015.04.042

[92] Zhang C, Zhang Y, Chen L, Jin J (2021) Effects of laser processing microgrooves on the shear strength of Ti6Al4V adhesively bonded joints. The Journal of Adhesion 98(10):1461-1479. https://doi.org/10.1080/00218464.2021.1907183

[93] Maressa P, Anodio L, Bernasconi A, Demir AG, Previtali B (2015) Effect of surface texture on the adhesion performance of laser-treated Ti6Al4V alloy. The Journal of Adhesion 91(7):518-537.

[94] Vorobyev AY, Guo C (2007) Femtosecond laser structuring of titanium implants. Applied Surface Science 253:7272-7280. https://doi.org/10.1016/j.apsusc.2007.03.006

[95] Rotella G, Orazi L, Alfano M, Candamano S, Gnilitskyi I (2017) Innovative high-speed femtosecond laser nano-patterning for improved adhesive bonding of Ti6Al4V titanium alloy. CIRP Journal of Manufacturing Science and Technology 18:101-106. https://doi.org/10.1016/j.cirpj.2016.10.003

[96] Moritz J, Götze P, Schiefer T, Stepien L, Klotzbach A, Standfuß J, Lopez E, Brückner F, Leyens C (2021) Additive manufacturing of titanium with different surface structures for adhesive bonding and thermal direct joining with fiber-reinforced polyether-ether-ketone (PEEK) for lightweight design applications. Metals 11:265. https://doi.org/10.3390/met11020265

[97] Shirasu K, Mizutani M, Takano N, Yoshinaga H, Oguri T, Ogawa K, Okabe T, Obayashi S (2022) Lap-shear strength and fracture behavior of CFRP/3D-printed Titanium alloy adhesive joint prepared by hot-press-aided co-bonding. International Journal of Adhesion and Adhesives 117:103169. https://doi.org/10.1016/j.ijadhadh.2022.103169

[98] Kurtovic A, Brandl E, Mertens T, Maier HJ (2013) Laser induced surface nano-structuring of Ti–6Al–4V for adhesive bonding. International Journal of Adhesion and Adhesives 45:112-117. https://doi.org/10.1016/j.ijadhadh.2013.05.004

[99] Löbbecke M, Bayerbasi TJ, Bartsch M, Haubrich J (2023) Role of surface structures on long term stability of adhesive joints between Ti–15V–3Cr–3Sn–3Al and polyether-ether-ketone. International Journal of Adhesion and Adhesives 120:103282. https://doi.org/10.1016/j.ijadhadh.2022.103282

[100] Specht U, Ihde J, Mayer B (2014) Laser induced nano-porous Ti–O-layers for durable titanium adhesive bonding. Materials Science & Engineering Technology 45:1116-1122. https://doi.org/10.1002/mawe.201400360

[101] Taube A, Kurtovic A, Niendorf T, Mertens T, Zinn C, Schaper M, Maier HJ (2016) Influence of surface pre-treatments on the high-cycle fatigue behavior of Ti–6Al–4V – from anodizing to laser-assisted techniques. International Journal of Fatigue 91:195-203. https://doi.org/10.1016/j.ijfatigue.2016.06.010

[102] Zimmermann S, Specht U, Spieß L, Romanus H, Krischok S, Himmerlich M, Ihde J (2012) Improved adhesion at titanium surfaces via laser-induced surface oxidation and roughening. Materials Science and Engineering: A 558:755-760. https://doi.org/10.1016/j.msea.2012.08.101

[103] Li Z, Zhang D, Su X, Yang S, Xu J, Ma R, Shan D, Guo B (2021) Removal mechanism of surface cleaning on TA15 titanium alloy using nanosecond pulsed laser. Optics & Laser Technology 139:106998. https://doi.org/10.1016/j.optlastec.2021.106998

[104] Zhou Z, Sun W, Wu J, Chen H, Zhang F, Wang S (2023) The Fundamental Mechanisms of Laser Cleaning Technology and Its Typical Applications in Industry. Processes 11:1445. https://doi.org/10.3390/pr11051445

[105] Belcher MA, List MS, Wohl CJ, Ghose S, Watson KA, Hopkins JW, Connell JW (2010) Laser surface preparation for adhesive bonding of Ti-6Al-4V. SAMPE Electronic Proceedings, Seattle, WA.

[106] Guyott CCH, Cawley P, Adams RD (1986) The Non-destructive Testing of Adhesively Bonded Structure: A Review. The Journal of Adhesion 20:129–159. https://doi.org/10.1080/00218468608074943

[107] Genest M, Martinez M, Mrad N, Renaud G, Fahr A (2009) Pulsed thermography for non-destructive evaluation and damage growth monitoring of bonded repairs. Composite Structures 88:112–120.https://doi.org/10.1016/j.compstruct.2008.02.010

[108] Yilmaz B, Ba A, Jasiuniene E, Bui HK, Berthiau G (2019) Comparison of different non-destructive testing techniques for bonding quality evaluation. IEEE 5th International Workshop on Metrology for AeroSpace, Turin, Italy, pp. 92–97. https://doi.org/10.1109/MetroAeroSpace.2019.8869692

[109] Machado JJM, Marques EAS, da Silva LFM (2018) Adhesives and adhesive joints under impact loadings: An overview. The Journal of Adhesion 94:421–452. https://doi.org/10.1080/00218464.2017.1282349

[110] Duncan B (2010) Developments in testing adhesive joints. In: Dillard DA (editor) Advances in Structural Adhesive Bonding. Woodhead Publishing, Cambridge, pp. 389–436. https://doi.org/10.1533/9781845698058.3.389

[111] Beck U, Reiners G, Lerche D, Rietz U, Niederwald H (2011) Quantitative adhesion testing of optical coatings by means of centrifuge technology. Surface and Coatings Technology 205:S182–S186. https://doi.org/10.1016/j.surfcoat.2011.02.016

[112] Hoffmann M, Tserpes K, Moutsompegka E, Schlag M, Brune K (2018) Determination of adhesion strength of pre-bond contaminated composite-to-metal bonded joints by centrifuge tests. Composites Part B: Engineering 147:114–121. https://doi.org/10.1016/j.compositesb.2018.04.014

[113] The International Organization for Standardization (2019) Adhesives - Determination of shear behaviour of structural adhesives - Part 1: Torsion test method using butt-bonded hollow cylinders ISO 11003-1.Vernier, Geneva.

[114] Kadioglu F, Vaughn LF, Guild FJ, Adams RD (2002) Use of the thick adherend shear test for shear stress-strain measurements of stiff and flexible adhesives. The Journal of Adhesion 78:355–381. https://doi.org/10.1080/00218460211818

[115] The International Organization for Standardization (2009) Adhesives - Determination of the mode 1 adhesive fracture energy of structural adhesive joints using double cantilever beam and tapered double cantilever beam specimens ISO 25217:2009. DIN Media, Berlin. Vernier, Geneva.

[116] ASTM International (2019) Standard Test Method for Determination of the Mode II Interlaminar Fracture Toughness of Unidirectional Fiber-Reinforced Polymer Matrix Composites ASTM D7905. West Conshohocken, PA.

[117] Deutsches Institut für Normung e. V (2010) Klebstoffe - Bestimmung des Schälwiderstandes von Klebungen - Rollenschälversuch DIN EN 1464:2010. DIN Media, Berlin. https://dx.doi.org/10.31030/1570421

[118] Deutsches Institut für Normung e. V (2022) Klebstoffe - T-Schälprüfung für geklebte Verbindungen aus flexiblen Fügeteilen DIN EN ISO 11339:2022. DIN Media, Berlin. https://dx.doi.org/10.31030/3338393

[119] Samborsky D, Mandell J, Sears A, Agastra P (2010) Fatigue Results and Analysis for Thick Adhesive Notched Lap Shear Test. 51st AIAA/ASME/ASCE/AHS/ASC Structures, Structural Dynamics, and Materials Conference, Orlando, Florida. https://doi.org/10.2514/6.2010-2821

[120] Deutsches Institut für Normung e. V (1995) Klebstoffe - Verfahren zur Prüfung der Ermüdungseigenschaften von Strukturklebungen bei Zugscherbeanspruchung DIN EN ISO 9664:1995. DIN Media, Berlin. https://dx.doi.org/10.31030/2792663

[121] Erpolat S, Ashcroft IA, Crocombe AD, Abdel-Wahab MM (2004) A study of adhesively bonded joints subjected to constant and variable amplitude fatigue. International Journal of Fatigue 26:1189–1196. https://doi.org/10.1016/j.ijfatigue.2004.03.011

[122] Abdel-Wahab MM (2012) Fatigue in Adhesively Bonded Joints: A Review. ISRN Materials Science 2012:1–25. https://doi.org/10.5402/2012/746308

[123] Bernasconi A, Carboni M, Comolli L, Galeazzi R, Gianneo A, Kharshiduzzaman M (2016) Fatigue Crack Growth Monitoring in Composite Bonded Lap Joints by a Distributed Fibre Optic Sensing System and Comparison with Ultrasonic Testing. The Journal of Adhesion 92:739–757. https://doi.org/10.1080/00218464.2015.1123153

[124] Lahuerta F, Westphal T, Nijssen RPL, van der Meer FP, Sluys LJ (2014) Measuring the delamination length in static and fatigue mode I tests using video image processing. Composites Part B: Engineering 63:1–7. https://doi.org/10.1016/j.compositesb.2014.03.003

[125] He Z, Luo Q, Li Q, Zheng G, Sun G (2022) Fatigue behavior of CFRP/Al adhesive joints — Failure mechanisms study using digital image correlation (DIC) technique. Thin-Walled Structures 174:109075. https://doi.org/10.1016/j.tws.2022.109075

[126] Thäsler T, Holtmannspötter J, Gudladt HJ (2019) Monitoring the fatigue crack growth behavior of composite joints using in situ 2D-digital Image correlation. The Journal of Adhesion 95(5-7):595-613. https://doi.org/10.1080/00218464.2018.1562923

[127] Viana G, Costa M, Banea MD, da Silva LFM (2017) A review on the temperature and moisture degradation of adhesive joints. Proceedings of the Institution of Mechanical Engineers, Part L: Journal of Materials: Design and Applications 231:488–501. https://doi.org/10.1177/1464420716671503

[128] Dillard DA, Pocius AV, editors (2002) Adhesion Science and Engineering - 1 – The Mechanics of Adhesion. Elsevier, Amsterdam. ISBN: 978-0-444-51140-9

[129] Costa M, Viana G, da Silva LFM, Campilho RDSG (2017) Environmental effect on the fatigue degradation of adhesive joints: A review. The Journal of Adhesion 93:127–146. https://doi.org/10.1080/00218464.2016.1179117

[130] ASTM International (2024) Standard Test Method for Adhesive-Bonded Surface Durability of Aluminum (Wedge Test) ASTM D3762-24. West Conshohocken, PA.

[131] Frömmel SA (2013) Untersuchungen zum mechanischen Verhalten von Klebverbindungen unter Berücksichtigung von Grenzflächendefekten. Dissertation, Universität der Bundeswehr München.

[132] Lambiase F, Scipioni SI, Lee CJ, Ko DC, Liu F (2021) A State-of-the-Art Review on Advanced Joining Processes for Metal-Composite and Metal-Polymer Hybrid Structures. Materials 14:1890. https://doi.org/10.3390/ma14081890

[133] Hamerton I, Kratz J (2018) The use of thermosets in modern aerospace applications. In: Guo Q (editor) Thermosets. Elsevier, Amsterdam, pp. 303–340. https://doi.org/10.1016/B978-0-08-101021-1.00009-5

[134] Bodjona K, Lessard L (2016) Hybrid bonded-fastened joints and their application in composite structures: A general review. Journal of Reinforced Plastics and Composites 35:764-781. https://doi.org/10.1177/0731684415627296

[135] Graham DP, Rezai A, Baker D, Smith PA, Watts JF (2014) The development and scalability of a high strength, damage tolerant, hybrid joining scheme for composite–metal structures. Composites: Part A 64:11-24. https://doi.org/10.1016/j.compositesa.2014.04.018

[136] Sarantinos N, Tsantzalis S, Ucsnik S, Kostopoulos V (2019) Review of through-the-thickness reinforced composites in joints. Composite Structures 229:111404. https://doi.org/10.1016/j.compstruct.2019.111404

[137] Dance BGI (2009) Rapid materials processing and surface sculpting using electron beam and laser processes. TMS 2009 138th annual meeting & exhibition on proceedings, San Francisco, California, pp. 167–174.

[138] Wang X, Ahn J, Kaboglu C, Yu L, Blackman BRK (2016) Characterisation of composite-titanium alloy hybrid joints using digital image correlation. Composite Structures 140:702-711. https://doi.org/10.1016/j.compstruct.2015.12.023

[139] Bagnato T, Ravindran AR, Mirabedini A, Ladani RB, Kandare E, Orifici AC, Chang P, Wang J, Mouritz AP (2023) Superior interfacial toughening of hybrid metal-composite structural joints using 3D printed pins. Composites Part A 168:107479. https://doi.org/10.1016/j.compositesa.2023.107479

[140] Nguyen ATT, Brandt M, Feih S, Orifici AC (2016) Pin pull-out behaviour for hybrid metal-composite joints with integrated reinforcements. Composite Structures 155:160-172. https://doi.org/10.1016/j.compstruct.2016.07.047

[141] Ucsnik S, Scheerer M, Zaremba S, Pahr DH (2010) Experimental investigation of a novel hybrid metal–composite joining technology. Composites: Part A 41:369-374. https://doi.org/10.1016/j.compositesa.2009.11.003

[142] Skhabovskyi I, Batista NL, Damato CA, Reis RP, Botelho EC, Scotti A (2017) Appraisal of fiber-metal laminate panels reinforced with metal Pins deposited by CMT welding. Composite Structures 180:263-275. https://doi.org/10.1016/j.compstruct.2017.07.043

[143] Sarantinos N, Kostopoulos V, Di Vita G, Campoli G, Bricout L (2019) Micro-pins: the next step in composite–Composite and metal–composite joining. CEAS Space Journal 11:351-358. https://doi.org/10.1007/s12567-019-00251-1

[144] Nguyen ATT, Amarasinghe CK, Brandt M, Feih S, Orifici AC (2017) Loading, support and geometry effects for pin-reinforced hybrid metal-composite joints. Composites Part A 98:192-206. https://doi.org/10.1016/j.compositesa.2017.03.019

[145] Bagnato T, Ravindran AR, Orifici AC, Kandare E, Ladani RB (2025) Interfacial fatigue performance of hybrid titanium to composite Joints reinforced with 3D printed pins. Composites Part A 196:108984. https://doi.org/10.1016/j.compositesa.2025.108984

[146] Huelsbusch D, Haack M, Solbach A, Emmelmann C, Walther F (2015) Influence of pin size on tensile and fatigue behavior of TI-CFRP hybrid structures produced by laser additive manufacturing. 20th International Conference on Composite Materials, Copenhagen, Denmark.

[147] Kralovec C, Dengg A, Schagerl M, Schiller A, Bisagni C, Löbbecke M, Haubrich J, Hanelt R (2025) Static strength and fatigue life of pinned hybrid titanium-composite single-lap-shear joints. Composite Structures 354:118765. https://doi.org/10.1016/j.compstruct.2024.118765

[148] Parkes PN, Butler R, Meyer J, de Oliveira A (2014) Static strength of metal-composite joints with penetrative reinforcement. Composite Structures 118:250-256. https://doi.org/10.1016/j.compstruct.2014.07.019

[149] Ertürk E, Bold J, Höfer P, Stark C, Höhn W (2022) 3D Material Model for Additive Manufactured Metallic Parts. In: Rieser J, Endress F, Horoschenkoff A, Höfer P, Dickhut T, Zimmermann M (editors) Proceedings of the Munich Symposium on Lightweight Design 2021. Springer Vieweg, Berlin, Heidelberg. https://doi.org/10.1007/978-3-662-65216-9_16

[150] ASTM International (2019) Standard Test Methods and Definitions for Mechanical Testing of Steel Products ASTM A370-19. West Conshohocken, PA.

[151] ASTM International (2014) Standard Test Method for Tensile Properties of Polymer Matrix Composite Materials ASTM D3039. West Conshohocken, PA.

[152] ASTM International (2019) Standard Test Method for Shear Properties of Composite Materials by the V-Notched Beam Method ASTM D5379. West Conshohocken, PA.

[153] ASTM International (2005) Standard Test Method for Apparent Shear Strength of Single-Lap-Joint Adhesively Bonded Metal Specimens by Tension Loading (Metal-to-Metal) ASTM D1002-05. West Conshohocken, PA.

[154] Henkel Corporation Aerospace (2013) Loctite EA 9396 AERO Technical Data Sheet. https://www.aero-consultants.ch/view/data/3285/Produkte/Henkel%20Adhesive/LOCTITE%20EA%209396%20AERO.pdf. Accessed 22 November 2025.

[155] Henkel Corporation Aerospace (2013) Loctite EA 9395 AERO Technical Data Sheet. https://www.pccomposites.com/wp-content/uploads/2015/07/PCRS9395-QT_TDS.pdf. Accessed 22 November 2025.

[156] European Union (2014) Commision Regulation (EU) No 895/2014 of 14 August 2014 amending Annex XIV to Regulation (EC) No 1907/2006 of the European Parliament and of the Council concerning the Registration, Evaluation,

Authorisation and Restriction of Chemicals (REACH). Official Journal of the European Union, Brussels.

[157] Mertens T, Gammel FJ, Kolb M, Rohr O, Kotte L, Tschöcke S, Kaskel S, Krupp U (2012) Investigation of surface pre-treatments for the structural bonding of titanium. International Journal of Adhesion and Adhesives 34:46–54. https://doi.org/10.1016/j.ijadhadh.2011.12.007

[158] Yu YS, Xie LS, Chen MH, Wang N, Wang H (2015) Surface characteristics and adhesive strength to epoxy of three different types of titanium alloys anodized in NaTESi electrolyte. Surface & Coatings Technology 280:122–128. https://doi.org/10.1016/j.surfcoat.2015.09.010

Appendix

A.1 Publications

This chapter includes the four peer-reviewed publications, summarized in Chapter 4. Please note that the fourth publication is included in its ‘Accepted Manuscript’ version, as this article was published under a subscription model, which prohibits reproducing the published “Version of Record”.

Publication 1 Ertürk E, Musil B, Diez G, Felber C, Höfer P (2023) Surface morphology influences of PBF-LB manufactured Ti6Al4V parts on adhesive bond strength – investigation of as-built and surface-treated conditions. Progress in Additive Manufacturing 8(4):719–731.
This article is a postprint of the article published in “Progress in Additive Manufacturing” (Springer Nature). The original authenticated version is available online at https://doi.org/10.1007/s40964-023-00450-7.

Publication 2 Ertürk E, Diez JG, Vitale P, Höfer P (2025) Surface morphology influences on the adhesive bond performance of PBF-LB manufactured Ti6Al4V parts – investigation of quasi-static and fatigue loading conditions. The Journal of Adhesion 101(10):1219–1251.
This article is a postprint of the article published in “The Journal of Adhesion” (Taylor & Francis Group). The original authenticated version is available online at https://doi.org/10.1080/00218464.2024.2441886.

Publication 3 Ertürk E, Wohninsland A, Diez JG, Höfer P (2025) Laser treatment of PBF-LB manufactured Ti6Al4V parts for structural adhesive bonding. International Journal of Adhesion and Adhesives 142:104114.
This article is a postprint of the article published in “International Journal of Adhesion and Adhesives” (ELSEVIER). The original authenticated version is available online at https://doi.org/10.1016/j.ijadhadh.2025.104114.

Publication 4 Ertürk E, Vitale P, Höfer P (2025) Hybrid structural joints between PBF-LB manufactured Ti6Al4V and CFRP – role of surface morphologies. The Journal of Adhesion.
This article (Accepted Manuscript version) is a postprint of the article published in “The Journal of Adhesion” (Taylor & Francis Group). The original authenticated version is available online at https://doi.org/10.1080/00218464.2025.2560880.

Progress in Additive Manufacturing
https://doi.org/10.1007/s40964-023-00450-7

FULL RESEARCH ARTICLE

Surface morphology influences of PBF-LB manufactured Ti6Al4V parts on adhesive bond strength—investigation of as-built and surface-treated conditions

Emre Ertürk[1] · Bruno Musil[1] · Gregor Diez[1] · Christian Felber[2] · Philipp Höfer[1]

Received: 7 September 2022 / Accepted: 28 April 2023
© The Author(s) 2023

Abstract
Additive manufacturing in combination with adhesive bonding enables high lightweight potential in structural design. A decisive factor for high adhesive bond performance are the surface properties. In the present work, the surface morphology of laser powder bed fusion (PBF-LB) processed Ti6Al4V parts was investigated in the as-built condition for the build orientations 0°, 45°, 90°. Furthermore, subsequent surface treatment by grit blasting or laser treatment allowed to modify the surface morphology and examine its effect on the bond strength. The surface characteristics were assessed using scanning electron microscopy, laser confocal microscopy and contact angle measurements. Evaluating the bond strength was done for tensile loading by centrifugal adhesion testing. The lowest bond strength was found for 0° oriented specimens, while the 45° and 90° oriented samples showed similar strengths. Fracture surface analysis of the as-built surfaces showed that the partially melted particles remain attached and cause mechanical interlocking. Furthermore, surface treatment by grit blasting allowed a minor improvement of the bond strength, while with laser treatment a significant increase was possible.

Keywords Adhesive bonding · Additive manufacturing · Surface morphology · Surface treatment

1 Introduction

As the productivity of 3D-printers continues to improve, additive manufacturing (AM) is becoming increasingly used in lightweight construction. A main advantage of AM is the high design freedom, which allows to manufacture load path optimized structures with a high degree of system integration. This enables a material efficient part design [1]. A commonly used material for metal-AM is the titanium alloy Ti6Al4V. It offers an excellent strength to weight ratio, good corrosion resistance and temperature stability and is, therefore, widely used in aerospace applications. To fully benefit from the high lightweight potential of additive manufactured titanium parts, it is necessary to also consider the joining process for the assembly design [2]. In conventional lightweight constructions with titanium, joining is often carried out by bolting and riveting, thus leaving room for further improvement. A suitable joining method for lightweight construction is adhesive bonding. The advantages compared to a mechanical joint include lower weight penalty, a more uniformly load transfer, not damaging the base material and in case of metals avoiding contact corrosion [3]. However, a common problem is that the load-bearing capability of an adhesive bond is often limited due to local stress concentrations in the bond. These stress concentrations cause premature failure and are often a result of large stiffness gradients between the joining partners [4]. With AM, the stiffnesses of the joining partners can be adjusted to achieve minimal load concentrations in the adhesive bond [5]. Therefore, the combination between AM and adhesive bonding seems promising.

This type of process combination is investigated in the research project BLANCA in the context of load introductions in sandwich structures. The project's main goal is to optimize the load introduction using AM to manufacture optimized load introduction elements and adhesive bonding to join them with the sandwich structure. The present paper is part of the project work on adhesive bonding of AM parts.

✉ Emre Ertürk
emre.ertuerk@unibw.de

[1] Institute of Lightweight Engineering, Universität der Bundeswehr München, Neubiberg, Germany

[2] Institute of Materials Science, Universität der Bundeswehr München, Neubiberg, Germany

Published online: 12 May 2023

A decisive factor for the adhesive bond performance are the surface properties. Most materials are in the untreated state not suitable for adhesive bonding. Therefore, surface treatment takes an essential role in high-performance bonding. A basic step in surface preparation is cleaning the substrate surfaces from contaminations and loose oxide layers. This is a crucial step to avoid weak boundary layers and achieve sufficient wetting of the surface by the adhesive. The simplest method to remove surface contaminations is degreasing. For organic impurities, cleaning with solvents is usually sufficient, while for strong contaminations on metals more intensive cleaning is required [6]. This is possible with physical treatment methods like laser ablation, plasma treatment and UV/Ozone treatment. These methods are not only used for cleaning, but also for modifying the surface properties. Adapting the surface chemistry to the adhesive type and creating surface roughness at the micro and nanometer scale are further steps that contribute to a high bond strength. In a study by Akram et al. [7], titanium surfaces were pretreated with atmospheric pressure plasma and evaluated for bonding with high temperature resistant polyimide adhesive in tensile shear tests. It was found that plasma treatment allows a significant improvement of the static bond strength. An important advantage of plasma treatment is the environmental friendliness, but the pretreated surfaces often require primer application due to high degradation rate when exposed to atmospheric environment [8]. A simple way of creating surface roughness at the macro- and microscopic level are mechanical surface treatments. Processes such as grit blasting are used to increase the effective contact area for bonding and to clean the surface to a certain extent. However, it is rather difficult to create desirable interlocking-features with mechanical treatment. In addition, the effectiveness of macro- and microroughness is significantly lower compared to roughness in the nanometer scale [4]. In aerospace, electrochemical processes such as phosphoric acid anodizing (PAA) are, therefore, often used for surface treatment of metals. PAA creates a thin oxide layer consisting of structures in the nanometer scale on the surface. This nano-porous layer provides a high contact area, promotes high capillary forces and allows a durable adhesive bond under environmental influences [4, 9]. However, the disadvantage of electrochemical processes is that they are environmentally unfriendly. A more sustainable method to create nano-porous layers is laser treatment. Specht et al. [10] investigated the adhesive bond performance of conventionally manufactured Ti6Al4V-samples after laser treatment. They showed that a laser induced nano-porous oxide layer improves the tensile shear strength and allows durability under hot-wet ageing. An increase of the shear lap bond strength up to 4.5 times was observed in a study by Cakir [11] for laser treatment of Ti6Al4V-sheets. A limitation of laser treatment is its tendency to produce an uneven oxide layer on the surface, with most of the oxide concentrated at the edges of the laser pulses. This has been shown in previous studies, such as Schneider and Wrobel's [12] work on a magnesium alloy treated with a ND:YAG-Laser. Optimizing the laser settings is, therefore, necessary to produce a predominantly uniform oxide layer. Additionally, the surface roughness must be kept as low as possible to improve fatigue behavior [13–15]. Furthermore, it has to be considered that laser treatment can cause residual tensile stresses in the near-surface area, which often deteriorate fatigue properties. Taube et al. [15] investigated the residual stresses in Ti6Al4V substrates caused by laser treatment for different laser intensities. They showed that at high laser intensities, the residual tensile stresses promote crack initiation. The laser treatment should, therefore, be conducted with the minimum possible laser intensity at which the oxide layer is still formed. In the present study, PBF-LB-processed Ti6Al4V samples are laser treated to examine the potential improvement in adhesive bond strength. Furthermore, surface treatment by grit blasting was also considered since it's a frequently used postprocessing step for PBF-LB-processed metallic parts.

Parts manufactured by PBF-LB have rough 'as-built' surfaces due to semi-sintered or partially melted particles [16]. The surface morphology is determined by the build parameters as well as by process-related effects. A comprehensive literature review on this topic was carried out in [17]. The build orientation is cited as an important parameter. A comparatively higher roughness is observed for inclined surfaces. This is mainly caused by a higher number of adhering particles from the powder bed and by stair-step structuring of the surface due to layer-wise production. Furthermore, a distinction is made between the upskin and downskin surface of inclined parts. The downfacing side is significantly rougher, since there is more adjacent powder that can be partially melted and due to a larger melt pool size caused by slower heat dissipation [18].

In several studies [19–21] it was shown, that the inherent roughness of AM-Ti6Al4V has a high bonding ability for static loading cases. Tensile shear testing of Ti6Al4V-PEEK joints in [19] showed that the adhesive bond strength with as-built Ti6Al4V surfaces produced by electron beam melting is comparable to laser structured surfaces. Nguyen et al. [20] conducted fracture toughness testing for metal–metal and metal–composite joints and found that the microroughness features on PBF-LB-processed Ti6Al4V surfaces can allow high adhesive bond performance. The build orientation influence on the adhesive bond performance was examined by Rodriguez et al. [21] for metal–metal joints with PBF-LB-processed Ti6Al4V parts. They evaluated the bond strength for the build orientations 0°, 45° (downskin) and 90° by means of butt joint testing. The results showed that the applied acetone cleaning was insufficient for the surface

with the highest roughness, here the 45° downskin surface. The lowest tensile strength was, therefore, measured for this surface. Only after UV/Ozone cleaning did the 45° and vertically oriented surfaces show comparable bond strengths, while for the horizontally oriented samples a slightly lower bond strength was found. The measured bond strengths are significantly influenced by the cleaning method and by the defined manufacturing parameters. Therefore, the build orientation influence was investigated in the present study for other manufacturing conditions and a different cleaning process. An overview of this work is illustrated in Fig. 1. The build orientation comparison was extended in this study by including the 45° upskin surface. Furthermore, the effect of surface treatment on the bond strength was examined for grit blasting and laser treatment. The surfaces were characterized by Scanning Electron Microscopy (SEM), Confocal Laser Scanning Microscopy (CLSM) and contact angle measurements. Afterwards, the adhesive bond performance for each surface was investigated for tensile loading.

2 Experimental

2.1 Manufacturing

Small plates with a length and width of 25 mm and a thickness of 4 mm were used as specimens in this study. Manufacturing was conducted by the project partner GERG on a Concept Laser M2 machine using standard parameters for Ti6Al4V Grade 23. For the scanning strategy a 45° stripes pattern was defined. The powder used fulfils the ASTM F3001 specification. It was supplied by GE Additive with a particle size range of 10–45 µm. After the build process, the specimens were stress relief heat treated under argon environment. In the next steps, the specimens were separated from the build plate using EDM Cutting and were then ultrasonically cleaned with deionized water to remove loose particles. Afterwards, ultrasonic cleaning with acetone was conducted to remove surface contaminations.

2.2 Surface treatment methods

2.2.1 Grit blasting

The specimens were grit blasted in a Peenmatik 1300 SDK (iepco, Switzerland) using silicon carbide as a blasting agent with a grain size range of 212–300 µm. Silicon carbide was selected since it's a standard blasting agent used in post-processing for AM. Alternatives are discussed in the results section. The grit blasting device was operated manually with a blasting angle of about 90°, a pressure of 3 bar and a nozzle size of 10 mm. The surfaces were blasted from a 20 cm distance for approximately 10 s until a uniform surface finish was achieved. Afterwards, ultrasonic cleaning was conducted to remove abrasive residues.

2.2.2 Laser treatment

The laser treatment was conducted on a TRUMPF Trumark Station 5000 marking laser system (TRUMPF, Germany) with a pulsed ND:YAG-Laser ($\lambda = 1064$ nm, $P_0 = 15$ W). The laser spot diameter was set to 30 µm using a lens with a focal length of 100 mm. All laser settings were adapted with the goal to create pronounced nanoroughness on the surface of Ti6Al4V. This was achieved with a laser power level of 35%, a scan speed of 0.4 m/s and a pulse frequency of 20 kHz. For the laser scanning strategy, a horizontal line pattern was

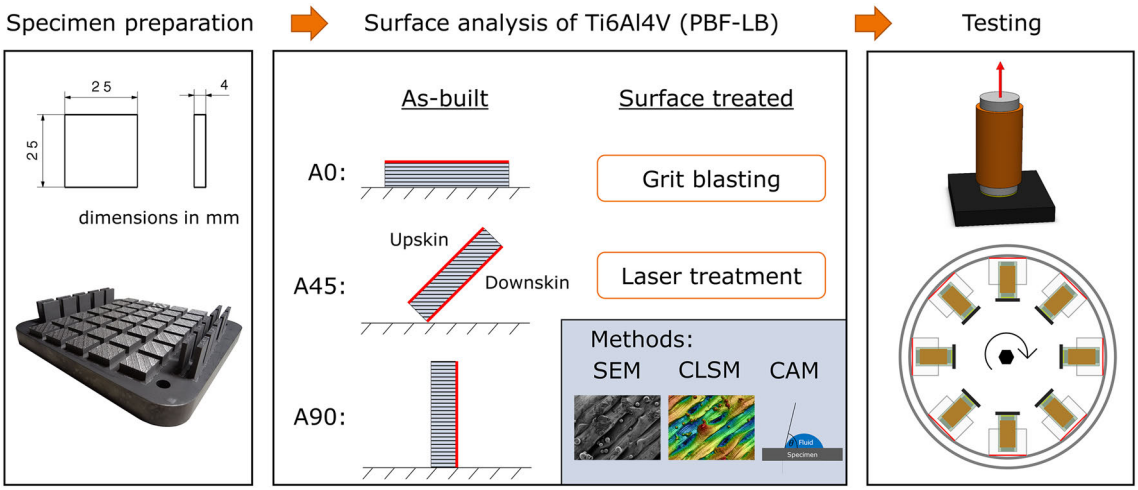


Fig. 1 Overview of the experimental investigations

defined with a laser track distance of 30 µm. With these settings, the laser scanned once over the entire surface.

2.3 Analytical methods

2.3.1 Surface morphology

Characterizing the surface textures was done in a first step by Scanning Electron Microscopy (SEM). The images were taken on a Zeiss Ultra 55 (Carl Zeiss, Germany) with a Secondary Electrons Detector (SE2) and an accelerating voltage of 1.0 kV. Quantitative information about the surface morphologies was obtained by Confocal Laser Scanning Microscopy (CLSM) using a Keyence VK-X3000 (Keyence International, Belgium). With CLSM, the height information of the topographies as well as the roughness values were determined. For each surface type at least five measurements were conducted on different locations and samples.

2.3.2 Contact angle measurement

The macroscopic wettability of the surfaces was examined by contact angle measurements using a DSA100E Drop Shape Analyzer (Krüss, Germany). First, the samples were ultrasonically cleaned with acetone. Afterwards, the measurements were conducted using the sessile drop method according to DIN EN ISO 19403–1 [22]. The contact angle is calculated by curve fitting the drop shape and averaging the contact angle measured at the ends of the droplet. As test liquids, deionized water and di-iodomethane were used in a quantity of 3 µl per drop. For each surface type at least five measurements were performed.

2.4 Adhesive joint preparation and testing

The adhesive bond performance was assessed for tensile loading by centrifugal adhesion testing (CATT). This test method is an alternative to classical butt-joint testing in a tensile testing machine. It allows time- and material-efficient testing. In this work, CATT was chosen since it is a preeminent testing method to investigate the adhesion strength. Moreover, it allows a uniform loading of the adhesive bond, which is in case of the highly irregular surfaces of PBF-LB-processed Ti6Al4V advantageous to reduce scattering of the bond strength results. In a first step, the samples were ultrasonically cleaned with acetone. After that, they were bonded with an aluminum test stamp using a bonding fixture to ensure alignment of the substrates. The bond surface of the test stamp was laser treated to avoid adhesive failure on the test stamp side. Thus, failure occurred either by cohesive failure in the adhesive or due to adhesive failure on the specimen surface. As an adhesive, the two-component epoxy adhesive Loctite EA 9395 AERO (Henkel, Germany) was used. After bonding, a test weight is screwed onto the specimen and the assembly is placed in a guide sleeve, as illustrated in Fig. 2. This setup is then finally mounted in the centrifugal testing device. In this test method, the rotational movement creates a centrifugal force, which induces a tensile loading of the adhesive bond. The load was increased linearly by 20 N/s until fracture occurred. Five tests were performed for each surface type.

3 Results and discussion

3.1 Surface morphology in as-built condition

SEM images of Ti6Al4V surfaces produced by PBF-LB are shown in Fig. 3 for the build orientations 0°, 45° and 90°. The images show the surfaces in as-built condition. The laser scanning direction is depicted for each surface. For the horizontally oriented surface A0, the main surface features are groves with an orientation of 45° and a few number of attached particles on the surface. The groves are created by the defined laser scanning pattern, while the attached particles can be caused by improper powder melting or other process related effects like the balling effect [23]. Regarding the A90 and A45-Downskin/Upskin oriented surfaces, it can be stated that the surface morphology is mainly characterized by partially melted particles. Within these three surfaces the A45-Upskin surface has the lowest quantity of attached particles, but still significantly more than on the A0 surface. A large number of ball-like particles are present on the A90 and A45-Downskin surfaces. Especially, at the downskin

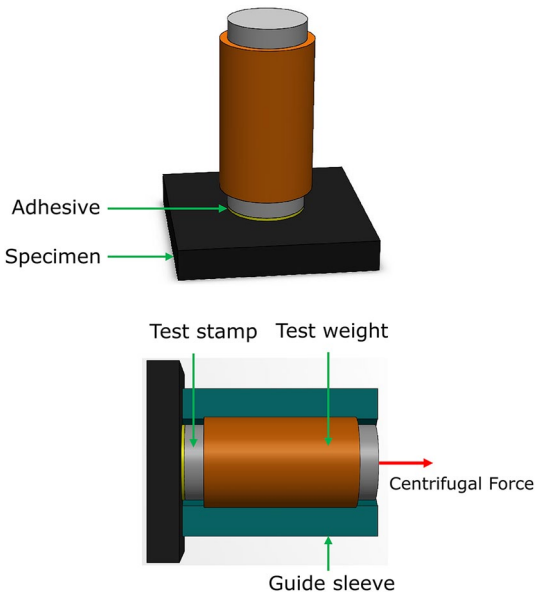


Fig. 2 Specimen setup for centrifugal adhesion testing

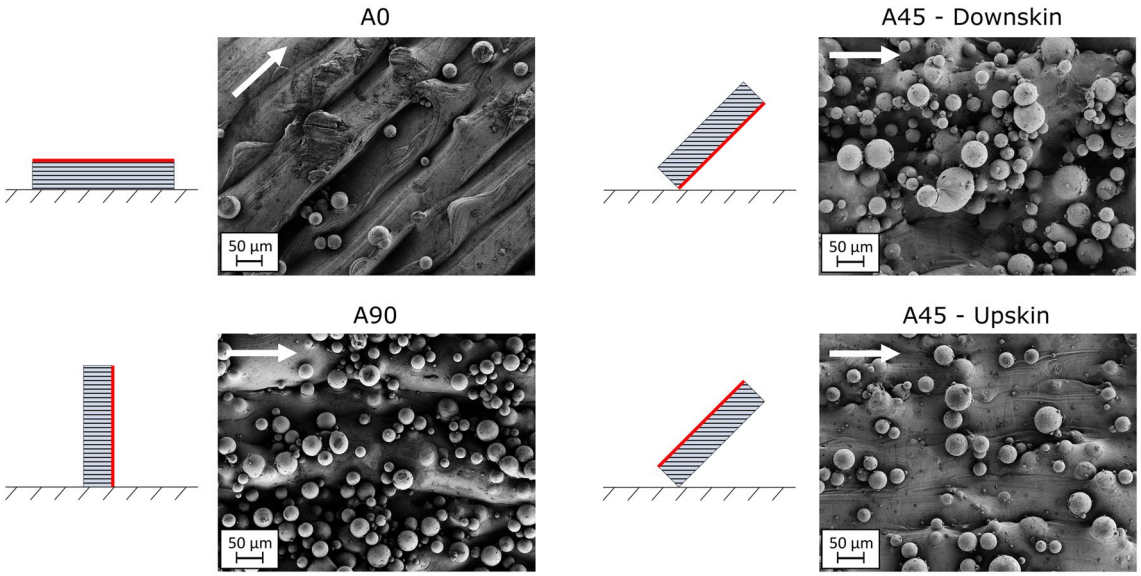


Fig. 3 SEM images of Ti6Al4V surfaces in as-built condition for the build orientations A0, A90, A45 Downskin/Upskin

surface, large particle accumulations are forming. This is caused by a slow heat dissipation at the downskin side and a high amount of adjacent particles in the powder bed [18]. Analyzing the surfaces with SEM revealed no distinct nano-roughness on the as-built surfaces.

Measurements with CLSM allowed to obtain quantitative information of the surface morphologies. The CLSM-images in Fig. 4 show the height information of the investigated surfaces. In addition, the corresponding roughness value S_a is given here, which describes the arithmetic mean roughness of a surface. Other roughness parameters which contain more specific information of certain surface aspects were also evaluated in this study. However, since S_a is still commonly used for describing the roughness, it was selected to examine its informative value for adhesive bonding. The highest roughness value was found for the A45-Downskin surface with about 21.86 µm, followed by the A90 surface. For the A0 and A45-Upskin surfaces the roughness analysis resulted in similar S_a values, which are the lowest among these surfaces. The S_a value only allows to state that the arithmetic mean roughness of the A0 and the upskin surfaces is similar. Differences in surface topography can't be expressed with this parameter. Therefore, the S_a value needs to be complemented with further roughness values or with images of the topography. For the shown surfaces, it can be concluded that the roughness is mainly influenced by the

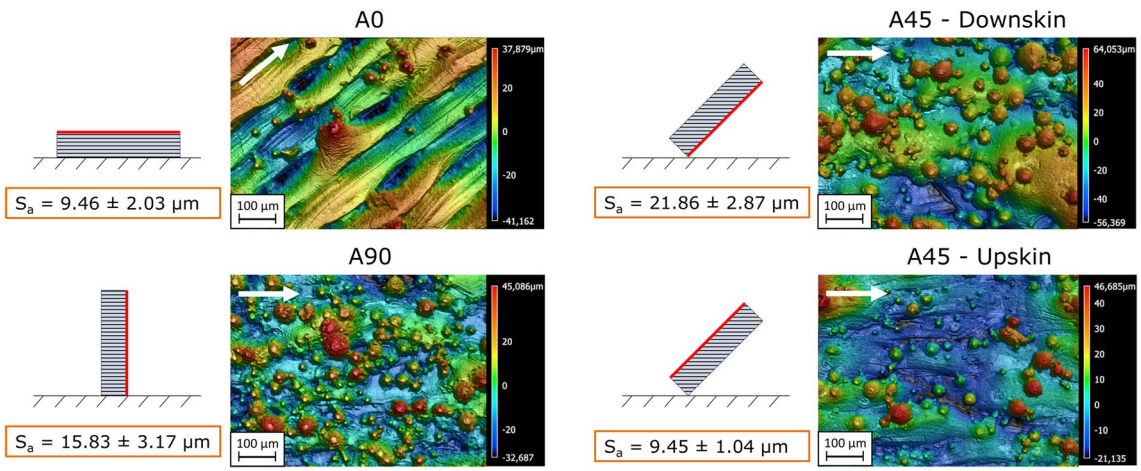


Fig. 4 CLSM images of Ti6Al4V surfaces in as-built condition for the build orientations A0, A90, A45 Downskin/Upskin and the corresponding roughness value S_a

number and size of attached particles and in case of the A0 surface by the groove structuring. Furthermore, it is interesting to note that the stair-step effect at the A45 surfaces is more pronounced on the downskin side.

3.2 Surface morphology in surface-treated condition

Surface treatment was conducted exemplary for the build orientations A0 and A90. This allowed to evaluate the surface treatment for a low and a high number of attached particles on the initial surface. CLSM images of the surface morphologies after grit blasting are shown in Fig. 5.

In case of the horizontally oriented surface A0, an increase in the mean roughness value S_a by 26.7% was observed. This is caused by texturing former smooth areas during the blasting process. For the A90 surface the roughness value was, however, decreased by around 62%, mainly due to removal of the attached particles on the surface. Furthermore, it can be stated that the topographies of both surfaces are more similar after grit blasting. Multiple areas of the grit blasted surfaces were further investigated by SEM. The images proved that residuals of the silicon carbide particles are present on the surfaces despite cleaning in the ultrasonic bath. Figure 6 exemplary shows the blasting agent residuals on the horizontally oriented surface A0.

During the blasting process, the silicon carbide particles were crushed in different sizes and have cut into the Ti6Al4V substrate. These incised blasting particles are distributed unevenly over the entire surface, but account only for a rather small proportion of the total substrate surface. However, it should still be considered that the grit blasting residues can influence the wettability of the surfaces and the adhesive bond strengths. Particularly under dynamic loads, the incised particles can cause crack initiation due to notch effects and thus worsen the fatigue performance. This

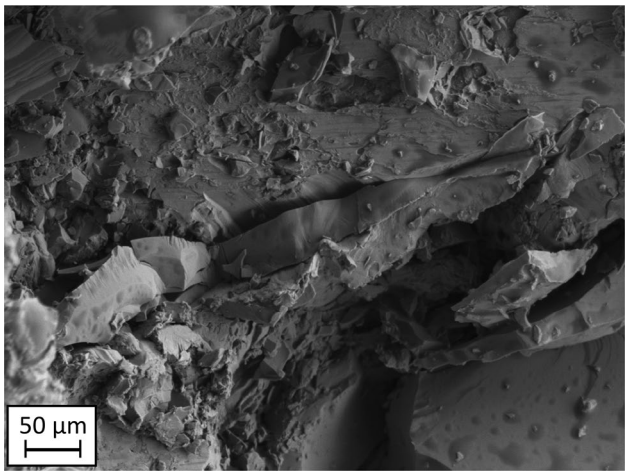


Fig. 6 Residuals of silicon carbide particles on a A0-oriented Ti6Al4V surface after grit blasting

was observed by Bagehorn et al. [14] during fatigue tests with PBF-LB-processed Ti6Al4V parts after grit blasting with corundum. Moreover, it can be noted that grit blasting mainly modifies the microroughness on the surface without generating a pronounced nanoroughness. In contrast, laser treatment allows to create roughness in two distinct scales. In the micrometer scale, the surface topography is mainly characterized by the laser pulses, as illustrated in Fig. 7 for the A0 and A90 build orientations.

Laser treatment of the A0 surface increased the mean roughness value S_a by around 50%, while a decrease of 35% was observed for the A90 surface. This decrease is due to the deformation of the attached particles on the surface caused by the laser pulses. As a result, the A0 surface shows a higher S_a value than the A90 surface after laser treatment. In addition to the microroughness it was possible to create a laser induced nano-porous layer on the surface.

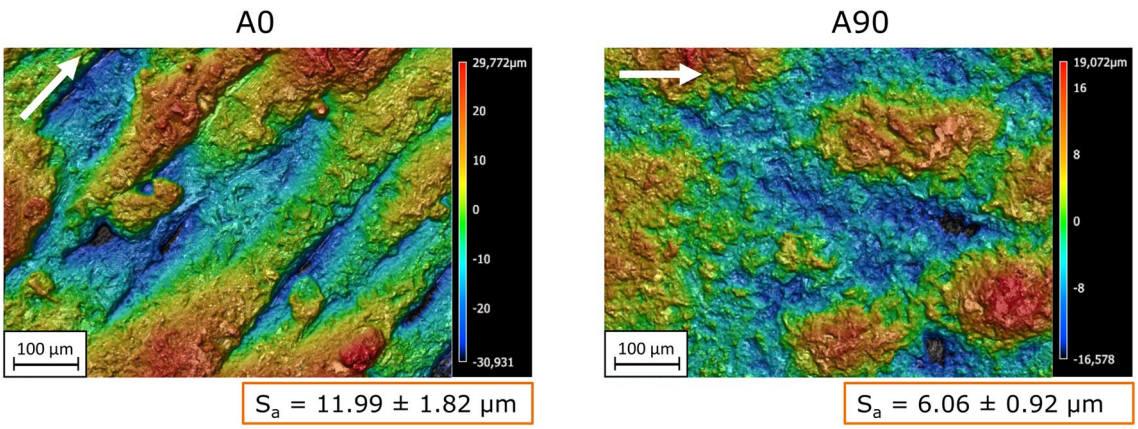


Fig. 5 CLSM images of Ti6Al4V surfaces after grit blasting for the build orientations A0, A90 and the corresponding roughness value S_a

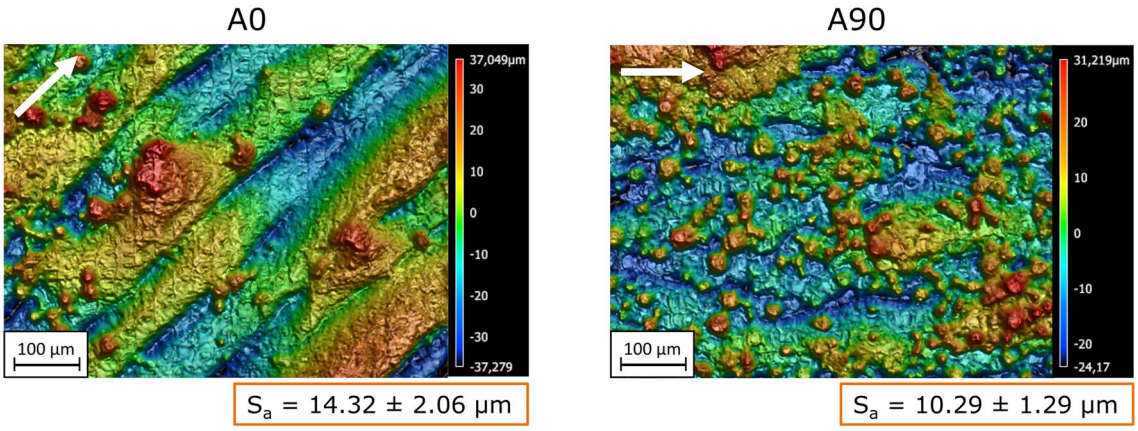


Fig. 7 CLSM images of Ti6Al4V surfaces after laser treatment for the build orientations A0, A90 and the corresponding roughness value S_a

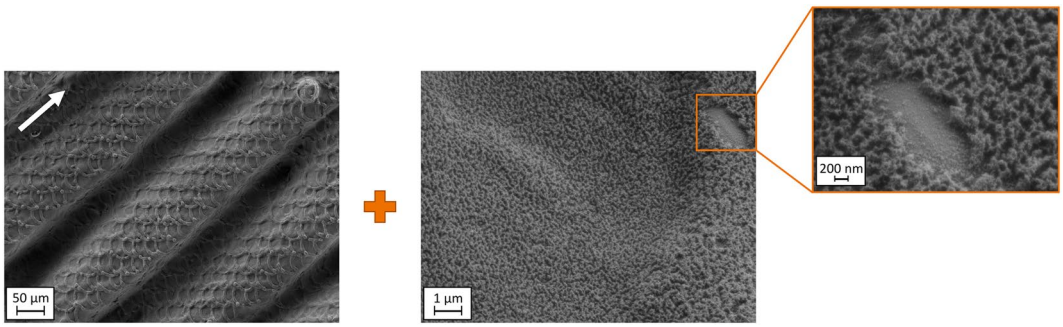


Fig. 8 SEM images of a A0-oriented Ti6Al4V surface after laser treatment

The microroughness created by the laser pulses is therefore superimposed by a pronounced nanoscale roughness. This is illustrated in Fig. 8 exemplary for a laser treated A0 surface. The nanoroughness layer has a thickness of 100–200 nm and consists of fine structures in the nanometer scale. In this study, no analysis was performed on the surface chemistry, but based on other investigations [10, 11] with a similar laser intensity it is assumed that the nanostructures are part of a TiO_2 layer. Regarding the adhesive bond performance, it was expected that the laser induced nanoroughness will cause a significant improvement in bond strength.

A comparison of the roughness S_a for the investigated surface topographies is shown in Fig. 9, including a reference value for a milled Ti6Al4V surface. In this study, a total of eight different surface topographies of PBF-LB-processed Ti6Al4V were considered, not counting the reference surface. The S_a value for these surfaces ranged from approximately 6 to 22 µm. The lowest roughness value was found for the A90 surface after grit blasting, which is still considerably higher than that of the milled reference surface. In contrast, the A45 downskin surface in the as-built condition showed the highest S_a value. It is important to note that the

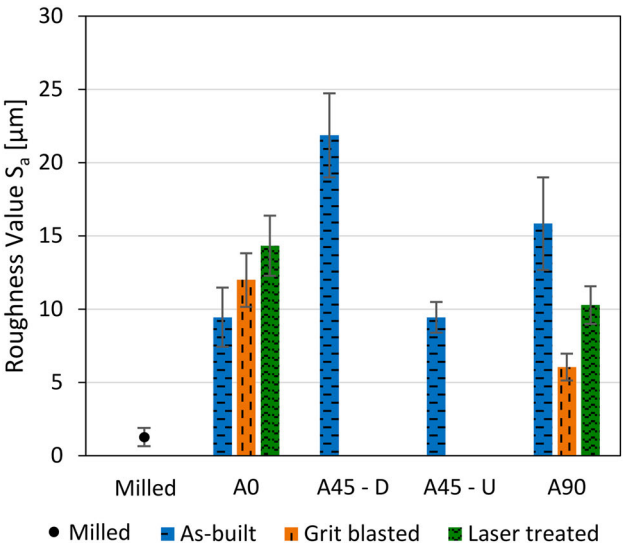


Fig. 9 Averaged roughness value S_a, shown for the different build orientations in as-built and surface-treated conditions. The results for a milled surface are also shown as a reference

S_a value characterizes the microroughness of the examined surface topographies. However, for evaluating the adhesion strength, it is essential to also consider the nanoscale roughness. In the present study, only the laser-treated surfaces showed a pronounced nanoroughness.

3.3 Surface wettability

In a study by Rodriguez et al. [21], contact angle measurements with deionized water were used to characterize the macroscopic wettability of PBF-LB-processed Ti6Al4V. The results indicated a correlation between the macroscopic contact angle and the adhesive bond strength of metal–metal joints bonded with an epoxy adhesive. However, based on the findings in [24, 25] it can be assumed that the macroscopic contact angle does not correlate with the adhesive bond strength. Given these discrepancies, the present study includes contact angle measurements to investigate the relation between macroscopic contact angles and adhesive bond strength. Moreover, performing the contact angle measurements allowed to assess the effectivity of the applied cleaning process, as this method is very sensitive to surface contaminations. Measuring the contact angles on the macroscopically rough surfaces required to adapt the volume of the liquid droplet. Initial measurements with 2 µm water drops resulted in highly irregular droplet shapes. After increasing the water drop volume to 3 µm approximately round droplets could be created on the surfaces, which allowed to measure the contact angles. However, it is important to note that the contact angles measured on rough surfaces have to be considered as approximations, since an exact measurement with the sessile drop method requires a macroscopically flat surface [25]. In case of highly anisotropic surfaces, the contact angles are also influenced by the anisotropy. In this work, the surface direction dependence of the contact angles was investigated for the highly anisotropic surface A0 in the as-built condition. This surface shows a pronounced anisotropy due to the groves on the surface induced by the defined laser scanning pattern. When applying a water drop on this surface, the droplet is aligning along the groves, resulting in an elliptical drop shape, as illustrated below. The contact angles were measured in the surface directions 0°, 45° and 90° relative to the groves on a defined surface spot. Figure 10 illustrates the contact angle measurements.

The elliptical drop shape causes varying contact angles along the different surface directions. Evaluating the mean contact angle of each direction after multiple measurements showed that the contact angles vary in the range of 48° to 62° on the evaluated spot. This implies a reasonable dependence of the measured contact angle on the surface direction. For a detailed comparison of the macroscopic wettability, this dependence has to be considered. In the present work, however, the anisotropic influence can only be evaluated for a subset of the investigated surfaces, namely "A0-as built", "A0-grit blasted" and "A90-grit blasted", since complete macroscopic wetting was observed for all the other considered surfaces. Furthermore, the macroscopic wettability of the surfaces is assessed only qualitatively due to the increased uncertainty when applying the contact angle measurement method to macroscopically rough surfaces [25]. Therefore, the surface direction dependence was not further investigated in this study.

The contact angles measured with deionized water for the investigated surfaces are shown in Fig. 11. In addition, the contact angle of a milled Ti6Al4V surface is depicted as a reference. It is important to note that the measured contact angles only describe the macroscopic wettability. The horizontally oriented surface A0 has a lower contact angle than the milled surface, thus showing better macroscopic wettability with deionized water. However, comparing the A0 surface with the other build orientations in the as-built condition shows that its macroscopic wettability is significantly worse, since for the 45° and 90° surfaces complete macroscopic wetting was observed. All samples were manufactured with the same process parameters and using the same inert gas. Therefore, it can be assumed that differences in surface chemistry can be neglected for the as-built surfaces. This leaves the surface topography as a main reason for the lower wettability of A0. A main difference in topography is that the A0 surface has the

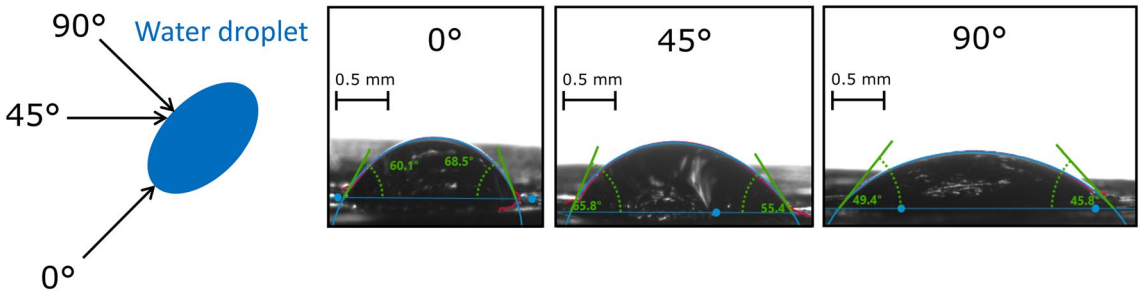


Fig. 10 Contact angle measurements on a A0-oriented Ti6Al4V surface in as-built condition. Contact angles are measured in the surface directions 0°, 45° and 90° relative to the surface groves

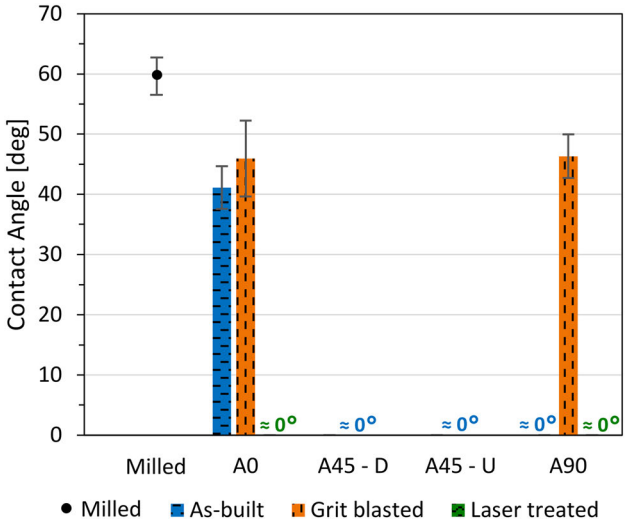


Fig. 11 Contact angles measured with deionized water, shown for the different build orientations in as-built and surface-treated conditions. The results for a milled surface are also shown as a reference

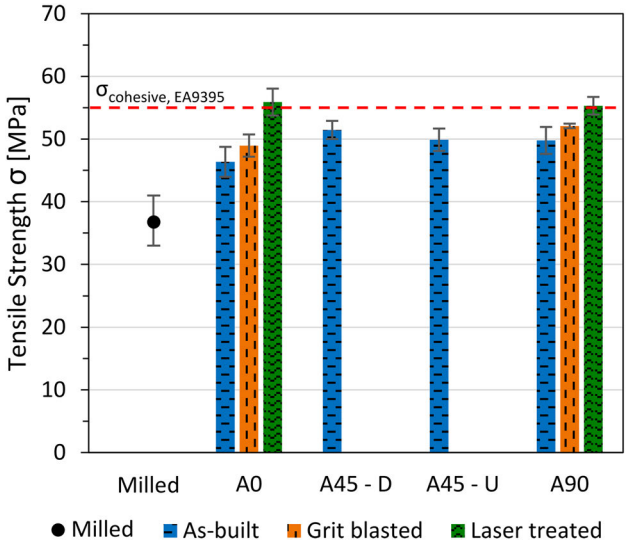


Fig. 12 Adhesive bond strength for tensile loading, shown for the different build orientations in as-built and surface-treated conditions. The results for a milled surface are also shown as a reference

lowest quantity of attached particles. It could therefore be assumed, that a higher number of ball-like particles can have a positive effect on the macroscopic wettability. However, a requirement for this is that the applied cleaning method is sufficient to remove contaminations on the surface. Especially at highly structured surfaces like A45-Downskin there is a risk that contaminations remain in the surface textures, which could cause poor wetting. This happened in [21], where due to improper cleaning the highest contact angle among the as-built Ti6Al4V surfaces was measured for the A45-Downskin surface. The measurements in the present study indicate that ultrasonic cleaning with acetone seems to be a sufficient cleaning process since complete macroscopic wetting was observed for the highly textured A45-Downskin surface.

Grit blasting resulted in an increase in the contact angle for the as-built surfaces, especially for A90. Thus, it can be assumed that grit blasting reduces the macroscopic wettability with a polar component. The wettability with a disperse component was also investigated in this study. It was observed that grit blasting only has a minor influence on the contact angles measured with di-iodomethane. It was, therefore, concluded that the overall macroscopic wettability is worsened by grit blasting. One reason for this could be that the oxygen content on the surface is decreased by grit blasting due to damaging the native oxide-layer of Ti6Al4V, as it was observed by Rodriguez et al. [26] and Brack [27]. Another reason could be the presence of blasting agent residues on the surface. Furthermore, it was found that after laser treatment all surfaces show complete macroscopic wetting. This can be attributed to the laser induced nano-porous layer on the surface.

3.4 Centrifugal adhesion testing

The adhesive bond strengths for tensile loading obtained by centrifugal adhesion testing are shown in Fig. 12. The cohesive strength of the used epoxy adhesive EA9395 [28] and the tensile strength for a milled Ti6Al4V surface are also depicted in this chart. It should be noted that all samples were ultrasonically cleaned with acetone before adhesive bonding.

The results show that all as-built surfaces are performing better than the milled surface, with a 25–35% higher tensile strength. Within the as-built surfaces, the lowest tensile strength was found for the horizontally oriented surface A0, while the A45 and A90 surfaces showed similar strengths between 50 and 51.5 MPa. Comparing the bond strengths with the average roughness value S_a of the surfaces shows, that a higher roughness in terms of the S_a value doesn't indicate a higher bond strength. This shows that it is not useful to describe the surface roughness only with the S_a value and to use this for assessing the potential adhesive bond performance. However, this is still an often used approach. Evaluating the surface topography shows that the surface with the lowest quantity of partially melted particles, here A0, also has the lowest bond strength. It can be therefore assumed, that a certain increase in particle numbers on the surface can have a positive effect on the bond strength. The particles increase the surface area and can also cause interlocking. Requirements for interlocking are that the particles don't break off from the base material and that the adhesive can flow around the particles. This was proven for the used epoxy adhesive by evaluating the fracture surfaces

using SEM. Figure 13 shows the fracture surface of a A0 surface in an area where adhesive failure occurred. It was observed that partially melted particles remain attached to the surface. This means, that the bond between particle and base material is stronger than the adhesion strength of the surface. Furthermore, it was found that adhesive residues are present around the particles, which indicates local interlocking. Nguyen et al. [20] also found that the attached particles remain on the surface for mode I static fracture toughness testing using a two component epoxy film adhesive. The stress loading in these tests is, however, much lower than in the tensile tests performed in the present study. The bond strength of the particles could, therefore, be further quantified with the shown results.

The results of the grit blasted samples show that the adhesive bond strength could be slightly increased, although grit blasting reduced the macroscopic wettability as shown by the contact angle measurements. This means that the bond strengths do not correlate with the measured contact angles. This is consistent with studies on polymer substrates [25], but contrary to what Rodriguez et al. [21] found in their investigation of the adhesive bond strength of PBF-LB-processed Ti6Al4V parts. In their study, the adhesive bond strengths were in line with the contact angle measurement results. It was found that the adhesive bond strength is higher for a lower contact angle of the surface. However, the results for grit blasting in the present study indicate that the adhesive bond strength is not in line with the contact angles. The problem with standard contact angle measurements is that only the macroscopic wettability is characterized. However, the relevant order of magnitude for adhesion is in the sub-micrometer scale. It is, therefore, not suitable to assess the adhesion strength of a surface with macroscopic contact angles [24]. This is also shown by the results in this study. Evaluating the surface topography by analyzing the surface features seems to be a more reliable approach, since it is known that roughness, especially in the nanometer scale, and interlocking have a major influence on the adhesive bond performance of metal joints [4]. Due to different effectiveness, it is important to distinguish between roughness in nano-, micro- and macro-scale. In case of grit blasting, the slight increase in tensile strength could be caused by roughening former smooth areas. The minor improvement can be explained by the fact that mainly microroughness is created, which contributes less to adhesion than nanoscale roughness. To improve the adhesive bond performance a different blasting agent could be used. For example, the SACO® process uses silane-coated corundum, which allows an in situ coating during the blasting process. This coating enhances the durability of the adhesive bond [6]. An application of the SACO® process for PBF-LB-processed Ti6Al4V parts needs to be investigated.

An increase in tensile strength by 8–20% was achieved by laser treatment. This increase can be attributed to the laser-induced nano-porous layer on the surface. However, the improvement of the bond strength by laser treatment was limited here for both built orientations A0 and A90 by the cohesive strength of the used epoxy adhesive. The real adhesion strength of the laser treated surfaces could, therefore, be even higher. The results confirm, that nanoroughening causes a more pronounced improvement than modifying the microroughness features on the surface. Evaluating the fracture surfaces also showed the effectiveness of laser treatment. In Fig. 14, the fracture surfaces are exemplarily shown for the horizontally oriented surfaces A0. It should be noted that the same fracture modes were also observed for the A90 build orientation.

In as-built condition the failure occurs in mixed mode, i.e., partial cohesive failure and partial adhesive failure at the surface of the specimen. Analyzing the fracture surface with SEM revealed that areas with more particles tend to show cohesive failure. This can be explained by an increased surface area and local interlocking of the adhesive close to the particles. Moreover, it was found that the

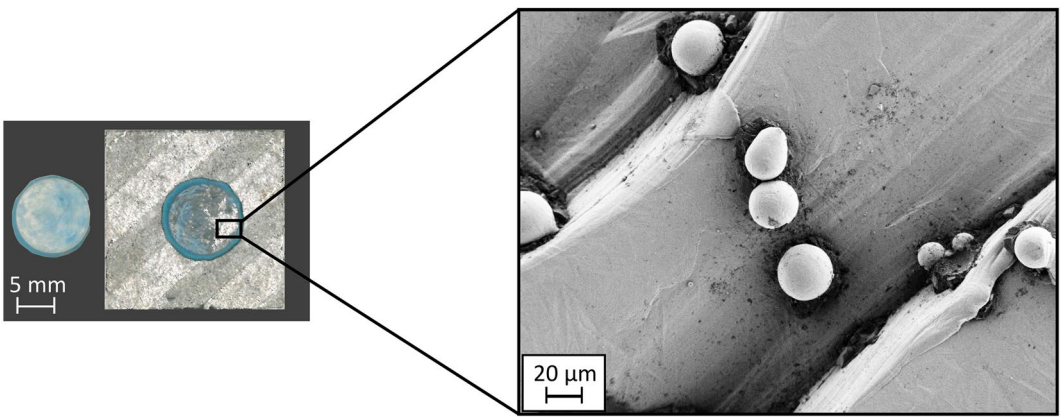


Fig. 13 Fracture surface of a A0 sample analyzed by SEM in an area of adhesive failure

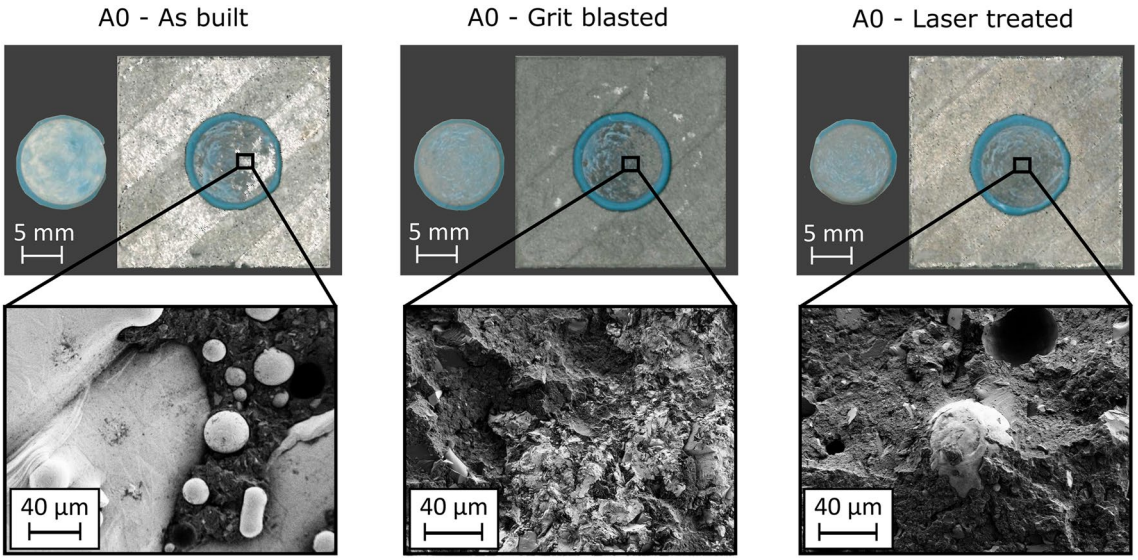


Fig. 14 Fracture surfaces for the build orientation A0 in as-built and surface-treated conditions

upper surface of the particles shows almost no adhesive residues. This indicates an insufficient bond strength on the particles top side. One reason for this could be the missing interlocking on this side of the particles. Grit blasting the A0-surface resulted in the same mixed failure mode. Compared to the as-built surface, the proportion of the two failure modes is similar. The adhesive residues and the grit blasted surface appear in the same color in the SEM (SE2 detector), which makes the distinction more difficult in this case. The darker areas in the SEM image correspond to the adhesive. After laser treatment, the failure mode switched from mixed mode to almost complete cohesive failure near the surface interface. A thin adhesive layer remains on the surface that covers the laser-induced nano-porous roughness. Evaluating the fracture surface with SEM showed that few particles are present with no adhesive residues on the upper side. This was only observed for a very few number of particles, which are located at elevations and have a larger size. In this case, the laser treatment couldn't create a pronounced nanoroughness on the upper surface of the particle. This can be explained by an insufficient laser intensity in these areas. Since the laser treated specimens failed after reaching the cohesive strength of the used epoxy adhesive, it can be assumed that these few local gaps in the nanoroughness layer didn't affect the adhesive bond strength for the investigated tensile loading case.

It can be concluded that the laser-induced nanoroughness layer allows a high adhesion strength. The surfaces in as-built and grit blasted condition are weaker, but with an adhesive bond strength between 46 and 51.5 MPa for tensile loading they are still on a level comparable to conventionally manufactured Ti6Al4V surfaces after grit blasting [21].

4 Conclusions

In this study, the effect of surface morphology on the adhesive bond performance of PBF-LB-processed Ti6Al4V parts was investigated for different built orientations in as-built and surface-treated conditions. The adhesive bond strength was assessed for tensile loading.

It was found that the adhesion strength of Ti6Al4V surfaces in the as-built condition shows a dependency on the built orientation. The lowest tensile strength was measured for a horizontally oriented surface, while the 45° upskin and downskin surfaces as well as the vertically oriented surface showed similar bond strengths. Aligning the parts in an appropriate build direction can, therefore, improve the bonding potential. Furthermore, it was shown that the adhesive bond strengths are not in line with the roughness value S_a of the surfaces and the contact angle measurement results. The results demonstrated that S_a-values and macroscopic contact angles are not suitable for assessing the adhesive bond strength. Evaluating the surface topography by analyzing the surface features seems to be a more reliable approach to assess the bond strength. This means to analyze the roughness shapes for assessing the interlocking potential and to evaluate the roughness distribution on the surface, as well as the roughness scales. Regarding the roughness shapes, it could be shown that the partially melted particles on the as-built Ti6Al4V surfaces can cause mechanical interlocking, since they remain

attached on the surfaces as shown by fracture surface analysis. An increase in adhesive bond strength was observed after surface treatment. Modifying the surfaces by grit blasting caused a minor improvement, while laser treatment allowed to achieve cohesive failure with an 8–20% increase in tensile strength. The results show the different effectiveness of micro- and nanoroughness. Grit blasting mainly causes microroughness, whereas with laser treatment a more effective nanoroughness can be created on the surface. It can be concluded that the inherent roughness of PBF-LB-processed Ti6Al4V surfaces shows a bonding potential that is comparable to grit-blasted surfaces. Laser treatment has been found to significantly enhance the adhesive bond strength by inducing nanoroughness on the surface. A cost efficient application of laser treatment could be to use it only for partial activation of surfaces in areas where stress concentrations in the adhesive bond are expected. In future work, the surface morphology influences need to be investigated for other static loading cases and fatigue loading. Especially for fatigue loading a significant influence of the surface morphology is expected [29]. Regarding laser treatment it is known that the laser pulses can damage the base material [15]. It is, therefore, necessary to investigate the extent to which these damages affect the fatigue behavior. In addition, the durability of the surfaces must be evaluated to define a suitable surface design for high adhesive bond performance.

Acknowledgements This study is part of the research project BLANCA, which is funded by the Bavarian Ministry of Economic affairs, Regional development and Energy (StMWi) within the program BayLu-25. We thank the partners within this research project, especially the project partner Modell- und Formenbau Blasius GERG GmbH, for manufacturing the specimens. Major part of this work was conducted in the laboratories of the Institute of Materials Science (Universität der Bundeswehr München) and the Bundeswehr research institute WIWeB. We would like to thank them for providing access to their laboratory equipment and for technical support.

Sponsored by



Bavarian Ministry of Economic Affairs,
Regional Development and Energy

Funding Open Access funding enabled and organized by Projekt DEAL.

Data availability The data that support the findings of this study are available from the corresponding author upon request.

Declarations

Conflict of interest The authors declare that there is no conflict of interest.

Open Access This article is licensed under a Creative Commons Attribution 4.0 International License, which permits use, sharing, adaptation, distribution and reproduction in any medium or format, as long as you give appropriate credit to the original author(s) and the source, provide a link to the Creative Commons licence, and indicate if changes were made. The images or other third party material in this article are included in the article's Creative Commons licence, unless indicated otherwise in a credit line to the material. If material is not included in the article's Creative Commons licence and your intended use is not permitted by statutory regulation or exceeds the permitted use, you will need to obtain permission directly from the copyright holder. To view a copy of this licence, visit http://creativecommons.org/licenses/by/4.0/.

References

1. Schwenke J, Krause D (2020) Optimization of load introduction points in sandwich structures with additively manufactured cores. Des Sci. https://doi.org/10.1017/dsj.2020.10
2. Türk DA, Kussmaul R, Zogg M, Klahn C, Leutenecker-Twelsiek B, Meboldt M (2017) Composites part production with additive manufacturing technologies. Procedia CIRP 66:306–311. https://doi.org/10.1016/j.procir.2017.03.359
3. European Cooperation for Space Standardization (2011) Space engineering Adhesive bonding handbook ECSS-E-HB-32–21A. ESA Requirements and Standards Division, Noordwijk
4. Da Silva LF, Öchsner A, Adams RD (2011) Handbook of adhesion technology. Springer, Berlin, Heidelberg. https://doi.org/10.1007/978-3-642-01169-6
5. DVS e.V. (2021) Gestaltungsempfehlungen zum Kleben additiv gefertigter Bauteile Merkblatt DVS 1401. DVS Media, Düsseldorf
6. Marques AC, Mocanu A, Tomic NZ, Balos S, Stammen E, Lundevall A, Abrahami ST, Günther R, de Kok JM, de Freitas ST (2020) Review on adhesives and surface treatments for structural applications: recent developments on sustainability and implementation for metal and composite substrates. Materials 13:5590. https://doi.org/10.3390/ma13245590
7. Akram M, Jansen KM, Ernst LJ, Bhowmik S (2011) Atmospheric pressure plasma surface modification of titanium for high temperature adhesive bonding. Int J Adhesion & Adh 31:598–604. https://doi.org/10.1016/j.ijadhadh.2011.05.009
8. Burchardt B (2010) Advances in polyurethane structural adhesives. In: Dillard DA (ed) Advances in structural adhesive bonding. Woodhead Publishing, pp 35–65
9. Nittel C (2017) Einfluss hybrider Strukturklebungen auf das Ermüdungsverhalten einer Aluminiumlegierung unter bruchmechanischer und kontinuumsmechanischer Betrachtungsweise. Dissertation, Universität der Bundeswehr München
10. Specht U, Ihde J, Mayer B (2014) Laser induced nano-porous Ti–O-layers for durable titanium adhesive bonding. Mat Sci Eng Tech 45:1116–1122. https://doi.org/10.1002/mawe.201400360
11. Cakir FH (2022) Enhancing the adhesive bonding strength of Ti6Al4V sheets with fiber laser texturing. Int J Adhesion & Adh 114:103117. https://doi.org/10.1016/j.ijadhadh.2022.103117
12. Schneider N, Wrobel C (2015) Use of high-energy laser radiation for surface preparation of magnesium for adhesive applications. Appl Adhes Sci 3:17. https://doi.org/10.1186/s40563-015-0044-2
13. Wagner L (1999) Mechanical surface treatments on titanium, aluminum and magnesium alloys. Mat Sci and Eng. https://doi.org/10.1016/S0921-5093(98)01168-X
14. Bagehorn S, Mertens T, Greitemeier D, Carton L, Schoberth A (2015) Surface finishing of additive manufactured Ti-6Al-4V - a comparison of electrochemical and mechanical treatments. 6th Eur Conf Aerosp Sci.
15. Taube A, Kurtovic A, Niendorf T, Mertens T, Zinn C, Schaper M, Maier HJ (2016) Influence of surface pre-treatments on the high-cycle fatigue behavior of Ti–6Al–4V – from anodizing to laser-assisted techniques. Int J Fat 91:195–203. https://doi.org/10.1016/j.ijfatigue.2016.06.010

16. Witkin DB, Patel DN, Helvajian H, Steffeney L, Diaz A (2019) Surface treatment of powder-bed fusion additive manufactured metals for improved fatigue life. J Mat Eng Perf 28:681–692. https://doi.org/10.1007/s11665-018-3732-9
17. Obilanade D, Dordlofva C, Törlind P (2021) Surface roughness considerations in design for additive manufacturing—a literature review. Proc Des Soc 1:2841–2850. https://doi.org/10.1017/pds.2021.545
18. Ilin A, Logvinov R, Kulikov A, Prihodovsky A, Xu H, Ploshikhin V, Günther B, Bechmann F (2014) Computer aided optimisation of the thermal management during laser beam melting process. Phys Procedia 56:390–399. https://doi.org/10.1016/j.phpro.2014.08.142
19. Moritz J, Götze P, Schiefer T, Stepien L, Klotzbach A, Standfuß J, Lopez E, Brückner F, Leyens C (2021) Additive manufacturing of titanium with different surface structures for adhesive bonding and thermal direct joining with fiber-reinforced polyether-ether-ketone (peek) for lightweight design applications. Metals 11:265. https://doi.org/10.3390/met11020265
20. Nguyen AT, Brandt M, Orifici AC, Feih S (2016) Hierarchical surface features for improved bonding and fracture toughness of metal-metal and metal-composite bonded joints. Int J Adhesion & Adh 66:81–92. https://doi.org/10.1016/j.ijadhadh.2015.12.005
21. Ardila-Rodriguez LA, Rans C, Poulis JA (2021) Effect of surface morphology on the Ti–Ti adhesive bond performance of Ti6Al4V parts fabricated by selective laser melting. Int J Adhesion Adh 110:102918. https://doi.org/10.1016/j.ijadhadh.2021.102918
22. Deutsches Institut für Normung e. V (2019) Beschichtungsstoffe - Benetzbarkeit - Teil 1: Begriffe und allgemeine Grundlagen DIN EN ISO 19403–1. Beuth, Berlin
23. Zhang LC, Attar H (2016) Selective laser melting of titanium alloys and titanium matrix composites for biomedical applications: a review. Adv Eng Mat 18:463–475. https://doi.org/10.1002/adem.201500419
24. Arikan ES (2020) Oberflächenmodifikation von Polyetheretherketon (PEEK) für das strukturelle Kleben in der Luftfahrt. Dissertation, Universität der Bundeswehr München. ISBN 9783843945844
25. Holtmannspötter J (2018) How surfaces of carbon fiber reinforced plastics with thermoset matrices need to be treated for structural adhesive bonding. The J of Adhesion. https://doi.org/10.1080/00218464.2018.1519702
26. Ardila-Rodriguez LA, Boshuizen B, Rans C, Poulis JA (2021) The influence of grit blasting and UV/Ozone treatments on Ti–Ti adhesive bonds and their durability after sol-gel and primer application. Int J Adhesion Adh 104:102750. https://doi.org/10.1016/j.ijadhadh.2020.102750
27. Brack N, Rider AN (2014) The influence of mechanical and chemical treatments on the environmental resistance of epoxy adhesive bonds to titanium. Int J Adhesion Adh 48:20–27. https://doi.org/10.1016/j.ijadhadh.2013.09.012
28. Henkel Corporation Aerospace (2013) Loctite EA 9395 AERO Technical Data Sheet. https://www.pccomposites.com/wp-content/uploads/2015/07/PCRS9395-QT_TDS.pdf. Accessed 11 Aug 2022
29. Thäsler T, Holtmannspötter J, Gudladt HJ (2019) Surface topography influences on the fatigue behavior of composite joints. Key Eng Mat 809:341–346. https://doi.org/10.4028/www.scientific.net/KEM.809.341

Publisher's Note Springer Nature remains neutral with regard to jurisdictional claims in published maps and institutional affiliations.

THE JOURNAL OF ADHESION
https://doi.org/10.1080/00218464.2024.2441886

Taylor & Francis
Taylor & Francis Group

OPEN ACCESS Check for updates

Surface morphology influences on the adhesive bond performance of PBF-LB manufactured Ti6Al4V parts – investigation of quasi-static and fatigue loading conditions

Emre Ertürk, Jörg Gregor Diez, Pablo Vitale, and Philipp Höfer

Institute of Lightweight Engineering, University of the Bundeswehr Munich, Neubiberg, Germany

ABSTRACT

Adhesive bonding of additively manufactured parts enables highly efficient lightweight designs. To achieve high adhesive bond performance, it is essential to consider the surface properties of the adherends. Previous studies have shown that the inherent roughness of Ti6Al4V parts fabricated by laser powder bed fusion (PBF-LB) can contribute to high bond strength under quasi-static loading. In the present work, the influences of surface morphology on adhesive bond performance were examined under static and fatigue loading conditions. Moreover, the environmental durability of the bonded joints was assessed for a hot-wet condition. In the as-built state (i.e. degreased PBF-LB-surface) the build orientations 0°, 45° (Up-/Downskin) and 90° were investigated, resulting in four different surface morphologies. Furthermore, grit blasting and laser treatment were used to modify the surface properties and examine their effect on the adhesive bond performance. Characterizing the surfaces was done by scanning electron microscopy and confocal laser scanning microscopy. The quasi-static bond strengths and fatigue lifetimes were examined through metal-metal single step-lap joint testing. The number of attached particles on the PBF-LB manufactured surfaces was found to correlate with the tensile shear strength and fatigue lifetime of the adhesive bond. Under fatigue loading, the particle-induced interlocking effect was mainly effective in the low-cycle-fatigue regime. A significantly enhanced bond performance was achieved by laser treatment, which created a hierarchical surface morphology, consisting of the inherent microscopic surface features of PBF-LB-Ti6Al4V and a laser-induced nanoporous oxide layer. This hierarchical surface structure increased the bond strengths by up to 162% and extended the fatigue lifetimes by at least 130% in comparison to the as-built surface condition. However, further improvements are necessary to enhance the environmental durability of the oxide layer.

ARTICLE HISTORY
Received 20 October 2024
Accepted 9 December 2024

KEYWORDS
Adhesive bonding; additive manufacturing; surface morphology; surface treatment

CONTACT Emre Ertürk emre.ertuerk@unibw.de Institute of Lightweight Engineering, University of the Bundeswehr Munich, Werner-Heisenberg-Weg 39, Neubiberg 85577, Germany

© 2025 The Author(s). Published with license by Taylor & Francis Group, LLC.
This is an Open Access article distributed under the terms of the Creative Commons Attribution License (http://creativecommons.org/licenses/by/4.0/), which permits unrestricted use, distribution, and reproduction in any medium, provided the original work is properly cited. The terms on which this article has been published allow the posting of the Accepted Manuscript in a repository by the author(s) or with their consent.

1. Introduction

Additive manufacturing (AM) enables the fabrication of complex, lightweight components with high design flexibility and structural efficiency. For aerospace applications, the titanium alloy Ti6Al4V is widely used due to its exceptional mechanical and thermal properties. However, despite the remarkable advancements in metal AM, the process still faces challenges, such as the need for effective joining methods to assemble printed parts.[1] In this context, structural adhesive bonding proves to be a suitable joining method for lightweight constructions, as it introduces low-weight penalties compared to mechanical fastening methods, offers enhanced resistance to fatigue and corrosion, and enables an improved load distribution.[2,3] Common failure modes of adhesively bonded joints involve adhesive failure (i.e., interfacial failure) between adherend and adhesive, cohesive failure in the adhesive layer and a combination of both (mixed-mode failure). In structural adhesive joints, adhesive failure is generally considered an unacceptable failure mode since it indicates an insufficient surface preparation.[4] Consequently, it is essential to ensure high adhesion between adherend and adhesive that can endure both quasi-static and fatigue loading conditions, while also maintaining durability under environmental aging influences.

In the case of PBF-LB manufactured Ti6Al4V parts, previous investigations[5–7] have demonstrated that the inherent surface roughness enables high adhesive bond strengths under quasi-static loading conditions. The surface topographies are primarily characterized by a specific quantity of partially melted particles, which varies depending on the build orientation.[6–8] These particles improve adhesive bond performance by increasing the total surface area and promoting mechanical interlocking of the adhesive.[6,7] Ardila-Rodríguez et al.[6] found that PBF-LB-Ti6Al4V surfaces in the as-built condition (i.e., referring to degreased PBFL-LB printed surfaces) exhibit tensile bond strengths comparable to those observed after grit blasting. This result shows the bonding potential of additively manufactured metal surfaces. However, fracture analysis in[6] revealed a significant amount of adhesive failure on these surfaces, indicating insufficient adhesion strength. The main reason for the observed adhesive failure is that the as-built surfaces lack distinct nanoroughness, which can significantly enhance adhesion.[9] The same issue applies to grit blasted surfaces, resulting often in similar mixed-mode failure of the adhesive joint.[6,7] The roughness scales present on the surface, along with the adhesive's capability to penetrate and fill micro- and nanoscale voids are decisive factors for high adhesion strength, as demonstrated in recent studies.[7,10–12] To achieve fully cohesive failure within the adhesive, it is therefore necessary to apply an appropriate surface treatment. In aerospace, the common standard for bonding preparation of metals like titanium or aluminum involves the use of electrochemical methods, such as

phosphoric acid anodizing (PAA)[13] and NaTESi,[14] which generate a pronounced nanoscale roughness on the surface. The main disadvantages of electrochemical treatments are their high process costs and the use of hazardous chemicals, which pose environmental and safety risks. A more sustainable method is laser treatment, which also offers the advantage of high automation. Kurtovic[15] conducted a comprehensive investigation into the effects of laser treatment on conventionally manufactured Ti6Al4V and its influences on adhesive bond performance. By conducting floating roller peel tests and wedge tests Kurtovic showed that a laser-generated nanoroughness can improve adhesion strength compared to wet chemical surface treatments like etching (Turco 5578) or anodizing (NaTESi). In a study by Tseng and Chen[16] laser treatment of conventionally manufactured Ti6Al4V substrates allowed to achieve a threefold increase in tensile shear bond strength compared to the untreated surface condition. Further, for pin-reinforced titanium/CFRP single-lap-shear (SLS) joints, Parkes et al.[17] found that laser treatment improves the consistency of co-bonding and increases the elastic limit of the joint. Regarding PBF-LB-Ti6Al4V surfaces, it was demonstrated in a previous work[7] that a laser-induced nanoporous oxide layer significantly increases tensile bond strength, leading to a shift from mixed-mode failure in the as-built condition to cohesive failure in the epoxy adhesive.

An extensive literature review on the effect of surface texture on adhesive bond performance was conducted by Naat et al.[18] This review highlighted that most research has focused on the effects of surface treatments on quasi-static bond strength, whereas only relatively few works have investigated the influences on fatigue resistance. Consequently, further research is needed to better understand the influence of surface morphology on the fatigue behavior of bonded joints. Barros et al.[19] investigated the effects of grit, sand and bristle blasting on the fatigue performance of steel joints bonded with an epoxy adhesive. Their end-notched flexure (ENF) tests showed that bristle-blasted surfaces, characterized by sharp asperities, exhibited significantly shorter fatigue lifetimes. The detrimental effect of sharp surface features on fatigue resistance was also observed by Thäsler et al.[20] and Morfini et al.[21] for peel-ply structured CFRP/CFRP SLS joints and hand-sanded aluminum/magnesium SLS joints, respectively. Several studies have shown that, compared to mechanical surface treatments, higher fatigue strengths can be achieved through electrochemical anodizing processes and laser treatments, due to the provided superior adhesion strength.[18] Gudladt and Frömmel[22] demonstrated for aluminum SLS joints bonded with a two-part epoxy adhesive that the application of a pulsed Nd:YAG-Laser with optimized settings can create a distinct nanoroughness, which substantially enhances fatigue lifetimes. Improved fatigue performance of aluminum alloy and stainless steel SLS joints was also achieved by Moroni et al.[23] through laser ablation with a Yb-fiber laser. The increased lifetime was strongly related to a prolonged crack

propagation phase. However, at higher laser energy density levels, void formations were observed in the surface valleys, which deteriorated the fatigue performance. Regarding the fatigue resistance of PBF-LB-Ti6Al4V adherends, existing literature primarily focuses on the effects of surface roughness on the fatigue behavior of the bulk Ti6Al4V substrate without adhesive bonding. Studies in[24,25] have shown that Ti6Al4V parts exhibit in as-built condition low fatigue strength due to their high surface roughness, necessitating a surface finishing process. In the case of grit blasted Ti6Al4V parts, Bagehorn et al.[24] reported that incised blasting residues can worsen fatigue performance by causing crack initiation. Furthermore, investigations on laser treated Ti6Al4V surfaces[15,26] have found that the laser process can deteriorate fatigue properties due to the introduction of laser-induced micro- and nanoroughness, surface cracking and tensile residual stresses near the surface. To the authors best knowledge, no studies have yet examined the fatigue behavior of bonded metal/metal joints with PBF-LB-Ti6Al4V substrates for different surface conditions. As shown in,[24,25] the as-built surface roughness of additively manufactured Ti6Al4V leads to low fatigue strengths of the metal substrate. However, the inherent surface roughness may prove advantageous in adhesive bonding, particularly when the surface morphology is further optimized through suitable surface treatments. This is a central aspect of the present work.

Durability under environmental conditions is another critical aspect of structural adhesive bonding and was therefore also considered in this study. A crucial factor influencing the long-term performance of adhesive joints is moisture diffusion into the adhesive, as it affects the mechanical properties of the adhesive and can lead to a reduction in adhesion strength.[27,28] To ensure sufficient adhesion under environmental stresses, surface treatment is often required prior to bonding. While mechanical surface treatments typically result in moderate durability, electrochemical anodizing can produce surfaces with high durability for adhesive bonds.[9,18,29] Regarding the aging behavior of bonded titanium (Ti15–3)-PEEK SLS joints under hot-wet conditions, Löbbecke et al.[30] demonstrated that long-term stable adhesion can be achieved through laser treatment of titanium if an open porous branched nanoroughness layer is formed on the surface. Freund et al.[31] reported that high durability under hot-wet aging was achieved for co-cured AW6082-T6–CFRP SLS joints when the laser treatment created significant surface enlargement, deep craters and undercut structures on the metal substrate. Similarly, hydrothermally stable SLS joints were achieved by Specht et al.[32] through laser treatment of conventionally manufactured Ti6Al4V. For PBF-LB-Ti6Al4V surfaces, it was shown in[6] that salt-spray aging significantly reduces the tensile bond strength in case of the as-built surfaces. However, the durability of the adhesive joint was substantially improved after a combination of sol-gel and primer application.

In this work, the surface morphology influences on the bonding behavior of PBF-LB-Ti6Al4V were investigated for quasi-static and fatigue loading conditions. The as-built condition was analyzed for the build orientations 0°, 45° (up-/downskin) and 90°. Furthermore, the effects of grit blasting and laser treatment on surface morphology and bonding performance were evaluated. Surface characterization was performed using Scanning Electron Microscopy (SEM), Ion Beam Milling (IBM) and Confocal Laser Scanning Microscopy (CLSM). Afterwards, quasi-static bond strengths and fatigue lifetimes were examined through single step-lap joint testing. To assess the environmental durability of the bonded joints, a subset of the specimens was hot-wet aged before quasi-static testing. In addition, Digital Image Correlation (DIC) was employed for strain measurement at the bondline and for monitoring crack growth during the fatigue tests.

2. Materials and methods

2.1. Specimen type and substrate manufacturing

Single step-lap joint (SLJ) specimens made of PBF-LB manufactured Ti6Al4V substrates were used in this study. For bonding, the two-component epoxy adhesive Loctite EA 9396 AERO was utilized. The specimen geometry was defined based on DIN EN 2243–6[33] and is depicted in Figure 1. Single lap joints are subjected to mixed-mode loading, comprising both non-uniform shear and peel stresses. A stepped geometry with thick adherends was used

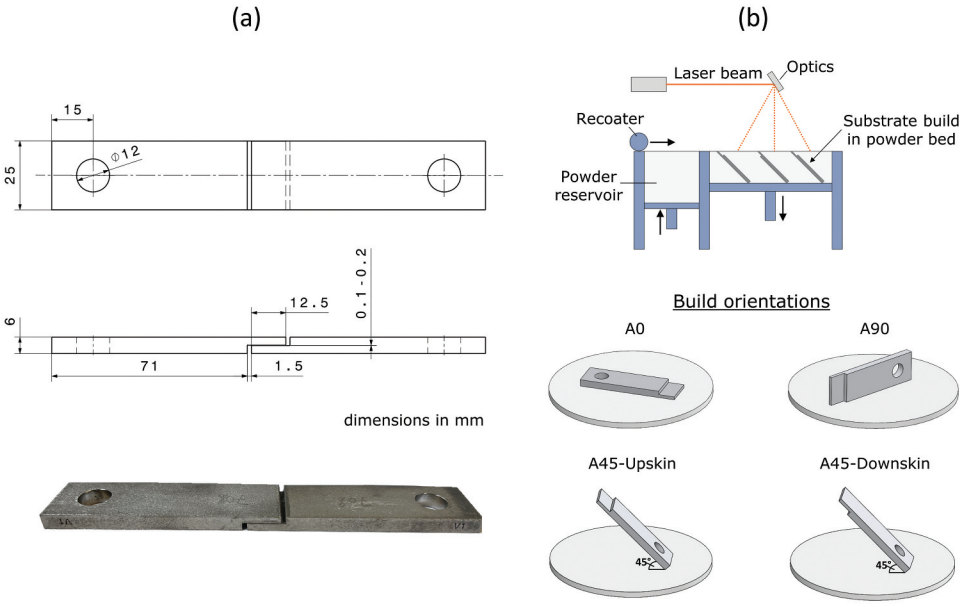


Figure 1. (a) SLJ specimen geometry and (b) substrate build orientations in the PBF-LB/M process.

here to reduce the peel stresses at the overlap ends induced by eccentric loading. This design allowed the investigation of a primarily shear-loaded adhesive joint with reduced peel stresses at the overlap ends. Such a load combination is representative of many technical applications, as adhesive joints are typically designed to minimize high peel stresses,[9] while non-uniform stress distributions, similar to those in this specimen type, are often encountered in practice.

The substrates for the metal-metal SLJ specimens were manufactured using a Trumpf TruPrint 5000 PBF-LB/M printer with standard parameters for Ti6Al4V Grade 23. The printing process utilized a layer thickness of 60 µm and a scanning strategy involving a 45° stripe pattern. To investigate the build orientation influence on bond performance, substrates were printed with the bonding surface oriented at 0°, 45° (upskin/downskin) and 90° relative to the base plate, as shown in Figure 1(b). For the 45°-oriented substrate, support structures were employed, as initial trials without support resulted in deformation during subsequent heat treatment. The utilized powder was supplied by GE Additive and has a particle size range of 10–45 µm, fulfilling the ASTM F3001–14[34] specification. Post-processing involved stress relief heat treatment under vacuum at 840°C for 2 hours, followed by EDM Cutting from the build plate and ultrasonic cleaning with deionized water to remove loose particles on the surface.

2.2. Surface treatment

The surface conditions as-built, grit blasted and laser treated were considered in this work. Grit blasting was selected since it is a widely used post-processing method for PBF-LB-manufactured metal parts, whereas laser treatment was investigated as an environmentally friendly alternative to electrochemical processes for creating distinct nanoroughness on metallic surfaces. The specimens in as-built condition were only degreased prior to bonding. Degreasing was conducted for all specimens in this work by ultrasonic cleaning in acetone.

Grit blasting was performed using a Peenmatik 1300 SDK system (iepco, Switzerland) with silicon carbide as the blasting agent, featuring a grain size range of 212–300 µm. Silicon carbide was chosen due to its widespread use as a standard blasting agent in post-processing for AM. The grit blasting process was conducted manually using a 10 mm nozzle and a pressure of 3 bar. The device was operated from a distance of 20 cm, at a blasting angle of approximately 90° and for a duration of about 10 s, ensuring a uniform surface finish was achieved. Post-treatment included ultrasonic cleaning in deionized water to remove abrasive residues, followed by degreasing in acetone.

Laser treatment was conducted under atmospheric conditions on a TRUMPF Trumark Station 5000 marking laser system (TRUMPF, Germany) equipped with a pulsed Nd:YVO4-Laser (TRUMPF TruMark

6350)). This laser system has a maximum average output power of 50 W and operates at a wavelength of 355 nm. The laser settings were adapted to induce pronounced nanoroughness on the surfaces of PBF-LB-Ti6Al4V, without creating unstructured high microroughness through laser splatter. This approach was used to prevent potential deterioration in fatigue performance associated with excessive microroughness and induced tensile residual stresses.[18–21,26] Based on this, the laser treatment was carried out with a power level of 70%, a scan speed of 0.4 m/s, a pulse frequency of 20 kHz and a laser spot diameter of 30 µm. This configuration resulted in a laser energy density of 248 J/cm^2. The laser scanned once over the entire surface, following a horizontal line pattern with a track distance of 30 µm. Degreasing of the specimens was conducted prior to laser treatment. After the laser processing, only cleaning with compressed air was performed to remove residual fine dust from the surface.

2.3. Analysis of surface characteristics

The characterization of the surface topographies was done by Scanning Electron Microscopy (SEM) using a Zeiss ULTRA Plus (Carl Zeiss, Germany) field emission scanning electron microscope. A Secondary Electrons detector (SE2) was primarily used, with the accelerating voltage set to 1.0 kV. For fracture surface analysis an In-Lens detector was additionally utilized to better differentiate between metal and adhesive residues on the surfaces. Furthermore, for selected specimens Ion Beam Milling (IBM) was performed using a Hitachi ArBlade 5000 system (12 h at a milling energy of 5 kV). For IBM, small pieces of about 10 × 10 mm were cut from the fractured specimens at the region of interest using a diamond wire-cutting machine. To prevent surface alteration during further preparation, the fractured surfaces were sputtered with gold. The specimens were then bonded to a sample carrier and ground to the final dimensions. In addition, Confocal Laser Scanning Microscopy (CLSM) was used during fracture analysis to detect fractured particles on the PBF-LB surfaces. The CLSM images were captured on a Keyence VK-X3000 (Keyence International, Belgium).

2.4. Adhesive joint preparation and aging

The two-component epoxy adhesive Loctite EA 9396 AERO (Henkel, Germany) was mixed based on a procedure suggested by Frömmel.[35] This involved mixing under a low atmospheric pressure of 30 mbar using a dual asymmetric centrifugal mixer. The low-pressure process significantly minimizes the presence of defects in the adhesive, such as entrapped gas bubbles, which particularly have a negative influence on fatigue behavior.[35] Afterwards, the degreased substrates were bonded

using a fixture designed for SLJ specimens. To prevent butt joint bonding and minimize the formation of adhesive chamfers, PTFE strips were inserted into the grooves at the overlap ends (Figure 1). Moreover, weight blocks were utilized to ensure sufficient contact pressure during curing. Based on recommendations in,[36] curing was done at 66°C for an extended duration of 80 min. Preliminary temperature control measurements with PT-sensors were conducted to ensure that the target temperature was maintained for at least 60 minutes within the bondline. After curing, excess adhesive on the sides was removed using sandpaper. Due to the highly structured nature of the PBF-LB surfaces, the adhesive bond thickness of the SLJ specimens varied along the overlap approximately between 0.1 and 0.2 mm.

To assess the durability of the SLJs under environmental conditions, a subset of the bonded specimens was immersion aged for 30 days at 60°C in deionized water. This aging process was defined by Frömmel[35] for aluminum/aluminum single-lap joints with similar specimen dimensions and the same adhesive. It was demonstrated that the specified aging duration is sufficient for water diffusion into the bondline, ensuring effective aging of the joints. Consequently, this aging process was applied in the present work.

2.5. Mechanical testing

Quasi-static SLJ-testing was conducted based on DIN EN 2243–6[33] using a Zwick Z150 (ZwickRoell, Germany) universal testing machine. The specimens were mounted using a cardanic suspension to ensure moment-free force application. Testing was carried out under nominal environmental conditions with a displacement rate of 1 mm/min. For strain measurement within the bondline, the DIC system Q400 (Limess GmbH, Germany) was used. Initially, 3D-DIC measurements were conducted with a two-camera setup to check for possible out-of-plane displacement during testing. The setup included 12 Mpx cameras with a spatial resolution of 4096×3000 pixels, paired with macro lenses (80 mm focal length) and distance rings to adjust the measurement area to around 14×10 mm. As shown in Figure 2, one camera (A) was aligned directly perpendicular to the measurement surface, while the other (B) was positioned at a 30° angle. Illumination was provided by three LED lights. The speckle pattern for DIC was created by first applying a base layer of black acrylic spray paint, followed by white speckles using an airbrush spray gun. The 3D-DIC measurements showed that the maximum out-of-plane displacement occurred close to specimen failure and amounted to approximately 0.05 mm, which would cause a strain error of 0.015% in the 2D-DIC measurements. Given this small error, subsequent evaluations within the bondline could be

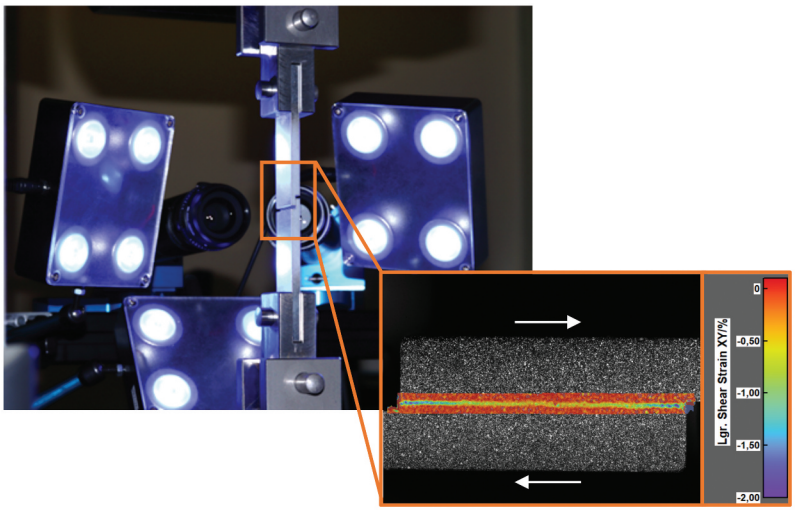


Figure 2. DIC setup for SLJ-testing.

conducted using only the straight camera (A). Following this procedure ensured that the 2D-DIC measurements were not affected by any out-of -plane displacements induced by the test setup. The single-camera setup with straight alignment provides the best camera focus of the bondline, which allows a fine discretization with DIC. Here a facet size of 25 pix and a grid spacing of 9 pix was applied, resulting in a resolution of 83 µm per facet. The adhesive layer was therefore discretized with at least one facet over its thickness.

Fatigue testing was carried out on a servo-hydraulic testing machine using a sinusoidal loading with a frequency of 10 hz and a load ratio of $R = 0.1$. The applied maximum stress was set depending on the quasi-static tensile shear strength. Similar to the quasi-static tests, specimen mounting in the testing machine was done using a cardanic suspension. For evaluating the crack growth, the described DIC setup was used. The DIC system functionality to trigger image acquisition at the maxima of the analog cyclic force signal enabled precise tracking of the crack growth. The image acquisition rate was adjusted for each specimen according to the expected lifetime. A total image count of 150 images per fatigue test was aimed, which resulted in acquisition rates between 1 image per 50 cycles and 1 image per 3000 cycles. A minimum of four specimens were tested for each surface type in each test case. The investigated test cases comprise quasi-static testing with non-aged specimens, quasi-static testing with hot-wet-aged specimens and fatigue testing with non-aged specimens.

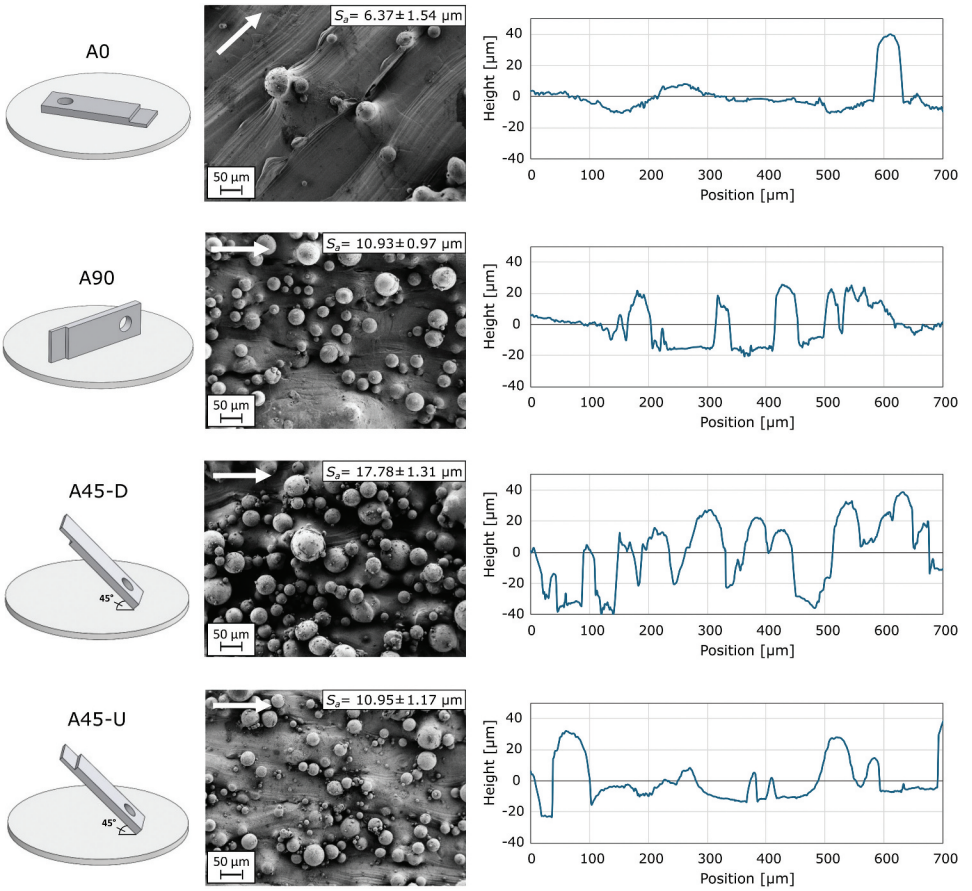


Figure 3. SEM images and height profiles of as-built Ti6Al4V surfaces for the build orientations A0, A45-D/U, A90.

3. Results and discussion

3.1. Surface morphologies

3.1.1. As-built condition

The surface morphologies in the as-built condition were investigated by SEM and CLSM for the build orientations 0° (A0), 45° downskin (A45-D), 45° upskin (A45-U) and 90° (A90). In Figure 3, SEM images are shown for each build orientation, alongside representative surface height profiles and the roughness value S_a obtained from CLSM. The laser scanning direction is depicted in the SEM images. In the as-built condition, the surfaces are mainly characterized by varying numbers of partially melted powder particles. These particles increase the surface area for adhesive bonding and serve as interlocking features.[5,37] Only very few particles are present on the A0 surface, which reflects in a relatively even height profile. In contrast, the A45-D surface is covered with the highest concentration of particles, resulting in a topography

with significant height variation. The attached particles on the A45-D surface are further superimposed with a wavy surface profile, caused by stair-step structuring due to the layer-wise manufacturing.[38,39] The A45-U and A90 surfaces display an intermediate number of attached particles, with large particle-free areas.

In the as-built condition, no distinct nanoscale roughness was observed on the titanium surfaces. Poor bonding behavior is therefore expected in areas with a low number of particles. This lack of nanoroughness on as-built surfaces was also identified in a previous study, where the same build orientations were evaluated for PBF-LB-Ti6Al4V specimens manufactured on a Concept Laser M2 printer.[7] In this investigation, it was demonstrated that commonly used parameters such as the average roughness S_a (arithmetical mean height) or macroscopic contact angles do not correlate with tensile bond strength. To assess the bonding capability of a surface, emphasis should therefore be on analyzing the surface features, particularly the roughness scales. Moreover, it was shown that the as-built PBF-LB-Ti6Al4V surfaces exhibit good to very good macroscopic wettability, which is a necessary requirement for achieving high adhesion strength.

3.1.2. Surface-treated condition

As in a previous study,[7] surface treatment was conducted for the build orientations A0 and A90. This allowed to evaluate the influences on a surface with low and intermediate number of attached particles. The highly structured A45-D surface was not investigated for surface treatment, since it was expected to already provide high adhesive bond strength in as-built condition. A grit blasted surface is exemplarily shown for the build orientation A90 in Figure 4, along with a surface height profile.

Grit blasting produced a more uniform roughness distribution over the surface, but it also removed the attached powder particles. This led to a 36% reduction in the mean roughness value S_a. A small number of blasting agent residues, in the form of incised silicon carbide particles, were observed on the

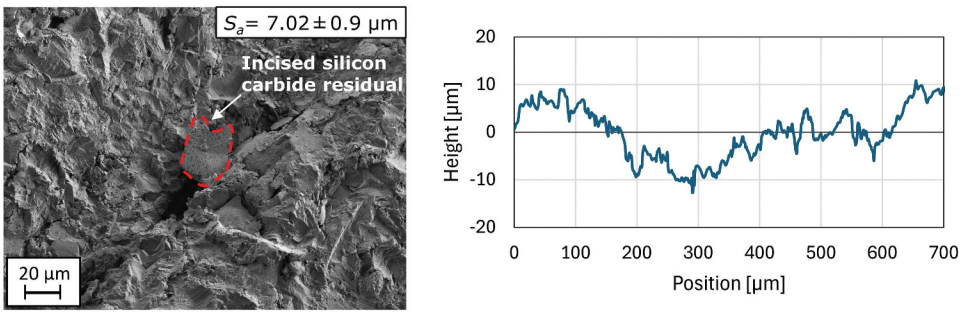


Figure 4. SEM image and height profile of a A90-oriented Ti6Al4V surface after grit blasting.

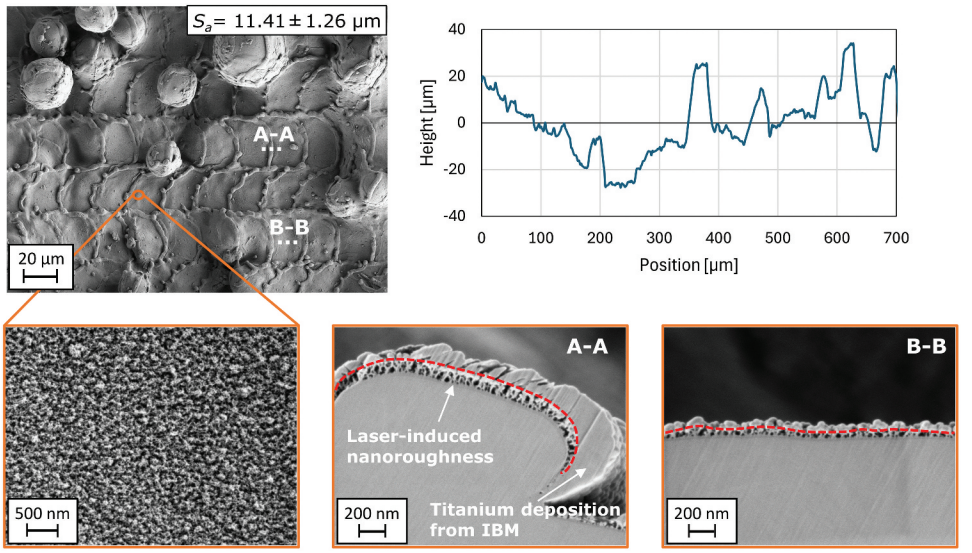


Figure 5. SEM images and height profile of a A90-oriented Ti6Al4V surface after laser treatment. The IBM-prepared cross section views were evaluated at a laser pulse edge (A-A) and laser pulse depression (B-B).

surface. In general, grit blasting mainly modified the microscopic roughness on the surface, without creating a pronounced nanoroughness. No significant differences in surface morphology were observed between A0 and A90 after this treatment.

In contrast, laser treatment allowed to generate roughness on two distinct scales: microroughness and nanoroughness. On the microscale, the laser pulses textured the entire surface, including the attached particles, on a low micrometer range, as illustrated in Figure 5 for the A90 surface. This microroughness is superimposed with a laser-induced nanoporous oxide layer, which is formed by local remelting of the surface under an atmospheric environment. A distinct nanoroughness was also developed on the attached particles surface. Based on investigations in[15,32] with similar laser settings, it can be assumed that the created nanoroughness mainly corresponds to a TiO_2 layer. By filling this nanoporous oxide layer with the adhesive, a high adhesion can be achieved due to the formation of interfacial bonds and mechanical interlocking. In particular, van der Waals interactions become highly effective, if the distance between the substrate surface and the adhesive remains in nanometer scale.[22,40] Wetting of the adhesive in the nanoscale pores is generally unproblematic since wetting is promoted here by high capillary forces.[9] Cross-sectional analysis after IBM revealed that the oxide layer morphology comprises an approximately 10 nm thin barrier layer, above which an open-pored, branched nanostructure with varying thickness and a pore size of approximately 10–40 nm is

formed. The oxide layer thickness generally ranges between 50–100 nm, with higher thickness at the laser pulse edges (Figure 5, A-A) compared to the pulse depressions (Figure 5, B-B). It is important to note that the topmost layer visible in the cross-section images in Figure 5 is not part of the nanoroughness, as it is titanium deposition from the ion milling process. To distinguish this material from the oxide layer, a thin gold layer was applied to the sample before the IBM process. This gold layer is marked with a red line. Similar thicknesses were observed on the surfaces of the attached particles. Moreover, no laser-induced defects or changes in grain structure in the near-surface area of the bulk titanium substrate were found. Laser treatment of the A0 surface resulted in a comparable oxide layer.

In comparison, chromic acid anodizing (CAA)-treated Ti6Al4V substrates, which provide high bond strength and durability, typically have a nanoporous oxide layer with a relatively uniform thickness ranging from 120 to 130 nm on the surface.[9] The laser-induced oxide layer in this work exhibits a more inhomogeneous thickness and is, particularly in the laser pulse depressions, thinner compared to CAA-generated nanoroughness on Ti6Al4V.

To compare the bond performance of laser treated PBF-LB-Ti6Al4V, a combination of the grit blasting and laser treatment process was also considered (GB+LT). This combination creates a surface morphology consisting of the grit blasting textures (Figure 4) superimposed with the laser-induced pulse structures and nanoporous oxide layer (Figure 5).

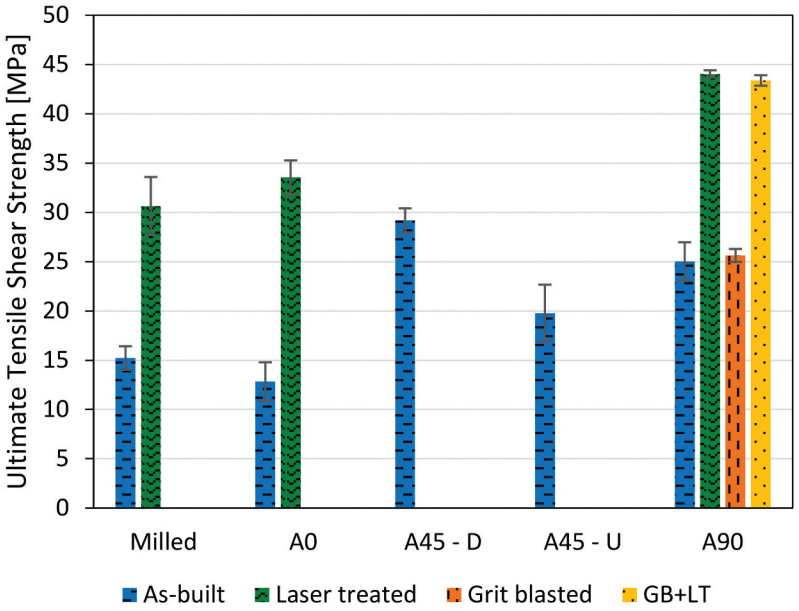


Figure 6. Ultimate tensile shear strengths, shown for the different build orientations in as-built and surface-treated conditions. The results for a milled surface are also shown as a reference.

3.2. Quasi-static loading

3.2.1. Initial adhesive bond performance

The ultimate tensile shear strengths obtained from the quasi-static SLJ-tests of the non-aged specimens are presented in Figure 6. As previously explained, the surface-treated variants were examined for the build orientations A0 and A90. Due to the similar surface morphologies of A0 and A90 after grit blasting, the grit-blasted variants of A0 were excluded from testing. Additionally, results for a milled Ti6Al4V surface are depicted as a reference. It should be noted that the laser treatment of the milled surface was conducted using the same settings, resulting in a comparable oxide layer, as shown in Figure 5.

The tensile shear strengths of the as-built surfaces show a significant dependence on the build orientation. The lowest bond strength, approximately 12.8 MPa, was found for the slightly structured A0-surface, which is comparable to the result of the milled surface without laser treatment. With an increasing number of attached particles on the surface higher bond strengths are reached. Among the as-built surfaces, the highly structured A45-D surface exhibits the highest bond strength of around 29.2 MPa. This enhanced bond strength can be attributed to the large particle accumulations and the wavy structure induced by the stair-stepping effect. The fracture surface of A45-D reveals a mixed-mode failure, with adhesive residues around the particles indicating pronounced interlocking, as shown in Figure 7(a). Compared to the other as-built surfaces, more cohesive failure is present on A45-D. The SEM image was evaluated at the overlap start of the fractured substrate to more clearly illustrate the failure type, as less adhesive residues are present in this region compared to the overlap end. The load direction F is depicted. Due to the significant interlocking on the A45-D surface, a bond strength similar to the milled surface with laser-induced nanoroughness is achieved. This highlights the critical role of mechanical interlocking in tensile shear loading. The

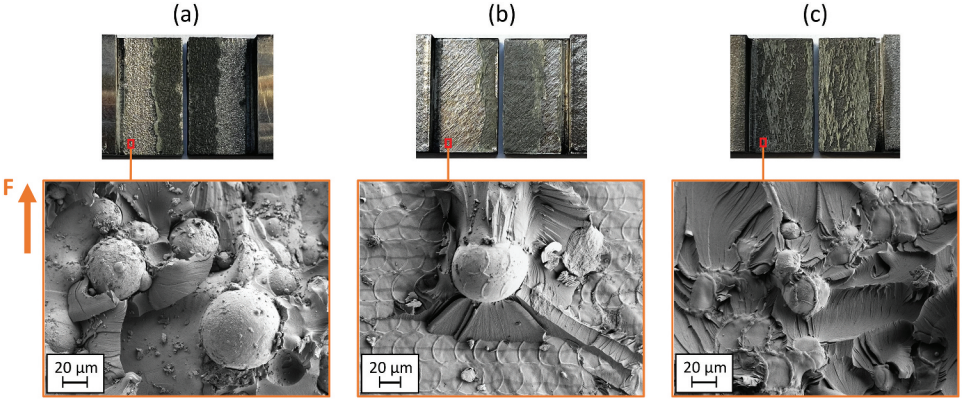


Figure 7. SEM images of the fracture surfaces of quasi-statically tested SLJ specimens with (a) A45-D as-built, (b) A0 laser treated and (c) A90 laser treated surface. The load direction F is depicted.

results show that the tensile shear strength and the extent of cohesive failure correlate with the number of attached particles on the surface. In surface areas with few or no attached particles, adhesive failure is dominant. This indicates that the adhesion strength of the as-built surfaces is mainly governed by mechanical interlocking rather than chemical or dispersive adhesion. The measured tensile shear strengths are therefore primarily determined by the particle density-dependent mechanical interlocking effect.

Grit blasting (GB) of the A90 surface resulted in a similar bond strength compared to the as-built condition, indicating similar effectiveness of the grit blasted surface and the inherent roughness of A90 under tensile shear loading. A significant increase in ultimate tensile shear strength was achieved by laser treatment (LT). For the A0-LT surface, an increase of 162% was observed, resulting in a comparable bond strength to the A45-D surface. This underscores the bonding potential of the inherent roughness of PBF-LB-Ti6Al4V. However, despite the substantial increase in bond strength with laser treatment of the A0 surface, the cohesive strength of the adhesive was not reached. The laser-induced nanoroughness was here insufficient to prevent adhesive failure, as illustrated in Figure 7(b). The interlocking effect of the particles is particularly evident, as demonstrated by an isolated particle on the surface in this SEM image, while no adhesive residues are present in the surrounding laser-structured area. In contrast, laser treatment of the A90 surface resulted in a significantly higher bond strength of around 44 MPa with cohesive failure in the adhesive layer, as shown in Figure 7(c). Furthermore, comparing the results of the A90-LT surface with the grit blasted and laser treated (GB+LT) A90 surface showed similar bond strength and failure mode. This indicates that the as-built A90 surface does not require grit blasting before bonding.

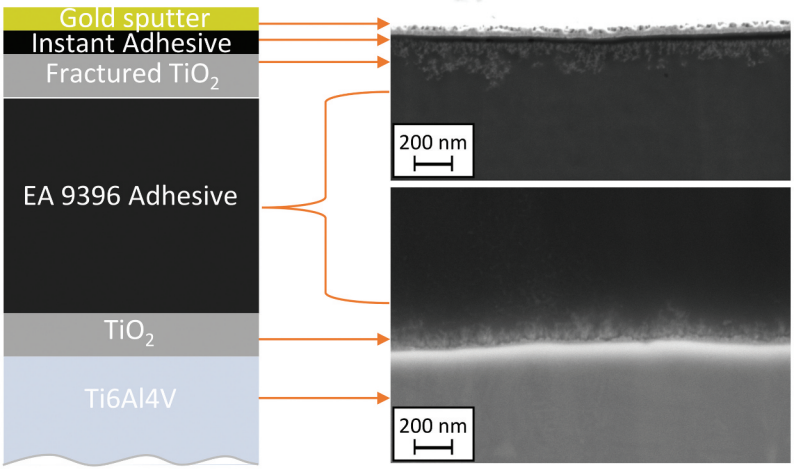


Figure 8. Fracture cross-section prepared by IBM and evaluated by SEM of a quasi-statically tested SLJ specimen with an A0 laser treated surface.

To further investigate the difference in bond strength between laser treated A0 and A90, IBM-prepared cross-sections of fractured specimens were analyzed by SEM. Figure 8 presents the cross-section of an A0-LT specimen after fracture, evaluated at the overlap end. The cross-section reveals two laser-generated nanostructured oxide layers. One belongs to the evaluated substrate, while the other corresponds to the oxide layer fractured from the overlap start region of the opposite substrate side. The adhesive successfully infiltrated the nanoporous roughness, providing enough adhesion strength. However, the cohesive strength of the laser-induced oxide layer was insufficient, which ultimately limited the bond strength. Fracture was found to occur close to the oxide barrier layer. It is assumed that the observed less pronounced nanoroughness in the laser pulse depressions caused failure initiation. Further optimization of the laser settings is therefore necessary. Fracture within the oxide layer also occurred for the milled surface after laser treatment (Milled-LT). A common factor between the A0-LT and Milled-LT surfaces is the absence of a significant microroughness.

In case of the A90-LT surface, no fracture of the oxide layer was found on either substrate side. Figure 9 shows that even in an area with a very thin oxide layer of approximately 50 nm, cohesive fracture does not occur. This can be attributed to the influence of the attached particles, which contribute to load-bearing through interlocking. As a result, the oxide layer experiences less stress, preventing fracture within the layer. This finding demonstrates how microscopic interlocking features can reduce the loading on laser-induced nanoporous roughness, thereby preserving the integrity of the adhesion mechanism. Therefore, the combination of the inherent microscopic interlocking features of PBF-LB-Ti6Al4V surfaces with a distinct nanostructured oxide layer appears to be a promising approach for achieving high adhesive bond performance with AM parts.

To further investigate the adhesive bond performance, the elastic limit was evaluated from the stress-strain curves obtained from SLJ-testing. The term

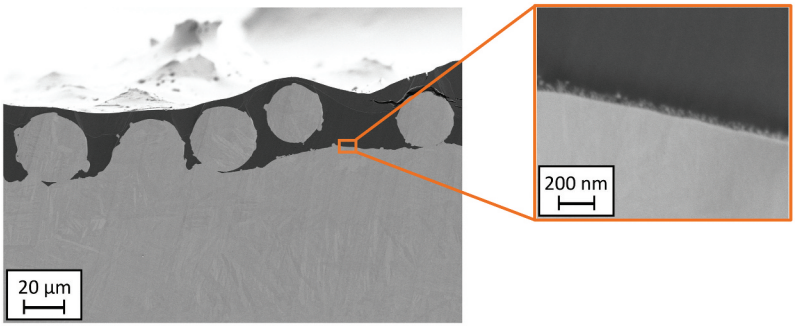


Figure 9. Fracture cross-section prepared by IBM and evaluated by SEM of a quasi-statically tested SLJ specimen with an A90 laser treated surface.

"elastic limit" is used here instead of "yield strength", because the initiation of inelastic deformations is caused for most of the investigated surfaces due to insufficient interfacial bond strength, which is not a material property. The elastic limit was evaluated since significant inelastic deformation was observed in the adhesive and because of its importance in the structural design process. Moreover, it is utilized here as an indicator for premature failure in the joint. For determining the elastic limit, stress-strain curves were calculated using mean stress and shear strain values. The mean shear strain values were determined by averaging the strain distribution, measured via DIC, along the bondline. It is important to note that DIC captured the macroscopic deformation behavior of the adhesive bond, meaning that microscopic effects, such as local plastic deformations around surface asperities, are not considered in detail. The resulting elastic limits are given for the different surface morphologies in Figure 10.

The elastic limits are between 31–66% lower than the ultimate strengths, showing that a significant load increase takes place during inelastic deformation in the adhesive bond. This is caused by the pronounced elastoplastic material behavior of the adhesive and by the load redistribution in the SLJs during damage progression, as observed with DIC. Upon reaching high strain at the overlap ends, progressively more load is transferred through the initially very low loaded inner region.

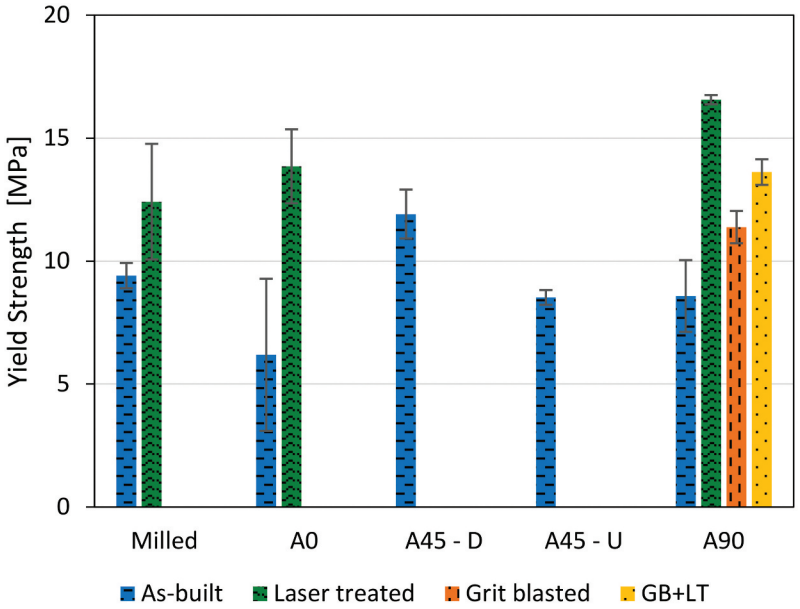


Figure 10. Elastic limits of quasi-statically tested SLJ specimens, shown for the different build orientations in as-built and surface-treated conditions. The results for a milled surface are also shown as a reference.

The relations between the elastic limits achieved with the different surface types are qualitatively similar to the ultimate strength results. For the A90-LT surface, macroscopic inelastic deformation starts due to yielding in the adhesive at the overlap ends at 16.6 MPa. This elastic limit is considerably higher than for the other laser treated surfaces. One possible reason for the lower elastic limit achieved with the Milled-LT and A0-LT surface is the early local fracture of the oxide layer at the overlap ends, due to insufficient adhesion strength. In case of the A90-GB +LT surface, fracture within the oxide layer did not occur. Here, the lower elastic limit could be due to the absence of particle-induced interlocking within the adhesive. Moreover, a low (A0) to intermediate (A90/A45-U) number of attached powder particles on the surface, without a distinct nanoroughness, was found to result in low elastic limits. In such surface morphologies, failure is likely to initiate in areas with no attached particles, leading to macroscopic inelastic deformation at relatively low loads. If large particle accumulations are present, as seen for A45-D, the elastic limit is comparable to the Milled-LT surface. This indicates again a similar effectiveness of distinct nanoroughness and pronounced particle-induced interlocking in enhancing tensile shear loading performance.

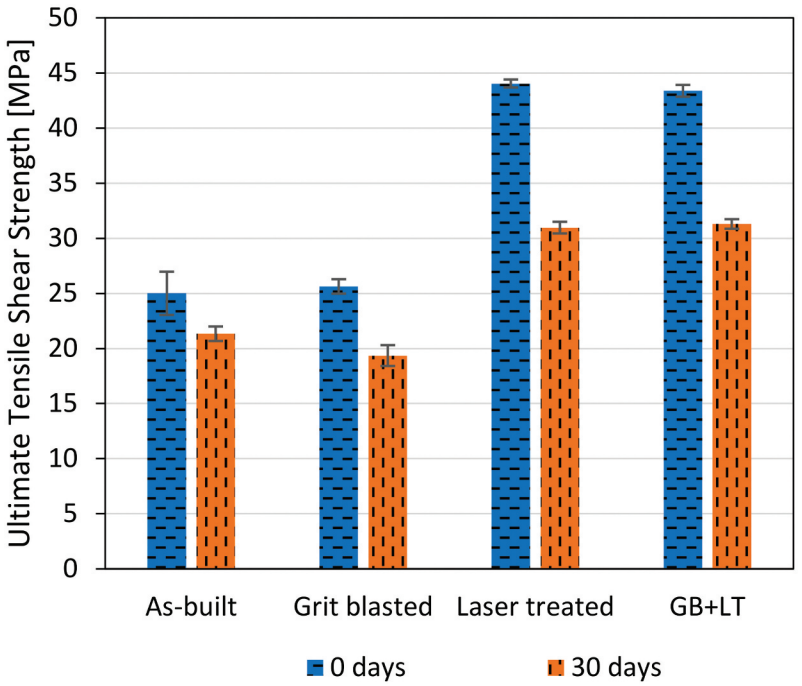


Figure 11. Hot-wet aging influence on ultimate tensile shear strength shown for the A90 build orientation.

3.2.2. Hot-wet-aged

The environmental durability of the adhesive joints was investigated exemplarily for the A90 surfaces, due to the limited number of specimens available. Before testing, the hot-wet-aged specimens were re-dried to eliminate the effect of increased ductility in the adhesive due to water diffusion.[40] The ultimate tensile shear strengths before and after aging are compared in Figure 11.

In all cases, the tensile shear bond strength was reduced due to hot-wet aging. For the grit blasted surface, the decrease in bond strength was slightly higher than for the as-built surface. A more pronounced reduction of 28–30% was observed for the laser treated surfaces. Moreover, evaluating the elastic limits of the aged specimens also revealed a significant reduction of 40–71%. SEM-analysis of the fracture surfaces of the laser treated specimens showed that the failure mode switched from cohesive failure to mixed-mode failure after hot-wet aging. This is illustrated in Figure 12 for the A90-LT surface evaluated at the overlap start region. The same failure mode was observed on the entire overlap region.

Cohesive failure in the adhesive is predominantly present around the edges of the laser pulse imprints, due to the microscopic surface topography and the more distinct nanostructured oxide layer in these areas. However, in the inner regions of the laser pulse imprints, areas with a very thin layer of adhesive residues were found that are adjacent to adhesive-free regions, as illustrated in the image taken with the In-Lens detector (Figure 12(b)). This indicates that the adhesion strength was insufficient in the laser pulse depressions, which corresponds to areas with a less distinct laser-induced oxide layer (Figure 5).

Cross-sectional analysis of a hot-wet-aged A90-LT specimen revealed that fracture of the laser-induced oxide layer occurred (see Figure 13). In the upper area of the cross-section, the fractured oxide layer from the opposite substrate

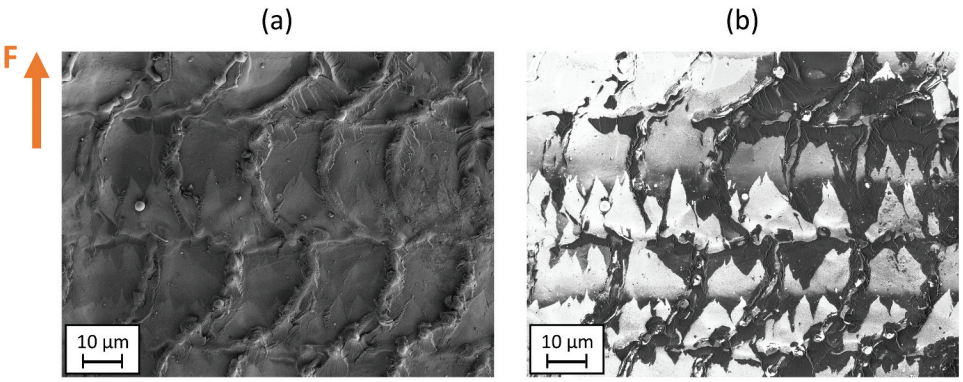


Figure 12. SEM images of the fracture surface of a hot-wet-aged and quasi-statically tested SLJ specimen with an A90 laser treated surface analyzed with (a) SE2 and (b) In-lens detector. The load direction F is depicted.

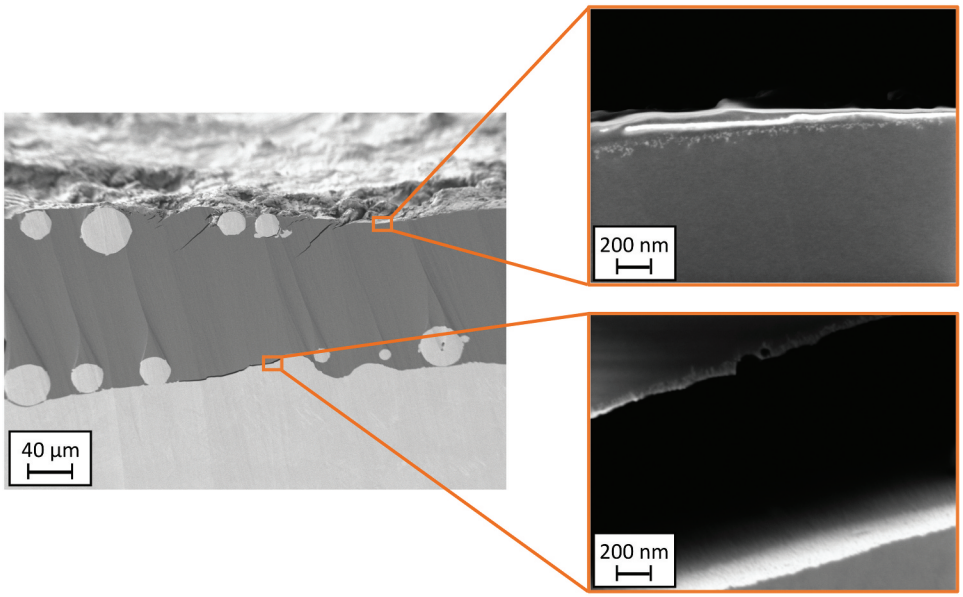


Figure 13. Fracture cross-section prepared by IBM and evaluated by SEM of a quasi-statically tested SLJ specimen with an A90 laser treated surface, after hot-wet aging.

is visible, while partial fractures of the titanium oxide were also found on the evaluated substrate side. Since no fracture of the laser-induced nanoroughness was observed in the non-aged condition of the A90-LT specimen, it is evident that the applied hydrothermal aging process deteriorated the structural integrity of the oxide layer. It is known that in presence of moisture, the cohesive strength of a nanostructured oxide layer can be reduced.[9,41] While this phenomenon is well known for aluminum-epoxy bonds, titanium adherends typically exhibit stable behavior under moderate temperature and humidity conditions.[9] However, prolonged hydration can lead to hydrolytic degradation and swelling of the nanostructured oxide layer, resulting in internal stresses that contribute to micro-cracking.[42] Löbbecke et al.[30] showed that a surface morphology with a pronounced open-pored, branched nanostructure is essential for achieving long-term stable adhesive bonds. The laser-induced nanoroughness created in this work fulfills this requirement, but the inhomogeneous thickness formation on the surface is assumed to cause premature failure of the titanium oxide layer. Further optimization of the laser treatment process is necessary to create a more uniformly distributed or stronger oxide layer. Alternatively, a sol-gel and primer application could help to improve the bond durability, as demonstrated in[6] for PBF-LB-Ti6Al4V adhesive joints subjected to salt-spray aging. Palmieri et al.[43] achieved long-term environmental durability of conventionally manufactured Ti6Al4V bonded joints only after combining laser treatment with sol-gel and primer application. The sol-gel treatment could also be beneficial for high-

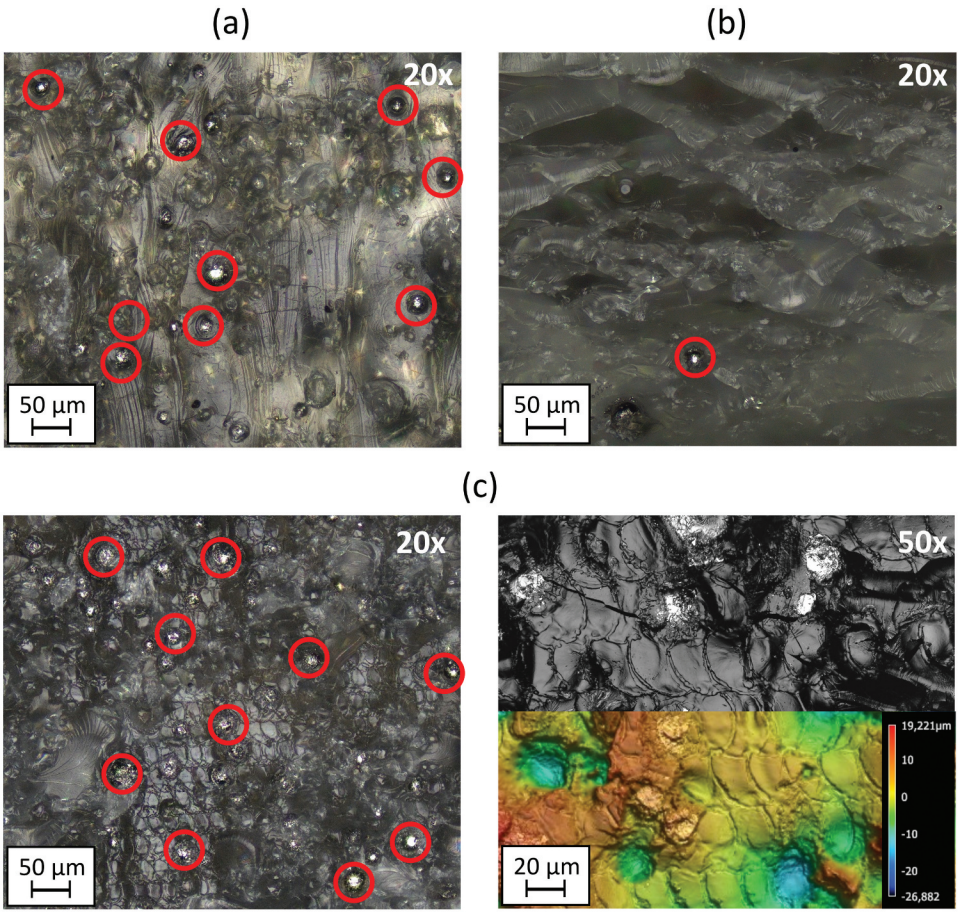


Figure 14. Fracture behavior of the attached powder particles under quasi-static loading, shown by CLSM images for the fracture surfaces of A90 with different surface conditions: (a) as-built, (b) laser treated and (c) laser treated+hot-wet-aged.

temperature applications, where oxide diffusion into the titanium base material can cause voids or microcracks at the metal – oxide interface.[9] The use of corrosion-inhibiting primers is often recommended, even for highly stable oxide layers created by PAA treatments, to further enhance durability.[41,42] If the optimization of the laser process doesn't result in satisfactory durability, a combination with sol-gel and primer application could be a viable alternative to achieve long-term environmental stability.

The upper area of the cross-section in Figure 13 also reveals multiple fractured powder particles, which was rarely observed in the non-aged condition for this surface type. It can be assumed that after failure initiation in the weakened oxide layer, the load was redistributed to the attached particles, leading to an increased number of detached particles. To further assess the fracture behavior of the partially melted powder particles, large areas of the fracture surfaces were examined by CLSM. Figure 14 shows the CLSM images

of A90 surfaces in as-built and laser treated condition. The detached particles are marked.

In the unaged condition, a moderate number of powder particles fractured from the A90 as-built surface under the applied tensile shear loading (Figure 14(a)). However, the majority of the particles remained attached, indicating that they were well connected to the titanium bulk. In contrast, almost no particles fractured on the laser treated A90 surface (Figure 14(b)) due to the nanoroughness contribution to load transfer. This demonstrates how a nanostructured oxide layer can enhance particle-induced interlocking of the adhesive. After hot-wet aging, the number of fractured particles on the A90-LT surface (Figure 14(c)) increased up to a level comparable to the A90 as-built surface (Figure 14(a)) due to the fracture of the oxide layer. It was observed that negative laser pulse imprints on the adhesive fracture surface generally indicate a nanoroughness fracture. It can be concluded, that a cohesively strong nanoroughness is essential to fully leverage the interlocking potential of the attached particles.

3.3. Fatigue loading

To assess the adhesive bond performance under fatigue loading, the investigated surface types were categorized into three groups with similar quasi-static tensile shear strengths, allowing a meaningful comparison. All fatigue tests were conducted with unaged specimens. Moreover, the Milled and A0 as-built surface types were excluded from these tests due to their relatively low adhesion strength. In each group, the maximum stress σ_{max} applied during cyclic loading was set to 40–45% of the mean quasi-static adhesive bond strength, resulting in the stress levels 11.2 MPa, 14.4 MPa and 18.4 MPa. The measured fatigue lifetimes are depicted in Figure 15.

Among the surfaces tested at a stress level of 11.2 MPa, the longest lifetime was reached with the A45-D surface. Compared to the next best surface, A90 grit blasted, a 750% longer lifetime was observed. The combination of a large

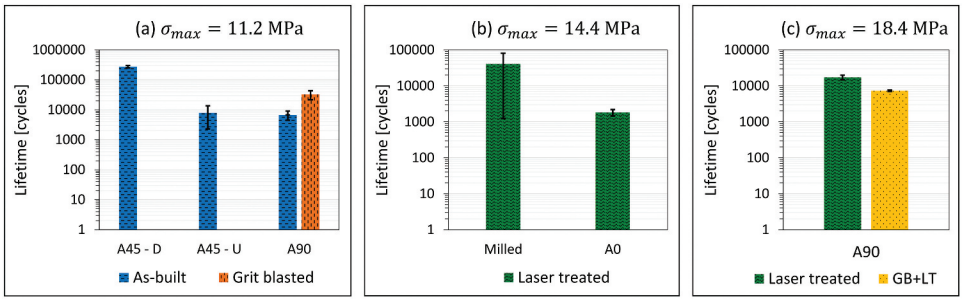


Figure 15. Fatigue lifetimes of SLJs with different surface morphologies, compared at (a) σ_{max}= 11.2 MPa, (b) σ_{max}= 14.4 MPa and (c) σ_{max}= 18.4 MPa.

number of attached particles and the stair-stepping-induced waviness present on the A45-D surface topography appears to be much more effective than the microroughness created by grit blasting for the given fatigue load. This superior performance is likely due to the significant particle-induced interlocking and the large surface area of A45-D. However, surface morphologies with an intermediate number of partially melted particles, such as A45-U and A90, resulted in a shorter lifetime than the grit blasted surface. These results are also reflected in the fracture surfaces, where the lowest amount of adhesive failure was found for the A45-D surface within the given comparison group. Similar to the results from the quasi-static tests, adhesive failure predominantly occurred in areas with few or no attached particles, indicating that these regions offer low fatigue resistance. Thus, the positive effect of the attached particles is significantly enhanced when a high particle concentration is present on the surface.

Comparing the milled and A0 surfaces after laser treatment at a fatigue stress level of 14.4 MPa showed that, on average, the lifetime achieved with Milled-LT is higher. However, considering the high standard deviation observed for Milled-LT, no significant statistical difference is present between both surfaces. The failure mode for both surfaces was fracture of the laser-generated oxide layer, which is consistent with the findings from the quasi-static tests. Very low standard deviations were observed for the A90 surfaces after laser treatment, shown in Figure 15(c). A 130% longer lifetime was achieved with A90-LT compared to A90-GB+LT, underscoring the effectiveness of the combination of attached particles and laser-induced nanoroughness. Evaluating the fracture surfaces showed that these two surface types exhibited a mixed-mode failure. For the A90-LT surface, the primary failure type was fracture of the laser-induced oxide layer, as illustrated in Figure 16(a). Since no fracture of the oxide layer was observed during quasi-static testing for

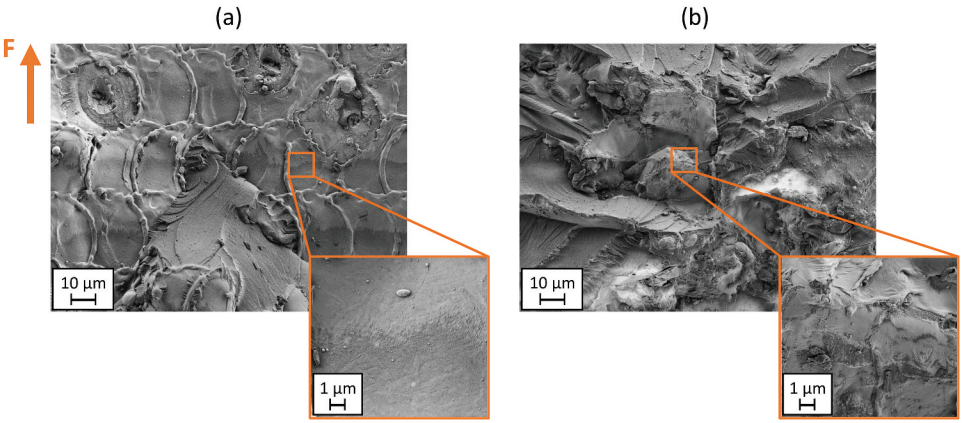


Figure 16. Fracture surfaces of fatigue-loaded SLJ specimens with (a) A90 laser treated and (b) A90 grit blasted+laser treated surface. The load direction F is depicted.

this surface type (Figure 9), it can be assumed that the oxide layer was more severely loaded under the applied fatigue loading condition. On the A90-GB +LT fracture surface, significantly more cohesive failure within the adhesive was found, with only a small portion of the surface showing adhesive failure (Figure 16(b), detail view). This revealed that, for the A90-GB+LT surface, the crack mainly propagated through the adhesive, while on the A90-LT surface, it propagated mostly through the oxide layer, which however resulted in a longer lifetime. Both surface types were treated using the same laser process parameters. No structural changes in the sub-surface area or detrimental effects of laser-induced residual stresses were detected in either case. Moreover, the low number of incised silicon carbide residues on the A90-GB+LT surface did not appear to negatively impact fatigue performance by causing crack initiation. Thus, it can be assumed that the superior fatigue performance achieved with the A90-LT is due to the influence of the attached particles. In addition to interlocking, the particles may also slow down the crack propagation, since it was found that the crack propagates close enough to the surface and is therefore under the direct influence of the particles.

3.3.1. S-N curves

For a more detailed comparison, further fatigue load levels were tested for selected surfaces. The A45-D as-built surface, characterized by its high particle density and the A90-LT surface, with its intermediate number of attached particles and nanoroughness, were chosen due to their remarkable adhesive bond performance. In addition, the particle-free, nanostructured Milled-LT surface was further considered to help differentiate the effects of particle-induced interlocking and nanoroughness on the fatigue behavior. The

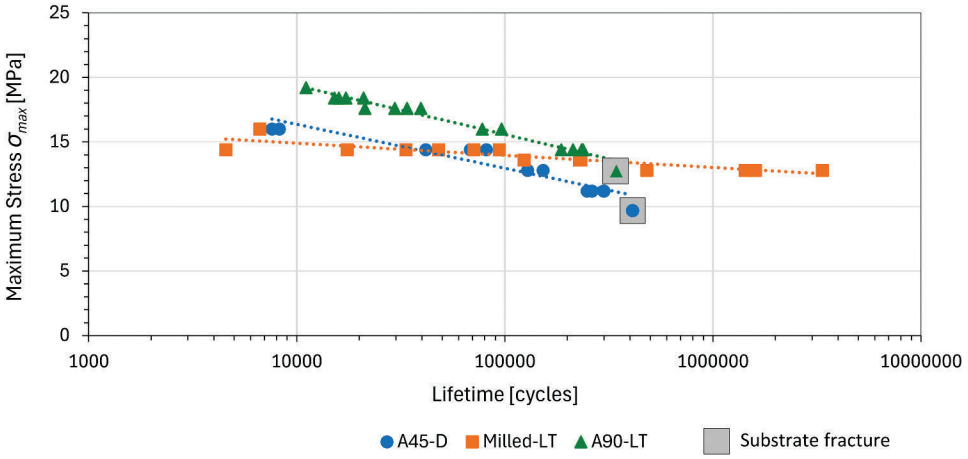


Figure 17. S-N curves of SLJ specimens with A45-D as-built, Milled-LT and A90-LT surface.

comparison is shown in Figure 17, by means of S-N curves in a semi-logarithmic presentation.

In the lifetime range up to 10^5 cycles, the best fatigue performance was reached with the A90-LT surface, while for the other two surfaces similar lifetimes were found. This shows that in the range of low cycle fatigue (LCF) the combination of attached particles and laser-induced nanoroughness provides the highest fatigue resistance. Moreover, it can be stated that both the extensive particle-induced interlocking effect of the A45-D surface and the laser-induced nanostructured oxide layer of the Milled-LT surface show similar effectiveness in LCF. However, above 10^5 cycles (high cycle fatigue (HCF)), bonding with the A45-D surface resulted in shorter lifetimes compared to the Milled-LT surface. Fracture surface analysis revealed that for both surface types, the same failure mode is present as in LCF, namely mixed mode failure for A45-D and oxide layer fracture for Milled-LT. The interlocking effect of the attached particles appears to be inferior in HCF compared to the enhanced adhesion provided by the nanoroughness of the Milled-LT surface. An explanation could be that due to the absence of significant plastic deformation in HCF the crack growth is less influenced by microscopic surface features like the attached particles. It should be noted that for the Milled-LT specimens a significantly higher scattering of the lifetime is present at each load level, indicating a relatively low reliability of this surface condition. Furthermore, the A90-LT surface shows in HCF also a higher fatigue resistance than Milled-LT. It appears that the difference between these two surfaces becomes lower with decreasing load level. This supports the observation that the fatigue behavior in HCF is mainly improved by the nanoroughness rather than by the attached particles. Failure of A90-LT in HCF occurred similarly to LCF due to fracture of the oxide layer. Moreover, the evaluation in HCF was limited since in a certain load range, depending on the surface type, fracture in the bulk titanium substrate occurred before the adhesive bond failed. This was caused by the bending moment present in SLJ-testing.[44] Locus of the failure was at the edge of the stepped specimen geometry, perpendicularly to the load axis. A similar failure mode was observed in[35] at certain fatigue load levels for aluminum-aluminum single-lap joints with flat plate specimens. In the present work, a single step-lap joint geometry was used to reduce the bending moment load at the overlap ends. This approach was effective for the milled specimens, as no fracture occurred in the metallic substrate. Therefore, it is assumed that the surface roughness at the edge was the primary cause of the substrate failure.

3.3.2. Crack growth

The surface morphology influences on crack growth during fatigue loading were investigated by DIC measurements. The main objective was to further

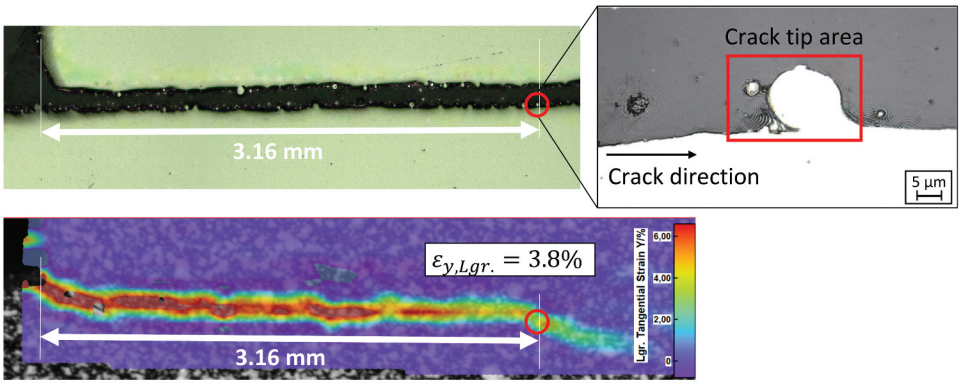


Figure 18. Correlation between crack tip position determined by CLSM and peel strain ε_y measured by DIC.

evaluate the influence of attached particles, nanoroughness and their combination on the fatigue behavior. First, a correlation between the crack tip position and the strain measured by DIC was established. A fatigue test was stopped after a certain number of cycles prior to bond failure. The cross-section of the adhesive joint was subsequently polished and analyzed by CLSM to determine the crack tip position. As shown in Figure 18, the crack tip was located in the vicinity of a particle. The crack length was then correlated with the peel strain ($\varepsilon_{y,Lgr.}$) calculated by the DIC system. The peel strain was used since it is suitable for characterizing crack opening. It was found that a peel strain of 3.8% correlates with the crack tip position. Considering that previous tensile tests of bulk adhesive specimens (EA 9396) resulted in a fracture strain of 3.9%, the determined value appears to be reasonable.

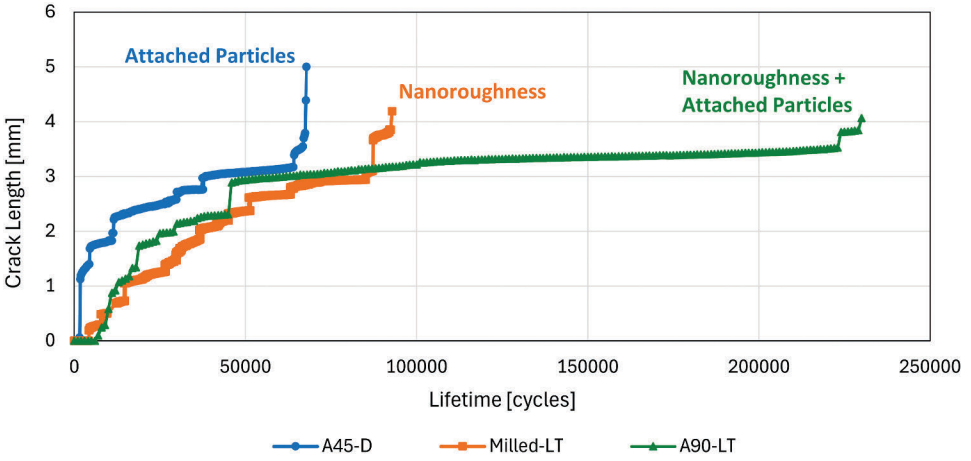


Figure 19. Crack growth of fatigue-loaded SLJs with different surface morphologies, tested at σ_{max}= 14.4 MPa.

In the SLJ specimen, cracks initiate at the overlap ends, resulting in two macroscopic crack paths. In the following, the crack growth results are shown for one crack path, since similar observations were made for both crack fronts. A comparison of the crack growth was conducted for the three detailly investigated surfaces A45-D, Milled-LT and A90-LT. This comparison is shown exemplarily for the maximum stress level of 14.4 MPa, illustrated in Figure 19. Crack initiation occurred already after a few thousand cycles for all three surfaces. No significant differences in crack initiation lifetime were observed between the surfaces, indicating that the varying roughness scales present on these surface morphologies do not cause substantial differences in crack initiation in the LCF regime. Despite the small differences, the results show that the crack initiation lifetimes correlate with the quasi-static bond strengths of the surfaces. It is important to note that none of the considered surfaces has pronounced sharp structures on the microscale that could promote crack initiation.

The overall lifetime was mainly determined by the crack propagation behavior. In the initial phase, the crack propagates significantly faster in case of A45-D, while a similar crack growth rate is observed for Milled-LT and A90-LT. Following this initial phase, the crack propagation rate gradually decreases for all three surfaces until a phase of minimal crack growth occurs. Upon reaching a surface-dependent critical total crack length, unstable crack growth initiates, leading to rapid fracture. Initiation of unstable crack growth occurs much earlier for A45D and Milled-LT than for A90-LT, correlating with the quasi-static bond strength reached with the respective surface morphology. Fracture analysis revealed that, in rare cases, microcracks may form around the attached particles on the surface, which propagate only a short distance before halting. Particle-induced negative effects on the crack growth were therefore not found in the LCF regime.

The positive influence of the attached particles on fatigue behavior can be mainly attributed to their mechanical interlocking effect, which not only increases overall bond strength but can also cause crack paths to be more tortuous, as cracks are forced to propagate around the particles. In addition, considering the pronounced plastic material behavior of the EA9396 adhesive and the applied high fatigue load, it can be assumed that the particles cause local plastic deformations in the adhesive, leading to energy dissipation and thereby reducing the amount of energy available to drive crack propagation. On the other hand, the contribution of the laser-induced nanoroughness to the adhesion strength is primarily based on the significant increase of surface area, allowing interfacial bonds to form and mechanical interlocking of the adhesive in the nanostructures. To combine the advantages of both attached powder particles and laser-induced nanoroughness, a hierarchical surface morphology was created, as seen in the A90-LT surface. With this surface the gradually slowed crack propagation was maintained significantly longer due to the given higher adhesion strength. The

described crack growth behavior was also observed similarly at a higher fatigue load. However, for load levels in the HCF regime, differences in crack initiation and propagation were found between the A45-D and Milled-LT surfaces. The crack initiation and growth were significantly slower in case of Milled-LT. A possible explanation is that the large surface area created by the nanoroughness is particularly effective in reducing stress concentrations, which is crucial under the predominantly elastic loading in HCF. In contrast, the absence of significant plastic deformations in HCF reduces the effectiveness of the attached particles.

4. Conclusions

The surface morphology influences of PBF-LB manufactured Ti6Al4V parts on adhesive bond performance were investigated for different build orientations and surface conditions. The bond strength and fatigue resistance were studied for tensile shear loading, while a hot-wet aging process was applied to assess the bond durability. The main results of this study can be summarized as follows:

- The build-orientation-dependent number of partially melted particles on the as-built surfaces correlates with the tensile shear strength and fatigue life of the adhesive bond.
- Grit blasting the PBF-LB-Ti6Al4V surfaces resulted in a similar bond performance to that of an as-built surface with an intermediate number of attached particles (A90).
- A significant improvement in bond strength and fatigue resistance was achieved by laser treatment, which created a hierarchical surface morphology consisting of the inherent attached powder particles of the PBF-LB process and a laser-induced nanoporous oxide layer. The influences of these surface features on the adhesive bond can be described as follows:
- The partially melted particles cause mechanical interlocking at the microscale and provide an increased surface on which the nanoroughness can be formed. Moreover, under fatigue loading, the particles can cause energy dissipation due to local plastic deformations in the adhesive, which slows down crack propagation in LCF.
- The laser-induced nanoroughness contributes to a significantly increased overall surface area, enhances nanoscale interlocking and improves fatigue behavior in both LCF and HCF.
- Interactions between the attached particles and the laser-induced oxide layer were determined. An increasing number of particles can prevent fracture of the oxide layer, thereby enabling cohesive failure in the adhesive layer. This was observed for the laser treated A90 surface (A90-LT) under quasi-static loading, whereas oxide fracture occurred for A0-LT due to the lower number of particles on the surface. Furthermore, it

was demonstrated that a cohesively strong nanoroughness allows more particles to remain attached to the surface, thus enhancing microscale interlocking.

- In LCF, a comparison of the fatigue lifetimes between a surface with a high number of attached particles (A45-D) and a particle-free, nanostructured surface (Milled-LT) revealed that the partially melted particles and the laser-induced nanoroughness are similarly effective in the adhesive bond.
- In HCF, lower fatigue lifetimes were found for A45-D compared to Milled-LT since the particle-induced interlocking effect diminishes at low loads due to the absence of significant plastic deformations. This lower effectiveness of the attached particles in HCF is also reflected in a faster crack initiation and propagation for A45-D.
- Hot-wet aging resulted in considerably reduced bond strengths, showing that the investigated surface morphologies lack sufficient environmental durability. For the laser treated surfaces, failure occurred due to fracture of the nanostructured oxide layer, which was mainly observed in the laser pulse depressions.
- SEM-analysis of IBM-prepared cross-sections of laser treated specimens revealed that the created nanoroughness was less distinct in the laser pulse depressions compared to the laser pulse edge regions. Therefore, it is assumed that the inhomogeneous thickness formation of the oxide layer caused its cohesive failure, observed after hot-wet aging and also under fatigue loading.
- Further optimization of the laser treatment process is necessary to create a more uniformly distributed or stronger oxide layer. Combinations with sol-gel and primer application could also be viable options to achieve environmental durability.

Acknowledgments

This work is part of the research project BLANCA, which was funded by the Bavarian Ministry of Economic affairs, Regional development and Energy (StMWi) within the program BayLu-25. We thank the project partner Modell- und Formenbau Blasius GERG GmbH, for printing the substrates. The authors also thank the Institute of Materials Science (University of the Bundeswehr Munich) and the Bundeswehr research institute WIWeB for providing access to their laboratory equipment.


Sponsored by
Bavarian Ministry of Economic Affairs,
Regional Development and Energy

Disclosure statement

No potential conflict of interest was reported by the author(s).

Funding

This work was supported by the Bavarian Ministry of Economic affairs, Regional development and Energy.

Data availability statement

The data that support the findings of this study are available from the corresponding author upon request.

References

[1] Koch, C.; Richter, J.; Vollmer, M.; Kahlmeyer, M.; Niendorf, T.; Böhm, S. Adhesively Bonded joints in Components Manufactured via Selective Laser Melting. *Proc. Inst. Mech. Eng. Part C: J. Mech. Eng. Sci.* 2021, *235*(3), 518–526. DOI: 10.1177/0954406220959376.

[2] European Cooperation for Space Standardization. *Space Engineering Adhesive Bonding Handbook ECSS-E-HB-32-21A*; ESA Requirements and Standards Division: Noordwijk, 2011.

[3] Marques, A. C.; Mocanu, A.; Tomic, N. Z.; Balos, S.; Stammen, E.; Lundevall, A.; Abrahami, S. T.; Günther, R.; de Kok, J. M.; de Freitas, S. T. Review on Adhesives and Surface Treatments for Structural Applications: Recent Developments on Sustainability and Implementation for Metal and Composite Substrates. *Materials* 2020, *13*(24), 5590. DOI: 10.3390/ma13245590.

[4] Campbell, F. C., Ed. Adhesive Bonding and Integrally Cocured Structure: A Way to Reduce Assembly Costs Through Parts Integration. In Manuf Process Adv Compos. Elsevier S: Amsterdam, 2004; pp 241–301. DOI: 10.1016/B978-1-85617-415-2.X5000-X .

[5] Nguyen, A. T.; Brandt, M.; Orifici, A. C.; Feih, S. Hierarchical Surface Features for Improved Bonding and Fracture Toughness of Metal-Metal and Metal-Composite Bonded Joints. *Int. J. Adhes. Adh* 2016, *66*, 81–92. DOI: 10.1016/j.ijadhadh.2015.12.005.

[6] Ardila-Rodriguez, L. A.; Rans, C.; Poulis, J. A. Effect of Surface Morphology on the Ti–Ti Adhesive Bond Performance of Ti6Al4V Parts Fabricated by Selective Laser Melting. *Int. J. Adhes. Adh* 2021, *110*, 102918. DOI: 10.1016/j.ijadhadh.2021.102918.

[7] Ertürk, E.; Musil, B.; Diez, G.; Felber, C.; Höfer, P. Surface Morphology Influences of PBF-LB Manufactured Ti6Al4V Parts on Adhesive Bond Strength—Investigation of As-Built and Surface-Treated Conditions. *Prog. Addit. Manuf.* 2023, *8*(4), 719–731. DOI: 10.1007/s40964-023-00450-7.

[8] Nusom, Y.; Srimanosaowapak, S.; Uthaisangsuk, V. Effects of 3D-Printing Surface Morphologies on Interfacial Bonding Strength Between Ti–6Al–4V and CFRTP with PMCs Interlayer. *Int. J. Adhes. Adh* 2023, *121*, 103313. DOI: 10.1016/j.ijadhadh.2022.103313.

[9] da Silva, L. F. M.; Öchsner, A.; Adams, R. D., editors *Handbook of Adhesion Technology*; Springer: Berlin, Heidelberg, 2018. DOI: 10.1007/978-3-319-55411-2.

[10] Avinç Akpinar, I. The Effect of Chemical Etching and Nanostructure Additive Epoxy Coating Technique on Adhesion Strength in Aluminum Joints Bonded with Nanostructure Additive Adhesive. *Int. J. Adhes. Adh* 2024, *129*, 103584. DOI: 10.1016/j.ijadhadh.2023.103584.

[11] Avinç Akpinar, I. Effect of Chemical Oxidation Process on Adhesive Performance in Two Component Adhesive with Nano Particle and Nano Fiber Additives. *Eur. Mech. Sci.* 2024, *8*(1), 29–37. DOI: 10.26701/ems.1385552.

[12] Akpinar, S.; Kars, A.; Bayramoglu, S.; Demiral, M. The Influence of Combination of Surface Roughness and Nanostructure of Adhesive on the Strength of Adhesively Bonded Joints. *Int. J. Adhes. Adh* 2024, *133*, 103743. DOI: 10.1016/j.ijadhadh.2024.103743.

[13] Wegman, R. F.; van Twisk, J. *Surface Preparation Techniques for Adhesive Bonding*; William Andrew: Norwich, 2013. DOI: 10.1016/C2012-0-02158-8.

[14] Matz, C. Optimization of the Durability of Structural Titanium Adhesive Joints. *Int. J. Adhes. Adh* 1988, *8*(1), 17–24. DOI: 10.1016/0143-7496(88)90053-X.

[15] Kurtovic, A. Laserinduzierte Nanostrukturierung von Titanoberflächen für das strukturelle Kleben - Einfluss auf die Oberflächenmorphologie, Ermüdungs- und Adhäsionseigenschaften. Dissertation, Universität Paderborn, 2014.

[16] Tseng, S. F.; Chen, Y. S. Surface Microtexturing of Ti-6Al-4V and SS316L Alloys Using High Pulsed Fiber Lasers for Improving the Adhesive Bonded Performance. *Opt. Las. Tech.* 2021, *143*, 107349. DOI: 10.1016/j.optlastec.2021.107349.

[17] Parkes, P. N.; Butler, R.; Meyer, J.; de Oliveira, A. Static Strength of Metal-Composite Joints with Penetrative Reinforcement. *Comp. Struc.* 2014, *118*(250), 250–256. DOI: 10.1016/j.compstruct.2014.07.019.

[18] Naat, N.; Boutar, Y.; Naimi, S.; Mezlini, S.; Da Silva, L. F. M. Effect of Surface Texture on the Mechanical Performance of Bonded Joints: A Review. *J. Adhes.* 2023, *99*(2), 166–258. DOI: 10.1080/00218464.2021.2008370.

[19] de Barros, S.; Kenedi, P. P.; Ferreira, S. M.; Budhe, S.; Bernardino, A. J.; Souza, L. F. G. Influence of Mechanical Surface Treatment on Fatigue Life of Bonded Joints. *J. Adhes.* 2017, *93*(8), 599–612. DOI: 10.1080/00218464.2015.1122531.

[20] Thäsler, T.; Holtmannspötter, J.; Gudladt, H. J. Surface Topography Influences on the Fatigue Behavior of Composite Joints. *Key Eng. Mat.* 2019, *809*, 341–346. DOI: 10.4028/www.scientific.net/KEM.809.341.

[21] Morfini, I.; Goglio, L.; Belingardi, G.; Nassar, S. A. Effect of Autoclave Cure Time and Bonded Surface Roughness on the Static and Fatigue Performance of Polyurethane Film Adhesive Single Lap Joints. *Int. J. Adhes. Adhes.* 2019, *92*(37), 37–43. DOI: 10.1016/j.ijadhadh.2019.03.015.

[22] Gudladt, H. J.; Frömmel, S. A. Fatigue and Fracture Behavior of Adhesive-Bonded Structures in the Light of the Surface Morphology. *Int. J. Adhes. Adh* 2019, *88*, 74–80. DOI: 10.1016/j.ijadhadh.2018.10.016.

[23] Moroni, F.; Musiari, F.; Favi, C. Effect of the Surface Morphology Over the Fatigue Performance of Metallic Single Lap-Shear Joints. *Int. J. Adhes. Adh* 2020, *97*, 102484. DOI: 10.1016/j.ijadhadh.2019.102484.

[24] Bagehorn, S.; Mertens, T.; Greitemeier, D.; Carton, L.; Schoberth, A. Surface finishing of additive manufactured Ti-6Al-4V - a comparison of electrochemical and mechanical treatments; 6th Eur Conf Aerosp Sci; Krakow, Poland, 2015.

[25] Kahlin, M.; Basu, D.; Kerwin, A.; Moverare, J. J.; Ansell, H.; Newton, L.; Smith, B. Improved Fatigue Strength of Additively Manufactured Ti6Al4V by Surface Post Processing. *Int. J. Fat.* 2020, *134*, 105497. DOI: 10.1016/j.ijfatigue.2020.105497.

[26] Taube, A.; Kurtovic, A.; Niendorf, T.; Mertens, T.; Zinn, C.; Schaper, M.; Maier, H. J. Influence of Surface Pre-Treatments on the High-Cycle Fatigue Behavior of Ti–6Al–4V – from Anodizing to Laser-Assisted Techniques. *Int. J. Fat.* 2016, *91*, 195–203. DOI: 10.1016/j.ijfatigue.2016.06.010.

[27] Costa, M.; Viana, G.; Da Silva, L. F. M.; Rdsg, C. Effect of Humidity on the Mechanical Properties of Adhesively Bonded Aluminium Joints. *Proc. Inst. Mech. Eng. Part L: J. Mater. Des. Appl* 2016, *232*(9), 733–742. DOI: 10.1177/1464420716645263.

[28] Bellini, C.; Parodo, G.; Polini, W.; Sorrentino, L. Influence of Hydrothermal Ageing on Single Lap Bonded CFRP Joints. *Frat. Ed. Integrità Strutt.* 2018, *12*(45), 173–182. DOI: 10.3221/IGF-ESIS.45.15.

[29] Clearfield, H. M.; McNamara, D. K.; Davis, G. D. Adherend Surface Preparation for Structural Adhesive Bonding. In Adhesive Bonding, Lee, L., Ed.; Springer: Boston, 1991. DOI: 10.1007/978-1-4757-9006-1_8.

[30] Löbbecke, M.; Bayerbasi, T. J.; Bartsch, M.; Haubrich, J. Role of Surface Structures on Long Term Stability of Adhesive Joints Between Ti–15V–3Cr–3Sn–3Al and Polyether-Ether-Ketone. *Int. J. Adhes. Adh* 2023, *120*, 103282. DOI: 10.1016/j.ijadhadh.2022.103282.

[31] Freund, J.; Lützenkirchen, I.; Löbbecke, M.; Tröster, T.; Haubrich, J.; Delp, A.; Wu, W. F. Transferability of the Structure–Property Relationships from Laser-Retreated Metal–Polymer Joints to Aluminum–CFRP Hybrid Joints. *J. Compos. Sci.* 2023, *7*(10), 427. DOI: 10.3390/jcs7100427.

[32] Specht, U.; Ihde, J.; Mayer, B. Laser Induced Nano-Porous Ti–O-layers for Durable Titanium Adhesive Bonding. *Mat. Sci. Eng. Tech.* 2014, *45*(12), 1116–1122. DOI: 10.1002/mawe.201400360.

[33] Deutsches Institut für Normung e. V. Aerospace Series - Non-Metallic Materials - Structural Adhesives – Test Method – Part 6: Determination of Shear Stress and Shear Strain EN 2243-6. DIN Media: Berlin, 2006. DOI: 10.31030/9663277.

[34] ASTM International. *Standard Specification for Additive Manufacturing Titanium-6 Aluminum-4 Vanadium ELI (Extra Low Interstitial) with Powder Bed Fusion ASTM F 3001:2014*; West Conshohocken, PA: ASTM International, 2014.

[35] Frömmel, S. A. Untersuchungen zum mechanischen Verhalten von Klebverbindungen unter Berücksichtigung von Grenzflächendefekten. Dissertation, Universität der Bundeswehr München, 2013.

[36] Henkel Corporation Aerospace. Loctite EA 9396 AERO Technical Data Sheet. 2013. https://www.aero-consultants.ch/view/data/3285/Produkte/Henkel%20Adhesive/LOCTITE%20EA%209396%20AERO.pdf. (accessed Aug 11, 2024).

[37] Bagnato, T.; Ravindran, A. R.; Mirabedini, A.; Ladani, R. B.; Kandare, E.; Orifici, A. C.; Chang, P.; Wang, J.; Mouritz, A. P. Superior Interfacial Toughening of Hybrid Metal-Composite Structural Joints Using 3D Printed Pins. *Compos. Part A* 2023, *168*, 107479. DOI: 10.1016/j.compositesa.2023.107479.

[38] Ventola, L.; Robotti, F.; Dialameh, M.; Calignano, F.; Manfredi, D.; Chiavazzo, E.; Asinari, P. Rough Surfaces with Enhanced Heat Transfer for Electronics Cooling by Direct Metal Laser Sintering. *Int. J. Heat Mass Transf.* 2014, *75*, 58–74. DOI: 10.1016/j.ijheatmasstransfer.2014.03.037.

[39] Viale, V.; Stavridis, J.; Salmi, A.; Bondioli, F.; Saboori, A. Optimisation of Downskin Parameters to Produce Metallic Parts via Laser Powder Bed Fusion Process: An Overview. *Int. J. Adv. Manuf. Technol.* 2022, *123*(7–8), 2159–2182. DOI: 10.1007/s00170-022-10314-z.

[40] Arikan, E. S. Oberflächenmodifikation von Polyetheretherketon (PEEK) für das strukturelle Kleben in der Luftfahrt. Dissertation, Universität der Bundeswehr München, 2020.

[41] Davis, G. D. Surface Treatment of Aluminum and Titanium: From Basic Research to Production Failure Analysis. *Surf. Interf. Anal.* 1991, *17*(7), 439–447. DOI: 10.1002/sia.740170706.

[42] Rider, A. N.; Arnott, D. R.; Mazza, J. J. Surface Treatment and Repair Bonding. In Aircraft Sustainment and Repair; Butterworth-Heinemann: Oxford, 2018; pp. 253–323. DOI: 10.1016/B978-0-08-100540-8.00007-8.

[43] Palmieri, F. L.; Crow, A.; Wohl, C. J.; Connell, J. W.; Belcher, M. A.; Blohowiak, K. Y.; Zetterberg, A.; Hopkins, J. Further Investigation into the Use of Laser Surface Preparation of TI-6AL-4V Alloy for Adhesive Bonding. Int SAMPE Tech Conf; Seattle, WA, 2014.

[44] Goland, M.; Reissner, E. The Stresses in Cemented Joints. *J. Appl. Mech.* 1944, *11*(1), A17–A27. DOI: 10.1115/1.4009336.

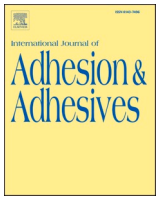
International Journal of Adhesion & Adhesives 142 (2025) 104114



Contents lists available at ScienceDirect

International Journal of Adhesion and Adhesives

journal homepage: www.elsevier.com/locate/ijadhadh



Laser treatment of PBF-LB manufactured Ti6Al4V parts for structural adhesive bonding

Emre Ertürk [a,*], Andreas Wohninsland [b], Jörg Gregor Diez [a], Philipp Höfer [a]

[a] Institute of Lightweight Engineering, University of the Bundeswehr Munich, Neubiberg, Germany
[b] Bundeswehr Research Institute for Materials, Fuels and Lubricants (WIWeB), Erding, Germany

ARTICLE INFO

Keywords:
Adhesive bonding
Additive manufacturing
Surface morphology
Laser treatment

ABSTRACT

Laser powder bed fusion (PBF-LB) processed Ti6Al4V parts exhibit inherent surface roughness features that are generally favorable for structural adhesive bonding. However, previous studies have shown that effective surface treatment of PBF-LB-Ti6Al4V is still crucial to prevent interfacial failure in adhesive bonds. In particular, laser treatment has demonstrated significant potential as a surface preparation process. Therefore, in this work, the effects of laser treatment on the adhesive bond performance of metal-metal joints were investigated for three different laser fluences. Surface characteristics were evaluated using scanning electron microscopy, confocal laser scanning microscopy and ion beam cross-section polishing. Laser-induced residual stresses in the titanium were measured by X-ray diffraction. The quasi-static bond strength was assessed for tensile loading via centrifugal adhesion testing and for mode I loading by double cantilever beam testing. Moreover, the surface treatment effects on environmental durability and fatigue performance were examined through single step-lap joint testing. It was found that the thickness and uniformity of the laser fluence-dependent nanoporous oxide layer are the decisive factors influencing quasi-static and fatigue adhesive bond performance. The laser fluence impact on the bond strengths was found to be significant, however, not for tensile loading. The overall best bond performance was achieved with the highest applied laser fluence, which produced a thicker and highly uniform oxide layer. Compared to the as-built surface state (i.e., degreased PBF-LB-surface), an increase of up to 52 % in tensile bond strength and around 600 % in mode I fracture toughness was achieved with laser treatment. Moreover, the tensile shear bond strength after hydrothermal aging was improved by up to 79 %, and the fatigue lifetimes were significantly enhanced as well.

1. Introduction

Structural adhesive bonding has proven to be a suitable joining method for highly loaded lightweight constructions, as it enables high strength and long-term stable joints while causing significantly lower weight penalties compared to mechanical joining methods [1]. Adhesive bonding of parts fabricated by additive manufacturing (AM) is particularly interesting, since AM allows tailoring the stiffness of the joining partners along the bondline. This can effectively reduce local stress concentrations within the adhesive bond, which are typically caused by large stiffness gradients between the adherends [2].

Laser powder bed fusion (PBF-LB) processed Ti6Al4V parts are extensively used for high-performance applications, such as in aerospace [3]. The surface properties are a decisive factor for the adhesive bond performance. For PBF-LB-Ti6Al4V, the surface morphology is mainly characterized by partially melted particles from the powder bed. Further surface features are created by other process-related effects, such as the "balling" [4] and "stair-step" [5] effects. The resulting morphology varies depending on the process parameters and build orientation [5–8]. Consequently, the surface roughness of as-printed parts ranges from low to very high microscopic roughness. Common practice for AM-metal parts is to remove the inherent roughness by e.g. milling since it is well known that the AM-induced surface roughness deteriorates the parts fatigue performance [9,10]. However, this roughness may be beneficial for adhesive bonding applications. Previous studies [5–7] demonstrated through butt-joint and single step-lap joint (SLJ) testing, that as-built PBF-LB-Ti6Al4V surfaces show comparable adhesive bond strengths to grit-blasted Ti6Al4V surfaces. The as-built condition refers to standard stress relief heat treated PBF-LB-parts with degreased surfaces. The bond strengths were found to correlate with the number of

* Corresponding author.
E-mail address: emre.ertuerk@unibw.de (E. Ertürk).

https://doi.org/10.1016/j.ijadhadh.2025.104114
Received 18 April 2025; Received in revised form 27 June 2025; Accepted 25 July 2025
Available online 26 July 2025
0143-7496/© 2025 Elsevier Ltd. All rights are reserved, including those for text and data mining, AI training, and similar technologies.

partially melted particles on the PBF-LB surfaces. These particles increase the total surface area and create significant mechanical interlocking within the adhesive layer. However, the as-built surfaces lack distinct nanometer-scale roughness, which is known to be highly effective in enhancing adhesion strength and improving the durability of adhesive joints under severe environmental conditions [2]. Fracture analysis of adhesive joints [5,6] revealed that even for as-built Ti6Al4V surfaces with a high density of attached particles, a considerable amount of adhesive (i.e., interfacial) failure occurs. This was observed mainly in areas with few or no attached particles, highlighting that particle-induced mechanical interlocking is the primary adhesion-promoting mechanism for the as-built surfaces. In particle-free areas, the adhesion strength can be limited by the brittle failure of the oxides present on the as-printed and standard stress relief heat-treated PBF-LB-Ti6Al4V surfaces [11]. Another drawback of the as-built surfaces is that long-term stable adhesive joints cannot be achieved, as demonstrated in a previous work [6] by SLJ-testing of hydrothermally aged PBF-LB-Ti6Al4V specimens. Ardila-Rodriguez et al. [7] showed that a combination of sol-gel treatment and primer application is required to achieve durable adhesive bonds on as-built Ti6Al4V surfaces in case of salt-spray aging conditions.

The adhesion on as-built PBF-LB-Ti6Al4V surfaces can be enhanced through suitable surface treatment. In aerospace applications, the bonding preparation of metallic surfaces typically involves anodization processes, such as phosphoric acid anodizing (PAA) [12], to replace weak native oxides on the surface with a pronounced nanoporous oxide layer. However, these electrochemical processes raise environmental concerns due to the use of hazardous chemicals and the generation of harmful waste. As a result, they are increasingly restricted by stringent safety and health regulations like REACH [13]. In contrast, laser processing is a more sustainable method to generate nanoroughness on the surface, with low safety risks and high automation potential [14]. In the literature, investigations on laser treatment of titanium for enhanced adhesive bonding have followed two main approaches. In one part of the studies, laser treatment was used to create distinct microstructures like grooves or dimples on the surface for improved mechanical interlocking, while the other part focused on the generation of a pronounced nanoporous oxide layer. All studies have in common that pulsed lasers are utilized.

Baburaj et al. [15] used an excimer laser for generating microcolumn arrays on flat titanium surfaces. In comparison to unstructured titanium plates, a significant increase in the tensile shear strength of epoxy-bonded specimens was achieved. The enhanced bond strength was attributed to the increased surface area, mechanical interlocking within the microcolumns and improved wettability due to the formation of oxide particles on the surface. Surface micro-texturing using a pulsed fiber laser has also proven effective in improving the peel resistance [16] and mode I fracture toughness [17] of Ti6Al4V/epoxy joints. However, laser surface structuring often induces undesirable effects, such as damage to the bulk material, the formation of pores and thermal stresses [18,19]. Therefore, some studies investigated the use of femtosecond lasers, which significantly reduce laser heat impact and enable higher manufacturing precision of microstructures compared to commonly used nanosecond lasers [20,21]. More recent studies have focused on integrating laser surface structuring directly into additive manufacturing processes like PBF-LB/M, thereby eliminating an additional surface preparation step [22,23]. Since conventional PBF-LB/M manufacturing is conducted under an inert environment, a distinct laser-induced nanoporous oxide layer does not form on the as-printed surfaces [5,6].

The effects of laser-induced nanoroughness on the adhesion behavior of conventionally manufactured Ti6Al4V were investigated by Kurtovic et al. [24], utilizing a pulsed Nd:YVO4 laser. It was shown by floating roller peel tests and wedge tests of Ti6Al4V/epoxy joints, that the laser-generated nanoporous oxide layer can lead to long-term stable adhesion behavior. This improvement can be attributed to an increased surface area, which allows more interfacial bonds to form, and mechanical interlocking of the adhesive within the nanostructured oxide layer. Through X-ray photoelectron spectroscopy, Li et al. [25] provided experimental evidence of Ti-O-C chemical bond formation between laser-induced amorphous titanium oxide and epoxy adhesive, which contributes to the adhesion strength. Regarding the structure of the laser-generated oxide layer on titanium, Löbbecke et al. [26] demonstrated that an open-porous, branched nanostructure allows to achieve durable adhesive joints. Nevertheless, laser treatment of titanium can also cause negative effects, such as defects in the sub-surface region [27] and tensile residual stress [28,29], which can promote crack initiation in the bulk titanium. Another challenge of laser treatment is its tendency to produce an inhomogeneous thick oxide layer on the surface, with more oxide concentrated at the laser pulse edges [6,30]. Due to the less pronounced oxide layer in the laser pulse depressions, oxide layer fracture is likely to initiate in these regions [6].

The authors have shown in previous studies [5,6] that laser treatment of PBF-LB-Ti6Al4V leads to a hierarchical surface morphology, where the inherent surface features from the as-built condition are superimposed with a laser-induced nanostructured oxide layer. This surface morphology was found to be highly effective in metal-metal joints, bonded with an epoxy adhesive and tested under quasi-static and fatigue loading conditions. However, long-term bond durability under hydrothermal aging was not achieved with these surfaces due to fracture of the laser-induced oxide layer. Moreover, fracture analysis of SLJs revealed that at the critically loaded overlap ends, the nanoporous oxide layer fractures locally in areas with no attached powder particles on the surface. To further improve the adhesive bond performance of laser treated PBF-LB-Ti6Al4V surfaces, this work investigated the structural changes induced by laser treatment and their impact on bond performance. This was done for three laser settings with low, medium and high laser power to determine laser fluence-related effects. Surface morphology and subsurface structural changes were analyzed using Scanning Electron Microscopy (SEM), Confocal Laser Scanning Microscopy (CLSM) and Ion Beam Milling (IBM), while laser-induced residual stresses were examined by X-Ray Diffraction (XRD). The adhesion strength under quasi-static conditions was assessed for tensile and mode I loading. Furthermore, laser treatment influences on bond durability and fatigue behavior were evaluated through SLJ-testing.

2. Materials and methods

2.1. Specimen types and substrate manufacturing

Metal-epoxy joints consisting of PBF-LB-Ti6Al4V adherends and the two-component epoxy adhesive Loctite EA9396 AERO were investigated. For assessing the adhesion strength of the bonded joints, centrifugal adhesion testing (CATT) was conducted for tensile loading and DCB testing for mode I loading. The specimen geometries were defined based on DIN EN ISO 4624 [31] for CATT and ISO 25217 [32] for DCB testing. Moreover, SLJ specimens based on DIN EN 2243–6 [33] were used for examining environmental durability and fatigue resistance. The utilized specimen types are depicted in Fig. 1.

The titanium substrates were manufactured on a Trumpf TruPrint 5000 PBF-LB/M printer using standard parameters for Ti6Al4V Grade 23. These parameters include a volumetric energy density of 40.5 J/mm^3, a layer thickness of 60 µm and a 45° stripe pattern as the scanning strategy. The substrates were printed with the bonding surface oriented at 90° relative to the build platform, as shown in Fig. 2. This orientation was chosen, because it represents a surface topography with an average number of attached powder particles compared to 0° and 45° oriented PBF-LB-Ti6Al4V surfaces [6]. The utilized powder has a particle size range of 10–45 µm and fulfills the ASTM F3001-14 [34] specification. Post-processing comprised stress relief heat treatment under vacuum at 840 °C for 2 h, followed by EDM-cutting from the build platform and cleaning in an ultrasonic bath with deionized water to remove loose

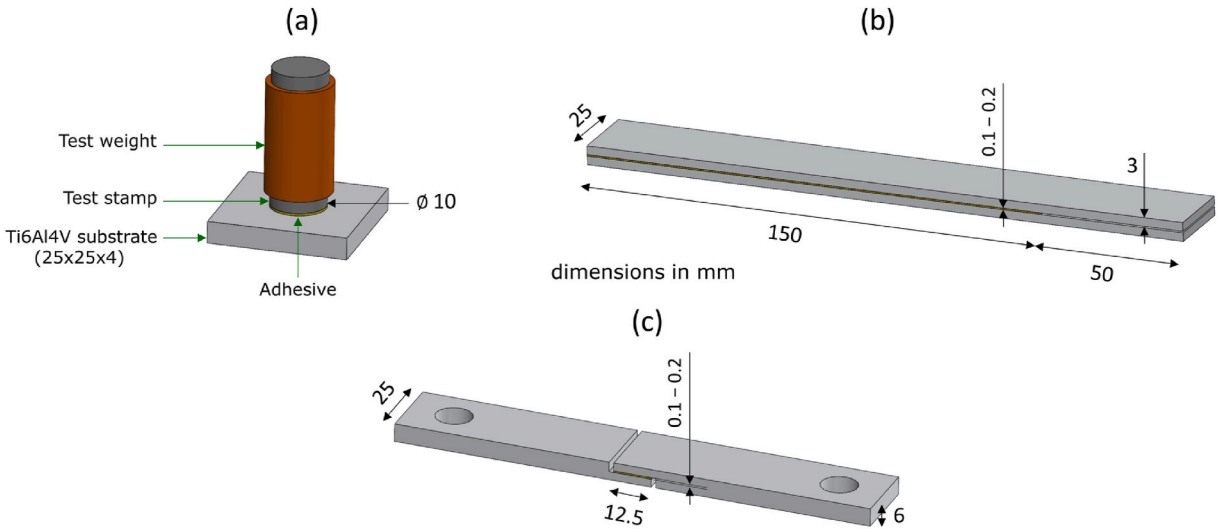


Fig. 1. Specimen types: (a) Centrifugal adhesion testing, (b) DCB testing and (c) SLJ-testing.

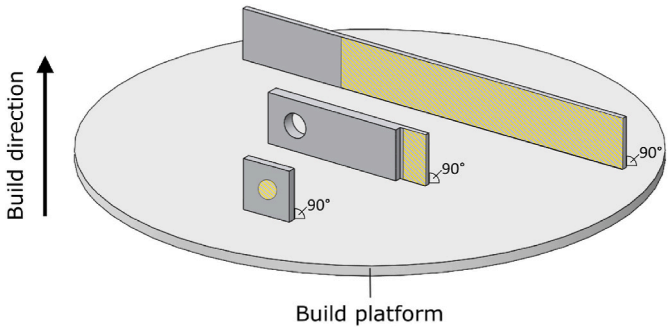


Fig. 2. Build orientation of the specimen substrates during PBF-LB/M-manufacturing. The bonding areas are marked.

particles on the surface. The adhesive layer thicknesses of the bonded joints varied within the range of 0.1–0.2 mm due to the high inherent roughness of the PBF-LB surfaces.

2.2. Surface treatment

Surface pre-treatment of the Ti6Al4V substrates involved degreasing with acetone in an ultrasonic bath, followed by laser treatment. A pulsed Nd:YVO4-Laser (TRUMPF TruMark 6350)) with a wavelength λ of 355 nm and a maximum average output power $P_{max,a}$ of 50 W was used for laser treatment under standard environmental conditions. The laser was equipped on a TRUMPF Trumark Station 5000 marking laser station (TRUMPF, Germany). The applied laser parameters are summarized in Table 1. The parameters pulse frequency f, focused laser spot diameter d and scan speed v were kept constant based on previous investigations [6]. Moreover, the laser scanned once over the entire surface, following a horizontal line pattern with a track spacing e of 30 µm. Only the average output power P_a was varied to assess its effects on the surface morphology of PBF-LB-Ti6Al4V. The power levels 60 %, 70 % and 90 % were investigated, as they generated distinctly different degrees of nanoroughness on the surface. The corresponding laser fluence values E_d were calculated using Eq. (1) and are given in Table 1.

Table 1
Laser parameters: General settings and power level variations.

General laser parameters	$\lambda = 355$ nm, $P_{max,a} = 50$ W, $f = 20$ kHz, $d = 30$ µm, $v = 0.4$ m/s, $e = 30$ µm		
Power level	**60 %**	**70 %**	**90 %**
Average output power P_a	30 W	35 W	45 W
Laser fluence (average) E_d	212 J/cm^2	248 J/cm^2	318 J/cm^2
Sample name	**P60**	**P70**	**P90**

$$E_d = \frac{P_a}{f \cdot A_s} \quad (1)$$

The laser spot area A_s was determined by approximating the beam diameter with the focused laser spot diameter d. Following the laser process, oil-free compressed air was used to remove residual fine dust from the surface.

2.3. Analytical methods

2.3.1. Analysis of surface characteristics

Scanning Electron Microscopy (SEM) was used to characterize the surface morphologies. A Zeiss ULTRA Plus field emission scanning electron microscope (Carl Zeiss, Germany) equipped with a Secondary Electron (SE2) detector and an In-Lens detector was utilized. The accelerating voltage was set to 1 kV. The SE-2 detector was primarily used, while the In-Lens detector served to enhance contrast between the metallic substrate and adhesive residues on the fracture surfaces. To further assist in fracture analysis, Confocal Laser Scanning Microscopy (CLSM) was applied using a Keyence VK-X3000 microscope (Keyence International, Belgium). Furthermore, for analyzing the laser-induced oxide layer thickness and potential structural changes in the surface-near bulk titanium region, Ion Beam Milling (IBM) was performed on cross-sections employing a Hitachi ArBlade 5000 system (12 h at a milling energy of 5 kV). For IBM, small samples of about 10 × 10 mm were cut from the laser treated substrates using a diamond wire-cutting machine. To prevent surface alterations during further preparation, the surfaces were sputtered with gold. The samples were subsequently bonded onto a sample carrier and ground to the final dimensions.

2.3.2. Residual stress measurement

Laser-induced residual stresses in the titanium substrates were measured by X-ray diffraction (XRD) using a Bruker D8 Discover. The $\sin^2\psi$ method [35] was applied with ψ tilts ranging from −60° to 60° with a stepsize of 6°. The XRD-setup included a Cu_Kα radiation source, operated at 40 kV and 40 mA, a poly capillary, a 0.02 mm Nickel filter, a 1 mm collimator and an Eiger500 2D detector. Additional settings comprised a 2θ angle of 139.2° and evaluation of the {213} diffraction plane of α-Ti. Stress calculations were performed using the Bruker Leptos 7.14 software, which includes a predefined material card for

titanium. The Young's modulus was adjusted to the experimentally determined value of 129000 MPa, while for the Poisson ratio the predefined value of 0.32 was used. The measurements were conducted only directly on the surface since the highest induced residual stresses are expected there [28,29]. This was done for the laser treated surfaces and additionally for an untreated surface area as a reference.

2.4. Adhesive joint preparation and aging

The two-component epoxy adhesive Loctite EA 9396 AERO (Henkel, Germany) was used in this study. To minimize defects in the adhesive, mixing was performed at a low atmospheric pressure of 30 mBar in a dual asymmetric centrifugal mixer. The pre-treated Ti6Al4V substrates were then bonded using fixtures designed for each specimen type, ensuring proper alignment. For the CATT specimens, small Ti6Al4V plates were bonded to an aluminum test stamp with a 10 mm diameter (see Fig. 1). To prevent adhesive failure on the test stamp side, the bonding surface of the stamp was laser treated using an optimized parameter set for aluminum. In case of the SLJ and DCB specimens, PTFE inserts were placed prior to bonding in areas that needed to remain free of adhesive. These included the grooves at the overlap ends of the SLJs and the 50 mm long region at the loading end of the DCB specimen. The PTFE film used in the DCB specimens had a thickness of approximately 10 µm. Afterwards, curing was conducted based on recommendations in the adhesive datasheet [36] at 66 °C for 80 min. The CATT and SLJ specimens were cured in a convection oven, while for the DCB samples a hot press was used, since a bonding fixture with steel spacers was utilized to achieve a nominal adhesive thickness of approximately 0.15 mm. In all cases, sufficient contact pressure was applied to ensure complete adhesive contact over the bond area while avoiding excessive adhesive squeeze-out. After curing, excess adhesive was removed from the side faces using sandpaper.

A subset of the SLJ specimens was immersion aged at 60 °C for 30 days in deionized water according to a hydrothermal aging process suggested by Frömmel [37]. This aging process was previously applied by the authors [6] for the same SLJ specimen geometry and materials, where it proved effective in aging Ti6Al4V-epoxy joints. To evaluate the surface-related degradation effects, the specimens were re-dried after aging, as recommended by Arikan [38]. This allowed to mitigate the influence of water-induced plasticization of the adhesive.

2.5. Mechanical testing

CATT was selected because it allows a time- and material-efficient investigation of adhesion strength under uniform tensile loading, while DCB testing was conducted to examine the mode I fracture toughness. Moreover, SLJ-testing was used as a continuation of previous research [6] for assessing adhesive bond durability and fatigue behavior. In contrast to the wedge test, which is commonly used to simulate service disbond behavior [2], SLJ testing was chosen here to allow for direct comparison with non-aged specimens from earlier work [6] and to quantify aging-induced reductions in bond strength. Testing was

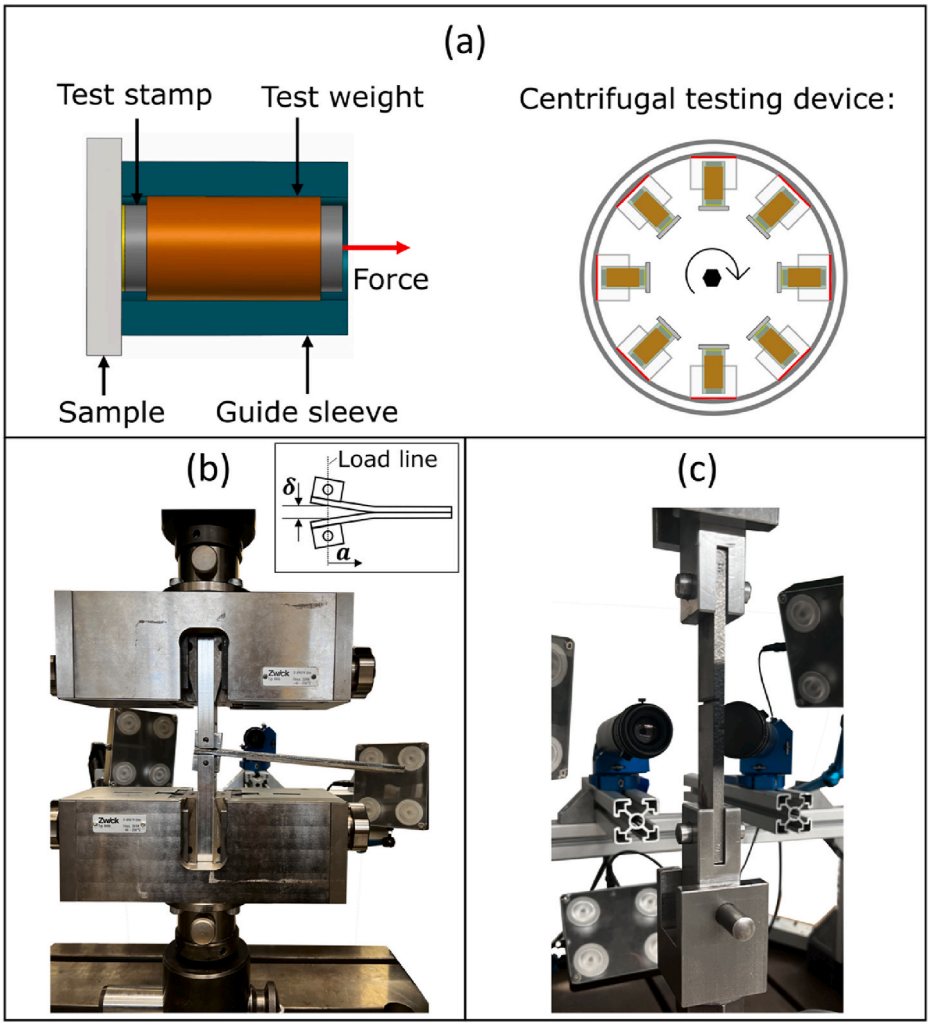


Fig. 3. Testing setups: (a) Centrifugal adhesion testing (CATT), (b) DCB testing and (c) SLJ-testing.

performed for all specimen types under nominal environmental conditions.

The CATT specimens consisted of a Ti6Al4V adherend bonded to a test stamp, onto which a test weight was attached. This assembly was placed in a guide sleeve before being mounted in the centrifugal testing device, as illustrated in Fig. 3(a). In this test method, the adhesive bond is subjected to a uniform tensile load due to the centrifugal force induced by the rotational movement. The load was increased linearly by 20 N/s.

DCB testing was carried out based on ISO 25217 [32] at a speed of 2 mm/min. Before testing, loading blocks were bonded to the loading end of each specimen to facilitate mounting in a Zwick Z150 (ZwickRoell, Germany) universal testing machine (Fig. 3(b)). The crack growth was monitored using a 12 Mpx camera, capturing images at 10 Hz. The image acquisition was synchronized with the force signal of the testing machine. For calculating the mode I fracture toughness values (G_{Ic}), the simple beam theory (SBT) method [39] was used, as recommended by the test standard [32] for stick-slip crack growth. This unstable crack growth was observed in the present work and for some surface types only two crack initiation/arrest points occurred, making it not possible to conduct linear regression used in compliant based data reduction methods, such as the experimental compliance method [39], for G_{Ic} calculation. Following the SBT method, the G_{Ic} values were evaluated as,

$$G_{Ic} = \frac{4P^2}{E_s B^2}\left(\frac{3a^2}{h^3} + \frac{1}{h}\right) \tag{2}$$

where P is the load, E_s is the tensile modulus of the substrate, B is the substrate width, a is the crack length measured starting from the load line and h is the thickness of the substrate. The tensile modulus E_s of PBF-LB-Ti6Al4V was determined to 129000 MPa, by conducting tensile tests according to ASTM A370-19 [40].

The quasi-static SLJ tests were also performed on a Zwick Z150 machine, following the DIN 2243–6 [33] standard. Mounting the SLJ specimens in the testing machine was done by a cardanic suspension. In contrast, the fatigue SLJ tests were conducted on a servo-hydraulic testing machine (Fig. 3(c)). A sinusoidal loading profile with a frequency of 10 Hz and a load ratio of $R = 0.1$ was used, as previously applied in Ref. [6] and recommended by ASTM D3166-99 [41]. Crack growth under fatigue loading was measured using the digital image correlation (DIC) system Q400 (Limess, GmbH, Germany). Two 12 Mpx cameras equipped with macroscopic lenses (80 mm focal length) and distance rings were used to capture a measurement area of around 14 × 10 mm. A speckle pattern was created in this area by using an airbrush spray gun. To precisely track the crack growth within the bondline, the DIC systems functionality to trigger image acquisition at the maxima of the analog cyclic force signal was used. The image acquisition rate was set based on the expected specimen lifetime, ensuring that approximately 300 total images per measurement were recorded. This resulted in acquisition rates ranging from 1 image per 50 cycles to 1 image per 3000 cycles. The determination of the crack tip position was done by analyzing the peel strain field ($\varepsilon_{y,Lgr.}$) calculated by the DIC software, as it is suitable for detecting crack opening [42]. Microscopic evaluation of the crack tip position in a fatigue-loaded specimen before fracture and correlation of the measured crack length to the DIC strain measurement field had shown that a peel strain of 3.8 % marks the crack tip position within the bondline [6]. A minimum of four tests were performed for each surface type (as-built, P60, P70, P90) in each test case.

3. Results and discussion

3.1. Surface morphologies

In the as-built state (i.e., only degreased), the PBF-LB-Ti6Al4V surfaces are characterized by a build orientation-dependent distribution and quantity of partially melted particles from the powder bed. While these particles contribute to roughness on the micrometer scale, no distinct nanoroughness is present on these surfaces. A SEM-image of an as-built surface with 90° build orientation is shown in Fig. 4(a).

Previous studies [5,6] have shown that most of the attached particles adhere strongly to the bulk titanium material, thereby significantly enhancing adhesion by mechanical interlocking. However, local areas without attached particles provide lower adhesion, as neither mechanical interlocking features nor distinct micro- or nanoroughness is present. The native oxide layer on the as-built surfaces was not found to exhibit distinct nanostructures. These particle-free surface regions are therefore prone to adhesive failure. An approach to introduce roughness in these areas while preserving the partially melted particles on the surface is laser treatment. The laser pulse structuring of the surface is illustrated in Fig. 4(b), exemplarily for a 90° oriented PBF-LB-Ti6Al4V surface processed with 70 % laser power. The alternating laser scanning direction and the slightly increased roughness value S_a, obtained from CLSM, is depicted. The effect of laser treatment on the surface topography is shown for different laser power levels in Fig. 5. To better highlight the variations in laser pulse structuring, a higher magnification was used in these SEM images.

Up to a power level of 50 %, no significant changes in surface topography due to the laser treatment were observed. At 60 % power, overlapping laser pulse structures become visible, introducing microroughness, while fine nanoscale structures corresponding to the laser-induced nanoporous oxide layer also begin to form. At 70 % power, both the laser pulse structures and the oxide layer become more pronounced. Further increasing the laser power leads to laser spattering. At 90 % power, the initial laser pulse structures are barely visible, instead a chaotic surface topography has formed characterized by extensive laser spatters. The entire surface is covered with the laser-induced nanoroughness. The power levels investigated in this work (60 %, 70 %, 90 %) represent three distinct surface morphologies, each exhibiting a different degree of laser treatment influence. To further assess the differences in the laser-generated oxide layers, cross-sections prepared via IBM were analyzed. For each oxide layer, SEM analysis was conducted at both the laser pulse edges and within the laser pulse depressions to evaluate variations in oxide layer thickness. The resulting SEM images are presented in Fig. 6. The upper edge of the oxide layer was marked with a red line. The material above consists of deposits formed during the IBM process. To distinguish these deposits from the oxide layer, the sample was coated with a thin gold layer prior to the IBM process.

Nanostructured oxide layers are typically comprised of a thin barrier layer, above which an open-pored nanostructure is formed [2,6]. Laser treatment at 60 % power (P60) resulted in a very thin nanoporous oxide layer, measuring roughly 15–25 nm in thickness. No distinct differences were observed between the oxide layer at the laser pulse edges and within the laser depressions. It should be noted that the oxide layer thicknesses were measured from cross-sectional SE2 images with sufficient contrast between the bulk titanium and oxide. Increasing the power level to 70 % (P70) led to a more pronounced oxide layer, particularly in the laser pulse edge regions, where thicknesses of up to around 100 nm were present. In contrast, the oxide layer within the laser depressions remained considerably thinner than at the laser pulse edges. An inhomogeneous oxide layer distribution was also reported by Schneider and Wrobel [30] for a magnesium alloy treated with a pulsed Nd:YAG Laser. The non-uniform oxide layer thickness is caused by the explosively expanding plasma induced by the laser pulse. The plasma transports ablated material in the form of nanoparticles to the outer areas of the laser-created depressions, where it condenses under reaction with atmospheric oxygen and redeposits on the surface [29,30,43]. The oxide layer created at 90 % power (P90) showed a significantly improved thickness homogeneity. In comparison to P70, the oxide thickness at the laser pulse edges is moderately higher, while the oxide thickness within the laser pulse depressions increased substantially from around 50 nm to 160 nm. It can be assumed that the extensive laser spattering at P90, combined with a larger laser-induced plasma, causes a more uniform oxide layer thickness distribution. Moreover, with

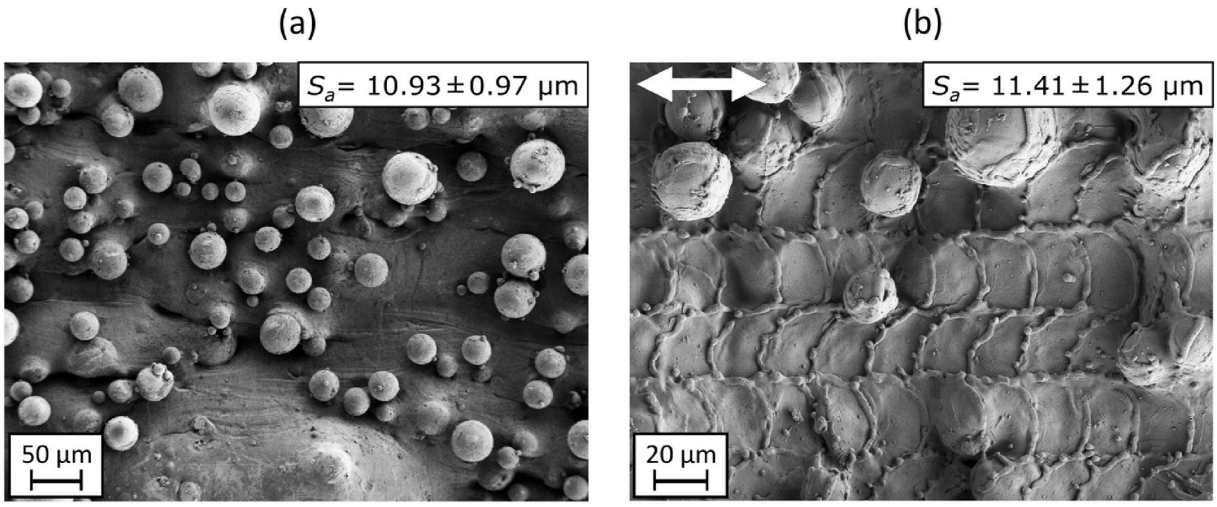


Fig. 4. SEM images of a PBF-LB-Ti6Al4V surface with 90° build orientation in (a) as-built condition (P0) and (b) after laser treatment with P = 70 %.

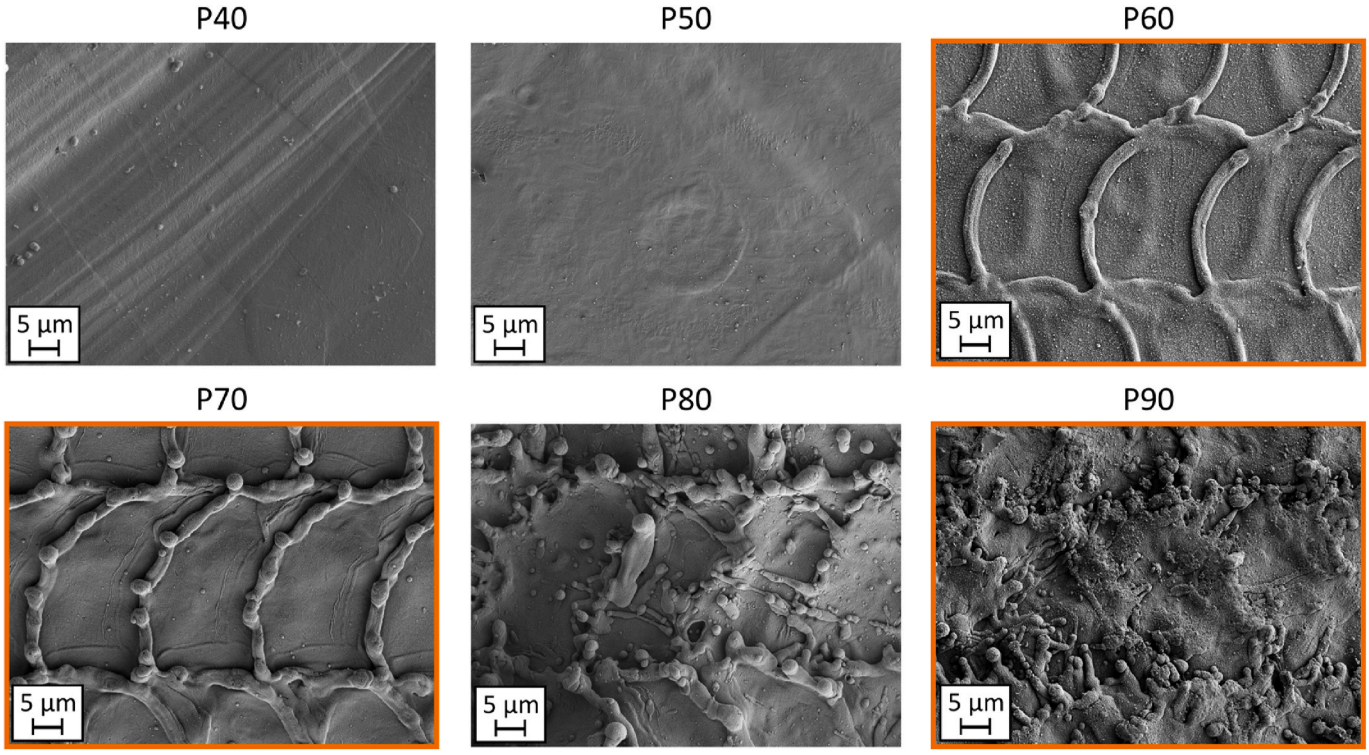


Fig. 5. SEM images of laser treated Ti6Al4V surfaces for different power levels P = 40–90 %. The power levels P60, P70, P90 were further investigated in this work.

increasing laser power, the generated oxide layer exhibits more branched nanostructures and the barrier layer becomes more pronounced.

A similar laser power-dependent oxide layer has formed on the attached particles of the PBF-LB surfaces. This is illustrated exemplarily for a P90 surface in Fig. 7. Only the undercut regions of the particles were found to have no distinct nanoroughness. Thus, the attached particles significantly increase the surface on which the nanoroughness is formed.

The macroscopic wettability of laser treated PBF-LB-Ti6Al4V surfaces was found to be excellent, as demonstrated by contact angle measurements in a preceding study [5]. The nanoscale pores contribute to the high wettability by inducing strong capillary forces [2]. Furthermore, cross-sectional SEM analysis in Ref. [6] confirmed that the applied epoxy adhesive can fully fill the nanoscale pores of the laser-induced oxide layer on PBF-LB-Ti6Al4V.

Laser-generated structural damage was not observed in the bulk titanium material for all three laser fluences. Kurtovic [29] reported, based on cross-sectional SEM analysis, that laser treatment can cause a locally refined grain microstructure in the subsurface region of conventionally manufactured Ti6Al4V. For the laser treated surfaces in this work, no distinct microstructural changes were found in the IBM-prepared cross-sections.

The XRD measurements revealed that laser treatment induces tensile stresses in the surface-near area of PBF-LB-Ti6Al4V. In the as-built surface condition, a maximum principal residual stress of 23.6 ± 3.3 MPa was measured. After laser processing, this residual stress increased in correlation with the laser power to 35.2 ± 3.4 MPa for P60, 51.1 ± 3.7

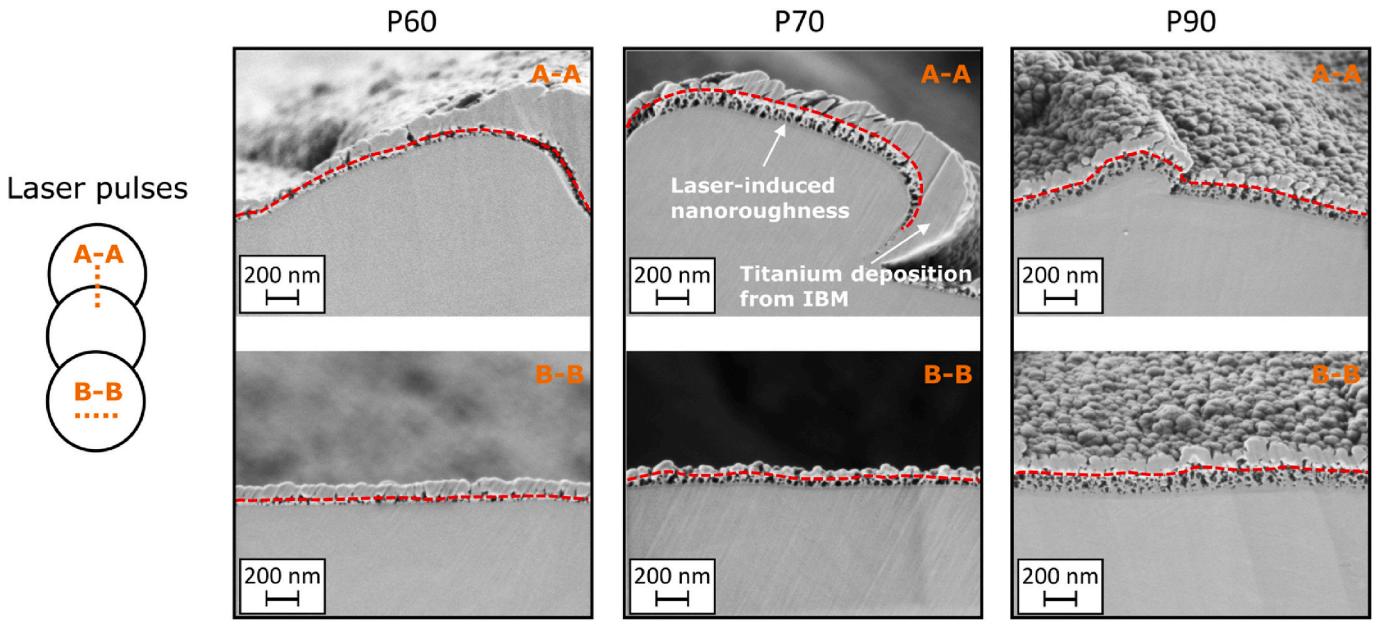


Fig. 6. SEM images of IBM-prepared cross-sections of laser treated Ti6Al4V surfaces for the power levels (a) P60, (b) P70 and (c) P90, evaluated at the laser pulse edge (A–A) and the laser pulse depression (B–B).

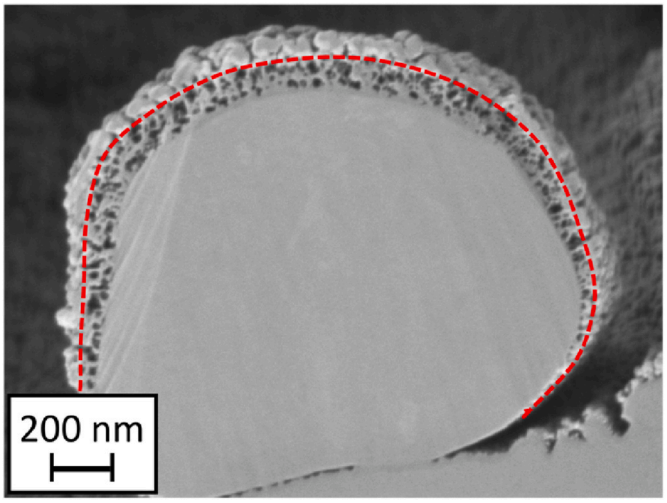


Fig. 7. SEM image of an IBM-prepared cross-section of the laser treated Ti6Al4V P90 surface, showing oxide formation on a partially melted particle.

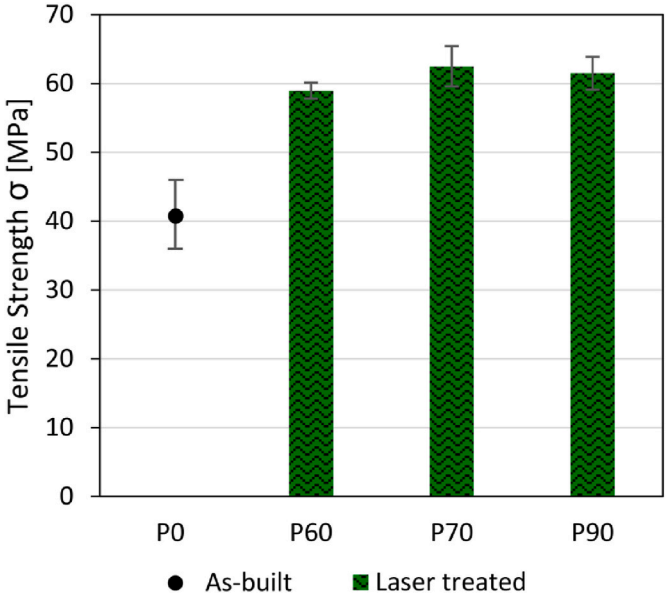


Fig. 8. Tensile bond strengths obtained from CATT, shown for the laser treated surfaces and the as-built surface as a reference.

MPa for P70 and 69.7 ± 5.2 MPa for P90. While these tensile stresses are relatively low compared to those in non-heat-treated PBF-LB-processed parts, they may still contribute to crack initiation in the bulk titanium material [28]. Therefore, laser treatment should only be conducted in areas used for adhesive bonding, since failure in these areas is expected to occur within the adhesive or at the interface rather than in the substrate.

3.2. Quasi-static loading

3.2.1. Tensile loading

The tensile bond strength results obtained from CATT are presented in Fig. 8 for the investigated laser power levels P60, P70 and P90. In addition, the result for an as-built PBF-LB-Ti6Al4V surface with the same build orientation (90°) is depicted as a reference (P0).

A similar tensile bond strength was found for all three laser power levels, with P60 exhibiting only a slightly lower strength. Compared to the as-built surface, laser treatment resulted in an increase of at least 43 % in bond strength. This shows that the laser-induced nanoroughness enhances adhesion in all three cases and is highly effective under tensile loading. Even the very thin oxide layer (15–25 nm) created in P60 resulted in a significant increase in tensile bond strength. Moreover, the test results of the laser treated surfaces showed low standard deviations, indicating high process quality and reliability for adhesive bonding. Fracture surface analysis proved that for P70 and P90, a fully cohesive failure in the adhesive was achieved, whereas for P60, a low amount of oxide layer fracture occurred in regions with few or no attached partially melted particles. The lack of particles causes higher loading of the oxide layer, which leads to the observed local oxide failure.

3.2.2. Mode I loading

DCB-testing according to ISO 25217 [32] involves the introduction of a precrack in the adhesive bond followed by crack propagation under mode I loading. A precrack of about 5 mm was created in the specimens with as-built and P60 surfaces. However, for the P70 and P90 surfaces, precracking was not possible due to highly unstable crack growth. As a result, these surfaces were tested directly from the end of the PTFE insert. The resulting load-displacement curves are shown in Fig. 9 for one representative specimen per surface type to remain clarity. The crack mouth opening displacement δ is plotted in this graph, representing the relative separation between the adherends at the load line (see Fig. 3(b)). Evaluation of δ was done based on the crosshead displacement of the testing machine. To account for mechanical clearance in the test setup, the crosshead displacement was corrected by visually identifying the onset of adherend separation using a 12 MPx camera, which was synchronized with the displacement signal of the testing machine.

For the laser treated surfaces, a stick-slip crack growth was observed, which is characterized in the load-displacement curves by repeating load drops and reloading phases. Particularly for the P70 and P90 surfaces, a highly unstable crack growth is evident. With both surfaces, a similar maximum load was reached, which is significantly higher compared to P60. In contrast, the as-built surface induced a stable crack growth, but generally at a lower load level than the laser treated surfaces. The specimens with as-built surface displayed primarily adhesive failure, while cohesive failure within the adhesive occurred only around the attached particles due to mechanical interlocking (Fig. 10(a)). For the surfaces pre-treated at low laser fluence (P60), SEM analysis revealed extensive fracture of the oxide layer (Fig. 10(b)). Almost no residues of the laser-induced nanoporous oxide structures were visible in the adhesive-free fracture areas, indicating failure near the substrate-oxide interface. Interestingly, the oxide layer remained intact during the two pronounced load drop phases ($\delta \approx 6$ mm, $\delta \approx 13.2$ mm). In these phases, the crack propagated abruptly within the adhesive layer. Thus, it can be assumed that the brittle behavior of the used EA 9396 adhesive caused the high load drops during the stick-slip crack growth. This adhesive has no distinct filler materials, rendering it more susceptible to unstable crack propagation. During the subsequent reloading phases, the crack growth transitioned back to a slow propagation through the oxide layer (Fig. 10(b)).

In contrast, complete cohesive failure within the adhesive was achieved with the medium (P70) and high (P90) laser fluence processed surfaces (Fig. 10(c–d)). The thicker oxide layer of P70, compared to P60, was found to be sufficient for preventing oxide fracture, despite exhibiting an inhomogeneous thickness distribution. Increasing the oxide layer thickness and developing more branched nanostructures enlarged the available surface area for adhesive bonding and enhanced mechanical interlocking within these structures. These factors collectively reduce the stress concentration at the substrate-oxide interface and thereby preserve its structural integrity. Since the crack propagated entirely within the adhesive layer, stress whitening zones can be seen on the fracture surfaces of P70 and P90, which mark the areas corresponding to the (re-)loading phases, where locale plastic deformation of the adhesive occurred.

The average mode I fracture toughness values were determined by evaluating G_{Ic} at several crack lengths between 37.5 and 125 mm and averaging it for each specimen. Across this crack length range, G_{Ic} remained either mostly constant or increased moderately with advancing crack length, as shown exemplarily in Fig. 11(a) for one specimen per surface type. For specimens exhibiting stick-slip crack growth (P60–P90), the number of G_{Ic} evaluation points was limited by the number of observable load drops. In these cases, the evaluation was conducted at the crack initiation points (i.e., start of the load drops), as recommended by Blackman et al. [44]. A comparison of the average mode I fracture toughness and the maximum load reached during testing is illustrated in Fig. 11(b) for the investigated surface types. It is important to note that the depicted average G_{Ic} values for P60-P90 represent an overall measure of fracture toughness rather than a steady-state value, as fracture toughness increased moderately with crack length in these cases with unstable crack growth. Furthermore, for the as-built and P60 surface, the maximum load from the precracking phase is depicted, since the load values during the subsequent crack propagation phase in DCB testing were significantly lower (see Fig. 9).

The lowest average G_{Ic} value ($\approx$144 J/m^2) was found for the as-built surface, which can be explained by the predominant oxide fracture on the surface. Upon application of the laser pre-treatment, the fracture toughness increased significantly due to a shift in the failure mode towards more cohesive failure within the adhesive. The very thin laser-induced nanoporous oxide layer (P60) already enhanced the average G_{Ic} by about 225 %, while for P70 and P90 an even greater improvement of around 600 % was achieved. The G_{Ic} values determined for P70 and P90 correspond to the fracture toughness of the used epoxy adhesive, as complete cohesive failure in the adhesive occurred for these surfaces. The beneficial effect of the laser treatment is also reflected in the maximum load reached under mode I loading.

Visual inspection after testing revealed no indications of plastic

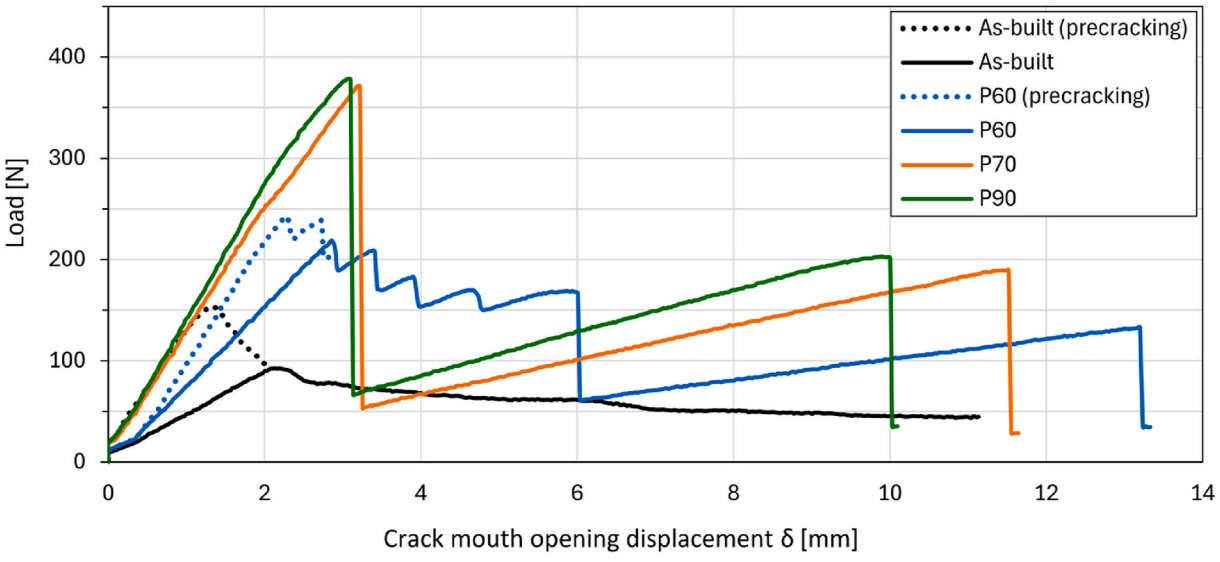


Fig. 9. Load-displacement curves obtained from DCB-testing for the as-built and laser treated surfaces.

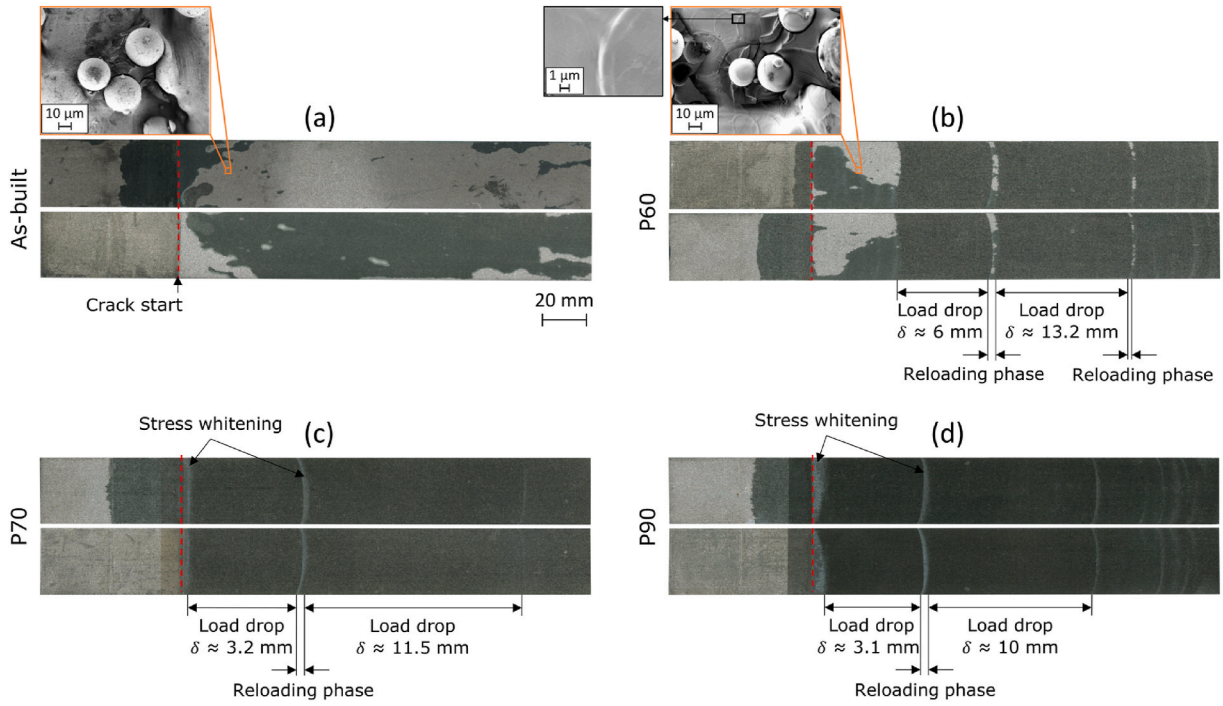


Fig. 10. Fracture surfaces of the DCB-specimens with (a) as-built, (b) P60, (c) P70 and (d) P90 surfaces. The regions corresponding to the crack start, load drop and reloading phases are marked.

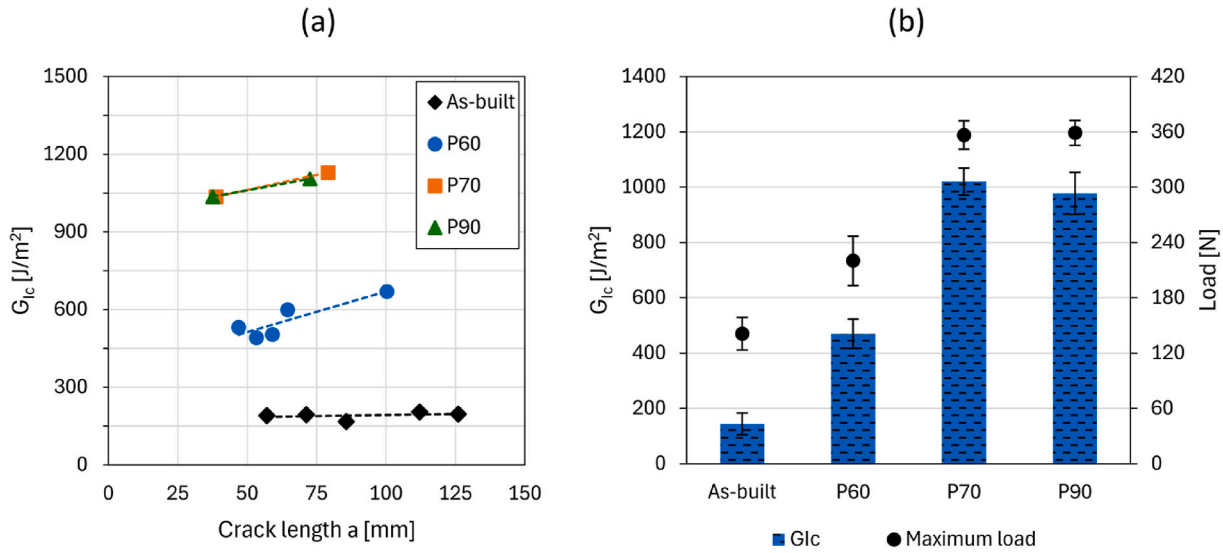


Fig. 11. (a) Mode I crack growth resistance curves and (b) average mode I fracture toughness G_{Ic} and maximum load during DCB-testing, shown for the laser treated surfaces and the as-built surface as a reference.

deformation of the DCB-adherends. In addition, a calculation of the maximum bending stress in the adherends using Euler–Bernoulli beam theory [45] resulted in stress values up to approximately 200 MPa, which is below the measured yield strength of 944 MPa for the PBF-LB Ti6Al4V material, obtained from tensile testing. Thus, it can be assumed that the titanium adherends remained in the elastic regime during DCB-testing.

3.3. Environmental durability

The tensile shear bond strengths after hot-wet aging obtained from quasi-static SLJ-testing are depicted in Fig. 12 for the three investigated laser fluences, along with the as-built PBF-LB-Ti6Al4V surface (P0) for comparison. Bonding with the laser treated surfaces resulted in a 27–79 % higher tensile shear bond strength after hydrothermal aging than with the as-built surface. The bond durability was found to enhance with increasing laser power, especially between P70 and P90. Evaluation of the SLJ fracture surfaces was conducted preferably at the overlap start of the fractured substrates (i.e., close to step geometry of the substrate), as this region exhibited fewer adhesive residues compared to the overlap end (i.e., free end of the substrate), allowing a more precise analysis of the failure mode. On the P60 surfaces, a large amount of oxide layer failure was observed across the entire bonding area of the SLJ (Fig. 13 (a)). This failure can be attributed to the low hydrothermal resistance of the very thin oxide layer in P60. Adhesive residues were primarily found near partially melted particles, where mechanical interlocking occurred.

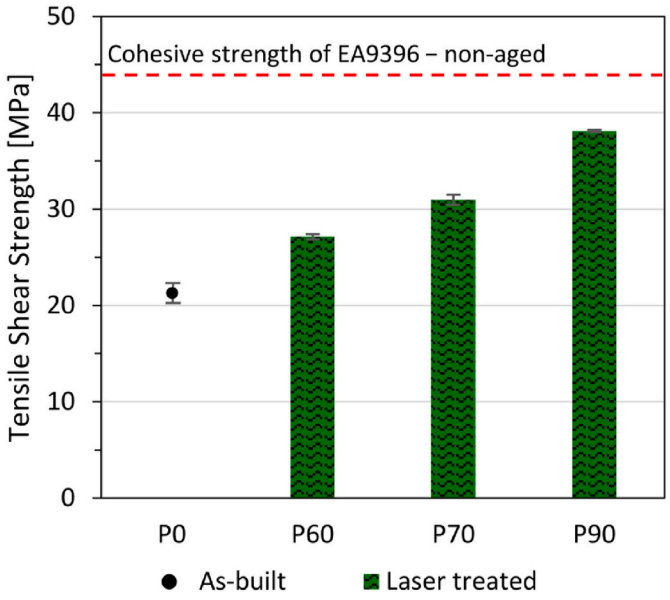


Fig. 12. Tensile shear bond strengths after hot-wet aging, shown for the laser treated surfaces and the as-built surface as a reference. The cohesive strength of the EA 9396 adhesive in the non-aged SLJ [6] is depicted.

For P70, more cohesive failure in the adhesive was observed, particularly in the laser pulse edge regions. In contrast, within the laser pulse depressions, predominantly oxide layer fracture was found, likely due to the less distinct oxide layer in these areas. An almost completely cohesive failure in the adhesive was achieved with P90 (Fig. 13(c)). Partial oxide fracture was present only at the overlap ends of the SLJ. Thus, the thicker and more uniformly distributed oxide layer on P90 was highly effective in minimizing oxide layer fracture. It should be noted that the bond performance differences between the laser treated surfaces are more pronounced in the hydrothermally aged SLJs compared to the investigated uniform tensile and mode I loading conditions.

Previous SLJ-testing had shown that the tensile shear bond strength of P70 in the non-aged condition amounts to around 44 MPa with complete cohesive failure in the adhesive as failure mode [6]. This shows that at best 86 % of the bond strength could be preserved in case of P90 after hydrothermal aging. Considering that the P90 specimens exhibited almost complete cohesive failure within the adhesive, the reduced bond strength can primarily be attributed to the aging of the adhesive itself. A minor improvement in bond strength may still be possible, as localized fracture of the oxide layer could not be entirely avoided.

3.4. Fatigue loading

Fatigue SLJ-testing was conducted at different load levels for the P60, P70, and P90 surfaces in non-aged condition. The as-built surface (P0) was only tested at one load level, as its tensile shear bond strength is significantly lower compared to the laser treated surfaces [6]. The applied maximum stress σ_{max} and the corresponding lifetime results are shown in a semilogarithmic representation in Fig. 14. Specimens that exceeded 10^7 cycles without failure are indicated as run-outs with an arrow.

Bonding with the laser treated surfaces resulted in substantially higher lifetimes than with the as-built surface. Among the laser processed specimens, P60 generally exhibited lower fatigue lifetimes compared to P70 and P90. The difference was found to be larger at lower fatigue loads, demonstrating higher influence of laser treatment towards the high-cycle fatigue (HCF) regime ($> 10^5$ cycles). Moreover, the medium (P70) and high (P90) laser fluence processed surfaces showed similar fatigue resistance. At a maximum load level of 18.4 MPa, the lifetime achieved with P90 is slightly lower than with P70, whereas in the HCF regime, P90 tends to offer slightly better fatigue resistance.

Fracture surface analysis revealed that, regardless of the applied fatigue load level, bond failure occurred for the P60 and P70 surfaces mainly due to fracture of the laser-induced oxide layer, as shown by SEM images in Fig. 15(a) and (b), exemplarily for the load level 18.4 MPa. These images were taken at the overlap start of the fractured substrates. The detail views confirm that no distinct oxide layer residues are present. However, a very thin layer of adhesive residues remains partially on the surfaces. For P70, more of these adhesive residues were observed than for P60. Furthermore, in areas where oxide layer fracture occurred, the partially melted particles also mostly detached from the surface. In contrast, the thicker and more homogeneous oxide layer on the P90 surface remained intact, thereby preserving the attached particles and enabling fully cohesive failure in the adhesive (Fig. 15(c)). The particle-induced interlocking effect in the adhesive is visible in this SEM image.

The lower lifetimes obtained with the P60 surface can be attributed to its thinner oxide layer, which makes it more prone to oxide fracture. For all laser treated surfaces, no distinct laser induced structural changes in the sub-surface region were detected that could lower the lifetime of the adhesive bond. Laser-induced tensile residual stresses were also not found to deteriorate fatigue behavior in the bonded regions. Moreover, the high microroughness created by extensive laser spattering on P90 was not observed to negatively affect the fatigue behavior. Therefore, it can be stated that the thickness and uniformity of the laser-induced oxide layer are decisive for the fatigue performance. Interestingly, although oxide layer fracture occurred for P70, its fatigue lifetime at 18.4 MPa was slightly higher than that of P90. This indicates that at high load levels, the crack propagation through the oxide layer results in a similar fatigue resistance as the crack advancing through the adhesive

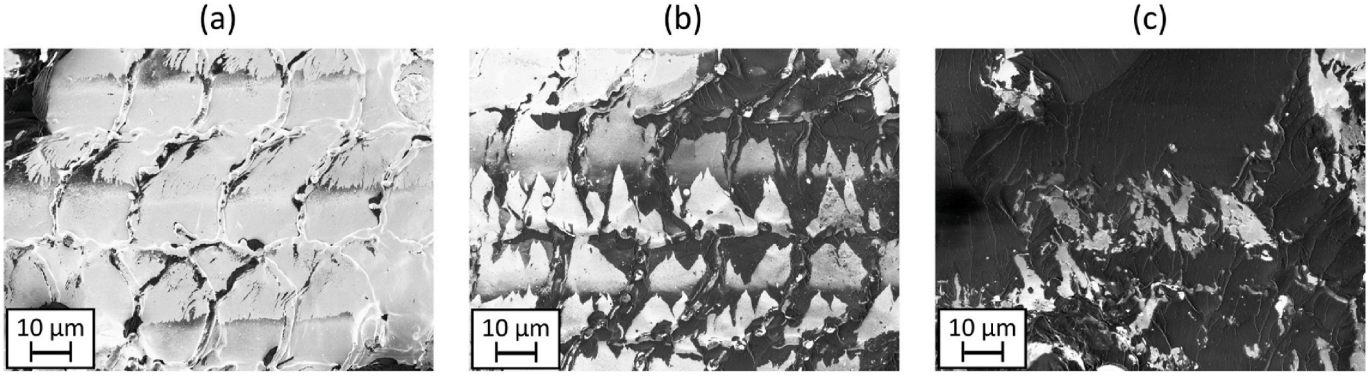


Fig. 13. Fracture surfaces of hot-wet-aged and quasi-statically tested SLJ specimens with (a) P60, (b) P70 and (c) P90 laser treated surfaces, evaluated by SEM with an In-Lens Detector.

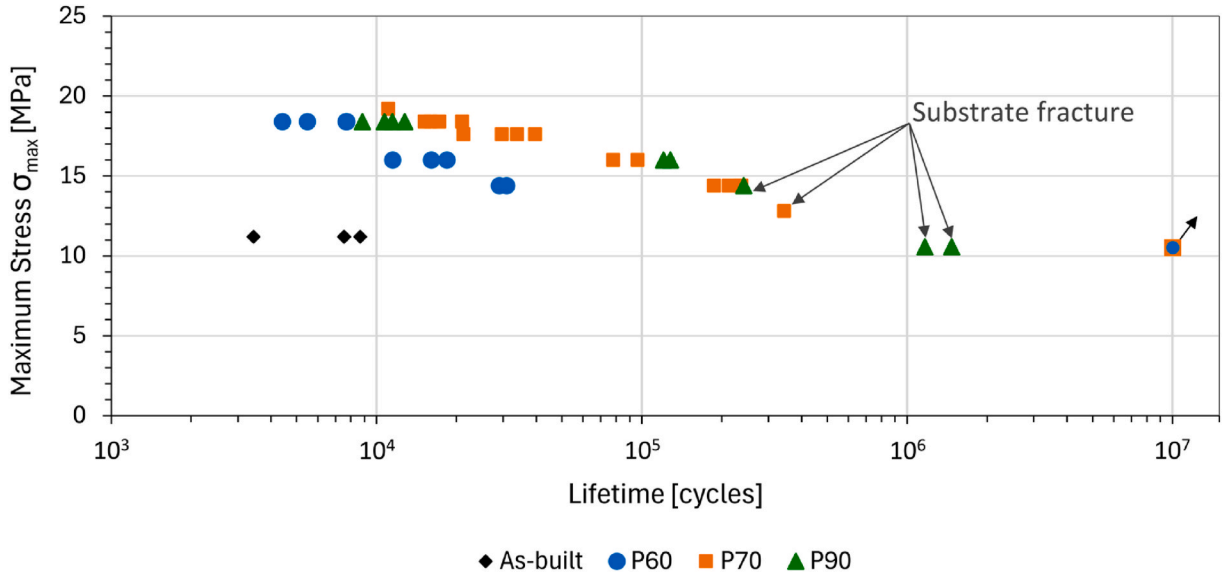


Fig. 14. S–N data of SLJ specimens, shown for the laser treated surfaces and the as-built surface as a reference.

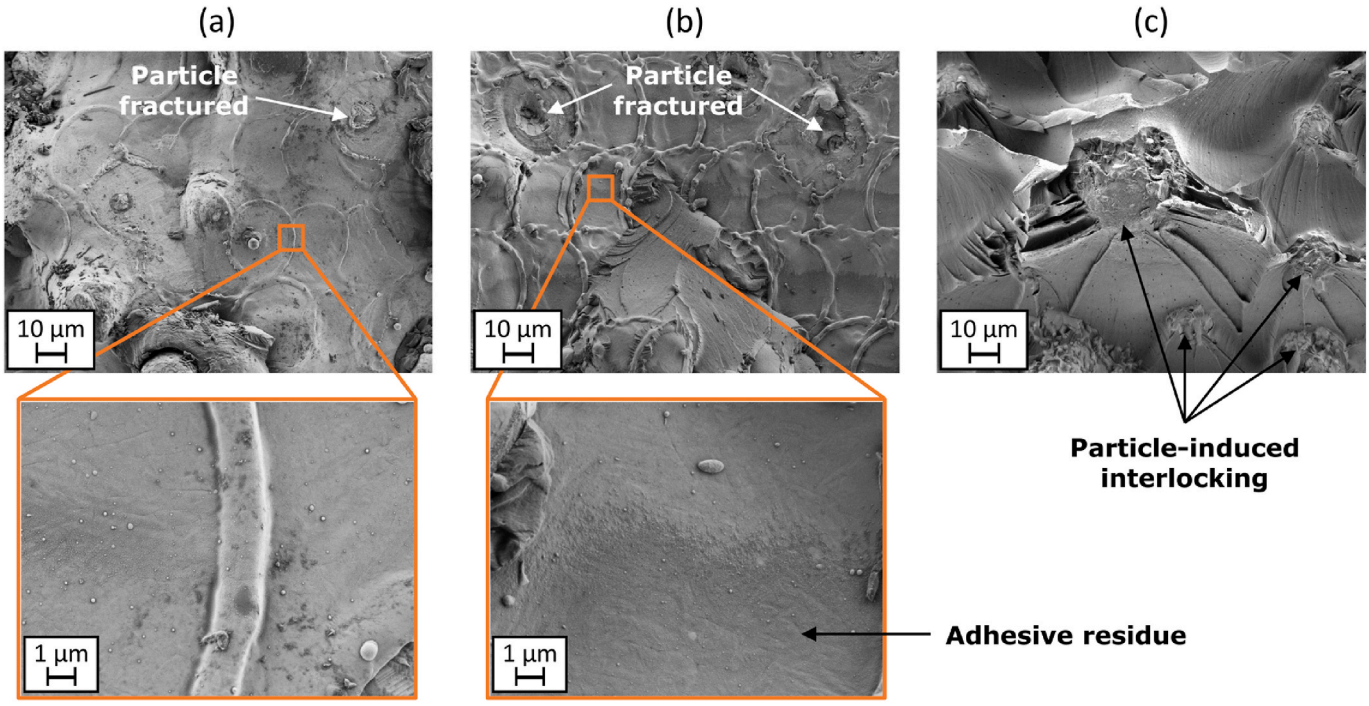


Fig. 15. Fracture surfaces of fatigue-loaded SLJ specimens with (a) P60, (b) P70 and (c) P90 laser treated surfaces, evaluated by SEM for σ_{max} = 18.4 MPa.

layer in P90. A possible reason is that in P70, the crack propagates closer to the titanium surface and is therefore directly influenced by the attached particles, whereas in P90, the crack mainly advances through the adhesive layer, hence mostly above the particles. The attached particles on PBF-LB-Ti6Al4V were found to be highly effective in the low-cycle fatigue (LCF) regime by inducing plastic deformations in the adhesive through interlocking and altering the crack growth [6]. However, in the HCF regime, the influence of these particles diminishes due to predominantly elastic deformation in the adhesive, which reduces the effectiveness of the particle-induced mechanical interlocking. Consequently, the primary contribution to fatigue resistance in HCF can be attributed to the laser-induced nanoporous oxide layer. This would explain the slightly longer fatigue lifetimes observed for P90 in HCF.

The evaluation of the adhesive bond fatigue behavior in HCF was limited due to fracture of the titanium substrate, which was caused by the bending load present in SLJ-testing [46]. This failure occurred only within a certain load range, depending on the surface type, and was located at the edge of the stepped specimen geometry, perpendicularly to the load axis. Previous fatigue tests using the same SLJ specimen types [6] demonstrated that the surface roughness at the step edge promotes substrate fracture in the unbonded region. The detrimental effect of surface roughness on the fatigue behavior of the titanium substrate is also evident when comparing the fatigue test results at a load level of 10.6 MPa. While P60 and P70 passed 10^7 cycles, P90 failed significantly earlier due to substrate failure. The highly unstructured surface topography on P90, caused by extensive laser spattering, is likely to be the main reason for the lower lifetime of the titanium part.

3.4.1. Crack growth

In fatigue-loaded SLJ specimens, two macroscopic crack paths initiate at the overlap ends. In the following analysis, the crack growth results are presented for one crack path, as both crack fronts showed a similar behavior. Fig. 16 presents the crack initiation and propagation data obtained by DIC for different maximum fatigue stress levels. A crack length of 6.25 mm indicates the complete failure of the adhesive bond.

Crack initiation occurred considerably later for P90 at all applied maximum stress levels, while P60 and P70 exhibited similar crack initiation lifetimes. This shows the differences between crack initiation in the oxide layer (P60, P70) and in the adhesive layer (P90). A negative influence of the high microroughness of P90 on crack initiation was not observed. Relative to the total lifetime, the crack propagation phase accounts for the largest proportion. In most cases, the crack propagation is characterized by a gradual slowdown in crack growth until a surface-dependent critical crack length is reached, at which point unstable crack propagation begins. For higher laser powers applied during surface treatment, the cracks in the bond generally propagated more slowly, and the critical crack length was in most cases higher. These results demonstrate how increasing the laser-induced oxide layer thickness and improving its uniformity can delay crack initiation and slow down crack propagation by preventing oxide layer fracture.

The slower crack growth behavior of P90 compared to the other laser treated surfaces was more pronounced at lower fatigue load levels, highlighting the importance of a strong laser-induced oxide layer in HCF. In contrast, at the maximum stress level of 18.4 MPa (Fig. 16(a)), the cracks propagating through the oxide layer (P70) were more effectively slowed down than the cracks advancing through the adhesive layer in P90. This demonstrates the beneficial influence of the attached particles in LCF. However, this positive effect is limited by the onset of unstable crack growth, which occurred early for P60 due to its weak oxide layer, resulting in lower lifetimes. Thus, it can be stated that the laser-induced oxide layer is also crucial for the fatigue performance in LCF and is further supported at high fatigue loads by the partially melted particles on the surface.

4. Conclusions

The effects of laser treatment on the adhesive bond performance of PBF-LB-Ti6Al4V joints were investigated for three different laser fluence settings, which produced differently pronounced nanoporous oxide layers on the surface: a uniform, thin oxide layer (P60), a non-uniform thick/thin oxide layer (P70) and a uniform, thick oxide layer but with extensive laser spattering on the microscale (P90). In all cases, a hierarchical surface morphology was created, consisting of the inherent attached powder particles of the PBF-LB process superimposed with the oxide layer generated by the laser treatment. The main results are summarized as follows:

- Under uniform tensile loading, all laser treated surfaces exhibited high and similar adhesion strength. The bond strengths were at least 43 % higher compared to the as-built PBF-LB surface. The low influence of the applied laser fluences on the tensile bond strength can be attributed to the uniform loading of the adhesive bond in these tests. In contrast, the high stress concentrations present in the DCB- and SLJ-tests caused locally severe loading of the laser-induced oxide layer, revealing significant differences between the applied laser fluences.
- Mode I loading caused extensive fracture of the oxide layer on the P60 surface, resulting in a comparatively low critical fracture toughness (G_{Ic}). The thicker oxide layer of P70 was able to withstand the applied load, despite its inhomogeneous thickness. This led to complete cohesive failure within the adhesive layer, which was also observed for P90. In comparison to the as-built surface, the average G_{Ic} value increased by approximately 225 % for P60 and by around 600 % for both P70 and P90.
- The environmental durability of SLJs under hydrothermal aging was found to improve with increasing laser fluence. The thicker and more uniform oxide layer of P90 significantly reduced oxide layer fracture, resulting in a substantial increase in tensile shear bond strength after aging by up to 40 % compared to the other laser treated surfaces and 79 % relative to the as-built surface.

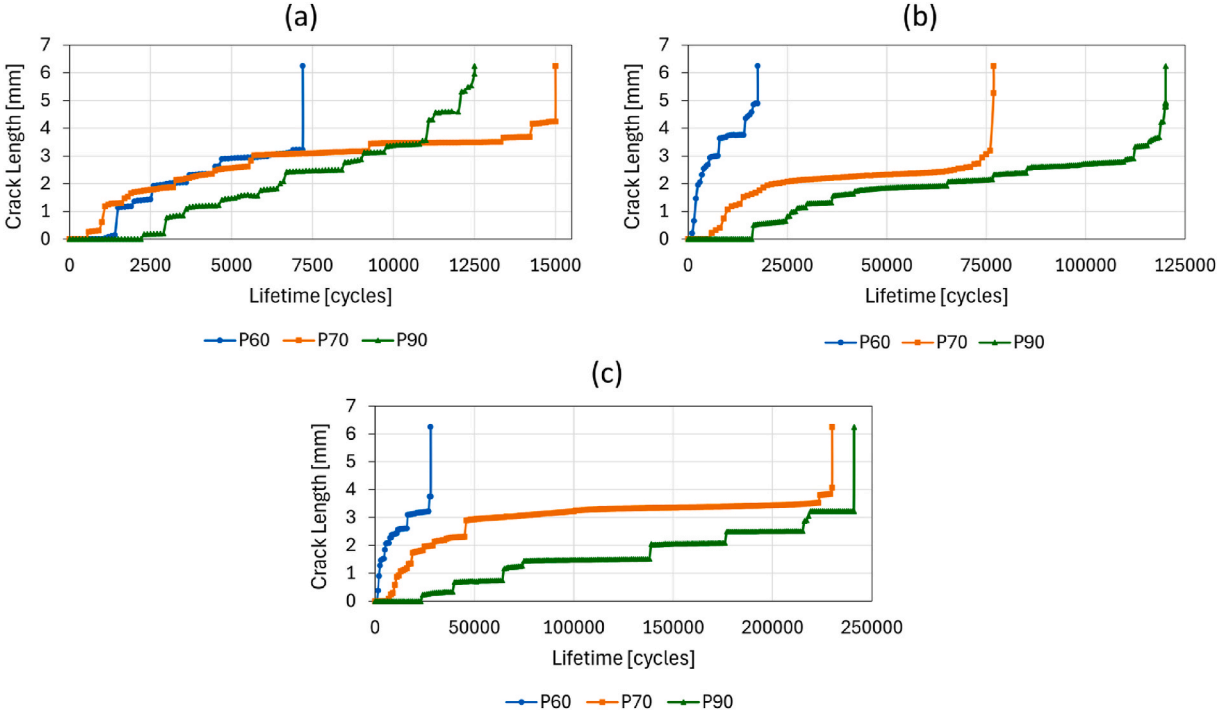


Fig. 16. Crack growth in the fatigue-loaded SLJs with laser treated surfaces evaluated by DIC for the applied maximum stress σ_{max} of (a) 18.4 MPa, (b) 16 MPa, (c) 14.4 MPa.

- Fatigue SLJ-testing revealed that the most critical laser treatment influence on the fatigue bond performance is the thickness and uniformity of the oxide layer. Neither laser-induced damage nor distinct microstructural changes in the titanium were found for the applied laser fluences. Moreover, the laser-generated increases in near-surface tensile residual stresses and microroughness were not observed to cause earlier fatigue failure of the adhesive bond. However, in the unbonded regions, the combination of elevated tensile residual stresses and pronounced microroughness created by extensive laser spattering (P90) was found to significantly reduce lifetime in HCF through titanium substrate fracture.
- In general, lower fatigue lifetimes were obtained with P60 compared to P70 and P90. This difference became more pronounced towards the HCF regime, highlighting the increased influence of the laser-induced oxide layer at lower fatigue loads. The medium (P70) and high (P90) laser fluence processed specimens exhibited similar fatigue resistance, despite showing different failure modes. Mainly oxide layer fracture occurred in P70, whereas complete cohesive failure in the adhesive was reached with P90 for all applied fatigue loads. In LCF, P70 showed an even slightly better fatigue performance than P90. This can be attributed to the beneficial influence of the attached particles in LCF [6], which was more pronounced in P70 since the cracks propagated significantly closer to the particles because of the oxide fracture. The mechanical interlocking effect of the particles diminishes at lower fatigue loads due to the absence of significant plastic deformations, leaving the laser-induced nano-roughness as the main contributor to fatigue resistance in HCF.
- Strengthening the oxide layer with increasing laser fluence resulted generally in a later crack initiation, slower crack propagation and postponed onset of unstable crack growth during fatigue loading.

In future studies, wedge tests should be conducted to investigate the environmental durability of the adhesive bonds under service-like conditions. Moreover, applying a recently developed experimental method, combining adhesive bond testing in SEM with DIC-based strain measurement [47], could provide valuable insights into local failure mechanisms, particularly within the oxide layer.

CRediT authorship contribution statement

Emre Ertürk: Writing – original draft, Conceptualization, Methodology, Investigation, Formal analysis, Validation, Visualization. **Andreas Wohninsland:** Writing – review & editing, Investigation. **Jörg Gregor Diez:** Writing – review & editing, Investigation. **Philipp Höfer:** Writing – review & editing, Supervision, Funding acquisition.

Declaration of competing interest

The authors declare that they have no known competing financial interests or personal relationships that could have appeared to influence the work reported in this paper.

Acknowledgements

This work is part of the research project BLANCA, which was funded by logo of the Bavarian Ministry of Economic affairs, Regional development and Energy (StMWi) within the program BayLu-25. We thank the project partner Modell-und Formenbau Blasius GERG GmbH, for printing the substrates. The authors also thank the Institute of Materials Science (University of the Bundeswehr Munich) and the Bundeswehr research institute WIWeB for providing access to their laboratory equipment.

Data availability

Data will be made available on request.

References

[1] Adams RD. Adhesive bonding: science, technology and applications. Cambridge: Woodhead Publishing; 2021. https://doi.org/10.1016/C2019-0-00395-0.
[2] da Silva LFM, Öchsner A, Adams RD, editors. Handbook of adhesion technology. Berlin, Heidelberg: Springer; 2018. https://doi.org/10.1007/978-3-319-55411-2.
[3] Cao S, Zou Y, Lim CVS, Wu X. Review of laser powder bed fusion (LPBF) fabricated Ti-6Al-4V: process, post-process treatment, microstructure, and property. Light. Adv Manuf 2021;2:20. https://doi.org/10.37188/lam.2021.020.
[4] Zhang LC, Attar H. Selective laser melting of titanium alloys and titanium matrix composites for biomedical applications: a review. Adv Eng Mater 2016;18:463–75. https://doi.org/10.1002/adem.201500419.
[5] Ertürk E, Musil B, Diez G, Felber C, Höfer P. Surface morphology influences of PBF-LB manufactured Ti6Al4V parts on adhesive bond strength – investigation of as-built and surface-treated conditions. Prog Addit Manuf 2023;8:719–31. https://doi.org/10.1007/s40964-023-00450-7.
[6] Ertürk E, Diez JG, Vitale P, Höfer P. Surface morphology influences on the adhesive bond performance of PBF-LB manufactured Ti6Al4V parts – investigation of quasi-static and fatigue loading conditions. J Adhes 2025. https://doi.org/10.1080/00218464.2024.2441886.
[7] Ardila-Rodriguez LA, Rans C, Poulis JA. Effect of surface morphology on the Ti–Ti adhesive bond performance of Ti6Al4V parts fabricated by selective laser melting. Int J Adhesion Adhes 2021;110:102918. https://doi.org/10.1016/j.ijadhadh.2021.102918.
[8] Nusom Y, Srimanosaowapak S, Uthaisangsuk V. Effects of 3D-printing surface morphologies on interfacial bonding strength between Ti–6Al–4V and CFRTP with PMCs interlayer. Int J Adhesion Adhes 2023;121:103313. https://doi.org/10.1016/j.ijadhadh.2022.103313.
[9] Witkin DB, Patel DN, Helvajian H, Steffeney L, Diaz A. Surface treatment of powder-bed fusion additive manufactured metals for improved fatigue life. J Mater Eng Perform 2019;28:681–92. https://doi.org/10.1007/s11665-018-3732-9.
[10] Kahlin M, Ansell H, Basu D, Kerwin A, Newton L, Smith B, Moverare JJ. Improved fatigue strength of additively manufactured Ti6Al4V by surface post processing. Int J Fatig 2020;134:105497. https://doi.org/10.1016/j.ijfatigue.2020.105497.
[11] Gulino M, Lima RAA, Moroni F, Pirondi A, de Freitas ST. Effect of the surface morphology of 3D printed titanium substrates on the mode I fracture toughness of metal-metal and metal-composite bonded joints. Theor Appl Fract Mech 2025;135:104778. https://doi.org/10.1016/j.tafmec.2024.104778.
[12] Wegman RF, van Twisk J. Surface preparation techniques for adhesive bonding. Norwich: William Andrew; 2013. https://doi.org/10.1016/C2012-0-02158-8.
[13] European Union. Regulation (EC) No 1907/2006 of the european parliament and of the council of 18 December 2006 concerning the registration, evaluation, authorisation and restriction of chemicals (REACH). Brussels: Official Journal of the European Union; 2006.
[14] Ledesma R, Palmieri F, Barrios E, Hopkins J, Connell J. Closed-loop control of laser surface treatment via laser induced breakdown spectroscopy. 20th Eur Conf Compos Mat (ECCM20). 2022. Lausanne, Switzerland.
[15] Baburaj EG, Starikov D, Evans J, Shafeev GA, Bensaoula A. Enhancement of adhesive joint strength by laser surface modification. Int J Adhesion Adhes 2007;27:268–76. https://doi.org/10.1016/j.ijadhadh.2006.05.004.
[16] Rotella G, Alfano M, Candamano S. Surface modification of Ti6Al4V alloy by pulsed Yb-laser irradiation for enhanced adhesive bonding. CIRP Ann-Manuf Technol 2015;64:527–30. https://doi.org/10.1016/j.cirp.2015.04.042.
[17] Loumena C, Cherif M, Ali MT, Jumel J, Kling R. Laser surface preparation for adhesive improvement of Ti6Al4V. Proc. SPIE 10092 Laser based Micro Nanoprocessing XI 2017:100921F. https://doi.org/10.1117/12.2252444.
[18] Maressa P, Anodio L, Bernasconi A, Demir AG, Previtali B. Effect of surface texture on the adhesion performance of laser treated Ti6Al4V alloy. J Adhes 2015;91(7):518–37. https://doi.org/10.1080/00218464.2014.933809.
[19] Zhang C, Zhang Y, Chen L, Jin J. Effects of laser processing microgrooves on the shear strength of Ti6Al4V adhesively bonded joints. J Adhes 2021;98(10):1461–79. https://doi.org/10.1080/00218464.2021.1907183.
[20] Rotella G, Orazi L, Alfano M, Candamano S, Gnilitskyi I. Innovative high-speed femtosecond laser nano-patterning for improved adhesive bonding of Ti6Al4V titanium alloy. CIRP J Manuf Sci Technol 2017;18:101–6. https://doi.org/10.1016/j.cirpj.2016.10.003.
[21] Vorobyev AY, Guo C. Femtosecond laser structuring of titanium implants. Appl Surf Sci 2007;253:7272–80. https://doi.org/10.1016/j.apsusc.2007.03.006.
[22] Moritz J, Götze P, Schiefer T, Stepien L, Klotzbach A, Standfuß J, Lopez E, Brückner F, Leyens C. Additive manufacturing of titanium with different surface structures for adhesive bonding and thermal direct joining with fiber-reinforced polyether-ether-ketone (PEEK) for lightweight design applications. Metals 2021;11:265. https://doi.org/10.3390/met11020265.
[23] Shirasu K, Mizutani M, Takano N, Yoshinaga H, Oguri T, Ogawa K, Okabe T, Obayashi S. Lap-shear strength and fracture behavior of CFRP/3D-printed titanium alloy adhesive joint prepared by hot-press-aided co-bonding. Int J Adhesion Adhes 2022;117:103169. https://doi.org/10.1016/j.ijadhadh.2022.103169.
[24] Kurtovic A, Brandl E, Mertens T, Maier HJ. Laser induced surface nano-structuring of Ti–6Al–4V for adhesive bonding. Int J Adhesion Adhes 2013;45:112–7. https://doi.org/10.1016/j.ijadhadh.2013.05.004.
[25] Li S, Lin J, Min J. Experimental investigation and molecular simulation on the chemical bonding between laser-treated titanium alloy amorphous surface and epoxy adhesive. J Adhes 2023. https://doi.org/10.1080/00218464.2023.2277298.
[26] Löbbecke M, Bayerbasi TJ, Bartsch M, Haubrich J. Role of surface structures on long term stability of adhesive joints between Ti–15V–3Cr–3Sn–3Al and polyether-

ether-ketone. Int J Adhesion Adhes 2023;120:103282. https://doi.org/10.1016/j.ijadhadh.2022.103282.
[27] Zimmermann S, Specht U, Spieß L, Romanus H, Krischok S, Himmerlich M, Ihde J. Improved adhesion at titanium surfaces via laser-induced surface oxidation and roughening. Mater Sci Eng 2012;558:755–60. https://doi.org/10.1016/j.msea.2012.08.101.
[28] Taube A, Kurtovic A, Niendorf T, Mertens T, Zinn C, Schaper M, Maier HJ. Influence of surface pre-treatments on the high-cycle fatigue behavior of Ti–6Al–4V – from anodizing to laser-assisted techniques. Int J Fatig 2016;91:195–203. https://doi.org/10.1016/j.ijfatigue.2016.06.010.
[29] Kurtovic A. Laserinduzierte Nanostrukturierung von Titanoberflächen für das strukturelle Kleben - Einfluss auf die Oberflächenmorphologie, Ermüdungs- und Adhäsionseigenschaften. 2014. Dissertation, Universität Paderborn.
[30] Schneider N, Wrobel C. Use of high-energy laser radiation for surface preparation of magnesium for adhesive applications. Appl Adhes Sci 2015;3:17. https://doi.org/10.1186/s40563-015-0044-2.
[31] Deutsches Institut für Normung e. V. Paints and varnishes - pull-off test for adhesion DIN EN ISO 4624. DIN Media, Berlin; 2023. https://doi.org/10.31030/3475823.
[32] The International Organization for Standardization. Adhesives - Determination of the mode 1 adhesive fracture energy of structural adhesive joints using double cantilever beam and tapered double cantilever beam specimens ISO 25217. Berlin: DIN Media; 2009.
[33] Deutsches Institut für Normung e. V. Aerospace series - non-metallic materials - structural adhesives – test method – part 6: determination of shear stress and shear strain EN 2243-6. DIN media, Berlin. https://dx.doi.org/10.31030/9663277; 2006.
[34] ASTM International. Standard specification for additive manufacturing Titanium-6 Aluminum-4 Vanadium ELI (Extra Low Interstitial) with powder bed fusion ASTM F 3001:2014. 2014. West Conshohocken, PA.
[35] Hauk V. Structural and residual stress analysis by nondestructive methods. Amsterdam: Elsevier; 1997.
[36] Henkel Corporation Aerospace. Loctite EA 9396 AERO technical data sheet. https://www.aero-consultants.ch/view/data/3285/Produkte/Henkel%20Adhesive/LOCTITE%20EA%209396%20AERO.pdf. [Accessed 16 April 2025].
[37] Frömmel SA. Untersuchungen zum mechanischen Verhalten von Klebverbindungen unter Berücksichtigung von Grenzflächendefekten. 2013. Dissertation, Universität der Bundeswehr München.
[38] Arikan ES. Oberflächenmodifikation von Polyetheretherketon (PEEK) für das strukturelle Kleben in der Luftfahrt. 2020. Dissertation, Universität der Bundeswehr München.
[39] Blackman BRK, Kinloch AJ, Paraschi M, Teo WS. Measuring the mode I adhesive fracture energy, GIC, of structural adhesive joints: the results of an international round-robin. Int J Adhesion Adhes 2003;23:293–305. https://doi.org/10.1016/S0143-7496(03)00047-2.
[40] ASTM International. Standard test methods and definitions for mechanical testing of steel products ASTM A370-19. 2019. West Conshohocken, PA.
[41] ASTM International. Standard test method for fatigue properties of adhesives in shear by tension loading (Metal/Metal) ASTM D3166-99. 2020. West Conshohocken, PA.
[42] Thäsler T, Holtmannspötter J, Gudladt HJ. Monitoring the fatigue crack growth behavior of composite joints using in situ 2D-digital image correlation. J Adhes 2019;95(5–7):595–613. https://doi.org/10.1080/00218464.2018.1562923.
[43] Tian YS, Chen CZ, Li ST, Huo QH. Research progress on laser surface modification of titanium alloys. Appl Surf Sci 2005;242:177–84. https://doi.org/10.1016/j.apsusc.2004.08.011.
[44] Blackman BRK, Kinloch AJ, Sanchez FSR, Teo WS, Williams JG. The fracture behaviour of structural adhesives under high rates of testing. Eng Fract Mech 2009;76:2868–89. https://doi.org/10.1016/j.engfracmech.2009.07.013.
[45] Öchsner A. Classical beam theories of structural mechanics. Cham: Springer; 2021. https://doi.org/10.1007/978-3-030-76035-9.
[46] Goland M, Reissner E. The stresses in cemented joints. J Appl Mech 1944;11(1):A17–27. https://doi.org/10.1115/1.4009336.
[47] Diez JG, Holtmannspötter J, Arikan E, Höfer P. Combination of scanning electron microscopy and digital image correlation for micrometer-scale analysis of shear-loaded adhesive joints. J Adhes 2025;101(3):557–73. https://doi.org/10.1080/00218464.2024.2370788.

Hybrid Structural Joints between PBF-LB Manufactured Ti6Al4V and CFRP – Role of Surface Morphologies

Emre Ertürk[1,*], Pablo Vitale[1], Philipp Höfer[1]

[1] Institute of Lightweight Engineering, University of the Bundeswehr Munich, Neubiberg, Germany
*Corresponding author: emre.ertuerk@unibw.de

Abstract. Highly effective metal-composite joints can be manufactured by co-curing a composite component with an additively manufactured metal part featuring printed pin-structures in the joining area. In this work, the mechanical performance of such hybrid joints between laser powder bed fusion (PBF-LB) processed Ti6Al4V and a carbon fiber reinforced polymer (CFRP) was investigated for tensile shear loading. Initially, the performance of co-cured hybrid joints with as-built titanium surfaces was compared to secondary bonded joints with properly pre-treated surfaces. Subsequently, the influence of different titanium surface conditions on the hybrid joint behavior was evaluated, considering three cases: as-built, release-agent-coated and laser treated surfaces. Surface morphologies were characterized using scanning electron microscopy and confocal laser scanning microscopy, while the mechanical joint performance was assessed by single step-lap joint testing. Compared to the secondary bonded joints, the co-cured hybrid joints exhibited, on average, a 44.4% higher ultimate tensile shear strength and a threefold increase in fracture shear strain. However, the limit load (i.e., load at damage initiation) of the co-cured joints was substantially lower due to premature adhesive bond failure at the overlap ends, caused by insufficient adhesion of the as-built titanium surface. A highly similar mechanical performance was found for the hybrid joints with as-built and release-agent-coated surfaces. In contrast, the laser treated titanium surface significantly enhanced joint stiffness, limit load, and energy absorption, while the ultimate tensile shear strength increased moderately by at least 9% relative to the other surface conditions.

Keywords: Hybrid joints, Adhesive bonding, Additive manufacturing, Surface morphology.

1 Introduction

In aerospace structures, composites are widely used to reduce weight and improve performance, while metals remain crucial in areas where strength, heat resistance, and damage tolerance are critical. Thus, many metal-composite joints are present in aerospace components [1]. Commonly used joints are between the titanium alloy Ti6Al4V and carbon fiber reinforced polymers (CFRP), which are particularly employed in highly loaded applications, such as load introduction structures. Titanium alloys offer excellent mechanical properties and corrosion resistance. Moreover, they are especially well-suited for joining with CFRP due to their electrochemical compatibility with carbon materials and relatively low coefficient of thermal expansion (CTE). This low CTE enables to minimize thermal stresses during both manufacturing and service conditions [2]. Since joints typically represent the weakest link in structures, the development of high-strength, durable joints is of great importance.
The most common methods for joining metal and composite materials are adhesive bonding and mechanical joining via bolts, screws, or rivets [3,4]. In practice, both methods are often combined to form hybrid joints, which offer several advantages over purely adhesively bonded configurations. These include enhanced structural redundancy (fail-safe behavior), higher joint strength, and improved damage tolerance [5]. However, the use of conventional mechanical fasteners in hybrid metal-composite joints also presents notable drawbacks. Drilling holes for fastener installation damages the composite material, introducing stress concentrations and promoting delamination, which can significantly reduce the load-bearing capacity of the joint. Additionally, the fasteners add significantly to the overall weight, highlighting the potential for further weight reduction.
To mitigate the disadvantages of conventional mechanical fasteners, through-thickness joining techniques have been developed, such as z-pinning [6,7]. A highly effective approach for metal-composite joints involves fabricating macroscopic pins on the metallic substrate, which are then joined to the composite part by co-curing (i.e., simultaneous curing of the composite and bonding to the metallic substrate) [8,9]. The pins are integrated into a prepreg or dry fabric, where they serve as mechanical interlocking features upon completion of the co-curing process. In contrast to bolted joints, the mechanical properties of the composite are less deteriorated with this method, as the fiber orientation is only altered locally without inducing fiber discontinuities. Methods for fabricating pin arrays onto metallic substrates include additive manufacturing (AM) [10,11], laser surface restructuring [12,13], and welding techniques like cold metal transfer (CMT) [14,15]. Among these processes, AM enables highly efficient production, since metal parts with pin-reinforcement can be manufactured in a single process step. Moreover, AM processes, such as the widely used laser powder bed fusion process (PBF-LB), offer

high design flexibility, which allows optimization of pin alignment and geometry according to the specific loading conditions in the metal-composite joint [16].

The mechanical properties of hybrid metal-composite joints incorporating additively manufactured macroscopic pins have been primarily investigated under mode I, mode II and tensile shear loading. Nguyen et al. [11] reported an increase of 377% in mode I steady-state fracture toughness, by integrating PBF-LB-manufactured pins in co-cured Ti6Al4V–CFRP joints. This enhancement was achieved using pins designed for complete pullout from the composite component without pin fracture. In a subsequent study, they were able to further improve the joint performance under mode I loading by structuring the pin surface with, e.g. grooves [17]. Similar Ti6Al4V-CFRP joints were investigated by Bagnato et al. [10] for both mode I and mode II loading. Their results showed significant improvements in interfacial toughness when using PBF-LB pins, although the enhancement was lower in mode II than in mode I. By conducting fatigue mode I and mode II tests, they further demonstrated that pin-reinforcements are also effective in improving the fatigue crack growth resistance due to the formation of a pin-induced crack bridging zone behind the crack tip [18]. Moreover, mixed-mode loading of co-cured Ti6Al4V–CFRP joints with AM-pins was analyzed in several studies [19-22] by performing tensile shear single-lap testing. Parkes et al. [19] reported an increase in ultimate tensile shear strength by up to 6.5 times compared to an unpinned reference joint. Ultrasonic inspection revealed that complete interfacial bond failure occurred first, followed by fracture of the pins. A similar failure mechanism was observed under fatigue loading of the same hybrid single-lap joint [20]. A 246% increase in fatigue strength by using AM-pins in Ti6Al4V–CFRP single-lap joints was shown by Hülsbusch et al. [21] through multi-step fatigue testing. The crack growth behavior under fatigue loading was assessed by Kralovec et al. [22] for similar joints. By utilizing digital image correlation (DIC), they demonstrated that the crack growth is effectively slowed once the crack front encounters a row of pins, resulting in a characteristic pattern of alternating slow and fast crack growth.

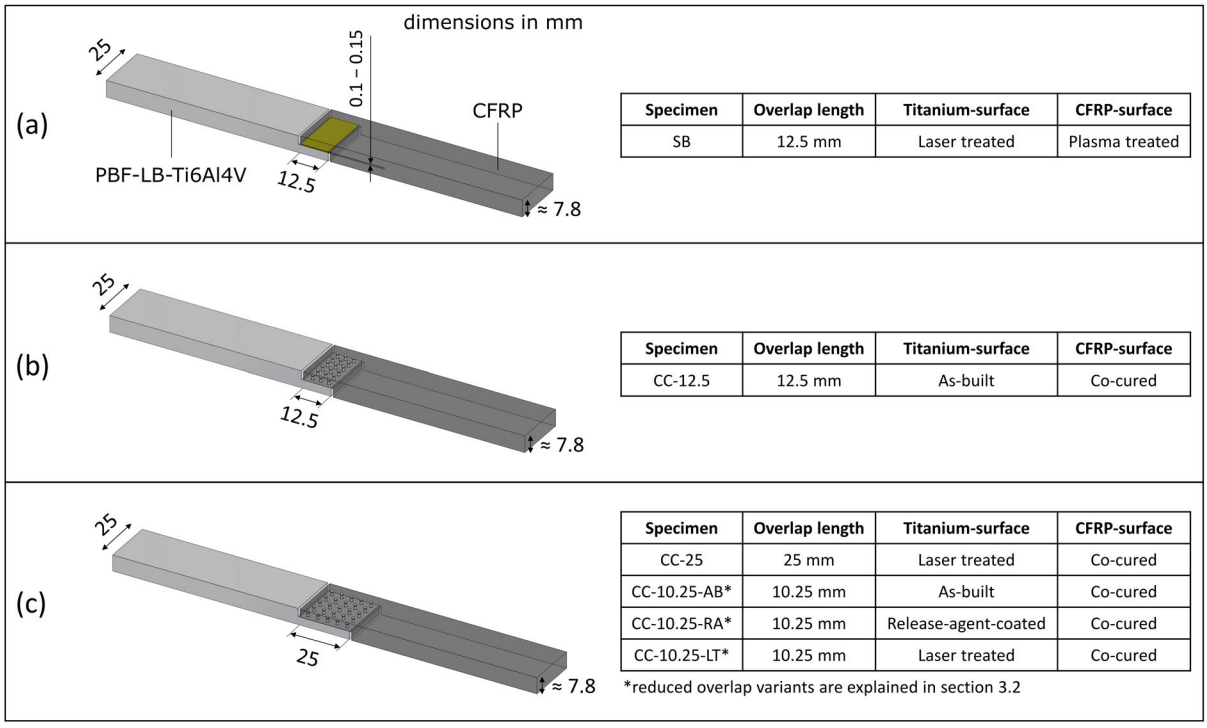
In addition to pin-induced effects, load transfer in co-cured pinned joints also occurs through the adhesive bond formed between the joining partners during the resin curing process, in which the resin acts as the adhesive. The surface properties of the metal part are a decisive factor for the bond performance of metal-composite joints. In case of PBF-LB-manufactured Ti6Al4V, the surfaces exhibit inherent roughness features that are generally favorable for adhesive bonding. However, previous studies [23,24] have shown that effective surface treatment is still necessary to obtain high adhesion under quasi-static, fatigue and environmental loading conditions. A commonly applied method to enhance adhesion between metal and composite surfaces is laser surface structuring, in which microstructures, such as grooves, are created on the metal surface [25-27]. Although laser structuring can significantly increase the bond strength of Ti6Al4V joints, it often leads to substrate damage and the formation of pores that prevent full adhesive penetration [28,29]. Moreover, low bond durability has been reported for additively manufactured Ti6Al4V adherends with laser micro-structured surfaces [26]. Alternatively, lasers can also be used to generate a nanoporous oxide layer on metallic surfaces, which has proven effective for producing high-strength and durable adhesive bonds [24,30,31]. As this technique employs lower laser intensities compared to micro-structuring, the risk of substrate damage is considerably reduced. The surface influence on the mechanical performance of co-cured Ti6Al4V–CFRP joints with pin-reinforcement was addressed by Parkes et al. [19]. However, in their study, only the pins were additively manufactured, while the titanium substrate itself was conventionally fabricated. Consequently, the effect of the inherent roughness of PBF-LB-Ti6Al4V was not fully considered. To the authors best knowledge, no studies have yet systematically addressed the influence of different surface conditions on the mechanical performance of hybrid joints between additively manufactured titanium substrates with pins and CFRP.

In this study, the mechanical properties of co-cured hybrid joints between PBF-LB-Ti6Al4V with pins and CFRP were investigated under tensile shear loading, with a particular focus on the surface morphology influences on load transfer. Initially, a co-cured hybrid joint featuring an as-built Ti6Al4V surface (i.e., only degreased PBF-LB printed surface) was compared to a secondary bonded joint with properly pre-treated surfaces to critically evaluate the enhancement achievable through hybrid joining. Afterwards, the influence of the titanium adherend surface conditions: as-built, release-agent-coated, and laser treated on the mechanical performance of the hybrid joints was analyzed.

2 Materials and methods

2.1 Specimen variants and substrate manufacturing

Three variants of single step-lap joint (SLJ) specimens were investigated, each comprised of a PBF-LB-Ti6Al4V and CFRP adherend. The stepped geometry was used as a continuation of previous work [23,24] on adhesively bonded joints between PBF-LB-Ti6Al4V parts. The first SLJ variant in the present study was a secondary bonded joint, assembled using the two-component epoxy adhesive Loctite EA9396 AERO (Henkel, Germany) (Fig. 1(a)), while the second type was a co-cured hybrid joint with PBF-LB pins (Fig. 1(b)). The same specimen dimensions were defined to enable a direct comparison of the mechanical performance between both joint types. The third variant was also a co-cured joint but with an increased overlap length of 25 mm, used for evaluating the surface influence on joint performance. The extended overlap allowed for the integration of additional pin rows, as this specimen type was originally intended for subsequent fatigue testing. A further difference between the joint variants was the surface condition of the adherends. The secondary bonded SLJs (SB) featured properly pre-treated bonding surfaces, while the titanium surface of the co-cured hybrid joints with 12.5 mm overlap (CC-12.5) was in the as-built condition. Initial testing of the 25 mm overlap configuration with laser-treated titanium surfaces (CC-25) resulted in no fracture at the joint interface. Consequently, the overlap length was reduced to enable investigation of the joint performance for the three titanium surface conditions: as-built, release-agent-coated, and laser treated (details explained in section 3.2).
In all SLJ variants, the CFRP adherend consisted of a combination of unidirectional (UD) and woven (W) prepreg layers, following the quasi-isotropic layup $[\pm 45^{W}, 0^{UD}, \pm 45^{W}, 90_2^{UD}, \pm 45^{W}, 0^{UD}]_S$. This stacking sequence resulted in a cured laminate thickness of approximately 7.8 mm. The UD prepreg Q110-UD-268-34-10/ITS55-24K (Teijin, Japan) and woven prepreg Q110-2/2TW-285-38-10/HTS40-6k (Teijin, Japan) were used. Both materials are based on epoxy thermoset resin systems.



Specimen	Overlap length	Titanium-surface	CFRP-surface
SB	12.5 mm	Laser treated	Plasma treated

Specimen	Overlap length	Titanium-surface	CFRP-surface
CC-12.5	12.5 mm	As-built	Co-cured

Specimen	Overlap length	Titanium-surface	CFRP-surface
CC-25	25 mm	Laser treated	Co-cured
CC-10.25-AB*	10.25 mm	As-built	Co-cured
CC-10.25-RA*	10.25 mm	Release-agent-coated	Co-cured
CC-10.25-LT*	10.25 mm	Laser treated	Co-cured

*reduced overlap variants are explained in section 3.2

Fig. 1 Specimen variants of single step-lap joints (SLJs) between PBF-LB-Ti6Al4V and CFRP: (a) secondary bonded joint, (b) co-cured hybrid joint with pins and 12.5 mm overlap and (c) co-cured hybrid joint with pins and 25 mm overlap.

The Ti6Al4V substrates were additively manufactured by PBF-LB/M on a Trumpf TruPrint 5000 printer, equipped with 500 W fiber lasers. The powder bed was filled with Ti6Al4V Grade 23 powder, featuring a particle size range of 10 to 45 µm. Standard process parameters for this material were used, including a volumetric energy density of 40.5 J/mm^3, a layer thickness of 60 µm and a layer-wise 45° rotating stripe pattern as the laser scanning strategy. All Ti6Al4V-substrates were built with the joining surface oriented parallel to the build platform, as illustrated in Fig. 2. This horizontal orientation was defined to facilitate the manufacturing of the pins, which were oriented orthogonal to the substrate surface. The pins were arranged in a regular grid, with a spacing of 4.75 mm between adjacent pin rows along the overlap direction and a 5 mm spacing between pins across the joint width. The pin

geometry was designed based on optimized shapes proposed by Sarantinos et al. [16] and Parkes et al. [19]. A conical pin head with an undercut geometry was used to enhance the pin-induced mechanical interlocking in the composite. Additionally, the conical shape aided pin integration in the CFRP prepreg layup. At the narrowest section of the undercut, the pin diameter amounted to 1 mm. The diameter was increased slightly towards the base of the pin to enhance resistance against mode II loading [16,19]. The total pin height was defined as 2.8 mm, corresponding to approximately two-thirds of the composite adherend thickness.

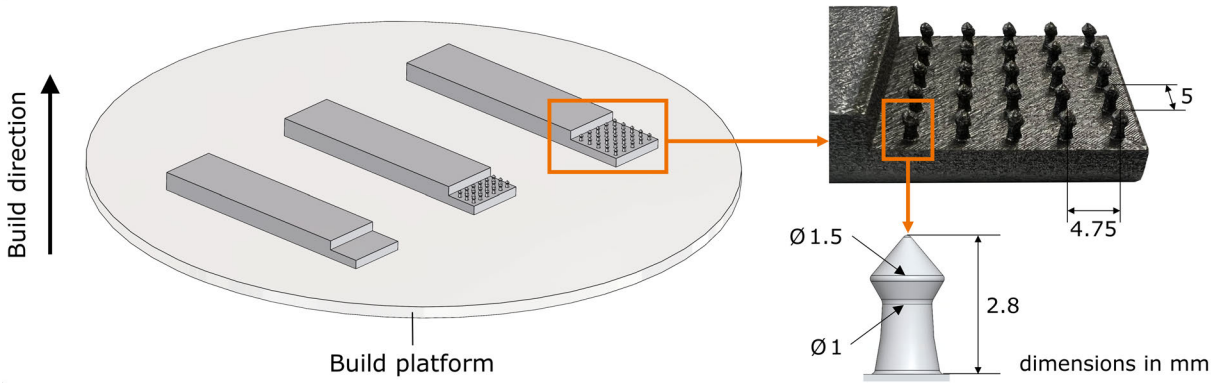


Fig. 2 Build orientation of the Ti6Al4V substrates during PBFLB/M manufacturing, along with the design and spatial pattern of the pin features.

After printing, a standard stress relief heat treatment was conducted under vacuum at 840°C for 2 hours. Subsequently, the substrates were separated from the build plate via electrical discharge machining (EDM) and cleaned in an ultrasonic bath with deionized water to remove loose particles on the surface. In Table 1, the mechanical properties of the adherends and adhesive are summarized. The material data of the PBF-LB-Ti6Al4V and the epoxy adhesive were obtained from tensile testing based on ASTM A370-19 [32] and ASTM D638-14 [33], respectively. Furthermore, the Young's modulus of the CFRP laminate was calculated by classical laminate theory [34], utilizing material data from the UD and woven prepreg materials, obtained in a prior material characterization.

Table 1. Mechanical properties of the used adherend and adhesive materials

	PBF-LB-Ti6Al4V	CFRP $[\pm 45^{W}, 0^{UD}, \pm 45^{W}, 90_2^{UD}, \pm 45^{W}, 0^{UD}]_S$	Loctite EA9396 AERO
Young's Modulus [MPa]	129000	54760	2557
Ultimate tensile strength [MPa]	1040	-	52.3
Fracture strain [%]	10	-	3.9

2.2 Surface preparation

The CFRP substrates used in the secondary bonded joints were first degreased by ultrasonic cleaning in isopropanol. Subsequently, a low-pressure plasma (LPP) treatment was conducted, since this pre-treatment is known to significantly enhance adhesion on polymer surfaces, as demonstrated in several studies [35,36]. The LPP treatment was performed using a Diener Nano SLPC device (Diener Electronic, Germany) with process parameters specified by Diez et al. [37] for epoxy-based CFRP. This process involved exposure to oxygen plasma for 20 minutes at an output power of 300 W and a gas flow rate of 200 sccm.

For the titanium substrates, three different surface conditions were examined: as-built, release agent coated and laser treated. The as-built surface was used to assess the mechanical performance of joints featuring the inherent surface roughness of PBF-LB-processed Ti6Al4V. In contrast, the release agent coating was applied to decouple the pin-induced mechanical interlocking contribution to load transfer from the adhesive bond influence in the co-cured joints. This was done by wiping the surface with the release agent Loctite Frekote 700-NC (Henkel, Germany) using a clean, lint-free cloth. Furthermore, laser treatment was used as an advanced treatment method, which can substantially increase the adhesion capability of the titanium adherend [24, 30].

In the as-built condition, the titanium surfaces were only degreased with acetone in an ultrasonic bath. These as-built surfaces of PBF-LB-Ti6Al4V are characterized by partially melted particles from the powder bed, as shown in Fig. 3. On the horizontally oriented base surface, only a few particles are attached (arithmetical mean surface height $S_a = 6.37 \pm 1.54$ µm), whereas the vertically oriented pin surfaces exhibit a significantly higher particle

density ($S_a = 10.93 \pm 0.97\mu m$). The S_a values were obtained in a previous study using confocal laser scanning microscopy (CLSM) [24].
The laser treated surfaces were first ultrasonically cleaned with acetone before laser treatment. A TRUMPF Trumark Station 5000 marking laser system, equipped with a pulsed Nd:YVO4-Laser (TRUMPF TruMark 6350, $\lambda = 355$ nm) was used for the laser processing. This laser system has a maximum average output power of 50 W and was operated under atmospheric conditions. The applied process parameters were developed in a previous work [24] for PBF-LB-Ti6Al4V to create an open-porous, nanostructured oxide layer on the surface. This nanoroughness promotes strong adhesion by enabling both the formation of interfacial bonds and mechanical interlocking through adhesive infiltration into the nanostructures [23,24,38]. The surface morphology of the titanium adherend after laser treatment is presented in Fig. 3. The surface is characterized by laser pulse structures on micrometer-scale, which are superimposed with the laser-induced nanoporous oxide layer. No surface modification was observed on the pins, as the side faces were oriented parallel to the laser direction and the pin heads were located outside the laser's focal zone. A power level of 70%, a pulse frequency of 20 kHz, a scan speed of 0.4 m/s, and a laser spot diameter of 30 µm were used for creating this surface. The laser followed a horizontal line pattern with a track distance of 30 µm, ensuring that the entire surface was processed once. These settings resulted in a laser energy density of 248 J/cm^2. Following laser processing, fine residual dust on the surface was removed by cleaning with oil-free compressed air. An overview of the applied surface treatments is given in Fig. 1 for the adherends of the investigated specimen variants. It should be noted that the surface of the CFRP prepreg is not pre-treated, since it is used for co-curing. Thus, in the case of the co-cured joints, the CFRP adherend surface condition is referred to as “co-cured”.

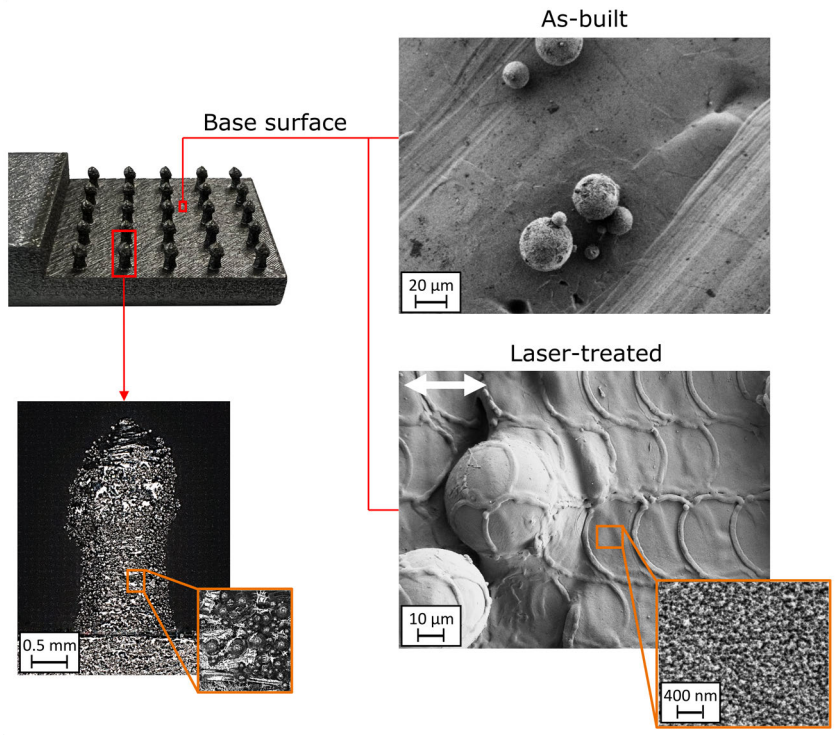


Fig. 3 SEM images of PBF-LB-Ti6Al4V surface morphologies in the as-built and laser treated conditions for the base surface of the titanium substrate, along with CLSM images illustrating the surface morphology of a PBF-LB-processed pin.

2.3 Joining processes

For secondary bonding, the two-component epoxy adhesive Loctite EA 9396 AERO was mixed in a dual asymmetric centrifugal mixer. Afterwards, the pre-treated Ti6Al4V and CFRP substrates were bonded using a fixture for SLJ specimens, ensuring proper alignment and sufficient contact pressure. To prevent butt joint bonding and minimize adhesive fillets, PTFE inserts were placed at the overlap ends. Curing of the adhesive was conducted based on manufacturer recommendations [39] at 66°C for 80 minutes in a convection oven. During post-processing, excess adhesive on the side faces of the specimen was removed using a grinding table. The resulting bond thickness varied along the overlap approximately between 0.1 and 0.15 mm due to the moderately structured PBF-LB surfaces in horizontal orientation.
The co-cured hybrid joints were manufactured by first embedding the PBF-LB pins of the titanium substrate into the CFRP prepreg layup. This was done by pushing the pin array through the prepreg layers, aided by localized

heating to temporarily soften the matrix material. In the next step, the PTFE inserts were positioned at the overlap ends. Subsequently, co-curing was performed in an autoclave using an optimized curing cycle for the used CFRP prepreg systems. This curing cycle was developed to reduce porosities within the composite and involved two constant heating stages at 80°C and 160°C for 20 min and 40 min, respectively, under a pressure of 6 bar. After curing, the side faces of the specimens were ground to remove resin residues on the metal adherends and to obtain a plane surface.

2.4 Surface analysis and mechanical testing

Surface morphologies and fracture surfaces were analyzed using Scanning Electron Microscopy (SEM) and Confocal Laser Scanning Microscopy (CLSM). For SEM, a Zeiss ULTRA Plus field emission scanning electron microscope (Carl Zeiss, Germany) equipped with a Secondary Electron (SE2) detector was utilized and operated at an accelerating voltage of 1 kV. The CLSM images were captured on a Keyence VK-X3000 microscope (Keyence International, Belgium).
The mechanical performance of the joints was evaluated by quasi-static SLJ-testing based on DIN EN 2243-6 [40]. Testing was performed under nominal environmental conditions using a Zwick Z150 universal testing machine (ZwickRoell, Germany) and applying a constant displacement rate of 1 mm/min. The test setup is illustrated in Fig. 4. Mounting the specimens was done by using wedge clamps to avoid damaging the joints during clamping. Furthermore, the digital image correlation (DIC) system Q400 (Limess GmbH, Germany) was used for strain measurement along the bondline. The DIC setup consisted of two 12Mpx cameras (4096x3000 px resolution), paired with macro lenses (80 mm focal length) and distance rings, as well as three LED lights for illumination. The speckle pattern required for DIC was created by airbrush painting the specimen side faces. Image analysis was conducted with a facet size of 29 pixels and a grid spacing of 11 pixels, providing adequate resolution to capture the strains in the bondline. Shear strain evaluation was performed by measuring the relative displacement between two control points (CP) positioned near the bondline at the center of the overlap, as defined in the testing standard [40]. Direct averaging of the strain field along the bondline was not feasible at higher load levels, since bond failure led to severe damage of the speckle pattern at the joint interface. In addition, fatigue SLJ tests were conducted on a servo-hydraulic testing machine for the co-cured hybrid joint with 25 mm overlap length (CC-25). A sinusoidal loading profile was defined, with a frequency of 10 Hz and a load ratio of R=0.1. For each specimen group (see Fig. 1), a minimum of three samples were tested.

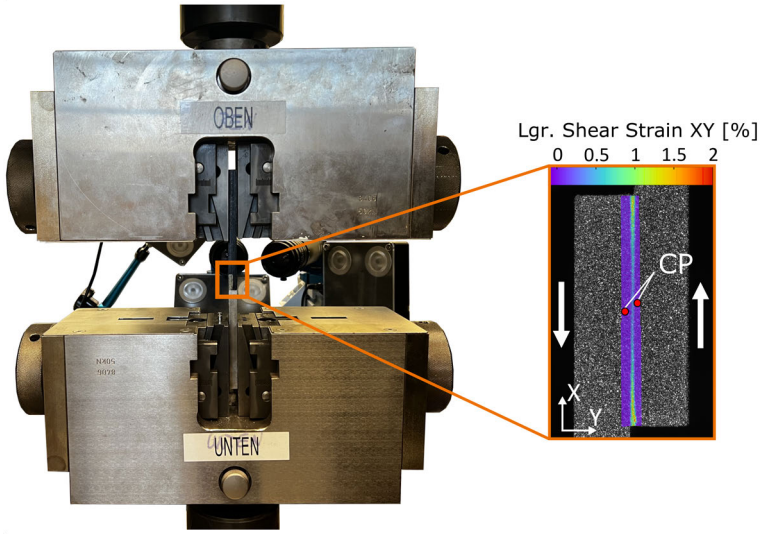


Fig. 4 SLJ test setup with DIC for strain measurement along the bondline. The control points (CP) used for shear strain evaluation are depicted.

3 Results and discussion

3.1 Comparison of secondary bonding and co-cured hybrid joining

The initial step of this study was to compare secondary bonded joints (SB) and co-cured hybrid joints with pin-reinforcements (CC-12.5), both featuring a 12.5 mm overlap length. Importantly, this was not designed as a direct comparison under similar surface conditions. Instead, SB specimens were manufactured using properly pre-treated

adherend surfaces to represent an optimized bonding scenario, whereas CC-12.5 specimens were produced with as-built titanium surfaces (i.e., characterized by lower adhesion strength [23,24]). The rationale was to investigate whether co-curing with as-built titanium adherends can nevertheless provide superior mechanical performance compared to secondary bonding with properly pre-treated adherends. The SLJ test results of the SB and CC-12.5 specimens are presented in Fig. 5. In the displayed stress-strain curves, the stress represents the average tensile shear stress, calculated from the crosshead load and the nominal bonding area, while the strain corresponds to the shear strain, evaluated by DIC.

Both SLJ types exhibited similar elastic stiffness under tensile shear loading. However, damage initiation occurred significantly earlier in the co-cured joints, resulting in an earlier onset of stiffness degradation. Thus, the overall stiffness of the co-cured joint was found to be lower compared to the secondary bonded configuration, despite its pin-reinforcement. This difference can be attributed to the different surface conditions of the titanium adherends. The as-built titanium surfaces in the CC-12.5 joints provided lower adhesion to the CFRP than the properly pre-treated surfaces used in the SB joints. Consequently, premature damage initiation occurred in the co-cured joints due to adhesive failure (i.e., interfacial failure), whereas in the secondary bonded joints, damage onset was observed at significantly higher loads and was associated with delamination of the CFRP adherend. The onset of damage initiation defines the limit load, which is a key design parameter in structural engineering and decisive for certification, as it sets the upper bound for safe operational loading without detrimental structural damage [19,41]. Therefore, appropriate surface pre-treatment of the titanium substrate is crucial to avoid adhesive failure and thereby increase the limit load of hybrid joints.

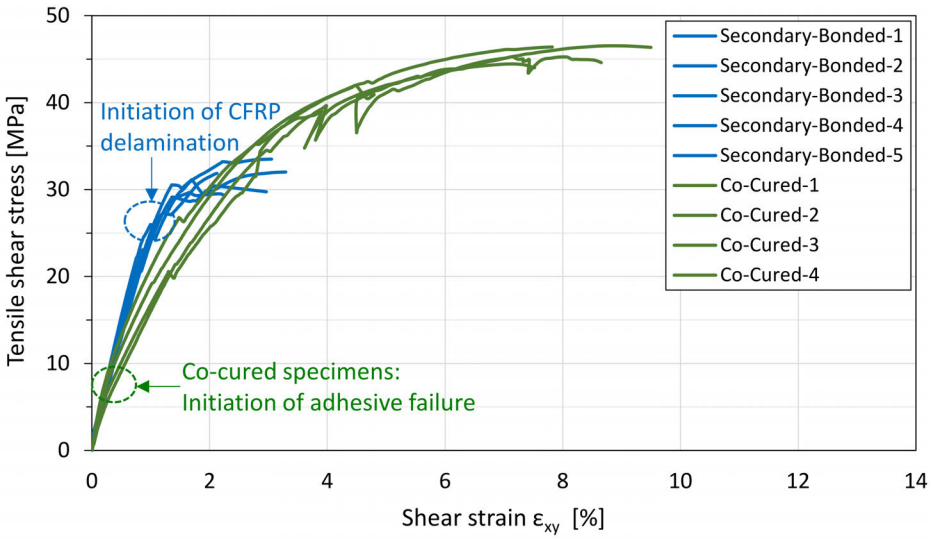


Fig. 5 Stress-strain curves of the secondary bonded SLJs (SB) and co-cured hybrid SLJs (CC-12.5), both featuring an overlap length of 12.5 mm.

In both joint types, the damage initiated at the overlap ends, resulting in two macroscopic crack paths that propagated toward the center of the overlap until complete failure of the adhesive bond occurred. Throughout crack growth, the failure mode of the adhesive bond remained unchanged for each joint. In the co-cured joints, the PBF-LB pins continued to carry loads beyond the adhesive bond failure, leading to an average increase of 44.4% in maximum tensile shear stress and a threefold increase in fracture shear strain compared to the secondary bonded joints. Moreover, the total energy absorption (i.e., area under the force-displacement curve) was enhanced by 554%. In other studies [19,21,22], higher improvements in joint strength by pin-reinforcement (up to 650%) were reported, since those studies compared secondary bonded and co-cured pinned Ti6Al4V-CFRP single-lap joints without applying optimized surface treatments to the secondary bonded joints. This highlights the strong influence of the surface conditions on the potential improvement achievable through hybrid joining over secondary bonding. It can be concluded that pin-reinforcements in co-cured hybrid joints are particularly effective in enhancing ultimate joint strength, ductility and energy absorption, while the adhesive bond contribution to load transfer is decisive for the joint stiffness and limit load.

Fracture in the secondary bonded joints occurred through delamination of the CFRP adherend, as illustrated in Fig. 6(a) by a CLSM image. In contrast, the insufficient adhesion in the co-cured joints led to almost complete adhesive failure on the as-built titanium surface. Matrix resin residues were only observed in areas surrounding partially melted powder particles (Fig. 6(b)). Following adhesive bond failure, the pins were sheared off from the substrate near their base.

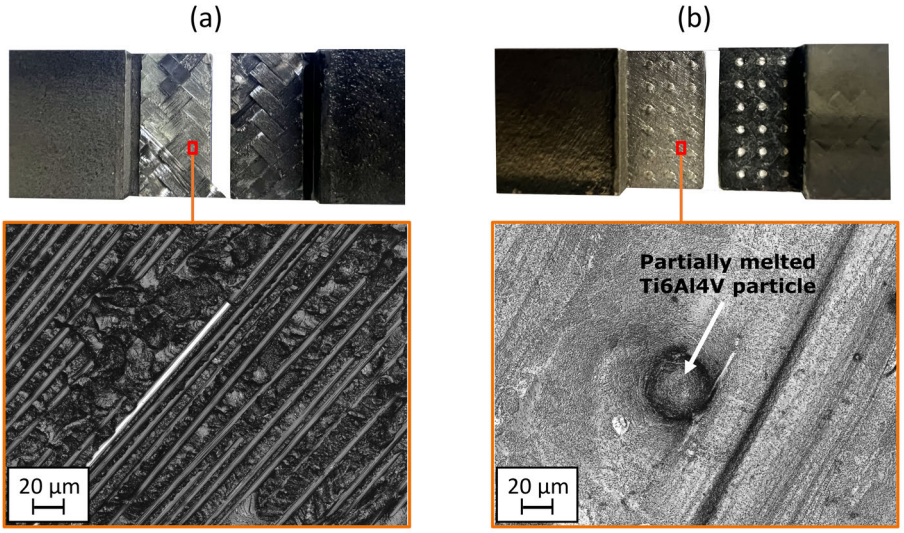


Fig. 6 CLSM images of fracture surfaces of quasi-statically tested SLJs: (a) secondary bonded SLJ with properly pre-treated surfaces (SB) and (b) co-cured hybrid SLJ with as-built titanium surface and a 12.5 mm overlap length (CC-12.5).

Evaluating the strain distributions along the overlap by DIC at different tensile shear stress levels provided additional insights into the loading conditions of the bondline. In general, SLJs are subjected to mixed-mode loading, characterized by a combination of non-uniform shear and peel stresses, with stress concentrations at the overlap ends. The corresponding shear strain distributions (Lagrangian strain) are illustrated for both SLJ variants in Fig. 7.

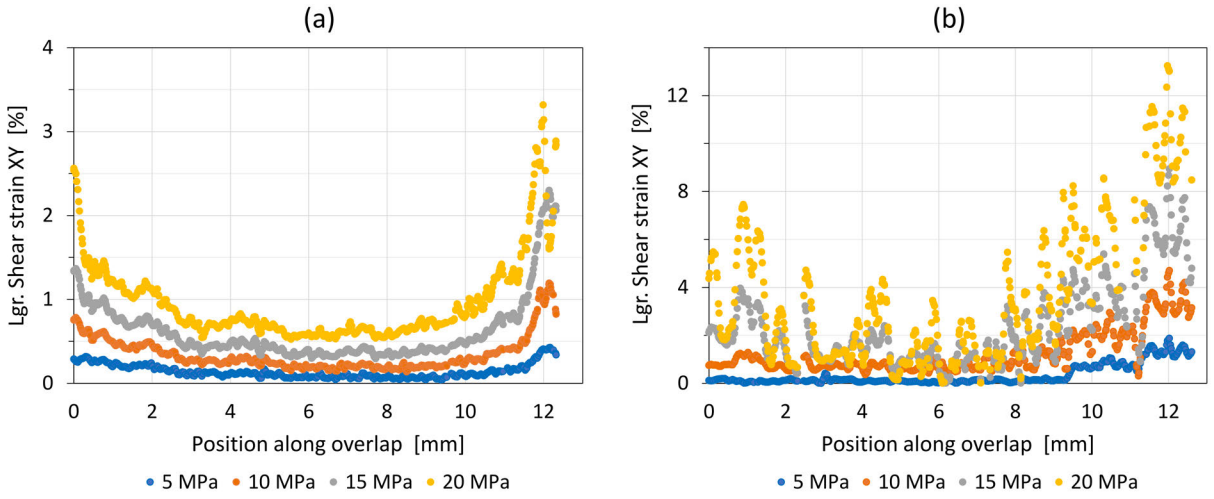


Fig. 7 Shear strain distributions along the bondline, evaluated by DIC at different load levels, for (a) a SB and (b) a CC-12.5 specimen.

The shear strains along the bondline are generally lower in the secondary bonded joint, due to the higher joint stiffness resulting from the properly pre-treated adherend surfaces. In both joint variants, an asymmetric shear strain distribution is present, which is caused by the stiffness mismatch between the titanium and CFRP adherends. The significantly lower transversal stiffness of the CFRP adherend led to a higher shear strain concentration at the overlap end, where the titanium adherend ends. This effect was also observed in the qualitatively similar peel strain distributions for both joint types. As a result, damage initiation occurred first at this overlap end, which is consistent with the observations of Kralovec et al. [22] for quasi-statically tested Ti6Al4V–CFRP single-lap joints.

The DIC measurements of the co-cured joints exhibited increased scatter in the strain data at load levels above 10 MPa (Fig. 7(b)), primarily due to microcracking in the surface coating used for the speckle pattern. These cracks were induced by the elevated local strains along the overlap. Although the quantitative reliability of the data is reduced under these conditions, the strain distributions can still be evaluated qualitatively to extract general trends. The results indicate that, with increasing load, the inner regions of the overlap progressively contribute to load transfer, similarly to the behavior observed in the secondary bonded joints. Moreover, comparing the shear strains at the overlap positions of approximately 10 mm and 12 mm in both joint variants reveals a smaller strain difference

in the co-cured joint. Since the first pin row is located at the 10 mm position, it can be assumed that the outermost pins contribute to a more uniform strain distribution. An optimization of the pin positions and geometry could further improve the uniformity of the strain distribution.

3.2 Co-cured hybrid SLJ with 25 mm overlap length

Increasing the overlap length of the co-cured hybrid SLJ from 12.5 mm with three pin-rows (CC-12.5) to 25 mm with five pin-rows (CC-25) resulted in a shift in failure mode from fracture at the joint interface to adherend fracture. This was observed in both fatigue and quasi-static SLJ tests.

Fatigue testing

It was initially planned to conduct fatigue testing of the co-cured joint with 25 mm overlap for the titanium surface conditions: as-built, release-agent-coated, and laser-treated. The objective was to evaluate the influence of surface morphology on joint performance by testing at several maximum stress levels σ_{max}. However, initial testing of the CC-25 specimens with laser-treated titanium surfaces revealed that no fracture at the joint interface can be achieved with this joint configuration. The damage state of a CC-25 specimen subjected to a relatively high maximum stress level of $\sigma_{max} = 12.8$ MPa (about 41% of the quasi-static joint strength) is illustrated in Fig. 8, shortly before ultimate failure.

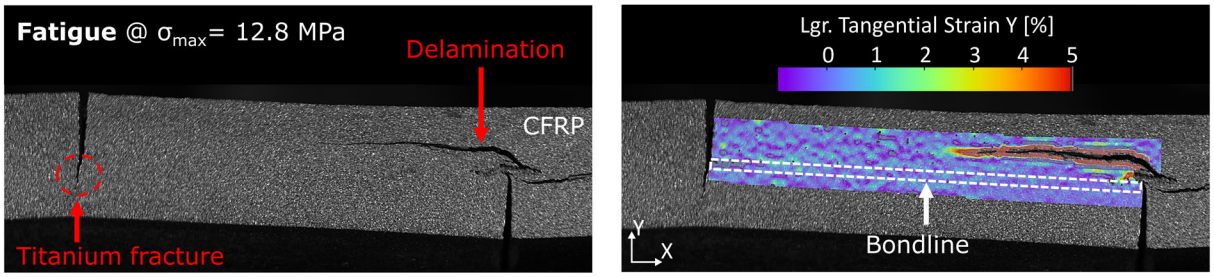


Fig. 8 Damage state in a fatigue-loaded CC-25 specimen near ultimate failure. The ultimate failure occurred through titanium adherend fracture.

Initial damage occurred in the CFRP adherend through multiple delaminations at the step geometry. One delamination propagated approximately at the height of the pin heads, toward the opposite overlap end. Before reaching it, a crack initiated in the titanium adherend at the inner corner of the step geometry. This crack rapidly led to ultimate failure through fracture of the titanium adherend after a total of 22490 load cycles. The local stress concentration at the inner corner of the step, in combination with the inherent surface roughness of the PBF-LB-Ti6Al4V material are the main factors for this adherend failure. Regarding the joint interface, almost no significant deformations were observed along the bondline, as confirmed by DIC strain measurements (Fig. 8). The peel strain ($\varepsilon_{y,Lagrange}$) field is shown in this figure since it is suitable for visualizing crack opening. Fatigue testing at lower σ_{max} levels increased the joint lifetime and prevented the formation of delaminations in the CFRP adherend. However, ultimate failure still occurred through fracture of the titanium adherend at the step geometry without considerable bondline damage. This outcome indicates that the fatigue durability of the CC-25 joint interface exceeds those of the adherends, regardless of the applied fatigue load level. The lifetime results are given in Table 2.

Table 2. Fatigue results of CC-25 specimens tested at different maximum stress levels σ_{max}

Maximum stress σ_{max} [MPa]	12.8	9.6	8	6.4
Lifetime [Cycles]	22490	109404	445970	1509879
Failure mode	Fracture of titanium adherend			

Since fracture at the joint interface could not be achieved, the effect of the titanium surface morphology on fatigue performance could not be assessed. Consequently, no further fatigue testing of the CC-25 joint was conducted.

Quasi-static testing

Under quasi-static loading, the CC-25 joint failed due to fracture of the CFRP adherend. The failure was initiated by delamination at the CFRP step geometry (Fig. 9). Contrary to fatigue loading, the delamination reached the opposite overlap end. This induced higher loading of the remaining load-carrying CFRP cross-section, which ultimately resulted in net-tension failure of the CFRP. DIC analysis revealed that, shortly before ultimate failure,

the bondline was fully damaged, leaving the PBF-LB pins as the sole remaining structural elements for load transfer. The bondline was more severely loaded compared to fatigue loading, but the intended fracture at the joint interface was not obtained, since the pins remained intact.

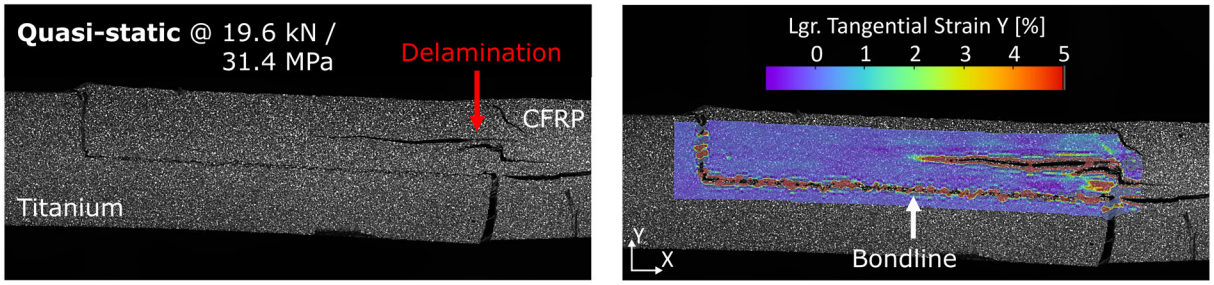


Fig. 9 Damage state in a quasi-statically-loaded CC-25 specimen near ultimate failure. The ultimate failure occurred through CFRP delamination, followed by net-tension failure of the CFRP adherend.

The results demonstrate that the number of pins used in the CC-25 joint design exceeds the structural requirements, suggesting potential for weight reduction. This underscores the need to carefully balance overlap length and pin-reinforcement to design weight-optimized hybrid joints suitable for both static and cyclic loading conditions.
To enable investigation of surface morphology effects, the overlap length of the co-cured joints with 25 mm overlap was reduced by milling the CFRP adherend. Removal of three pin rows resulted in an overlap of 10.25 mm, as illustrated in Fig. 10. Quasi-static testing of this modified configuration successfully led to fracture at the joint interface, while fatigue testing still resulted in titanium adherend fracture. Therefore, the specimen geometry shown was used for conducting quasi-static SLJ tests with the different titanium surface conditions.

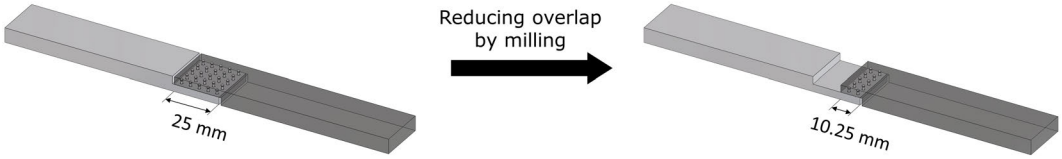


Fig. 10 Transition from the co-cured hybrid joint with 25 mm overlap length and 5 pin rows to a reduced 10.25 mm overlap with two pin rows, by milling the CFRP adherend.

3.3 Effects of titanium adherend surface condition

The stress-strain curves obtained from quasi-static testing of the co-cured hybrid SLJs with a reduced overlap length of 10.25 mm (CC-10.25) are presented in Fig. 11. The test results show a comparison of the titanium surface conditions: as-built (AB), release-agent-coated (RA) and laser treated (LT).
For the specimens with the titanium surface conditions AB and RA, similar stress-strain curves were found. Only the elastic stiffness was significantly higher when using the AB surface, since adhesive bonding between the adherends was intentionally prevented in the RA specimens. This demonstrates that, except for elastic stiffness, the adhesive bond contribution to load transfer in co-cured hybrid joints with pin-reinforcement offers no significant benefit when using the as-built PBF-LB-Ti6Al4V surface with horizontal build orientation. The insufficient adhesion of the as-built surface substantially limited the effectiveness of the adhesive bond, as it caused early damage initiation due to adhesive failure at the overlap ends (see DIC evaluation in Fig. 11), similar to the CC-12.5 joint. Fracture surface analysis confirmed that nearly complete adhesive failure occurred on the as-built surfaces (Fig. 12(a)). A predominant adhesive failure on the as-built titanium surface was also observed in a previous study [24] by SEM analysis of fracture surfaces from metal-metal SLJs bonded with an epoxy adhesive. The as-built fracture surface is highly similar to that of the release-agent-coated surface (Fig. 12(b)), underscoring the poor adhesion. Notably, even on the release-agent-coated surface, adhesive residues are present around partially melted particles, indicating local mechanical interlocking. Increasing the number of attached particles on the PBF-LB-processed surface is therefore assumed to enhance the adhesive bond contribution to load transfer in pin-reinforced hybrid joints. The particle density could be increased by modifying the AM process parameters and fabricating the titanium substrate at an inclined build angle rather than the horizontal orientation used in this study. However, it should be noted that an inclined build orientation may negatively affect the geometric accuracy of the produced pins.

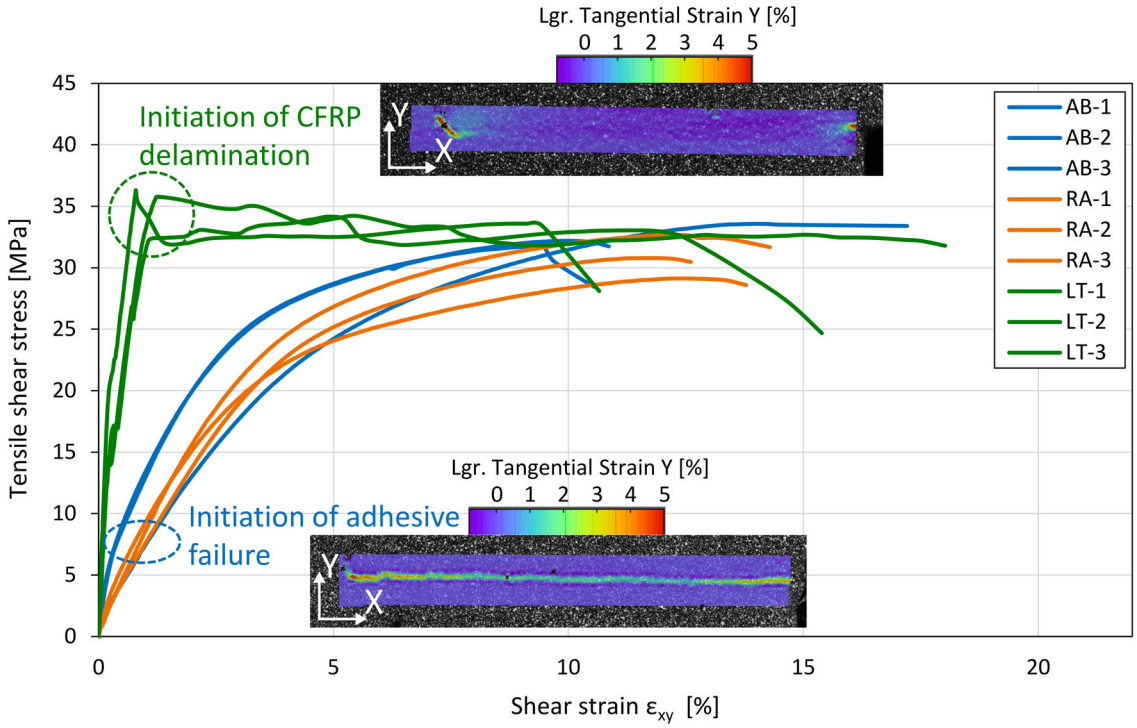


Fig. 11 Stress-strain curves of the co-cured hybrid SLJs with a reduced overlap length of 10.25 mm (CC-10.25) for the PBF-LB-Ti6Al4V adherend surface conditions: as-built (AB), release-agent-coated (RA) and laser treated (LT).

In contrast, using the laser treated titanium surface significantly improved the mechanical joint performance. On average, the joint's elastic stiffness E increased by 188.8%, the total energy absorption W by 48.4%, the fracture shear strain $\varepsilon_{xy,max}$ by 14.1% and the maximum tensile shear stress σ_{max} by 9% in comparison to the AB surface condition. The elastic stiffness was evaluated by applying a linear fit to the elastic region of the stress-strain curve, with a coefficient of determination of $R^2 \geq 0.995$. A comparison of the mechanical joint performance between the different surface conditions is given in Table 3.

Table 3. Mechanical properties of the CC-10.25 specimens with the titanium adherend surface conditions: as-built (AB), release-agent-coated (RA) and laser treated (LT).

	E [MPa]	σ_{max} [MPa]	$\varepsilon_{xy,max}$ [%]	W [J]
CC-10.25-AB	1498,53 ± 390.04	32.49 ± 0.97	12.87 ± 3.76	1.87 ± 0.56
CC-10.25-RA	360,13 ± 42.25	30.87 ± 1.78	13.56 ± 0.86	1.83 ± 0.2
CC-10.25-LT	4328,33 ± 675.86	35.41 ± 1.11	14.69 ± 3.73	2.78 ± 0.84

The significantly higher elastic stiffness of the CC-10.25-LT joint can be attributed to the laser-induced increase in interfacial stiffness between the titanium adherend and the CFRP matrix resin. The laser-generated nanoporous oxide layer promotes mechanical interlocking through adhesive infiltration into the nanostructures and facilitates the formation of chemical and dispersive bonds at the interface [23,24,38], thereby reducing early micro-slip along the bondline. This improvement in interfacial stiffness is reflected in the observed overall higher joint stiffness and also in the increase of the total energy absorption compared to the AB and RA surface conditions. Regarding the ultimate strength (σ_{max}) of pin-reinforced metal-composite joints, Parkes et al. [19] reported that laser nano-structuring of conventionally manufactured titanium substrates led to an improvement of only 1-2%. The higher, though still moderate, enhancement of σ_{max} in the present study may be related to the formation of a more pronounced nanoporous oxide layer.

The high adhesion provided by the laser-induced nanoporous oxide layer almost completely prevented premature adhesive failure, leading instead to fracture by delamination in the CFRP adherend (Fig. 12(c)). Localized fracture of the nanoporous oxide layer was found, but this accounted for only a negligible portion of the overall fracture surface. It can therefore be assumed that the local oxide fracture had no considerable effect on the measured stress-strain response. The delamination in the CFRP initiated at the overlap ends under tensile shear stresses above 30 MPa (see DIC image in Fig. 11) and propagated toward the center of the overlap. This late damage onset demonstrates that the LT surface condition enables a significantly higher limit load compared to the other surface

conditions. An improvement of the limit load by laser treatment was also observed in a preceding work [24], but for metal-metal SLJs with PBF-LB-Ti6Al4V adherends.
The stress-strain curves of the LT-specimens exhibit minor irregularities prior to reaching the maximum stress. However, the DIC measurements showed no indication of damage initiation in the joint area that could be related to these irregularities. Furthermore, such nonlinearities were not observed in the more compliant joints with the AB and RA titanium surface conditions. It is therefore assumed that these irregularities are related to the high joint stiffness and do not indicate structural damage. Possible reasons are micro-slippage in the wedge clamps and increased uncertainties in the strain evaluation due to the low strain values. Following the onset of delamination in the LT-specimens, the load rapidly plateaued until ultimate failure occurred through fracture of the pins from the titanium adherend. The pins failed after substantial elongation, demonstrating the high energy absorption offered by the pin-induced mechanical interlocking. It can be stated that the surface condition of the titanium adherend in co-cured hybrid SLJs has a significant influence on joint stiffness, damage initiation, and total energy absorption, while its effect on maximum shear stress and fracture strain is comparatively moderate.

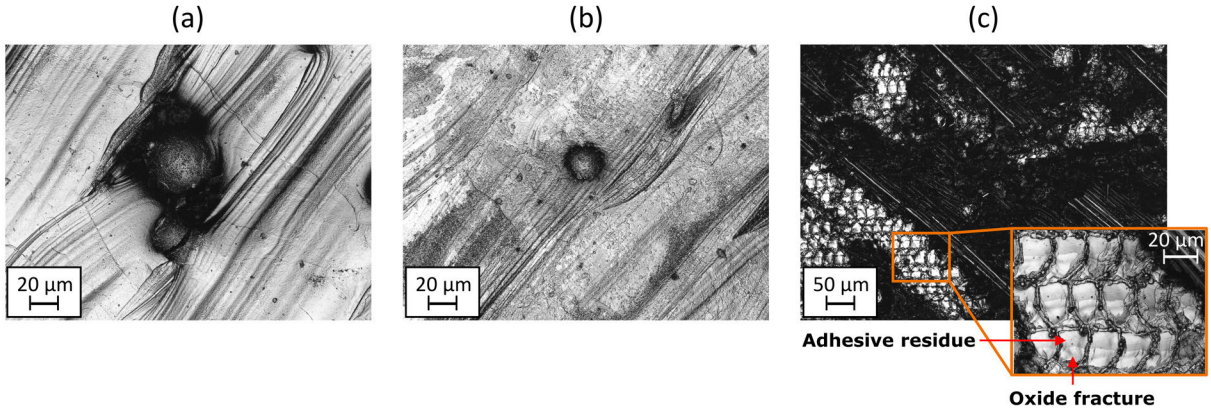


Fig. 12 Fracture surfaces of the quasi-statically tested CC-10.25 specimens with the titanium adherend surface conditions: (a) as-built, (b) release-agent-coated and (c) laser treated, obtained from CLSM.

4 Conclusions

The mechanical performance of co-cured hybrid SLJs with pin-reinforcement between PBF-LB-Ti6Al4V and CFRP was investigated, with a particular focus on the influence of the titanium surface condition. A comparison between co-cured hybrid joints with as-built titanium surfaces and secondary bonded joints with properly pre-treated surfaces revealed that the limit load of the co-cured joints is significantly lower, despite its pin-reinforcement. This was caused by the insufficient adhesion of the as-built titanium surface, which induced earlier damage initiation due to adhesive failure. Apart from that, the PBF-LB-processed pins proved highly effective in increasing the ultimate tensile shear strength (+44.4%) and fracture shear strain (+206%), thereby also enhancing the energy absorption capacity of the joint by 554%. Furthermore, increasing the overlap length of the hybrid joints from 12.5 mm to 25 mm and using five pin rows instead of three, resulted in fracture of the titanium adherend under fatigue loading and net-tension failure of the CFRP adherend under quasi-static loading. A direct comparison of quasi-statically tested co-cured hybrid SLJs with different titanium surface conditions showed almost no significant differences in mechanical joint performance between as-built and release-agent-coated surfaces. Only the elastic joint stiffness was substantially higher when using the as-built surface. This demonstrated that the adhesive bond contribution to the load transfer is highly limited, when using the as-built PBF-LB-Ti6Al4V surface with horizontal build orientation. In contrast, application of laser treatment for this surface led to a significant increase in the joint's elastic stiffness (+188.8%), total energy absorption (+48.4%) and limit load, while the ultimate tensile shear strength improved moderately by at least 9% compared to the other surface conditions.
In the case of properly pre-treated titanium surfaces, damage initiation in the SLJs occurred through delamination in the CFRP. The delamination initiated at the overlap ends due to local stress concentrations. Thus, to further increase the limit load, improvements towards more uniform loading along the overlap are needed. In this context, the potential benefits of optimizing pin alignment and geometry should be investigated. Additionally, future investigations are necessary to assess the environmental durability of hybrid metal-composite joints with pin-reinforcement.

CRediT authorship contribution statement

Emre Ertürk: Writing - original draft, Conceptualization, Methodology, Investigation, Formal analysis, Validation, Visualization. **Pablo Vitale:** Writing - Review & Editing, Investigation. **Philipp Höfer:** Writing - Review & Editing, Supervision, Funding acquisition.

Disclosure statement

The authors report there are no competing interests to declare.

Data availability

Data will be made available upon request.

Acknowledgements

This work is part of the research project BLANCA, which was funded by the Bavarian Ministry of Economic affairs, Regional development and Energy (StMWi) within the program BayLu-25. We thank the project partner Modell- und Formenbau Blasius GERG GmbH, for printing the substrates. The authors also thank the Institute of Materials Science (University of the Bundeswehr Munich) and the Bundeswehr research institute WIWeB for providing access to their laboratory equipment.



References

1. Xu J, Mkaddem A, Mansori M (2016) Recent advances in drilling hybrid FRP/Ti composite: A state-of-the-art review. Compos Struct 135:316-338. http://dx.doi.org/10.1016/j.compstruct.2015.09.028
2. Kolesnikov B, Herbeck L, Fink A (2008) CFRP/titanium hybrid material for improving composite bolted joints. Compos Struct 83:368-380. https://doi.org/10.1016/j.compstruct.2007.05.010
3. Galinska A (2020) Mechanical Joining of Fibre Reinforced Polymer Composites to Metals—A Review. Part I: Bolted Joining. Polymers 12:2252. https://doi.org/10.3390/polym12102252
4. Galinska A, Galinski C (2020) Mechanical Joining of Fibre Reinforced Polymer Composites to Metals—A Review. Part II: Riveting, Clinching, Non-Adhesive Form-Locked Joints, Pin and Loop Joining. Polymers 12:1681. https://doi.org/10.3390/polym12081681
5. Bodjona K, Lessard L (2016) Hybrid bonded-fastened joints and their application in composite structures: A general review. J Reinf Plast and Compos 35:764-781. https://doi.org/10.1177/0731684415627296
6. Venugopal A, Sudhagar E, Rajamohan V, Suresh V, Karthikeyan N, Naveen J (2025) The impact of graphene reinforcement on z-pin and adhesively bonded composite for enhancing flexural strength of co-cured single lap joints. The J of Adhesion 101(11):1363–1394. https://doi.org/10.1080/00218464.2025.2462223
7. Karimi S (2024) Enhancing mechanical properties of GFRP–aluminum joints through Z pinning: a low velocity shear impact study. J of Adhesion Sci and Tech 38(24):4391-4404. https://doi.org/10.1080/01694243.2024.2375282
8. Graham DP, Rezai A, Baker D, Smith PA, Watts JF (2014) The development and scalability of a high strength, damage tolerant, hybrid joining scheme for composite–metal structures. Compos Part A 64:11-24. https://doi.org/10.1016/j.compositesa.2014.04.018
9. Sarantinos N, Tsantzalis S, Ucsnik S, Kostopoulos V (2019) Review of through-the-thickness reinforced composites in joints. Compos Struct 229:111404. https://doi.org/10.1016/j.compstruct.2019.111404
10. Bagnato T, Ravindran AR, Mirabedini A, Ladani RB, Kandare E, Orifici AC, Chang P, Wang J, Mouritz AP (2023) Superior interfacial toughening of hybrid metal-composite structural Joints using 3D printed pins. Compos Part A 168:107479. https://doi.org/10.1016/j.compositesa.2023.107479
11. Nguyen ATT, Brandt M, Feih S, Orifici AC (2016) Pin pull-out behaviour for hybrid metal-composite joints with integrated reinforcements. Compos Struct 155:160-172. https://doi.org/10.1016/j.compstruct.2016.07.047
12. Smith F (2005) Comeld™: An Innovation in Composite to Metal Joining. Mat Tech 20:91-96. https://doi.org/10.1080/10667857.2005.11753117
13. Wang X, Ahn J, Kaboglu C, Yu L, Blackman BRK (2016) Characterisation of composite-titanium alloy hybrid joints using digital image correlation. Compos Struct 140:702-711. https://doi.org/10.1016/j.compstruct.2015.12.023
14. Ucsnik S, Scheerer M, Zaremba S, Pahr DH (2010) Experimental investigation of a novel hybrid metal–composite joining technology. Compos Part A 41:369-374. https://doi.org/10.1016/j.compositesa.2009.11.003

15. Skhabovskyi I, Batista NL, Damato CA, Reis RP, Botelho EC, Scotti A (2017) Appraisal of fiber-metal laminate panels reinforced with metal Pins deposited by CMT welding. Compos Struct 180:263-275. https://doi.org/10.1016/j.compstruct.2017.07.043
16. Sarantinos N, Kostopoulos V, Di Vita G, Campoli G, Bricout L (2019) Micro-pins: the next step in composite–Composite and metal–composite joining. CEAS Space J 11:351-358.
17. Nguyen ATT, Amarasinghe CK, Brandt M, Feih S, Orifici A (2017) Loading, support and geometry effects for pin-reinforced hybrid metal-composite joints. Compos Part A 98:192-206. https://doi.org/10.1016/j.compositesa.2017.03.019
18. Bagnato T, Ravindran AR, Orifici A, Kandare E, Ladani RB (2025) Interfacial fatigue performance of hybrid titanium to composite Joints reinforced with 3D printed pins. Compos Part A 196:108984. https://doi.org/10.1016/j.compositesa.2025.108984
19. Parkes PN, Butler R, Meyer J, de Oliveira A (2014) Static strength of metal-composite joints with penetrative reinforcement. Compos Struct 118:250-256. https://doi.org/10.1016/j.compstruct.2014.07.019
20. Parkes PN, Butler R, Almond DP (2013) Fatigue of Metal-Composite Joints with Penetrative Reinforcement. 54th AIAA/ASME/ASCE/AHS/ASC Struct, Struct Dynamic and Mat Conf, Boston, USA. https://doi.org/10.2514/6.2013-1879
21. Huelsbusch D, Haack M, Solbach A, Emmelmann C, Walther F (2015) Influence of pin size on tensile and fatigue behavior of TI-CFRP hybrid structures produced by laser additive manufacturing. 20th Int Conf Compos Mat, Copenhagen, Denmark.
22. Kralovec C, Dengg A, Schagerl M, Schiller A, Bisagni C, Löbbecke M, Haubrich J, Hanelt R (2025) Static strength and fatigue life of pinned hybrid titanium-composite single-lap-shear joints. Compos Struct 354:118765. https://doi.org/10.1016/j.compstruct.2024.118765
23. Ertürk E, Musil B, Diez G, Felber C, Höfer P (2023) Surface morphology influences of PBF-LB manufactured Ti6Al4V parts on adhesive bond strength – investigation of as-built and surface-treated conditions. Prog Addit Manuf 8:719–731. https://doi.org/10.1007/s40964-023-00450-7
24. Ertürk E, Diez JG, Vitale P, Höfer P (2025) Surface morphology influences on the adhesive bond performance of PBF-LB manufactured Ti6Al4V parts – investigation of quasi-static and fatigue loading conditions. The J of Adhesion 101(10): 1219–1251. https://doi.org/10.1080/00218464.2024.2441886
25. Shirasu K, Mizutani M, Takano N, Yoshinaga H, Oguri T, Ogawa K, Okabe T, Obayashi S (2022) Lap-shear strength and fracture behavior of CFRP/3D-printed Titanium alloy adhesive joint prepared by hot-press-aided co-bonding. Int J Adhesion & Adh 117:103169. https://doi.org/10.1016/j.ijadhadh.2022.103169
26. Moritz J, Götze P, Schiefer T, Stepien L, Klotzbach A, Standfuß J, Lopez E, Brückner F, Leyens C (2021) Additive manufacturing of titanium with different surface structures for adhesive bonding and thermal direct joining with fiber-reinforced polyether-ether-ketone (PEEK) for lightweight design applications. Metals 11:265. https://doi.org/10.3390/met11020265
27. Nguyen ATT, Brandt M, Orifici AC, Feih S (2016) Hierarchical surface features for improved bonding and fracture toughness of metal-metal and metal-composite bonded joints. Int J Adhesion & Adh 66:81–92. https://doi.org/10.1016/j.ijadhadh.2015.12.005
28. Maressa P, Anodio L, Bernasconi A, Demir AG, Previtali B (2015) Effect of surface texture on the adhesion performance of laser treated Ti6Al4V alloy. The J of Adhesion 91(7):518-537. https://doi.org/10.1080/00218464.2014.933809
29. Zhang C, Zhang Y, Chen L, Jin J (2021) Effects of laser processing microgrooves on the shear strength of Ti6Al4V adhesively bonded joints. The J of Adhesion 98(10):1461-1479. https://doi.org/10.1080/00218464.2021.1907183
30. Kurtovic A, Brandl E, Mertens T, Maier HJ (2013) Laser induced surface nano-structuring of Ti–6Al–4V for adhesive bonding. Int J Adhesion & Adh 45:112-117. https://doi.org/10.1016/j.ijadhadh.2013.05.004
31. Löbbecke M, Bayerbasi TJ, Bartsch M, Haubrich J (2023) Role of surface structures on long term stability of adhesive joints between Ti–15V–3Cr–3Sn–3Al and polyether-ether-ketone. Int J Adhesion & Adh 120:103282. https://doi.org/10.1016/j.ijadhadh.2022.103282
32. ASTM International (2019) Standard test methods and definitions for mechanical testing of steel products ASTM A370-19. West Conshohocken, PA.
33. ASTM International (2014) Standard test method for tensile properties of plastics. ASTM D638-14. West Conshohocken, PA.
34. Öchsner A (2021) Foundations of Classical Laminate Theory. Springer, Cham. https://doi.org/10.1007/978-3-030-82631-4
35. Pizzorni M, Lertora E, Gambaro C, Mandolfino C, Salerno M, Prato M (2019) Low-pressure plasma treatment of CFRP substrates for epoxy-adhesive bonding: an investigation of the effect of various process gases. Int J Adv Manuf Technol 102:3021-3035. https://doi.org/10.1007/s00170-019-03350-9
36. Arikan E, Holtmannspötter J, Zimmer F, Hofmann T, Gudladt HJ (2019) The role of chemical surface modification for structural adhesive bonding on polymers - Washability of chemical functionalization without reducing adhesion. Int J Adhesion & Adh 95:102409. https://doi.org/10.1016/j.ijadhadh.2019.102409
37. Diez JG, Holtmannspötter J, Arikan E, Höfer P (2025) Combination of scanning electron microscopy and digital image correlation for micrometer-scale analysis of shear-loaded adhesive joints. The J of Adhesion 101(3):557-573. https://doi.org/10.1080/00218464.2024.2370788

38. da Silva LFM, Öchsner A, Adams RD, editors (2018) Handbook of adhesion technology. Springer, Berlin, Heidelberg. https://doi.org/10.1007/978-3-319-55411-2
39. Henkel Corporation Aerospace (2013) Loctite EA 9396 AERO Technical Data Sheet. https://www.aero-consultants.ch/view/data/3285/Produkte/Henkel%20Adhesive/LOCTITE%20EA%209396%20AERO.pdf. Accessed 29 June 2025
40. Deutsches Institut für Normung e. V (2006) Aerospace series - Non-metallic materials - Structural adhesives – Test method – Part 6: Determination of shear stress and shear strain EN 2243-6. DIN Media, Berlin. https://dx.doi.org/10.31030/9663277
41. Wright JR, Cooper JE (2014) Introduction to Aircraft Aeroelasticity and Loads. Wiley, Chichester, U.K. https://doi.org/10.1002/9781118700440

Extended list of publications

Additional publications and conference contributions, which are not included in this thesis, are listed below:

Reviewed conference paper (not directly related to this thesis):

- Ertürk E, Bold J, Höfer P, Stark C, Höhn W (2022) 3D Material Model for Additive Manufactured Metallic Parts. In: Rieser J, Endress F, Horoschenkoff A, Höfer P, Dickhut T, Zimmermann M (editors) Proceedings of the Munich Symposium on Lightweight Design 2021. Springer Vieweg, Berlin, Heidelberg. https://doi.org/10.1007/978-3-662-65216-9_16.
- Ertürk E, Bold J, Stark C, Höhn W, Höfer P (2024) Analytical and Numerical Modeling of Aramid Honeycomb Cores. In: Endress F, Rieser J, Horoschenkoff A, Höfer P, Dickhut T, Zimmermann M (editors) Proceedings of the Munich Symposium on Lightweight Design 2023. Springer, Cham. https://doi.org/10.1007/978-3-031-64669-0_14.

Conference presentations:

- Ertürk E, Bold J, Höfer P, Stark C, Höhn W (2021) 3D Material Model for Additive Manufactured Metallic Parts. 18th Munich Symposium on Lightweight Design, Munich, Germany.
- Ertürk E, Musil B, Diez G, Felber C, Höfer P (2022) Surface morphology influences on the adhesive bond of Ti6Al4V parts fabricated by laser powder bed fusion for as-built and surface treated conditions. 15th International Conference on Advanced Computational Engineering and Experimenting, Florence, Italy.
- Ertürk E, Bold J, Stark C, Höhn W, Höfer P (2022) Structural bonding of additively manufactured metal parts: Surface preparation and variations in bonding geometry. 19th Munich Symposium on Lightweight Design, Munich, Germany.
- Ertürk E, Bold J, Stark C, Höhn W, Höfer P (2023) Analytical and numerical modeling of Aramid honeycomb sandwich structures with CFRP face sheets. 20th Munich Symposium on Lightweight Design, Munich, Germany.
- Ertürk E, Bold J, Stark C, Höhn W, Höfer P (2024) Bonded Additively Manufactured Load Introductions in Sandwich Parts Certified with Support of Numerical Analysis. 21th Munich Symposium on Lightweight Design, Munich, Germany.

A.2 NaTESi anodization

Prior to NaTESi anodization, the milled PBF-LB-Ti6Al4V substrates were degreased using an alkaline cleaner, followed by a pickling step to remove the native oxide layer. After anodizing, the surfaces were rinsed with deionized water and dried at room temperature. The parameters of the NaTESi process are summarized in Table 5.

Table 5: NaTESi process parameters [78,79]

Chemicals	NaOH: 300 g/l	EDTA: 30 g/l
	Na-tartrate: 65 g/l	Na_2SiO_3: 6 g/l
Voltage [V]	10	
Current density [A/dm^2]	2	
Temperature [°C]	30 ± 3	
Time [min]	15	